National Library of Canada
Bibliothèque nationale du Canada

Canadian Theses Service
Service des thèses canadiennes

Ottawa, Canada
K1A 0N4

NOTICE

The quality of this microform is heavily dependent upon the quality of the original thesis submitted for microfilming. Every effort has been made to ensure the highest quality of reproduction possible.

If pages are missing, contact the university which granted the degree.

Some pages may have indistinct print especially if the original pages were typed with a poor typewriter ribbon or if the university sent us an inferior photocopy.

Reproduction in full or in part of this microform is governed by the Canadian Copyright Act, R.S.C. 1970, c. C-30, and subsequent amendments.

AVIS

La qualité de cette microforme dépend grandement de la qualité de la thèse soumise au microfilmage. Nous avons tout fait pour assurer une qualité supérieure de reproduction.

S'il manque des pages, veuillez communiquer avec l'université qui a conféré le grade.

La qualité d'impression de certaines pages peut laisser à désirer, surtout si les pages originales ont été dactylographiées à l'aide d'un ruban usé ou si l'université nous a fait parvenir une photocopie de qualité inférieure.

La reproduction, même partielle, de cette microforme est soumise à la Loi canadienne sur le droit d'auteur, SRC 1970, c. C-30, et ses amendements subséquents.

NL-339 (r. 88/04) c

Canada

University of Alberta

Experimental Investigation of Developing and Fully Developed Flow in a Curved Duct of Square Cross Section

by

© Barry M. Bara

A thesis
submitted to the Faculty of Graduate Studies and Research
in partial fulfillment of the requirements for the degree of

Doctor of Philosophy

Department of Mechanical Engineering

Edmonton, Alberta

Fall 1991

National Library of Canada
Bibliothèque nationale du Canada

Canadian Theses Service
Service des thèses canadiennes

Ottawa, Canada
K1A 0N4

The author has granted an irrevocable non-exclusive licence allowing the National Library of Canada to reproduce, loan, distribute or sell copies of his/her thesis by any means and in any form or format, making this thesis available to interested persons.

L'auteur a accordé une licence irrévocable et non exclusive permettant à la Bibliothèque nationale du Canada de reproduire, prêter, distribuer ou vendre des copies de sa thèse de quelque manière et sous quelque forme que ce soit pour mettre des exemplaires de cette thèse à la disposition des personnes intéressées.

The author retains ownership of the copyright in his/her thesis. Neither the thesis nor substantial extracts from it may be printed or otherwise reproduced without his/her permission.

L'auteur conserve la propriété du droit d'auteur qui protège sa thèse. Ni la thèse ni des extraits substantiels de celle-ci ne doivent être imprimés ou autrement reproduits sans son autorisation.

ISBN 0-315-70029-7

Canada

University of Alberta

Release Form

Name of Author: **Barry M. Bara**

Title of Thesis: **Experimental Investigation of Developing and Fully Developed Flow in a Curved Duct of Square Cross Section**

Degree: Doctor of Philosophy

Year this degree granted: Fall 1991

Permission is hereby granted to the **University of Alberta Library** to reproduce single copies of this thesis and to lend or sell such copies for private, scholarly or scientific research purposes only.

The author reserves all other publication and other rights in association with the copyright in the thesis, and except as hereinbefore provided neither the thesis nor any substantial portion thereof may be printed or otherwise reproduced in any material form whatever without the author's prior written permission.

Barry Bara

(Student's signature)

Barry M. Bara
c/o 5411-115 St.
Edmonton, Alberta
Canada
T6H 3P4

Date : July 22, 1991

University of Alberta

Faculty of Graduate Studies and Research

The undersigned certify that they have read, and recommend to the Faculty of Graduate Studies and Research for acceptance, a thesis entitled **Experimental Investigation of Developing and Fully Developed Flow in a Curved Duct of Square Cross Section** submitted by **Barry M. Bara** in partial fulfillment of the requirements for the degree of **Doctor of Philosophy**.

.....

D. J. Wilson (Supervisor)

.....

S. A. Berger

.....

J. H. Masliyah

.....

K. Nandakumar

.....

K. C. Cheng

Date : JUNE 26, 1991

dedicated to my wife

Abstract

An experimental and numerical study investigating the flow development and fully developed flows of an incompressible Newtonian fluid in a curved duct of square cross section for a curvature ratio of 15.1 is presented. Numerical simulations of flow development were performed using a parabolized form of the steady three-dimensional Navier-Stokes equations without imposing numerical symmetry. In addition, the two-dimensional solution structure was calculated using a steady formulation of the governing equations with a symmetry condition applied at the horizontal duct centerline. Both the three-dimensional and two-dimensional computer codes used in this study had been developed by previous investigators.

Laser doppler measurements of axial velocity and flow visualization at $Dn = 125$, 137 and 150, revealed a steady and symmetric two-vortex flow at $Dn = 125$, and a steady and symmetric four-vortex flow at both $Dn = 137$ and $Dn = 150$ ($Dn = Re/\sqrt{R/a}$ where Re is the Reynolds number, R is the radius of curvature of the duct and a is the width of the duct). Axial velocity measurements showed that the four-vortex flow at $Dn = 150$ developed to the solution predicted by the two-dimensional numerical simulation. However, the four-vortex flow at $Dn = 137$ was still developing when the flow had reached the end of the 240° axial length of the duct. A numerical investigation for Dean numbers below $Dn = 175$ revealed that at the limit point of the two-cell to four-cell transition the development length

appeared to be infinite and thereafter decreased for increasing Dean numbers. The behavior of decreasing development length of the four-vortex flow with increasing Dean number has not been reported previously.

Using a symmetrically positioned pin at $\theta = 5°$ to induce the four-cell flows, the two-dimensional solution structure for $Dn \leq 150$ was experimentally observed for the first time. Experiments confirmed the numerical prediction that four-vortex flows are stable to symmetric perturbations, but unstable to asymmetric perturbations. An experimental and numerical investigation suggested that the four-vortex flow might evolve to flows with sustained spatial oscillations farther downstream. However without sufficient axial length to experimentally verify this, the state of the four-vortex flow at large axial distances still remains an unknown.

Acknowledgments

I would like to thank my family and friends for their love, support and encouragement throughout this project. Special thanks to my wife, Sheelagh, for her love, support and understanding through what must have seemed to be a never ending task.

I wish to thank Dr. D. J. Wilson, Dr. J. H. Masliyah and Dr. K. Nandakumar for their encouragement, guidance and patience. The Departments of Mechanical and Chemical Engineering are gratefully acknowledged for their cooperation in allowing my research to be carried out in the Department of Chemical Engineering.

Assistance in the form of operating and equipment grants from the Natural Sciences and Engineering Research Council (NSERC) to Dr. J. H. Masliyah and Dr. K. Nandakumar made this study possible. Financial assistance in the form of scholarships and fellowships from NSERC and the Province of Alberta are gratefully acknowledged.

Thanks are also due to the Chemical Engineering machine shop for their excellent work in the fabrication of many devices for the experimental system. Special thanks is due to John VanDoorn for his excellent craftsmanship in the construction of the curved duct apparatus. I am also grateful to the Mechanical and Chemical Engineering technicians who provided assistance throughout this project.

Contents

Chapter 1

Introduction 1

1.1 Overview of Thesis 3

Chapter 2

Literature Review 6

2.1 Fully Developed Flow in Curved Ducts of Rectangular Cross Section . 8

2.2 Bifurcation Phenomena 11

2.2.1 Bifurcation Phenomena in Curved Pipes 12

2.2.2 Bifurcation Phenomena in Curved Ducts of Rectangular Cross Section 15

2.2.3 Bifurcation Phenomena in Other Related Problems 18

2.3 Developing Flow in Curved Ducts 19

2.3.1 Developing Flow in Curved Pipes: Parabolic Inlet 20

2.3.2 Developing Flow in Curved Pipes: Free Vortex and Uniform Inlet 21

2.4 Developing Flow in Curved Ducts of Rectangular Cross Section . . . 27

2.5 Summary 33

Chapter 3

Governing Equations **36**

3.1 Developing Flow Equations 38

3.2 Fully Developed Flow Equations 40

3.3 Definition of Dean Number 42

3.4 Comparison of Fully Developed Solutions from 3-D and 2-D Codes . . 43

Chapter 4

Experimental System **47**

4.1 Experimental Apparatus 47

4.1.1 Construction of Experimental Apparatus 50

4.1.2 Design of Inlet Section 53

4.1.3 Temperature Control 57

4.2 Velocity Measurements 59

4.3 Flow Visualization 61

4.3.1 Laser Light Sheet 61

4.3.2 Photographing Secondary Flows 63

4.3.3 Digital Enhancement of Photographs 65

Chapter 5

Experimental Errors **67**

5.1 Uncertainty in Dean Number 67

5.2 Uncertainties in LDV Calibration 69

5.2.1 Measurement of Beam Crossing Angle 70

5.2.2 Spinning Wheel as Velocity Standard 70

5.2.3 Inlet Profile as Velocity Standard 72

5.3 Uncertainties in Velocity Measurements 76

5.3.1 Uncertainty in a Typical Velocity Measurement 76

5.3.2 Output Bias of Tracker Processor 78

5.3.3 Effect of Curved Wall 81

5.3.4 Traversing Errors 83

5.3.5 Errors in Measuring Vertical Profiles 86

5.3.6 Wall Location Error 88

5.4 Summary 90

Chapter 6

Investigation of Developing Flows **92**

6.1 Inlet Flow 92

6.2 Flow Development at Dn=125 97

6.3 Flow Development at Dn=137 110

6.4 Flow Development at Dn=150 121

6.5 Development Length 138

Chapter 7

Two-Dimensional Solution Structure 150

7.1 Experimental Difficulties in Observing Two-Dimensional Solution Structure 153

7.2 Reduction of Development Length 158

7.3 Experimental Observation of Dual Solutions 162

7.4 Role of Pin in Inducing Four-Vortex Flows 168

Chapter 8

Stability of Flows 172

8.1 Steadiness of Flows 173

8.2 Numerical Investigation of Flow Behavior at Large Axial Distances . 183

8.3 Response of Flow to Asymmetric Inlet Perturbations 199

Chapter 9

Conclusions and Recommendations 206

9.1 Future Studies 208

9.2 Equipment Improvements 209

References 210

Appendix A

Uncertainty Analysis Method 219

Appendix B

Correcting Velocity for Surface Curvature 221

B.1 Traversing Along a Radial Line 222

B.2 Traversing Along an Arbitrary Path 226

Appendix C

Physical Properties **231**

C.1 Water 231

C.2 Plexiglass 232

C.3 Rhodamine Dye 232

C.4 Silicon Carbide Particles 233

Appendix D

Tabulated Data **234**

List of Tables

D.1 Dean numbers of measured horizontal velocity profiles at $Dn = 125$. 235

D.2 Dean numbers of measured horizontal velocity profiles at $Dn = 137$. 235

D.3 Dean numbers of measured horizontal velocity profiles at $Dn = 150$. 236

D.4 Dean numbers of measured vertical velocity profiles at $Dn = 150$ . . . 236

D.5 Tabulated data for figure 6.64 237

List of Figures

3.1 Cylindrical coordinate system. 37

3.2 Comparison of radial simulations at $Dn = 125$ and $z'/a = 0.0$. 45

3.3 Comparison of vertical simulations at $Dn = 125$ and $x'/a = 0.0$. . . . 45

3.4 Comparison of radial simulations at $Dn = 150$ and $z'/a = 0.0$. 46

3.5 Comparison of vertical simulations at $Dn = 150$ and $x'/a = 0.0$. . . . 46

4.1 Schematic of curved duct apparatus 48

4.2 Photograph of experimental system 51

4.3 Schematic of stilling chamber, straight section and curved section . . 54

4.4 Detailed schematic of stilling chamber 55

4.5 Schematic of fixed laser light sheet 62

4.6 Schematic of fiber optic light sheet 64

5.1 Comparison of measured inlet profiles to analytical prediction 73

5.2 Comparison of tracker measurements to FFT measurements 79

5.3 Effect of tracker range setting on measured velocities 80

5.4 Correction factor vs. radial position in duct. 82

5.5 Traversing distance in water compared to traversing distance in air. . 82

5.6 Effect of positioning errors on a velocity profile 85

5.7 Effect of traversing direction on measured vertical profile 87

5.8 Shape of vertical profiles for a $\pm 5\%$ change in duct position 87

5.9 Correction to radial positions of axial velocities by relocation of inner wall 89

6.1 Comparison of inlet velocity profiles calculated from analytical and approximate formulations 94

6.2 Comparison of measured inlet velocity profiles to analytical predictions 96

6.3 Measured velocity profile vs. simulation at $Dn = 125$, $\theta = 20°$ and $z'/a = 0.0$ 101

6.4 Measured velocity profile vs. simulation at $Dn = 125$, $\theta = 40°$ and $z'/a = 0.0$ 101

6.5 Measured velocity profile vs. simulation at $Dn = 125$, $\theta = 60°$ and $z'/a = 0.0$ 102

6.6 Measured velocity profile vs. simulation at $Dn = 125$, $\theta = 80°$ and $z'/a = 0.0$ 102

6.7 Measured velocity profile vs. simulation at $Dn = 125$, $\theta = 100°$ and $z'/a = 0.0$ 103

6.8 Measured velocity profile vs. simulation at $Dn = 125$, $\theta = 120°$ and $z'/a = 0.0$ 103

6.9 Measured velocity profile vs. simulation at $Dn = 125$, $\theta = 140°$ and $z'/a = 0.0$ 104

6.10 Measured velocity profile vs. simulation at $Dn = 125$, $\theta = 160°$ and $z'/a = 0.0$ 104

6.11 Measured velocity profile vs. simulation at $Dn = 125$, $\theta = 180°$ and $z'/a = 0.0$ 105

6.12 Measured velocity profile vs. simulation at $Dn = 125$, $\theta = 200°$ and $z'/a = 0.0$ 105

6.13 Measured velocity profile vs. simulation at $Dn = 125$, $\theta = 220°$ and $z'/a = 0.0$ 106

6.14 Measured velocity profile vs. simulation at $Dn = 125$, $\theta = 240°$ and $z'/a = 0.0$ 106

6.15 Measured velocity profile vs. simulation at $Dn = 125$, $\theta = 20°$ and $x'/a = 0.0$ 107

6.16 Measured velocity profile vs. simulation at $Dn = 125$, $\theta = 220°$ and $x'/a = 0.0$ 107
6.17 Arrow plots showing secondary flow development at $Dn = 125$ 108
6.18 Flow visualization showing secondary flow development at $Dn = 125.5$ 109
6.19 Measured velocity profile vs. simulation at $Dn = 137$, $\theta = 20°$ and $z'/a = 0.0$ 113
6.20 Measured velocity profile vs. simulation at $Dn = 137$, $\theta = 40°$ and $z'/a = 0.0$ 113
6.21 Measured velocity profile vs. simulation at $Dn = 137$, $\theta = 60°$ and $z'/a = 0.0$ 114
6.22 Measured velocity profile vs. simulation at $Dn = 137$, $\theta = 80°$ and $z'/a = 0.0$ 114
6.23 Measured velocity profile vs. simulation at $Dn = 137$, $\theta = 100°$ and $z'/a = 0.0$ 115
6.24 Measured velocity profile vs. simulation at $Dn = 137$, $\theta = 120°$ and $z'/a = 0.0$ 115
6.25 Measured velocity profile vs. simulation at $Dn = 137$, $\theta = 140°$ and $z'/a = 0.0$ 116
6.26 Measured velocity profile vs. simulation at $Dn = 137$, $\theta = 160°$ and $z'/a = 0.0$ 116
6.27 Measured velocity profile vs. simulation at $Dn = 137$, $\theta = 180°$ and $z'/a = 0.0$ 117
6.28 Measured velocity profile vs. simulation at $Dn = 137$, $\theta = 200°$ and $z'/a = 0.0$ 117
6.29 Measured velocity profile vs. simulation at $Dn = 137$, $\theta = 220°$ and $z'/a = 0.0$ 118
6.30 Measured velocity profile vs. simulation at $Dn = 137$, $\theta = 240°$ and $z'/a = 0.0$ 118
6.31 Arrow plots showing secondary flow development at $Dn = 137$ 119
6.32 Flow visualization showing secondary flow development at $Dn = 137.1$ 120
6.33 Measured velocity profile vs. simulation at $Dn = 150$, $\theta = 20°$ and $z'/a = 0.0$ 124

6.34 Measured velocity profile vs. simulation at $Dn = 150$, $\theta = 40°$ and $z'/a = 0.0$ 124
6.35 Measured velocity profile vs. simulation at $Dn = 150$, $\theta = 60°$ and $z'/a = 0.0$ 125
6.36 Measured velocity profile vs. simulation at $Dn = 150$, $\theta = 80°$ and $z'/a = 0.0$ 125
6.37 Measured velocity profile vs. simulation at $Dn = 150$, $\theta = 100°$ and $z'/a = 0.0$ 126
6.38 Measured velocity profile vs. simulation at $Dn = 150$, $\theta = 120°$ and $z'/a = 0.0$ 126
6.39 Measured velocity profile vs. simulation at $Dn = 150$, $\theta = 140°$ and $z'/a = 0.0$ 127
6.40 Measured velocity profile vs. simulation at $Dn = 150$, $\theta = 160°$ and $z'/a = 0.0$ 127
6.41 Measured velocity profile vs. simulation at $Dn = 150$, $\theta = 180°$ and $z'/a = 0.0$ 128
6.42 Measured velocity profile vs. simulation at $Dn = 150$, $\theta = 200°$ and $z'/a = 0.0$ 128
6.43 Measured velocity profile vs. simulation at $Dn = 150$, $\theta = 220°$ and $z'/a = 0.0$ 129
6.44 Measured velocity profile vs. simulation at $Dn = 150$, $\theta = 240°$ and $z'/a = 0.0$ 129
6.45 Measured velocity profile vs. simulation at $Dn = 150$, $\theta = 20°$ and $x'/a = 0.0$ 130
6.46 Measured velocity profile vs. simulation at $Dn = 150$, $\theta = 40°$ and $x'/a = 0.0$ 130
6.47 Measured velocity profile vs. simulation at $Dn = 150$, $\theta = 60°$ and $x'/a = 0.0$ 131
6.48 Measured velocity profile vs. simulation at $Dn = 150$, $\theta = 80°$ and $x'/a = 0.0$ 131
6.49 Measured velocity profile vs. simulation at $Dn = 150$, $\theta = 100°$ and $x'/a = 0.0$ 132

6.50 Measured velocity profile vs. simulation at $Dn = 150$, $\theta = 120°$ and $x'/a = 0.0$ . . . 132

6.51 Measured velocity profile vs. simulation at $Dn = 150$, $\theta = 140°$ and $x'/a = 0.0$ . . . 133

6.52 Measured velocity profile vs. simulation at $Dn = 150$, $\theta = 160°$ and $x'/a = 0.0$ . . . 133

6.53 Measured velocity profile vs. simulation at $Dn = 150$, $\theta = 180°$ and $x'/a = 0.0$ . . . 134

6.54 Measured velocity profile vs. simulation at $Dn = 150$, $\theta = 200°$ and $x'/a = 0.0$ . . . 134

6.55 Measured velocity profile vs. simulation at $Dn = 150$, $\theta = 220°$ and $x'/a = 0.0$ . . . 135

6.56 Measured velocity profile vs. simulation at $Dn = 150$, $\theta = 240°$ and $x'/a = 0.0$ . . . 135

6.57 Arrow plots showing secondary flow development at $Dn = 150$ . . . 136

6.58 Flow visualization showing secondary flow development at $Dn = 149.9$ 137

6.59 Numerically calculated state diagram showing flow development at $Dn = 137$ . . . 139

6.60 Experimental state diagram of flow development at $Dn = 125$ 141

6.61 Experimental state diagram of flow development at $Dn = 137$ 142

6.62 Experimental state diagram of flow development at $Dn = 150$ 143

6.63 Numerically generated state diagram for $Dn = 125$, 131, 133, 137 and 150 . . . 145

6.64 Numerical simulation of development length vs. Dean number 146

6.65 Numerical comparison of development length for different inlet profiles 148

7.1 State diagram showing 2-D solution structure . . . 152

7.2 Natural occurring solution structure at $\theta = 220°$ . . . 155

7.3 Arrow plots of natural occurring solution structure at $\theta = 220°$ 156

7.4 Flow visualization of natural occurring solution structure at $\theta = 220°$ 157

7.5 State diagram showing reduction of development length at $Dn = 137$ 159
7.6 Axial velocity profiles at $Dn = 137$ with a symmetric trip at $\theta = 5°$. 160
7.7 Flow visualization of development at $Dn = 133.9$ with a symmetric trip at $\theta = 5°$ 161
7.8 State diagram showing measured 2-D solution structure 163
7.9 Role of pin in observing 2-D solution structure 164
7.10 Measured axial velocity profile of a two-cell flow at $Dn = 125$ 166
7.11 Measured axial velocity profile of a four-cell flow at $Dn = 125$ 166
7.12 Flow visualization and secondary flow streamlines of two-cell flow at $Dn = 123.4$ 167
7.13 Flow visualization and secondary flow streamlines of four-cell flow at $Dn = 123.4$ 167
7.14 3-D axial velocity plot of two-cell flow at $Dn = 123.4$ 169
7.15 3-D axial velocity plot of four-cell flow at $Dn = 123.4$ 169
7.16 Axial velocity profile at $Dn = 125$, $\theta = 20°$ and $x'/a = 0.32$ with and without pin 170
7.17 Axial velocity profile at $Dn = 125$, $\theta = 20°$ and $x'/a = 0.0$ with and without pin 171
7.18 Axial velocity profile at $Dn = 125$, $\theta = 20°$ and $x'/a = 0.0$ with and without pin 171

8.1 Steadiness of flows in straight duct inlet section 176
8.2 Steadiness of a two-cell and four-cell flow at $Dn \simeq 125$ 177
8.3 Steadiness of the four-cell flow at $Dn = 137.6$ 178
8.4 Steadiness of the four-cell flow at $Dn = 149.8$ 179
8.5 Flow at $Dn = 199.5$ showing heat transfer related time dependence . 180
8.6 Steadiness of an asymmetric four-cell flow at $Dn = 198.8$ 181
8.7 Flow visualization at $\theta = 220°$ with hand warming inlet 182
8.8 Flow development to $\theta = 2000°$ at $Dn = 125$ 187
8.9 Flow development to $\theta = 4000°$ at $Dn = 130$ 188

8.10 Flow development to $\theta = 3000°$ at $Dn = 137$ 189
8.11 Flow development to $\theta = 2000°$ at $Dn = 150$ 190
8.12 Flow development to $\theta = 2000°$ at $Dn = 200$ 191
8.13 Spatial oscillation between $\theta = 600°$ and $\theta = 1200°$ at $Dn = 150$ . . . 192
8.14 Arrow plots for $\theta = 620°$ to $\theta = 840°$ at $Dn = 150$ 193
8.15 Arrow plots for $\theta = 860°$ to $\theta = 1080°$ at $Dn = 150$ 194
8.16 Arrow plots for $\theta = 1100°$ to $\theta = 1200°$ at $Dn = 150$ 195
8.17 Period of oscillation in the axial and vertical direction at $Dn = 137$. 196
8.18 Flow development to $\theta = 2000°$ at $Dn = 250$ 197
8.19 Flow development at $Dn = 110$, 125 and 137 with a four-cell flow inlet profile 198
8.20 Flow development at $Dn = 150$ with and without asymmetric trip at $\theta = 5°$ 202
8.21 Flow visualization at $\theta = 220°$ with different perturbations at $\theta = 5°$. 203
8.22 Axial velocity profiles at $Dn = 133.9$ showing perturbation asymmetries 204
8.23 Measured state diagram at $Dn = 137$ with asymmetric trip 205

B.1 Schematic of laser beam passing through a curved surface. 223
B.2 Correction factor vs. radial position in duct. 227
B.3 Traversing distance in water compared to traversing distance in air. . 227
B.4 Schematic of typical laser beam passing through a circular curved surface. 228

Nomenclature

a	width of rectangular duct; radius of pipe for a curved pipe
b	height of rectangular duct (for a square cross section $b = a$)
c_f	calibration factor for LDV
Dn	Dean number, $Re/\sqrt{R_c}$
d_h	hydraulic diameter, $2ab/(a+b)$; for a square cross section $d_h = a$; (for a pipe $d_h = 2a$)
d_p	diameter of seeding particle
f_d	measured doppler frequency
g	gravitational acceleration
$\dot{m}$	mass flow rate
p	pressure
R	radius of curvature of the duct
Ra	Rayleigh number, $g\beta d_h{}^3 \Delta T/\nu\alpha$
R_c	curvature ratio, R/d_h (for a square duct $R_c = R/a$)
ΔT	temperature difference
Re	Reynolds number, $\overline{v'_\theta} d_h/\nu$
r', r	radial coordinate
v', v	velocity
$\overline{v'_\theta}$	average axial velocity

v'_{cal}	calibration velocity
x', x	radial coordinate with origin at duct center
z', z	vertical coordinate

Superscripts

$'$	denotes dimensional quantity

Subscripts

r	radial direction
z	vertical direction
θ	axial direction

Greek

ψ	stream function
Ω	vorticity
α	coefficient of thermal diffusivity
β	coefficient of thermal expansion
α, δ	curvature ratio for a curved pipe, a/R
γ	aspect ratio, b/a
θ	axial coordinate
μ	absolute viscosity of working fluid
ν	kinematic viscosity of working fluid
ρ	density of working fluid
ρ_p	density of seeding particle
τ_p	time constant of particle velocity

Chapter 1

Introduction

Curved ducts of various cross sections are found in many engineering applications. Due to the centrifugally induced secondary flows in curved ducts they exhibit behavior quite different from straight pipes, some desirable, others undesirable. An undesirable effect of the secondary flows in curved ducts is the increase in pressure drop as compared to a straight section. On the other hand, the secondary motions enhance heat transfer, making curved ducts very effective in heat exchanger applications. Also, increased residence time of the fluid particles (due to their helical motion through the duct) is a favorable feature in some continuous chemical reactors. The desire to better understand the unique features of curved duct flow (also known as the Dean problem) has made it a subject of extensive research for over one hundred years.

As fluid flows through a curved duct, the axial velocity component is continuously changing direction. This results in a centrifugal force perpendicular to the main flow direction. Different magnitudes of the centrifugal forces, due to a non-uniform axial velocity distribution, result in a pressure gradient across the duct cross section. The pressure is greatest at the outer wall and less at the inner, top and bottom walls

where the centrifugal force is small due to slow moving fluid in the boundary layers. As a result, a secondary flow occurs as the fluid in the central core of the duct moves outward toward the outer wall and the fluid near the top and bottom walls flows inward toward the center of curvature. The resulting motion of the fluid particles as they move around the duct is a double helix symmetrically positioned about the horizontal duct centerline.

In most engineering applications the flow through a curved duct will be in the turbulent regime. However, in order to understand the fundamentals of curved duct flow much of the work done has focused on the laminar regime. In the last few years much effort has been directed towards the study of the non-linear aspects of the Navier-Stokes equations as the flow progresses toward the turbulent regime. As the Reynolds number is increased, the unique double helix flow can give way to a flow where an additional pair of vortices appear. Masliyah (1980) numerically and experimentally confirmed the existence of both a symmetric two-vortex and symmetric four-vortex flow at the same Dean number in a curved duct of semicircular cross section with a flat outer wall. A recent numerical study of the fully developed flow in a curved square duct by Winters (1987) showed the solution structure as a complex bifurcation diagram involving regions of multiple solutions consisting of symmetric and asymmetric flows. The solution structure of the flow in Winter's study was presented in a state diagram of a velocity value plotted against the pressure gradient.

All the numerical work on predicting the bifurcation structure of curved duct flow concerns itself with two-dimensional solutions of the Navier-Stokes equations. In reality, the flow must go through a development length to reach the fully developed state, so it is possible for the inlet conditions to have an effect on the solution observed in the fully developed region. In fact, a numerical study by Soh (1988)

suggested that the flow in a curved square duct developed into two quite different downstream states depending on the inlet condition.

The investigation of the developing flow and the fully developed states that it might evolve into, along with the investigation of the stability of the flows in a curved square duct, was the focus of the present study. Both numerical and experimental investigations were carried out with the numerical simulations being the "road map" for the experimental investigations. Much of the work on curved duct flows has dealt with the numerical analysis of the flow. Even though numerical studies are a powerful tool in the understanding of the flow, experimental studies are required to establish their validity.

1.1 Overview of Thesis

The purpose of this study was to investigate the developing and fully developed laminar flows of an incompressible Newtonian fluid in a curved duct of square cross section. The main focus of the study was the experimental verification of the numerical predictions of the flow development and the fully developed bifurcation structure at moderate Dean numbers.

Chapter two of this thesis gives a review of the relevant work that has been done on curved duct flows. Special attention is given to the previous work done on the non-linear aspect of the Navier-Stokes equations and the flow development.

In chapter three the governing equations for both the developing and fully developed flows, along with the definition of Dean number are given. The computer code used for the developing flow predictions was based on a parabolized form of the steady three-dimensional Navier-Stokes equations. Fully developed flows were computed by a computer code based on a vorticity stream function formulation of the

steady two-dimensional Navier-Stokes equations. The three-dimensional computer code used in this study had been developed by Sankar *et al.* (1988) and the two-dimensional code had been developed by Shanthini (1985).

Chapters four and five describe the experimental system and errors associated with making experimental measurements. The curved duct manufactured for this study had a 1.27 cm square cross section with an axial length of 270° and a curvature ratio, $R_c = R/d_h = 15.1$. A laser doppler velocimeter (LDV) was used to measure the axial flow velocities and dye injection was used to visualize the secondary flow patterns.

In chapter six measurements of flow development, starting from a fully developed straight section inlet profile, are compared to numerical predictions for both a two-vortex and four-vortex flow. Measurement of a developing four-vortex flow to its numerically predicted fully developed state was accomplished for the first time in this study. For the four-vortex flows investigated in this study it was discovered that the development length decreased as the Dean number increased. The existence of this behavior has not been previously reported. Flow visualization of the secondary flow patterns presented in this chapter show the development of symmetric two and four-vortex flows.

The occurrence of dual solutions in a curved duct of square cross section was experimentally verified for the first time in this study. Chapter seven shows the experimental verification of the first dual solution region that had been previously predicted by Shanthini and Nandakumar (1986) and Winters (1987). In order to achieve the dual solutions experimentally, a pin had to be inserted along the duct's symmetry plane to induce some of the four-vortex solutions. The nature of the disturbance created by the pin was investigated experimentally to determine its role in inducing the four-vortex flows.

In the numerical study of Winters (1987) all four-vortex flows calculated were unstable to asymmetric disturbances. Given that any experimental apparatus has inherent asymmetries in it, the physical stability of the four-vortex flows are in question. It is shown in chapter eight that the four-vortex flows observed in this study were stable to symmetric disturbances but unstable to asymmetric disturbances. An experimental and numerical investigation suggested that the four-vortex flow might evolve to flows with sustained spatial oscillations farther downstream.

Chapter nine summarizes the conclusions of this present study and identifies some areas that require further study. Also included in this chapter are some recommendations for equipment improvements to the present LDV system that would increase the accuracy of future velocity measurements.

Chapter 2

Literature Review

The earliest investigation of flow in a curved geometry was performed over a century ago by Thompson (1876), who examined the role of the centrifugal force in the erosion and deposition of material on banks of winding rivers. He suggested that his analysis for winding rivers also explained the increased frictional losses in curved pipes. Williams *et al.* (1902) observed that the maximum axial velocity was shifted towards the outer wall in a curved pipe due to the centrifugal force. The existence of secondary flows in curved ducts of both circular and rectangular cross section was shown in the dye experiments of Eustice (1910, 1911, 1925). For the same pressure gradient, Eustice observed that the volumetric flow rate through a curved pipe was less than that of a straight pipe with the same length.

Using a perturbation analysis, Dean (1927, 1928a) was the first to show the existence of one pair of counter-rotating vortices for the fully developed viscous flow of a Newtonian fluid in a curved pipe. His analysis involved expanding the solution in a power series of Dean number with the leading term being Poiseuille flow in a straight pipe. This method is a perturbation analysis about Poiseuille flow where the influence of the centrifugal force is calculated by successive approximations. Dean

(1928a) carried out his analysis up to the fourth power of Dean number and assumed that the radius of curvature of the pipe was large in comparison to the radius of the pipe cross section. This assumption later became known as the loose coiling approximation. With this approximation, Dean non-dimensionalized the equations of motion and found them to be characterized by a single non-dimensional parameter now known as the Dean number, Dn.

Dean's original work was expanded by Topakoglu (1967), Larrain and Bonila (1970), Sankaraiah and Rao (1973), and Van Dyke (1978) who extended Dean's power series to 24 terms with the aid of a computer. Typically the series solution approach is only valid for small Dean numbers (i.e. $Dn \leq 25$). Investigators such as Alder (1934), Barua (1963), Mori and Nakayama (1965), Itō (1969) and Smith (1976) developed boundary-layer methods to analyze the flow at large Dean numbers (i.e. $Dn \geq 250$). The boundary-layer method divides the flow into two regions, an inner core where centrifugal and pressure forces are important, and a thin boundary layer at the walls where viscous forces are important. The core flow convects the fluid towards the outer wall where it is then returned towards the inner wall in the thin boundary layer.

For intermediate Dean numbers, numerical methods employing either a finite difference or finite element technique have been the most common flow analysis method. These methods are attractive because the equations of motion can be solved without simplifying assumptions (e.g. loose coiling). Finite difference methods have been used by Truesdell and Adler (1970), Akiyama and Cheng (1971), Austin and Seader (1973), Greenspan (1973), Collins and Dennis (1975), Dennis (1980), Manlapaz and Churchill (1980) and Nandakumar and Masliyah (1982). The finite element approach was used by Tabarrok and Lin (1978). As pointed out by Nandakumar and Masliyah (1986), the main thrust of these studies, until the mid

1970's, was to obtain more accurate solutions over a larger range of Dean numbers and curvature ratios.

Since Dean's original analysis, much work, both theoretical and experimental, has been done in the area of flows in curved pipes. Apart from the hydrodynamic aspects, there has also been considerable work done in the area of forced convection heat transfer in coiled pipes. Many of the studies have been on the fully developed flow region and focused on examining frictional and heat transfer characteristics. The focus of this study was flow in a curved duct of square cross section, so much of the past work in curved pipes has not been covered. The interested reader is directed to review articles by Berger *et al.* (1983), Nandakumar and Masliyah (1986) and Itō (1987) that deal with the area in considerable depth.

2.1 Fully Developed Flow in Curved Ducts of Rectangular Cross Section

The first theoretical analysis of flow in a curved duct of rectangular cross section was performed by Itō (1951). Using a perturbation analysis he showed the existence of secondary flows in both a square and elliptic cross section. Unaware of Itō's work, Cuming (1952) also used a power series approach to show the existence of secondary flows in a square and elliptic cross section. His analysis showed that the intensity of the secondary flow in a square section was greater than that in a pipe of circular cross section. Replacing the secondary flow by a uniform stream, Dean and Hurst (1959) analyzed the flow in curved ducts of both circular and square cross section. With their assumption, they showed the effect of secondary flows on reducing the rate of flow through the duct.

A boundary-layer approach was used by Ludwieg (1951) to study the fully

developed laminar flow in a coiled square tube rotating about its axis. Ludwieg also measured the friction factors in the laminar and turbulent regimes for both rotating and stationary ducts. Forced convection heat transfer for fully developed laminar flow in a curved channel with a square cross was analyzed by Mori *et al.* (1971) using a boundary-layer approach. Fully developed velocity profiles measured with a hot wire anemometer in a square duct of $R_c = 14.0$ showed their boundary layer assumption to be valid for $Dn \geq 250$. Their analytical relation between resistance coefficient and Dean number was in good agreement with the experimental results of Ludwieg (1951).

Cheng and Akiyama (1970) used a finite-difference formulation to calculate the secondary flows in curved rectangular ducts of aspect ratio, $\gamma = 0.2 - 5.0$. Starting from a Dean number of zero and proceeding gradually, they calculated the familiar two-vortex pattern. However, when the Dean number was increased beyond a certain critical value, a new four-vortex pattern emerged. The additional vortices were smaller in size and located near the central part of the outer wall. The existence of the additional vortices were only briefly mentioned by Cheng and Akiyama (1970) and later presented by Cheng *et al.* (1975).

A numerical simulation by Joseph *et al.* (1975) for a curved duct of square cross section, also showed the switch from the twin counter-rotating vortices to the four-vortex pattern above a critical Dean number. Stream function contour plots of the four-vortex pattern showed the additional vortices near the central part of the outer wall. Flow visualization experiments by Joseph *et al.* in a helically coiled tube of square cross section confirmed the existence of an additional swirling pattern near the outer wall. Photographs of the additional vortices, for square as well as other aspect ratio cross sections, have been presented by Cheng *et al.* (1977) and Sugiyama *et al.* (1983).

Cheng *et al.* (1976) extended the earlier work of Cheng and Akiyama (1970) to higher Dean numbers and also included the effect of curvature in the numerical formulation. They again observed the appearance of the additional pair of vortices at certain higher Dean numbers, depending on the aspect ratio. For a square channel of $R_c = 100$, the additional vortices were present over a certain range of Dean numbers ($202 \leq Dn \leq 520$) then disappeared at a higher Dean number. Cheng *et al.* believed the appearance of the additional pair of vortices posed a question as to the validity of the boundary-layer approximation for the high Dean number flow regime.

Cheng *et al.* (1976) suggested that the appearance of the additional pair of vortices was consistent with Dean's (1928b) instability problem for a curved parallel-plate channel flow. In a curved channel of infinite height the flow is purely streamwise for sufficiently small Dean numbers. The velocity profile is similar to the parabolic profile of plane channel flow, but the maximum velocity is slightly shifted towards the outer wall. As the Dean number becomes high enough, a centrifugal instability develops causing the formation of a secondary flow with streamwise-orientated vortices. Cheng *et al.* believed the same type of centrifugal instability was responsible for the formation of the additional pair of vortices in low aspect ratio rectangular ducts.

Driving the flow electromagnetically, Baylis (1971) experimentally investigated the flow of mercury in a square cross section torus. By keeping the current across the channel height uniform, the resulting flow resembled a simple pressure driven flow. Since a two-dimensional flow would result for any torus used, he was able to investigate the dependence of friction factor on Dean number for a large range of curvature ratios. For low values of Dean number, Baylis was able to approximately validate the numerical analysis of Cheng and Akiyama (1970). A finite element

analysis of flow and heat transfer in curved ducts by Tabarrok and Lin (1978) was in good agreement with the results of Cheng and Akiyama (1970). Tabarrok and Lin (1978) also presented flow and heat transfer results for some ducts of irregular cross sections.

2.2 Bifurcation Phenomena

The existence of multiple solutions to the Navier-Stokes equations for curved duct flow is not surprising, given that the equations are non-linear. As shown in recent studies by Winters and Brindley (1984), Yang and Keller (1986), Winters (1987) and Daskopoulos and Lenhoff (1989), the solution structures contained bifurcations where regions of multiple solutions existed. Starting at a Dean number of zero a unique solution existed, but as the Dean number was increased, critical values were reached where multiple solutions appeared. The solution structures were visualized by plotting a quantity such as friction factor or velocity against the dynamic parameter (i.e. *Dn* or axial pressure gradient).

For flow in a curved duct, the first mention of dual solutions was reported in a numerical study by Cheng and Akiyama (1970). Their study was for loosely coiled ducts of rectangular cross section. Due to uncertainties associated with the double-solutions they did not present any results, however, the double-solutions were described in Akiyama (1969). The existence of dual solutions was established by Masliyah (1980), both numerically and experimentally, for the flow in a curved duct of semicircular cross section with a flat outer wall.

2.2.1 Bifurcation Phenomena in Curved Pipes

The existence of dual solutions in a circular cross section was discovered in numerical studies by Nandakumar and Masliyah (1982) and Dennis and Ng (1982). Nandakumar and Masliyah used a bipolar-toroidal coordinate system to formulate the problem and discretization was done with central-difference approximations. Their formulation allowed the cross section to be easily changed from a semicircle with a flat outer wall to a full circle, then to a semicircle with a curved outer wall. Starting with a four-vortex solution in a semicircle with a flat outer wall, the geometry of the outer wall was gradually changed to a full circle thus preserving the four-vortex solution. An abrupt change from a semicircle to a full circle would not preserve the four-vortex solution. A four-vortex solution for a semicircle with a curved outer wall was achieved by starting with a four-vortex solution in a full circle and gradually changing the geometry of the inner wall until it was flat. Once a four-vortex solution was achieved in a certain geometry, the Dean number could be varied to follow the solution branch. Nandakumar and Masliyah noted that it was easiest to achieve the four-vortex solution when the outer wall was flat.

In order to calculate the flow in a curved pipe, Dennis and Ng (1982) reduced the governing two-dimensional partial differential equations to an infinite set of ordinary differential equations using substitution of Fourier series. The series was then truncated to a finite series and solved numerically using central-differencing. Starting with a two-vortex solution, solutions at higher Dean numbers were achieved with the appropriate choice of relaxation factor. During the course of numerical experimentation at a high Dean number, a relation factor was chosen such that the solution obtained was a four-vortex solution rather than a two-vortex solution. It was not clear to Dennis and Ng exactly how the procedure converged to the four-vortex solution. However, once the four-vortex solution was achieved, it was used as

the initial guess to calculate a four-vortex solution at a lower Dean number. Using this procedure, the four-vortex solution branch was followed until it disappeared at a critical Dean number (i.e. limit point). This critical Dean number where the four-vortex solution changed back to the two-vortex solution was in very good agreement with the value determined by Nandakumar and Masliyah.

In a numerical study for the fully developed flow in a curved pipe, Yang and Keller (1986) discovered that the solution structure had numerous folds or limit points. Carrying out their calculations to Dean numbers about six times larger than the highest values of Nandakumar and Masliyah (1982) and Dennis and Ng (1982), they observed four folds with five distinct solution branches. In order to follow the solution structure, they used a truncated Fourier series approach like Dennis and Ng (1982) combined with a path following method. This numerical technique allowed solution branches to be followed around limit points, while the methods used by Nandakumar and Masliyah, and Dennis and Ng would jump solution branches if a limit point was encountered.

The first solution branch observed by Yang and Keller, which started with a unique solution at a Dean number of zero, corresponded to the two-vortex solution branches found by Nandakumar and Masliyah, and Dennis and Ng. Similarly, the four-vortex branches found by Nandakumar and Masliyah, and Dennis and Ng corresponded to the third solution branch discovered by Yang and Keller. The critical Dean numbers observed by Nandakumar and Masliyah, and Dennis and Ng corresponded to the second limit point discovered by Yang and Keller. Basically, the studies of Nandakumar and Masliyah, and Dennis and Ng revealed a small portion of the complex bifurcation structure observed by Yang and Keller.

The procedures used by Nandakumar and Masliyah (1982) and Dennis and Ng (1982) to trace the dual solution branches parallels the work of Benjamin (1978a)

very closely. In his work, Benjamin provided a general framework for general properties of multiple solutions and stability in steady motion of bounded flows. Benjamin pointed out that a primary solution branch starts at a zero value of the dynamic parameter (e.g. Re, Dn) with a unique flow. As the flow increases, a critical value in the dynamic parameter can be reached where additional solution branches occur. Depending on the situation, the bifurcation structure can have many different forms. In the case of curved ducts, the solution branch originating from the unique solution at zero Dean number appears to contain one or more folds depending on the cross-sectional geometry. According to Benjamin, the solution will follow the primary branch if the dynamic parameter is changed gradually, and will not change to another solution branch unless a limit point is encountered, or some "trick" is used to force the solution to another branch. However, once a solution is found on another branch it can be followed until another critical point is reached where the solution can again jump branches.

Yang and Keller (1986) used a continuation scheme to follow the solution branches around limit points, while Nandakumar and Masliyah (1982) and Dennis and Ng (1982) used a "trick" to change solution branches. In the work of Nandakumar and Masliyah (1982), the "trick" that was used to achieve the four-vortex solution in a full circle was to start with a four-vortex in a semicircle and gradually change the geometry. The four-vortex in the semicircle was originally achieved by using an appropriate initial guess of the controlling parameters. In the work of Dennis and Ng (1982), their "trick" was the appropriate choice of a relaxation factor that resulted in the four-vortex solution. In both studies, the four-vortex solution branch was followed once an originating solution on the branch had been found, and a change back to the two-vortex solution was observed when a limit point was encountered.

In the experimental work of Benjamin (1978b), on the flow between concentric cylinders with the outer stationary and the inner one rotating (i.e. Taylor problem), he could only reach certain flow patterns experimentally by a sudden start of his apparatus. Similarly, in their experimental investigation of the Taylor problem, Pfister *et al.* (1988) also used sudden starts of their apparatus to reach certain solution branches. In an experimental investigation of the non-linear flow phenomena in a symmetric sudden expansion, Fearn *et al.* (1990) had to impulsively start the flow to observe one of the asymmetric solutions. For the Dean problem, Masliyah (1980) and Cheng and Yuen (1987) used a needle to disturb the flow in order to achieve a four-vortex solution in a semicircle and full circle cross-sectioned curved duct respectively.

The stability of the dual solutions in a curved circular tube of slight curvature was considered by Yanase *et al.* (1988). Using the Fourier-Chebyshev spectral method, they numerically investigated the two-dimensional linear stability of the dual solutions. Their investigation extended up to a Dean number that was twice as high as the largest value investigated by Dennis and Ng (1982). For their lower Dean numbers they observed the same solution structure as Dennis and Ng, while the higher Dean numbers revealed the continuation of the dual solution region. They found that the two-vortex solution was stable for any disturbance while the four-vortex solution was unstable to asymmetric disturbances.

2.2.2 Bifurcation Phenomena in Curved Ducts of Rectangular Cross Section

Shanthini and Nandakumar (1986) numerically investigated the bifurcation phenomena of generalized Newtonian fluids in rectangular ducts. Their study was an effort to map the regions of multiple solutions in the parameter space of Dean

number, aspect ratio, power-law index and curvature ratio. Using a finite-difference formulation, they would set values of aspect ratio, power-law and curvature ratio and march in pressure gradient. Starting with a converged solution for a straight duct as an initial guess, they would calculate the familiar two-vortex solution at a low Dean number for the curved duct. Gradually increasing the Dean number, by small increases in the pressure gradient, they would follow the two-vortex branch until a critical Dean number (i.e. limit point) was reached where the solution would suddenly jump to a four-vortex solution, as previously observed by Joseph *et al.* (1975) and Cheng *et al.* (1976). However, once the four-vortex solution was obtained, Shanthini and Nandakumar continued their calculations for both increasing and decreasing pressure gradient. On increasing the pressure gradient, a four-vortex solution was found up to their highest Dean number. Decreasing the pressure gradient, a four-vortex solution was maintained until another discontinuous jump was observed, where the solution changed back to a two-vortex flow. Using a bisection method, they attempted to locate the critical Dean numbers or limit points where the solutions suddenly changed.

Using the method described above, Shanthini and Nandakumar (1986) investigated the loci of limit points in the parameter space of Dean number and aspect ratio for a given curvature ratio. For an aspect ratio of unity and a constant curvature ratio, they calculated the limit points for different values of the power-law index. They concluded that the bifurcation set in the Dean number-aspect ratio space remains qualitatively the same at any value of power-law index or curvature ratio.

A more complete picture of the solution structure for rectangular cross section ducts has been presented in a numerical study by Winters (1987). He non-dimensionalized the governing equations in terms of the pressure gradient, aspect

ratio and curvature ratio in order to study the flow as each of these parameters changed. Using continuation methods and Newton's method to solve the appropriate extended system of equations, he was able to follow solutions around limit points plus explicitly locate the limit point. Winters presented a detailed state diagram of velocity versus pressure gradient for a square duct with a curvature ratio of $R_c = 25$. For the same curvature ratio, he investigated the paths of limit points and symmetry-breaking bifurcation points as the aspect ratio was varied. He also presented results of the effect of curvature ratio on the axial pressure gradient, Dean number and aspect ratio for the singular points. Winters determined the stability of each of the calculated solution branches by a linear stability analysis.

Daskopoulos and Lenhoff (1989) performed a numerical study of the bifurcation structure in curved ducts of rectangular and circular cross section. They used orthogonal collocation in conjunction with continuation techniques to characterize the bifurcation structure. In order to examine the bifurcation structure, their approach was to start with the "perfect" problem of flow in an infinite slit, which bifurcates to form a vortex structure. By adding "stickiness" at the vortex boundaries, they turned each pair of vortices into a curved duct of rectangular cross section, which, by a geometry change, was then turned into a curved circular tube. Starting with the perfect problem, a large number of solution branches were present, but the addition of stickiness made them vanish as the no-slip limit was reached. At the no slip limit, the remaining solution branches revealed the solution structure.

The results of Shanthini and Nandakumar (1986), Winters (1987) and Daskopoulos and Lenhoff (1989) are in very good agreement. However, Winters numerical formulation allowed for the existence of asymmetric solutions, while the studies of Shanthini and Nandakumar, and Daskopoulos and Lenhoff imposed symmetry about the horizontal mid-plane. This difference in formulations is

obvious, since all the solutions of Shanthini and Nandakumar, and Daskopoulos and Lenhoff are symmetric, while Winters computed asymmetric solution branches that bifurcated from the primary solution branch. Using continuation methods, Daskopoulos and Lenhoff, and Winters were able to follow entire solution branches and explicitly determine singular points. The stability analysis of Winters revealed that the symmetric two-vortex flows were stable, and that the symmetric four-vortex flows were stable to symmetric disturbances, but unstable to asymmetric disturbances. The study of Daskopoulos and Lenhoff also revealed that the four-vortex solutions were stable to symmetric disturbances.

2.2.3 Bifurcation Phenomena in Other Related Problems

Bifurcation phenomena is common to systems that are governed by non-linear equations. Of particular interest are the systems that have bifurcation diagrams very similar to the Dean problem, such as mixed convection heat transfer in a horizontal duct, flow through rotating ducts and convective heat transfer in porous media. Each of these problems exhibit secondary flows in the cross section perpendicular to the main flow with the familiar two and four-vortex solutions. Numerical studies on mixed convection heat transfer in a horizontal duct by Nandakumar *et al.* (1985) and Nandakumar and Weinitschke (1991), with Grashof number as the dynamic parameter, revealed a similar bifurcation structure to the Dean problem. The first study by Nandakumar *et al.* used methods analogous to Shanthini and Nandakumar (1986) to determine solution branches and limit points. Using an arc length continuation scheme, Nandakumar and Weinitschke revealed a much more complicated solution structure than what was found in the first study. It is not surprising that there is a strong similarity to the Dean problem given that the governing equations of each problem are quite similar.

Numerical studies by Weinitschke *et al.* (1990) on convective heat transfer in porous media and by Nandakumar *et al.* (1991) on flow through rotating rectangular ducts also revealed solution structures similar to the Dean problem. For example, in all the problems a primary branch exists with a stable two-vortex solution, but the four-vortex branch is only stable to symmetric and not asymmetric disturbances. Given the similarities between the problems, careful numerical and experimental investigations in one area could provide valuable insight to all the areas.

Much insight to the Dean problem can be obtained through studying the vast amount of work that has been done on Taylor-Couette flow (i.e. Taylor problem). As mentioned before, Taylor-Couette flow is the flow between two concentric cylinders with the inner one rotating and the outer one stationary. Even though the Taylor problem is a closed system, while the Dean problem involves the introduction of the fluid and a development length, experimental and numerical methods such as those used by Pfister *et al.* (1988) can be useful in the Dean problem. Given the similar nature of the governing equations for the Taylor and Dean problems and the fact that much is known about how Taylor flow progresses to turbulence, provides a good base for speculation in the Dean problem.

2.3 Developing Flow in Curved Ducts

Developing flow in a curved duct has been of interest because of its classical engineering importance as well as its recent biological significance to problems such as the entry flow in the aorta. The amount of work done on the developing flow problem has been small in comparison to the number of studies on the fully developed region. As in the case of studies on the fully developed region, the majority of the studies on developing flow have focused on the laminar regime and

on curved pipes.

As seen in the studies of Olson and Snyder (1985) and Soh (1988), the flow development can have a strong dependence on the inlet condition to the curved section. For a piping system a common inlet condition would be a fully developed straight pipe flow while in the case of the aorta the inlet might be approximated by a reservoir condition. As a result, three different entry conditions that have been used in developing flow analysis are: constant dynamic pressure (i.e. a free vortex), uniform axial velocity and fully developed straight duct flow. The actual condition existing at the inlet will be influenced by the degree of curvature of the duct and flow rate, thus resulting in a condition slightly different than the ideal case. However, for practical purposes analytical and numerical analysis have used the approximation of ideal conditions at the inlet.

2.3.1 Developing Flow in Curved Pipes: Parabolic Inlet

One of the earliest investigations of the flow development in a curved duct was by Hawthorne (1951) for the inlet condition of fully developed straight duct flow. He analyzed the flow development in a curved pipe using an inviscid flow approach, then compared his theory with experiments on curved ducts with circular and rectangular cross section. Axial velocity measurements of the developing flow in a curved pipe, starting from a Poiseuille flow inlet, were performed by Austin and Seader (1974). They proposed an empirical relationship for the entrance length that was accurate to within 10% for each of their experimental data sets. Numerical predictions of the flow development in a curved pipe by Patankar *et al.* (1974) were in good agreement with the experimental results of Austin and Seader (1974). Tracking of the flow to its fully developed state was accomplished using a parabolic formulation of the steady three-dimensional Navier-Stokes equations.

Elliptic forms of the Navier-Stokes equations were solved numerically by Humphrey (1978) for flow development in a strongly curved 90° bend with straight pipe Poiseuille flow at the inlet. He observed strong ellipticity in the flow field plus for his largest Dean number he observed flow reversal in the axial direction at the outer wall.

2.3.2 Developing Flow in Curved Pipes: Free Vortex and Uniform Inlet

Flow development for an inlet condition of a uniform injection velocity or potential vortex is distinctly different from the flow development with an inlet condition of a fully developed straight duct flow. The influence of the inlet condition persisting far downstream has been shown in the experimental measurements of Olson and Snyder (1985) for flow development in a curved pipe, and in the numerical results of Soh (1988) for a square duct. This difference is to be expected, since for the fully developed straight section inlet the axial boundary layer is fully developed, while for the uniform and free-vortex inlet the axial boundary layer has to develop. A detailed review of the literature up to 1983 for the developing flow starting from a uniform or free-vortex inlet condition is given by Berger *et al.* (1983).

Singh (1974) studied analytically the entry flow into a curved pipe for the inlet conditions of constant dynamic pressure (i.e. a potential vortex) and uniform velocity. He divided the flow into an inviscid core region and a thin boundary layer region. In the inviscid core centrifugal forces due to the curvature were balanced by pressure gradients in the direction of curvature, while in the boundary layer a balance existed between viscous and inertial forces. His perturbation analysis, which treated centrifugal effects as second order, was valid for all Dean numbers in the region of O(a) immediately downstream of the inlet. Further downstream the flow

development depends on the Dean number. For small Dean numbers the centrifugal effects remain as second order and the boundary layer grows until it fills the pipe and the flow becomes fully developed. At large Dean numbers the centrifugal forces in the boundary layer become as important as the inertial and viscous forces, and the displacement effect of the boundary layer on the core flow causes the centrifugal forces to become more significant in that region.

For the free vortex inlet, Singh observed that the location of the maximum axial shear stress was initially at the inner wall and then crossed over to the outer wall at $R\theta \approx 1.9a$. This is consistent with the axial velocity initially being a maximum at the inner wall and then further downstream shifting towards the outer wall. For a uniform inlet, Singh found that a crossover in the maximum axial shear also occurred from the inner to the outer wall, but at half of the downstream distance as compared to the free-vortex case. He attributed the crossover in this case as solely being due to the shorter/longer wall length on the inner/outer walls of the pipe. This crossover in maximum axial shear stress was experimentally verified by Choi *et al.* (1979) using an electrochemical technique. They also observed a slight movement of the crossover point towards the inlet as the Dean number was increased.

Using a boundary-layer approach, Smith (1976) analyzed the influence of curvature on a pipeflow for a pipe that started bending uniformly after an initial straight section. He found that the core flow remained practically undisturbed until it reached the curved section, but the boundary layer had to react in the upstream section to adjust for the downstream curvature. As a result of this, a maximum of the axial shear occurred at the inner wall of the curved section then crossed over to the outer wall at 1.51 pipe-radii from the start of the curvature. Smith found this crossover to be independent of Reynolds number, curvature and the initial entry profile.

The flow development for large Dean numbers, starting from a uniform inlet condition to its fully developed state, was studied analytically by Yao and Berger (1975). Their formulation included one set of equations for the inviscid core and one set for the three-dimensional boundary layer. The boundary layer equations were solved using the Kármán-Pohlhausen integral technique. The technique consisted of assuming an arbitrary velocity distribution in the boundary layer that satisfied the no-slip condition at the boundary, as well as matched the outer solution at the edge of the boundary layer and satisfied the boundary-layer momentum integrals. The fully developed flow results of Barua (1963) were used as the downstream conditions in their analysis. Yao and Berger also assumed that the flow in the inviscid core was parallel to the horizontal plane of symmetry. This assumption, which has been used by many investigators, was confirmed by the numerical simulation of Yeung (1980).

Yao and Berger (1975) found that in the developing region the secondary boundary layer separated at the inner wall. The width of the separation zone increased with downstream distance, asymptotically approaching a width of 54° in the fully developed region. In their analysis Yao and Berger also identified two regions besides the initial development region of Singh (1974). They found that most of the flow development occurred in a region of $O(\sqrt{aR})$ from the inlet where centrifugal forces became as important as inertial and viscous forces. The final approach to the fully developed state was found to happen in the region of $O(\sqrt{aRDn})$ from the inlet. They also observed that Singh's series solution was a special case of their equations for the region of $O(\sqrt{aR})$. An experimental investigation of developing flow in a curved pipe by Agrawal *et al.* (1978), using the laser-doppler technique, indicated that the circumferential boundary layer separated at the inner wall. With respect to the axial velocity development the experiments were in poor agreement quantitatively with the analysis of Yao and Berger (1975),

but the qualitative agreement was good. An interesting feature discovered by Agrawal *et al.* was that their uniform entry profile quickly developed into a free-vortex-like flow. The development of a uniform profile to a potential vortex immediately downstream was also shown in the numerical investigation of Yeung (1980) for developing flow in the entry region of a curved pipe.

In the downstream region of $O(\sqrt{aR})$ for large Dean number, it was believed that the flow was characterized by a cross-flow that locally became stagnation-like at the outer wall. This caused the secondary boundary layer near the outer wall to remain thin and act as a reservoir receiving the fluid flowing towards the outer wall. The nature of the secondary boundary layer near the inner wall as the flow became fully developed was not clear, since the analysis of Barua (1963) had shown the existence of boundary-layer separation, while other studies such as Collins and Dennis (1975) showed no separation. In order to throw some light on the interaction of the boundary layer with the core flow in the inner wall region, Stewartson *et al.* (1980) performed a numerical analysis of the three-dimensional boundary-layer equations. Their analysis assumed a free-vortex inlet condition, and was valid for loosely coiled pipes as the Dean number approached infinity.

A major finding of Stewartson *et al.* (1980) was that in the developing flow region the axial shear stress at the inner wall vanished at $R\theta = 0.943a/\sqrt{\delta}$, where a is the radius of the pipe, R is the radius of curvature, θ is the angular position from the inlet and $\delta = a/R$ is the curvature ratio. Given their findings, they conjectured that the two secondary boundary layers collided at the inner wall and formed a radial jet conveying fluid from the inner bend to the outer core. Talbot and Wong (1982) experimentally examined the nature of this boundary layer collision using an electrochemical technique to measure the axial shear stress at the inner wall. Talbot and Wong found that their measured shear stress dipped to a minimum at

the proposed singular point, but did not vanish even though they observed a trend of decreasing axial shear with increasing Dean number. Their experimental results were in good agreement with the analytical predictions of Stewartson *et al.* upstream of the collision point, but agreement was poor downstream. Axial shear measurements by Kluwick and Wohlfart (1986) showed the same quantitative trend as the data of Talbot and Wong, but their values were consistently higher. They attributed the discrepancy to the fact that their shear stress values were not as accurate because they were estimated from hot wire measurements of the boundary-layer velocity profiles.

Numerical simulations of the flow development in a curved pipe using the full three-dimensional Navier-Stokes equations were performed by Soh and Berger (1984) and Humphrey *et al.* (1985). Soh and Berger used a fully elliptic formulation of the governing equations, while Humphery *et al.* used a semi-elliptic truncation of the equations allowing a finer numerical mesh. A free-vortex inlet condition was used by Soh and Berger while a uniform injection velocity was used by Humphery *et al.*. The same two curvature ratios, 7:1 and 20:1, were investigated in both studies.

Soh and Berger (1984) observed that secondary flow separation occurred at the inner wall in the developing region, but disappeared by the time the flow had become fully developed. They found the location of the separation region and magnitude of the secondary flows to be greatly influenced by curvature. A minimum in axial shear stress was observed at the inner wall but it did not vanish. In agreement with the experimental results of Talbot and Wong (1982), they observed a trend of decreasing axial shear stress near the proposed singular point as the Dean number was increased. This observation is consistent with the fact that the singular point is predicted for an analysis that assumes the Dean number approaches infinity. The computed axial velocity profiles of Soh and Berger were in good agreement with the

experimental measurements of Agrawal *et al.* (1978).

Streamwise velocity profiles computed by Humphrey *et al.* (1985) were in excellent agreement with the measured results of Agrawal *et al.* (1978). Less favorable agreement between computed secondary velocities and experimental measurements were attributed to the inherent difficulties in making the measurements. Consistent with the findings of Soh and Berger (1984), the numerical results of Humphrey *et al.* indicated a gradual approach towards the behavior of the shear stress predicted by Stewartson *et al.* (1980) as the Dean number was increased. Humphrey *et al.* also observed that the axial shear stress downstream of the minimum displayed a damped oscillatory behavior, with the amplitude of the oscillations increasing with increasing Dean number.

Yao and Berger (1988) investigated the developing flow in curved pipes with finite curvature using a three-dimensional boundary-layer approach. The boundary-layer equations were solved numerically to investigate the developing flow for non-zero curvature ratios, $\alpha = a/R$. They found that the series solution of Singh (1974) was valid only for $\alpha \leq 0.1$ and $R\theta/\sqrt{aR} \leq 0.1$, where a is the radius of the pipe, R is the radius of curvature and θ is the angular position from the inlet. Yao and Berger also discovered that the crossover location of the axial shear stress, from the inner to the outer wall, strongly depended on α and that the crossover location moved downstream as α increased. No crossover was predicted for the limit of $\alpha = 0$. Their analysis also revealed that the crossover phenomena was strictly a geometric effect and not associated with the inlet velocity profile.

The boundary-layer solution of Yao and Berger (1988) showed that the location of the singular point, where the axial shear stress vanishes, is dependent on the curvature ratio α. For $\alpha = 0$ they found good agreement with the location predicted by Stewartson *et al.* (1980). They also found that for $\alpha < 0.5$ the separation point

moved towards the pipe inlet as α was increased. A similar trend was observed for curvature ratios up to $\alpha = 0.2$ in a boundary-layer analysis by Kluwick and Wohlfart (1984). For $\alpha > 0.5$ Soh and Berger observed that the separation point moved downstream as α was further increased. Excellent agreement was observed between their prediction and the experimental axial shear stress data of Talbot and Wong (1982) for a curvature ratio of $\alpha = 1/7$.

2.4 Developing Flow in Curved Ducts of Rectangular Cross Section

Compared to developing flow in curved pipes, little work has been done on developing flow in curved ducts of rectangular cross section. Of the work that has been done, the focus has been on the numerical and experimental analysis of developing flow in square cross sections. No analytical work has appeared in the literature. The most probable reason for this is the inherent difficulty of treating the singular points at the duct corners in a boundary-layer analysis.

The earliest numerical investigation of developing flow in a curved duct of rectangular cross section was performed by Ghia and Sokhey (1977). Starting with a uniform entry profile, they investigated the effect of aspect ratio (i.e. height of duct divided by width of duct) and curvature ratio (i.e. radius of curvature divided by hydraulic diameter) on the development of axial velocity profiles. In the fully developed region, they found that as the aspect ratio decreased the maximum axial velocity increased with a simultaneous outward shift in the location of the maximum. Maintaining a constant Dean number while varying the curvature ratio, Ghia and Sokhey found a small variation of the axial velocity profiles in the fully developed region. The aspect ratios and curvature ratios investigated in their study were 0.5,

1.0, 2.0 and 100, 14, 3 respectively.

For a curved duct of square cross section Ghia and Sokhey (1977) investigated the flow development as the Dean number was increased. They found that for a small Dean number ($Dn = 55$) the flow developed into a two-vortex pattern, while for a larger Dean number ($Dn = 210$) the flow developed into a four-vortex pattern. On further investigation they discovered that the critical Dean number for the appearance of the four-vortex flow was at $Dn = 143$. Conducting a numerical experiment, they also showed that the entrance length, $R\theta$, to reach fully developed flow increased as the Dean number was increased. In their numerical experiment they held the Reynolds number constant and changed the curvature ratio to change the Dean number.

A combined experimental and numerical study of the laminar flow development in a square duct of strong curvature (curvature ratio, $R/d_h = 2.3$), starting from a fully developed straight section profile, was performed by Humphery *et al.* (1977). Laser-doppler measurements of axial velocity in the 90° bend confirmed that the maximum velocity shifted towards the outer wall as the flow developed. Only the two-vortex flow was observed in the experiments. Numerical predictions of the developing axial velocity profiles showed the same trends as the measured profiles. Discrepancies were attributed to the available computer time and storage which limited the number of node points in the fully elliptic finite difference formulation. The calculations also revealed that the secondary flow, with velocities of up to 15% of the mean, was already established at the 0° inlet plane. Small regions of flow recirculation in the axial direction were revealed by the numerical calculations and later confirmed by flow visualization. The recirculation regions, which were caused by the adverse pressure gradient along the outer wall, occurred close to the outer corners of the duct. As mentioned earlier, this behavior was also observed by

Humphery (1978) in a pipe of strong curvature.

An extension of the work of Humphery *et al.* (1977) was carried out by Taylor *et al.* (1982). Their curved section was identical to Humphery *et al.*'s with only the length of the upstream and downstream tangents being different. They used a shorter upstream entrance section to provide an inlet profile to the bend with a smaller axial boundary layer (i.e. not fully developed) for the same Reynolds number used by Humphery *et al.*. They observed that the different inlet profile affected the flow development in the bend, with the largest difference occurring in the first half of the bend. Laser-doppler measurements of the radial component of the secondary flow revealed secondary velocity maxima of 60% of the mean velocity. Only the two-vortex flow pattern was observed in this work.

A numerical study of the developing flow and heat transfer in strongly curved ducts of rectangular cross section was performed by Yee *et al.* (1980). They numerically investigated ten cases of flow development for different wall heating, inlet temperature, inlet profile, curvature ratio and aspect ratio. In order to test their calculation procedure for flow development, they numerically simulated the axial velocity measurements of Humphery *et al.* (1977). Using both elliptic and parabolic formulations of the governing equations, Yee *et al.* found the elliptic results to be in better agreement with the experimental data. Even though a finer numerical mesh could be used with the parabolic formulation, it lacked the ability to provide as accurate results because of the strong curvature effects. According to Yee *et al.*, the decoupling of longitudinal pressure links in the parabolic formulation leads to an inaccurate determination of the pressure, which, in turn, affects the development of the axial velocity. Even though the flow field was parabolic in that it contained no flow reversals, the ellipticity in the pressure field could not be neglected.

The most detailed set of velocity measurements in a curved duct of rectangular cross section have been presented by Hille *et al.* (1985) for a 180° bend of a square cross section with a curvature ratio of $R/d_h = 6.45$. A fully developed straight duct flow was created at the inlet to the curved section by using a 2 m long straight section fitted with a calming chamber and a honeycomb grid at its upstream end.. Axial and radial velocities were measured as a function of Dean number and axial duct position using a laser-doppler anemometer. In their axial velocity measurements Hille *et al.* observed the characteristic transfer of momentum towards the outer wall between $\theta = 0°$ and $\theta = 60°$. A partial back-transfer of momentum towards the duct center was observed between $\theta = 45°$ and $\theta = 108°$, with little further change of momentum near the outer wall after $\theta = 108°$.

Measurements of the radial velocity component by Hille *et al.* showed the existence of a four-vortex structure at Dean numbers between 150 and 300. The additional pair of vortices developed near the outer wall in the region between $\theta = 108°$ and $\theta = 171°$. It was not possible for them to identify the existence of the additional vortices between $\theta = 60°$ and $\theta = 108°$. From a full two-dimensional measurement of the secondary velocities at $\theta = 136°$, it was observed that the additional pair of vortices near the outer wall were asymmetric. Experimentally determined stream functions of the second vortex pair revealed that their strength was still increasing when the end of the 180° bend had been reached. Using published results of fully developed vortex strengths, Hille *et al.* conjectured that 220° of development length would have been required to reach fully developed flow in their experiment.

According to Hille *et al.*, the Dean number at which the additional vortex pair first occurred in their work ($Dn = 150$) was in good agreement with the numerical result of Ghia and Sokhey (1977) ($Dn = 143$). Even though Hille *et al.* observed a

four-vortex flow they did not observe any region of dual solutions. They believed that dual solutions might only be reached by using large perturbations which involved not just the developed flow but the developing flow region as well. Thus, having found no evidence of the existence of dual solutions, Hille *et al.* concluded that the question as to whether the flow structure was subject to a bifurcation remained unanswered.

Sankar *et al.* (1988) numerically investigated the flow development in curved ducts of square cross section using a parabolized and time-independent formulation of the three-dimensional Navier-Stokes equations. Starting from a fully developed straight duct inlet profile, they investigated the flow development at three Dean numbers (50, 100, 200) for three curvature ratios ($R_c = R/a = 4$, 10, 100, where R is the radius of curvature and a is the duct width). For $R_c = 4$ and 10, and up to $Dn = 200$, they found that the flows developed into the previously known two and four-vortex states. However, for a curvature ratio of $R_c = 100$ and $Dn > 125$, they observed that sustained oscillations developed in the axial direction. They performed grid refinements and concluded that the observed spatial oscillations were not a numerical artifact.

In order to reconcile the appearance of symmetric and axially invariant four-vortex flows for $R_c = 4$ and 10 with the conclusion of Winters (1987) that two dimensional symmetric four-vortex flows were unstable, Sankar *et al.* introduced symmetric and asymmetric perturbations at their inlet. In order to simulate a symmetric or asymmetric disturbance, axial velocities at 5° downstream of the inlet were set to zero along symmetric or asymmetric lines extending from the duct outer wall to its center. For $R_c = 4$ and $Dn = 200$, Sankar *et al.* observed that a symmetric perturbation resulted in a symmetric four-vortex flow that was axially invariant, but an asymmetric perturbation resulted in a sustained oscillation in the

axial direction. They concluded that this behavior was consistent with Winters result that four-vortex solutions were unstable to asymmetric perturbations.

Developing flow in a curved duct of square cross section was also studied numerically by Soh (1988). He used a factored ADI finite-difference method on a staggered grid to solve the fully elliptic time-independent Navier-Stokes equations. Starting with an inlet condition of either a fully developed straight duct flow or a free vortex, he followed the flow development around a 180° bend with a curvature ratio $R/a = 6.45$. Both developing flows were calculated for a Dean number of $Dn = 226$. Soh observed that the flow developed into quite different states downstream depending on the inlet condition. For the free-vortex inlet the flow the flow appeared to develop to a four-vortex flow. The flow was not fully developed by the end of the 180° bend, but the additional pair of vortices was quite evident. For the fully developed straight duct inlet, the flow appeared to develop to a state with a primary vortex pair and a weaker vortex pair at the outer wall. Recalculating this inlet condition case for a duct of 240°, Soh found that the solution remained the same for the additional 60° of duct length. Solving the two-dimensional Navier-Stokes equations for fully developed flow, Soh conjectured that with the appearance of dual solutions, the developing flow becomes fully developed along either of the two branches into which the solution is bifurcated. The free-vortex inlet develops into the four-vortex fully developed solution, while the fully developed straight duct inlet develops into some other state. Soh had imposed a symmetry condition when he calculated the fully developed solutions, so he only calculated a symmetric four-vortex solution at a Dean number of $Dn = 226$. Given that Winters (1987) had calculated an asymmetric solution branch, plus the fact Hille *et al.* (1985) observed a weak asymmetric vortex pair near the outer wall, led Soh to believe that the fully developed inlet case could develop to a state that was asymmetric far downstream.

Soh also conjectured that the flow far downstream might evolve into a flow that was periodic in the axial direction.

2.5 Summary

The major focus of this chapter was to review the literature on fully developed and developing flow in curved ducts of both circular and rectangular cross section. For fully developed flow in a curved pipe, the numerical studies of Yang and Keller (1986), Nandakumar and Masliyah (1982), and Dennis and Ng (1982) revealed the existence of dual solutions. Flow visualization by Masliyah (1980) and Cheng and Yeun (1987) confirmed their existence in a curved pipe of semicircular and circular cross section respectively. A stability analysis of the dual solutions, performed by Yanase *et al.* (1988), showed the two-vortex flow to be stable to an arbitrary perturbation, while the four-vortex flow was stable to a symmetric perturbation but unstable to an asymmetric perturbation.

For fully developed flow in a curved duct of square cross section, the numerical study of Winters (1987) showed the solution structure as a complex bifurcation diagram involving regions of multiple solutions consisting of symmetric and asymmetric solutions. Similar to the case of the curved pipe, a linear stability analysis by Winters also revealed that the two-vortex flows were stable to an arbitrary perturbation, and the four-vortex flows were stable to a symmetric perturbation but unstable to an asymmetric perturbation. Even though four-vortex flows have been visualized by Cheng *et al.* (1977) and Sugiyama *et al.* (1983), the experimental confirmation of the dual solutions in a rectangular cross section has not appeared in the literature.

The majority of the theoretical studies of flow development in a curved pipe

have used a boundary-layer analysis to examine the details of the developing flow. In contrast, the inherent difficulty in applying a boundary-layer analysis to a rectangular cross section has resulted in all the theoretical work on this geometry being numerical (i.e. numerical solution of the Navier-Stokes equations). Theoretical investigations in a curved pipe have only shown the development of a two-vortex flow, while the numerical studies in a rectangular geometry have shown the development of both a two-vortex and four-vortex flow. For both a circular and rectangular cross section, no experimental measurements exist for the development of a symmetric four-vortex flow to its fully developed state.

The most detailed measurements of the flow development in a curved duct of square cross section were performed by Hille *et al.* (1985). Their measurements revealed the development of an asymmetric four-vortex structure at Dean numbers between 150 and 300, but the flow had not reach a fully developed state within the 180° axial length of their duct. In a numerical study of the flow development in a curved duct of square cross section, Sankar *et al.* (1988) found that it was possible for a four-vortex flow to develop sustained spatial oscillations in the axial direction. A numerical study by Soh (1988) showed that the flow might develop into quite different states downstream depending on the inlet condition. Soh conjectured that for the two inlet conditions, the flow might develop to the two branches into which the fully developed solution bifurcates. However, due to the short development length used in his calculations, his results are not conclusive.

After considering the work done on the developing and fully developed flows in curved ducts it can be seen that there still exists some unresolved issues. In the case of fully developed flows in a curved duct of square cross section it is still to be determined experimentally if dual solutions exist. The existence of four-vortex flows has been shown both numerically and experimentally, but there are

no detailed measurements of the development of a symmetric four-vortex flow to its fully developed state. If four-vortex flows are unstable to asymmetric perturbations, what happens to them as they are allowed to evolve in the downstream direction? Given the flow development observations of Hille *et al.* (1985), Sankar *et al.* (1988) and Soh (1988), how do they relate to the fully developed solution structure that has been presented by Winters (1987)? The present study was performed with these issues in mind.

Chapter 3

Governing Equations

A square cross section curved duct is best described by a cylindrical coordinate system as shown in figure 3.1. The origin of the coordinate system is at the center of curvature of the duct, and the duct boundaries are located at $-a/2 \leq z' \geq a/2$ and $R - a/2 \leq r' \geq R + a/2$. By introducing the coordinate x', where $x' = r' - R$, the side boundaries of the duct can more conveniently be located at $-a/2 \leq x' \geq a/2$.

In cylindrical coordinates the velocities v'_r, v'_z and v'_θ are in the radial, axial and tangential directions respectively. However, to avoid confusion with existing literature, terminology will be used that is not completely consistent with a cylindrical coordinate system. The secondary velocity components v'_r and v'_z, in the plane perpendicular to the main flow, will be referred to as the radial and vertical velocities respectively. This does not create any confusion, but an inconsistency arises when the term, "axial velocity", is used to refer to the velocity in the primary flow direction. In the cylindrical coordinate system the primary velocity is actually in the tangential direction and not the axial direction. The reason "axial velocity" is used for the primary flow is because, in the analysis of curved pipe flow, which uses a toroidal coordinate system, the primary velocity is truly in the axial direction.

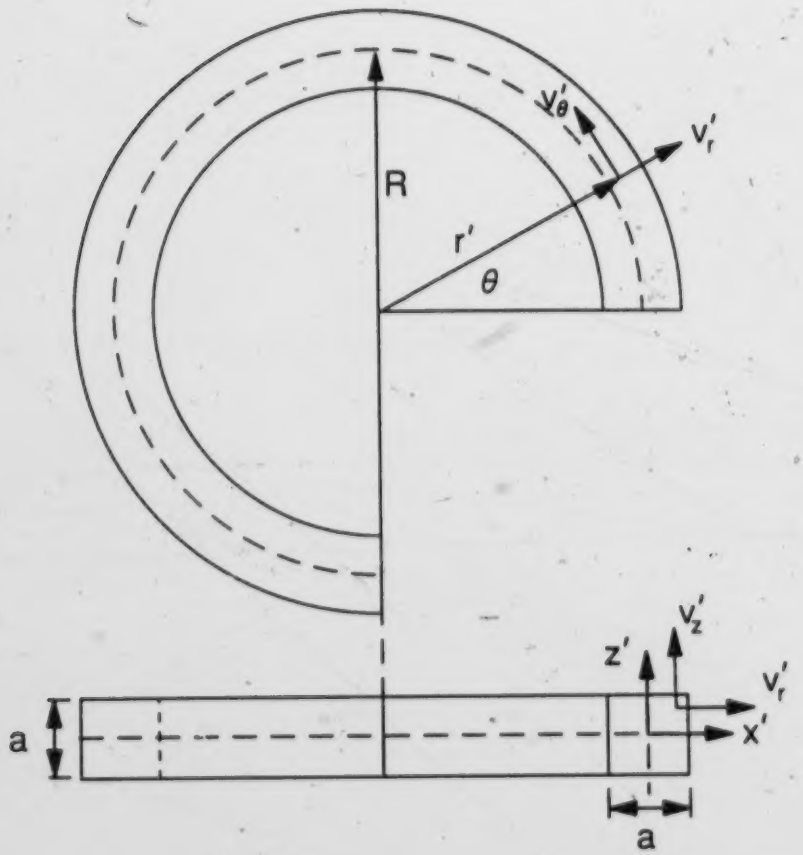

Figure 3.1: Cylindrical coordinate system.

Curved pipe flow analysis has set the precedent on how the velocity components are referred to, therefore, in order to maintain consistency, "axial velocity" will be used to mean the velocity perpendicular to the secondary flow plane containing the radial and vertical velocities.

In this study it was desired to investigate the flow development and the flow structure once the flow had reached a fully developed state. In order to calculate the flow development, the three-dimensional (3-D) Navier-Stokes equations need to be solved. However, fully developed solutions require the two-dimensional (2-D) Navier-Stokes equations to be solved. Therefore, a numerical formulation of both the two-dimensional and three-dimensional Navier-Stokes equations were used in this study. The three-dimensional computer code used in this study had been developed by Sankar *et al.* (1988), and the two-dimensional code had been developed by Shanthini (1985).

3.1 Developing Flow Equations

In order to track the flow as it developed, it was necessary to solve a three-dimensional formulation of the Navier-Stokes equations. The most accurate solution would have required a full elliptic formulation, but due to available computing power, this would have severely limited the number of simulations that could have been run. In order to work around this problem, the equations used in this study had been simplified by neglecting the axial diffusion of momentum. This changed the equations from an elliptic form to a parabolic form which was much easier to solve. The non-dimensional parabolized Navier-Stokes equations for a steady flow of an incompressible Newtonian fluid are:

continuity

$$\frac{1}{r}\frac{\partial}{\partial r}(rv_r) + \frac{1}{r}\frac{\partial v_\theta}{\partial \theta} + \frac{\partial v_z}{\partial z} = 0 \tag{3.1}$$

momentum in r direction

$$v_r\frac{\partial v_r}{\partial r} + \frac{v_\theta}{r}\frac{\partial v_r}{\partial \theta} - \frac{{v_\theta}^2}{r} + v_z\frac{\partial v_r}{\partial z} = -\frac{\partial p}{\partial r} + \frac{1}{Re}\left[\frac{\partial}{\partial r}\left(\frac{1}{r}\frac{\partial}{\partial r}(rv_r)\right) - \frac{2}{r^2}\frac{\partial v_\theta}{\partial \theta} + \frac{\partial^2 v_r}{\partial z^2}\right] \tag{3.2}$$

momentum in θ direction

$$v_r\frac{\partial v_\theta}{\partial r} + \frac{v_\theta}{r}\frac{\partial v_\theta}{\partial \theta} + \frac{v_r v_\theta}{r} + v_z\frac{\partial v_\theta}{\partial z} = -\frac{1}{r}\frac{\partial p}{\partial \theta} + \frac{1}{Re}\left[\frac{\partial}{\partial r}\left(\frac{1}{r}\frac{\partial}{\partial r}(rv_\theta)\right) + \frac{2}{r^2}\frac{\partial v_r}{\partial \theta} + \frac{\partial^2 v_\theta}{\partial z^2}\right] \tag{3.3}$$

momentum in z direction

$$v_r\frac{\partial v_z}{\partial r} + \frac{v_\theta}{r}\frac{\partial v_z}{\partial \theta} + v_z\frac{\partial v_z}{\partial z} = -\frac{\partial p}{\partial z} + \frac{1}{Re}\left[\frac{1}{r}\frac{\partial}{\partial r}\left(r\frac{\partial v_z}{\partial r}\right) + \frac{\partial^2 v_z}{\partial z^2}\right] \tag{3.4}$$

Global continuity requires that

$$\int_{z=-0.5}^{z=0.5}\int_{r=R_c-0.5}^{r=R_c+0.5} v_\theta dr dz = 1.0 \tag{3.5}$$

The variables have been non-dimensionalized as follows

$$r = \frac{r'}{a} = R_c + x \qquad x = \frac{x'}{a} \qquad z = \frac{z'}{a} \qquad R_c = \frac{R}{a}$$

$$v = \frac{v'}{\overline{v'_\theta}} \qquad p = \frac{p'}{\rho\overline{v'_\theta}^2} \qquad Re = \frac{\rho a\overline{v'_\theta}}{\mu}$$

where the prime denotes dimensional quantities.

The above equations were solved using the computer code of Sankar *et al.* (1988). Their formulation did not impose any reflective symmetry about the $z'/a = 0.0$ axis, therefore, it allowed for the evolution of asymmetric flows in the θ direction. The equations were discretized by integrating them over a control volume and solved according to the method given by Patankar (1980). For all developing flow calculations, a grid of 31 × 31 was used in the cross plane and a marching step of

0.5° was used in the axial direction. Typical computing times, in order to march 400° of axial length (i.e. 800 marching steps), were 1.2 hours of cpu usage on a FPS-164 Scientific Computer (Floating Point Systems Inc.).

The terms that were dropped from the full three-dimensional steady flow equations in Sankar *et al.'s* formulation were

$$\frac{1}{Re\,r^2}\frac{\partial^2 v_r}{\partial\theta^2}, \qquad \frac{1}{Re\,r^2}\frac{\partial^2 v_z}{\partial\theta^2}, \qquad \frac{1}{Re\,r^2}\frac{\partial^2 v_\theta}{\partial\theta^2}, \qquad \frac{2}{Re\,r^2}\frac{\partial v_r}{\partial\theta}$$

The terms are multiplied by $1/Re$ and $1/r^2$, therefore, they will become less important as Re and the radius of curvature increase. It is not shown in Sankar *et al.*, but on a careful examination of the details of their numerical formulation (Sankar *et al.* private communication), the gradient of v_r in the θ direction was also neglected.

3.2 Fully Developed Flow Equations

For the two-dimensional formulation of the Navier-Stokes equations, all the terms involving gradients in the axial direction, except for the axial pressure gradient, were dropped. As a result, the governing equations for fully developed steady flow of an incompressible Newtonian fluid are:

continuity

$$\frac{\partial v_r}{\partial r} + \frac{\partial v_z}{\partial z} + \frac{v_r}{r} = 0 \tag{3.6}$$

momentum in r direction

$$v_r\frac{\partial v_r}{\partial r} + v_z\frac{\partial v_r}{\partial z} - \frac{v_\theta^2}{r} = -\frac{\partial p}{\partial r} + \frac{\partial}{\partial r}\left(\frac{1}{r}\frac{\partial}{\partial r}(rv_r)\right) + \frac{\partial^2 v_r}{\partial z^2} \tag{3.7}$$

momentum in θ direction

$$v_r\frac{\partial v_\theta}{\partial r} + v_z\frac{\partial v_\theta}{\partial z} + \frac{v_r v_\theta}{r} = -\frac{1}{r}\frac{\partial p}{\partial \theta} + \frac{\partial}{\partial r}\left(\frac{1}{r}\frac{\partial}{\partial r}(rv_\theta)\right) + \frac{\partial^2 v_\theta}{\partial z^2} \tag{3.8}$$

momentum in z direction

$$v_r\frac{\partial v_z}{\partial r}+v_z\frac{\partial v_z}{\partial z}=-\frac{\partial p}{\partial z}+\frac{1}{r}\frac{\partial}{\partial r}\left(r\frac{\partial v_z}{\partial r}\right)+\frac{\partial^2 v_z}{\partial z^2} \tag{3.9}$$

The equations have been non-dimensionalized as follows

$$r=\frac{r'}{a}=R_c+x \qquad x=\frac{x'}{a} \qquad z=\frac{z'}{a} \qquad R_c=\frac{R}{a}$$

$$p=\frac{a^2\rho p'}{\mu^2} \qquad v_r=\frac{a\rho v_r'}{\mu} \qquad v_\theta=\frac{a\rho v_\theta'}{\mu} \qquad v_z=\frac{a\rho v_z'}{\mu}$$

where the prime denotes dimensional quantities.

Equations 3.6 through 3.9 can be transformed to a vorticity stream-function formulation by introducing a dimensionless stream function and vorticity function. The dimensionless stream function which automatically satisfies continuity is determined by

$$v_r=\frac{1}{r}\frac{\partial \psi}{\partial z} \qquad v_z=-\frac{1}{r}\frac{\partial \psi}{\partial r} \tag{3.10}$$

the dimensionless vorticity function is defined as

$$\Omega=\frac{\partial v_z}{\partial r}-\frac{\partial v_r}{\partial z} \tag{3.11}$$

Substituting equation 3.10 into equation 3.11 results in the vorticity stream-function equation

$$\frac{\partial^2 \psi}{\partial r^2}+\frac{\partial^2 \psi}{\partial z^2}-\frac{1}{r}\frac{\partial \psi}{\partial r}=-r\Omega \tag{3.12}$$

Using equation 3.11, the radial and vertical momentum equations can be combined to eliminate the pressure terms and form the vorticity-transport equation

$$v_r\frac{\partial \Omega}{\partial r}+v_z\frac{\partial \Omega}{\partial z}-\frac{v_r\Omega}{r}=\frac{-2v_\theta}{r}\frac{\partial v_\theta}{\partial z}+\frac{\partial^2 \Omega}{\partial r^2}+\frac{\partial^2 \Omega}{\partial z^2}+\frac{1}{r}\frac{\partial \Omega}{\partial r}-\frac{\Omega}{r^2} \tag{3.13}$$

The axial momentum equation remains as

$$v_r\frac{\partial v_\theta}{\partial r}+v_z\frac{\partial v_\theta}{\partial z}+\frac{v_r v_\theta}{r}=-\frac{1}{r}\frac{\partial p}{\partial \theta}+\frac{\partial^2 v_\theta}{\partial r^2}+\frac{\partial^2 v_\theta}{\partial z^2}+\frac{1}{r}\frac{\partial v_\theta}{\partial r}-\frac{v_\theta}{r^2} \tag{3.14}$$

The solution to the two-dimensional flow field can now be found by solving equations 3.12, 3.13 and 3.14.

For a square duct, the boundary conditions with imposed symmetry about the horizontal centre line are

no slip at the walls

$$\psi = v_r = v_\theta = v_z = 0$$

at the top wall

$$\Omega = -\frac{1}{r}\frac{\partial^2 \psi}{\partial z^2}$$

at the side walls

$$\Omega = -\frac{1}{r}\frac{\partial^2 \psi}{\partial r^2}$$

along horizontal centre line

$$\psi = \Omega = \frac{\partial v_\theta}{\partial z} = \frac{\partial v_r}{\partial z} = v_z = 0$$

The equations were solved using the computer programs written by Shanthini (1985). In her formulation equations 3.12, 3.13 and 3.14 were discretized using a three-point central-difference approximation. The imposed symmetry about $z'/a = 0.0$ did not allow any asymmetric solutions to be calculated. A grid of 41×21 was used in all of the two-dimensional calculations performed in this study. Typical computing times for one two-dimensional simulation were four to five minutes of cpu usage on the FPS-164 Scientific Computer.

3.3 Definition of Dean Number

The non-dimensional equations of motion for the developing and fully developed flow used in this study are not characterized by a single non-dimensional parameter.

In the developing flow equations the Reynolds number and radius of curvature appear as separate parameters. Similarly, in the fully developed flow equations the axial pressure gradient and radius of curvature appear as separate parameters. Only with the loose coiling approximation would these individual parameters collapse into one parameter. Even though the equations are not characterized by a single non-dimensional parameter, it is common practice to present results characterized by a non-dimensional Dean number.

The Dean number, Dn, used throughout this study, was defined as

$$Dn = \frac{Re}{\sqrt{R_c}} \tag{3.15}$$

This Dean number is similar to Dean's (1928a) non-dimensional grouping which included a curvature ratio and a slightly different form of Reynolds number. The Dean number is a ratio of the inertial and centrifugal forces to the viscous forces. Secondary flows are a result of the interaction of the centrifugal forces with the viscous forces, so the Dean number is a measure of the strength of the secondary flow. Many definitions of Dean number have been used in the analysis of curved ducts and a review is given by Berger *et al.* (1983).

3.4 Comparison of Fully Developed Solutions from 3-D and 2-D Codes

One way of checking the integrity of a numerical simulation is to compare it to the result of an independent numerical simulation. The two and three-dimensional simulations should give the same result in a region where a fully developed symmetric solution exists. In figures 3.2 and 3.3 the two-dimensional solution for $Dn = 125$ is compared to the axially invariant result of the three-dimensional simulation at the

same Dean number. For both the radial and vertical profiles of axial velocity the results of the two simulations differ by less than 0.5%.

Figures 3.4 and 3.5 show a comparison of the two-dimensional and axially invariant three-dimensional solution for $Dn = 150$. From figure 3.4 it is seen that the two-dimensional simulation predicts values that are about 2-4% lower than the three-dimensional simulation in the region of $0.15 \leq x'/a \geq 0.4$. As a result of continuity, the two-dimensional values in the flat region of the vertical profile in figure 3.5 are about 0.7% higher than the three-dimensional simulation predictions. The cause of this discrepancy is likely due to the different grid spacings used in the cross plane for the two-dimensional and three-dimensional simulations.

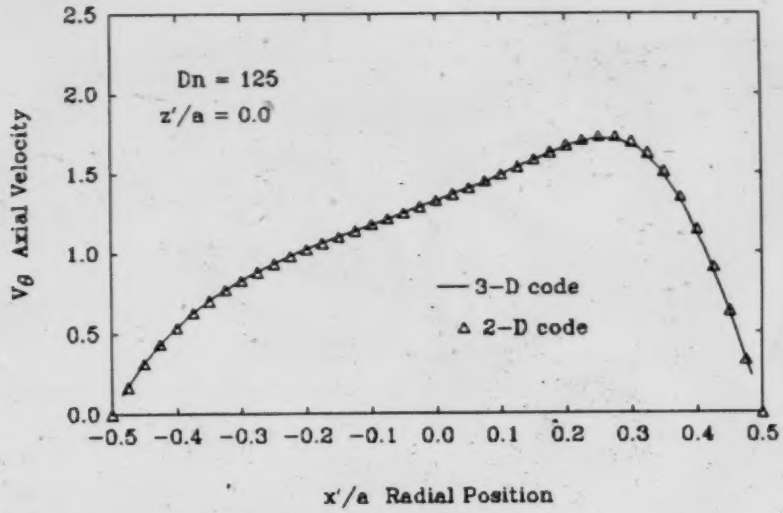

Figure 3.2: Comparison of two and three-dimensional simulations of axial velocity profiles in the radial direction at $Dn = 125$ and $z'/a = 0.0$.

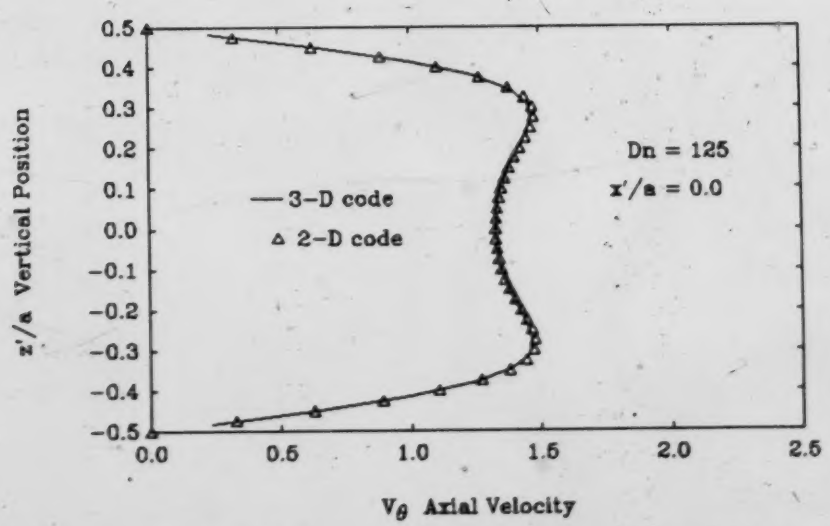

Figure 3.3: Comparison of two and three-dimensional simulations of axial velocity profiles in the vertical direction at $Dn = 125$ and $x'/a = 0.0$.

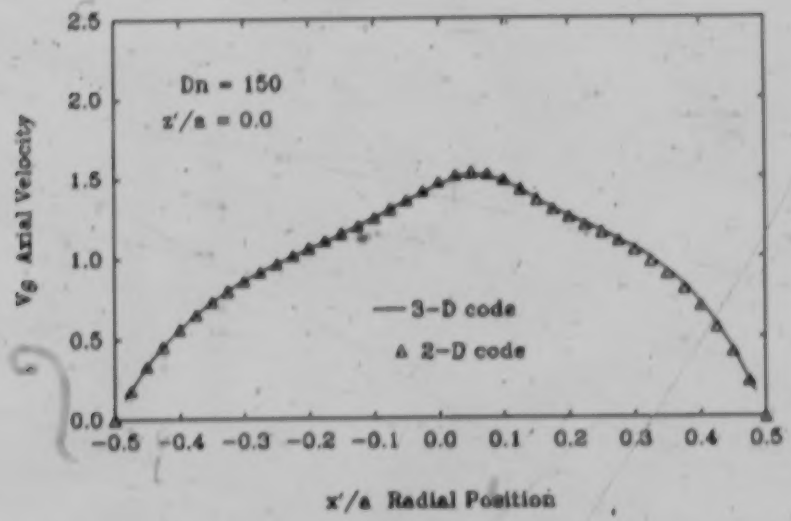

Figure 3.4: Comparison of two and three-dimensional simulations of axial velocity profiles in the radial direction at $Dn = 150$ and $z'/a = 0.0$.

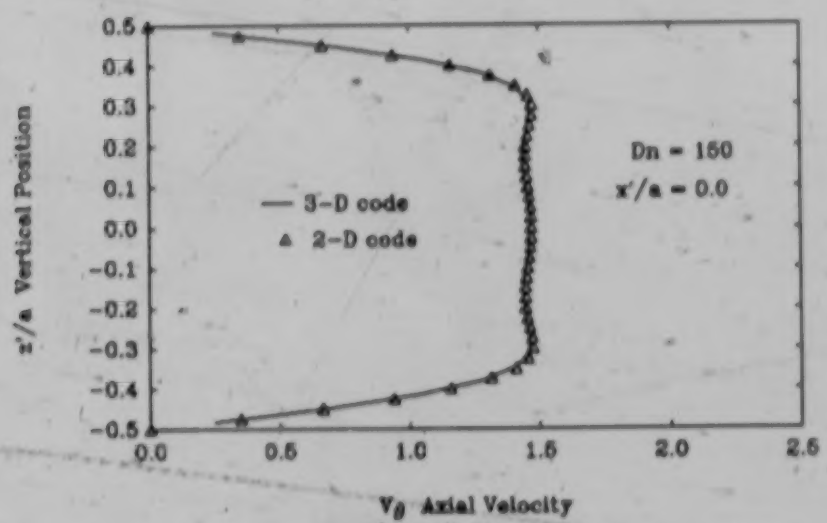

Figure 3.5: Comparison of two and three-dimensional simulations of axial velocity profiles in the vertical direction at $Dn = 150$ and $z'/a = 0.0$.

Chapter 4

Experimental System

The purpose of this study was to experimentally investigate the developing and fully developed flow in a square cross section curved duct. The investigation consisted of measuring axial flow velocities and visualizing the corresponding secondary flow structure at various axial locations throughout the duct. Design of an experimental apparatus with water as the working fluid, and the development of techniques to measure velocities and visualize the flow composed the main parts of the experimental study. Flow velocities were measured with a laser-doppler velocimeter (LDV). Flow visualization was accomplished by illuminating a cross section of the duct with a thin sheet of laser light and then injecting fluorescent dye into the flow. Careful attention to detail was required in all areas of the experimental system to ensure that reliable results would be obtained.

4.1 Experimental Apparatus

A schematic of the curved duct apparatus is shown in figure 4.1. The curved duct section had a 1.27 cm square cross section with an axial length of 270° and a

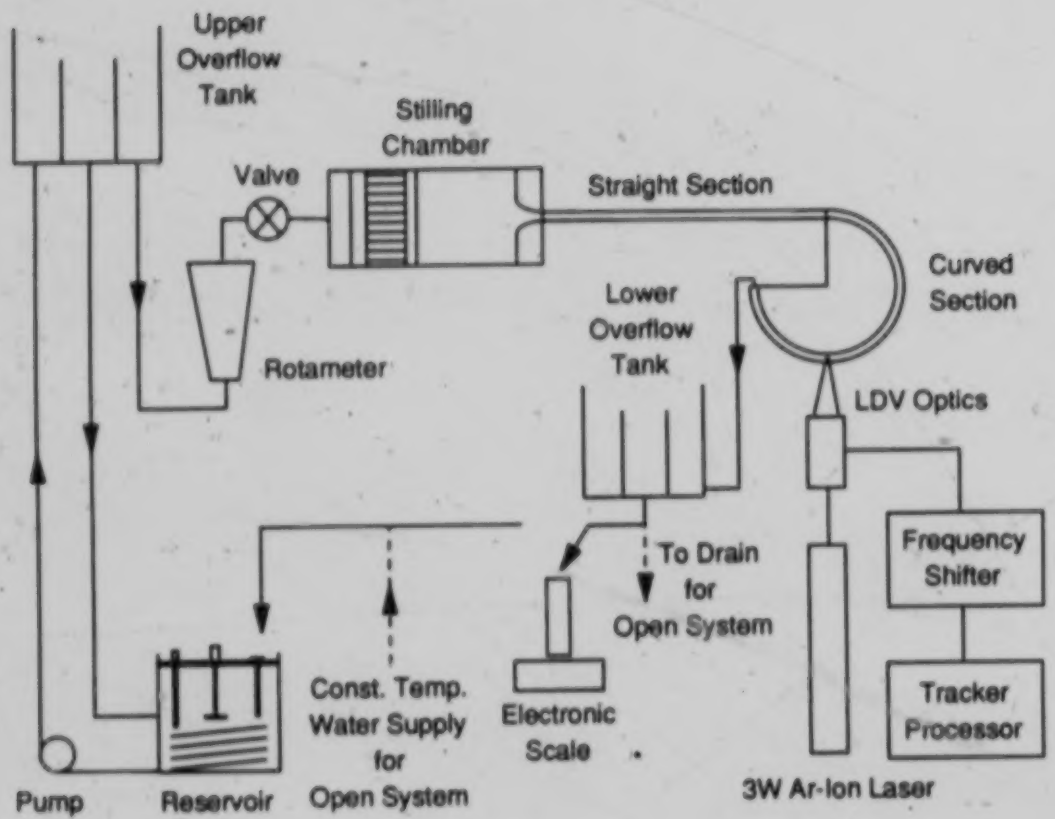

Figure 4.1: Schematic of curved duct apparatus.

curvature ratio, $R_c = R/d_h$=15.1. A stilling chamber, with a smooth contraction connected to a 1 m straight duct inlet section, was used to provide a well controlled inlet profile to the curved section. A 10 cm long by 1.9 cm diameter straight pipe was fastened directly to the exit of the curved section. A tee connection fastened to the end of the straight pipe was fitted with a flexible tubing coupling and an air bleed valve.

The curved section, inlet section and stilling chamber were all made of plexiglass to facilitate LDV measurements and flow visualization. The assembly was mounted on a platform that allowed rotation about the center of the curved section and the ability to traverse vertically and horizontally. Due to physical limits in the amount that the assembly could be rotated, only about 240° of axial length was accessible for measurement purposes. Traversing of the apparatus was necessary because the LDV optics were held stationary.

In order to provide a steady flow rate, a constant head system consisting of stainless steel overflow tanks positioned above and below the apparatus was used. The distance between water levels in the two overflow tanks was approximately 3.5 m with the apparatus being about 0.5 m higher than the lower tank. A reservoir with a centrifugal pump supplied the upper overflow tank, while the lower overflow tank would return to the reservoir or drain depending on if the system was run as a closed or opened loop. Two bleed valves, one located on the stilling chamber and the other at the exit of the curved section, were installed to allow air to be purged from the system. A set point temperature controller was used to keep the working fluid at a constant temperature. A constant temperature working fluid was required when measuring velocities in the closed system or injecting dye in the open system configuration.

Two Brooks 600 mm Full-View Model 6-1110-24 rotameters, each with a

maximum flow rate capacity of 0.7 liters/min, were used to aid in the setting of a desired flow rate. Since all flows investigated were below 0.7 liters/min, only one rotameter was used to set flow rates. The mass flow rate for a given run was determined by weighing the amount of water collected in a timed interval. Timing was done with a hand held digital stop watch with a resolution of 0.01 s, and the sample was weighed on a Mettler PC 8000 electronic balance accurate to 0.1 g.

4.1.1 Construction of Experimental Apparatus

A photograph of the experimental apparatus and LDV system is shown in figure 4.2. The curved section was manufactured from a 3.3 cm thick block of plexiglass that had been machined into a circular disk. The top, bottom and inside walls of the 1.27 cm square channel were formed by machining a rectangular grove into the edge of the disk. A 3.3 cm wide and 1.5 mm thick sheet of plexiglass was glued around the edge of the disk to form the outer wall of the duct.

At 5° from the curved section inlet, three holes were drilled along radial lines through the outer wall to allow a 0.4 mm diameter pin to be inserted across the duct. The holes were drilled at $z'/a = 0.0$ and $z'/a = \pm 0.25$. A rubber seal, through which the pin could be inserted, was placed over the holes to ensure that no leakage would take place. In order to allow for a slight adjustment of the pin's vertical position, two small bends (i.e. a few degrees) were made in the pin to create a straight section that was offset from the pin's axis (i.e. resembling a crank). The bends were positioned to coincide with the location of the pin's guiding hole when the pin had been inserted across the duct. When the section of the pin that was outside of the duct was rotated, the section that was inside the duct would experience vertical movement. The purpose of the pin was to allow the introduction of symmetric and asymmetric perturbations into the flow.

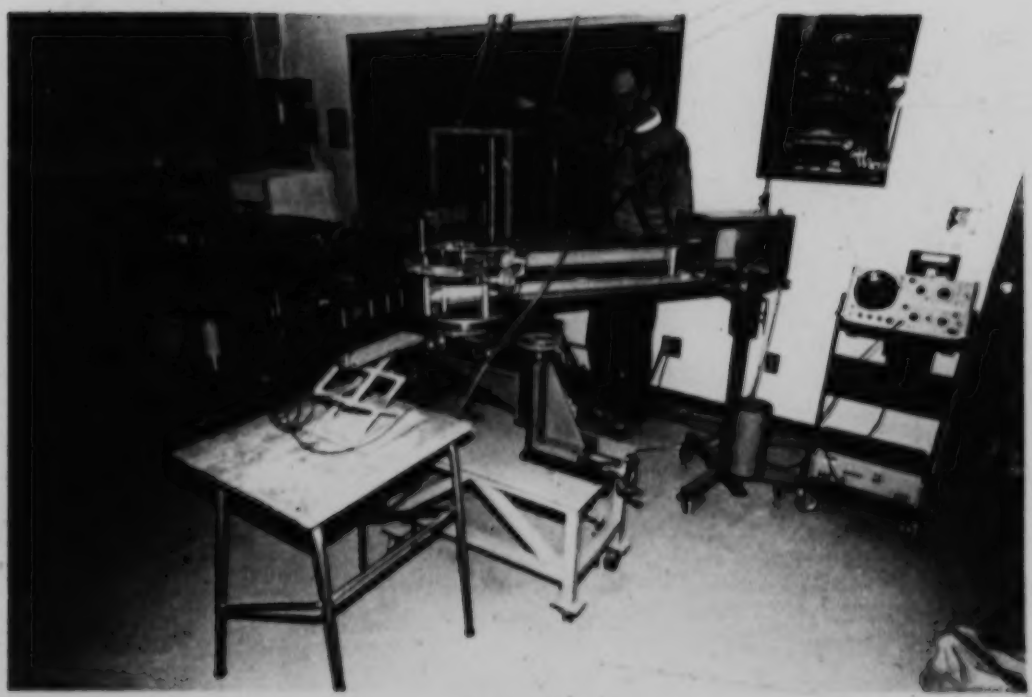

Figure 4.2: Photograph of experimental system showing curved duct apparatus, LDV system and fiber optic laser light sheet.

The 1 m straight channel section was constructed by machining a rectangular grove into the larger section of a 5 cm diameter plexiglass rod that had been split along its axial length. The rod had been split 0.635 cm above the centerline of its cross section. The grove, which formed the bottom and two side walls of the square channel, was machined such that its center coincided with the center of the circular rod. The smaller section of the plexiglass rod was glued back onto the larger section to form the top wall of the duct. Each end of the rod was machined to a diameter of 4.0 cm and two O-rings installed to form the male ends of a leak proof coupling with the female ends on the curved section and stilling chamber. The rod was fastened to a 2.5 cm wide by 5.5 cm high section of aluminum along its length to maintain straight alignment. At 6.5 cm upstream of the curved section a port hole was machined into the side of the straight channel to allow measurement of the inlet flow profile.

In order to facilitate dye injection, a 0.4 mm diameter hole was drilled through the top wall of the straight section duct at 9.3 cm from the end which was connected to the stilling chamber. A fitting installed on the straight section allowed dye to be supplied by a 1 mm inside diameter tygon tube.

The stilling chamber was manufactured from 1.2 cm thick plexiglass sheet. Each end of the chamber was made to detach allowing the insertion of screens and flow straighteners. Holes, fitted with leak proof fittings, were drilled in the top of the chamber to hold a thermometer and a thermocouple. An elliptic shaped contraction that fed the straight section was fastened to the detachable front end of the stilling chamber.

The curved section, straight section and stilling chamber were all mounted on a 1.3 cm thick aluminum plate that had been stiffened by the addition of a 7.6 cm wide by 3.8 cm high by 0.5 cm thick channel section along its length. The curved section

end of the base plate was bolted to a rotary table mounted to a horizontal-vertical traverse. The rotary table had markings with a resolution of 1°, while the resolution of the traverse was 0.025 mm in each direction. In order to allow vertical traversing and rotation of the entire apparatus, the stilling chamber end of the base plate was supported by a counter weight mechanism mounted on wheels. The respective dimensions of the stilling chamber, straight section and curved section are shown in a detailed schematic in figure 4.3.

4.1.2 Design of Inlet Section

The inlet section of the curved duct apparatus consisted of the stilling chamber and the 1 m long straight section. Careful attention was paid to the design of these two components to ensure that a well behaved flow was present at the inlet of the curved section. One major aspect of this study was to investigate the effect of perturbations on the curved duct flow, so a stable and clean inlet condition was absolutely necessary. A fully developed straight duct flow was chosen to be the inlet profile to the curved section. A 1 m straight section was used, based on the measurements of Goldstein and Kreid (1967). Using their experimentally determined relation of, $L/d_h = 0.09Re$, where L is the development length, d_h is the hydraulic diameter and Re is the Reynolds number, a 1 m length of duct would provide a fully developed inlet profile up to a Dean number of, $Dn = 225$.

In order to ensure that the profile would develop properly in the straight duct, a stilling chamber with a contraction was used to feed the straight section. A detailed schematic of the stilling chamber is shown in figure 4.4. The major components of the chamber are two fine meshed screens, a flow straightener and a contraction. The four curved surfaces of the contraction are quarter ellipses with minor and major axis of 2.5 cm and 5.0 cm respectively. This results in a contraction with a contraction

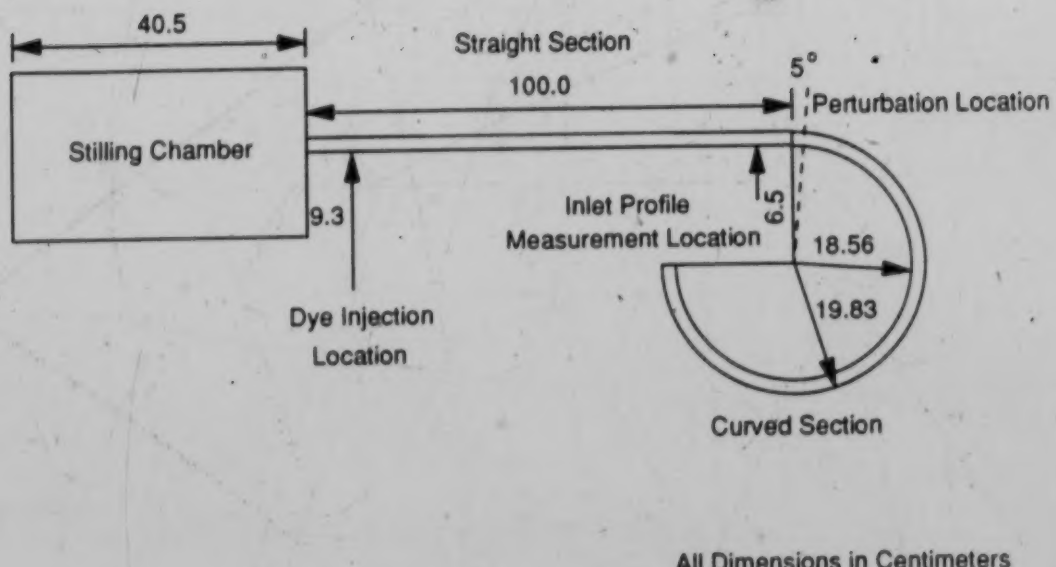

Figure 4.3: Schematic of stilling chamber, straight section and curved section showing their respective dimensions.

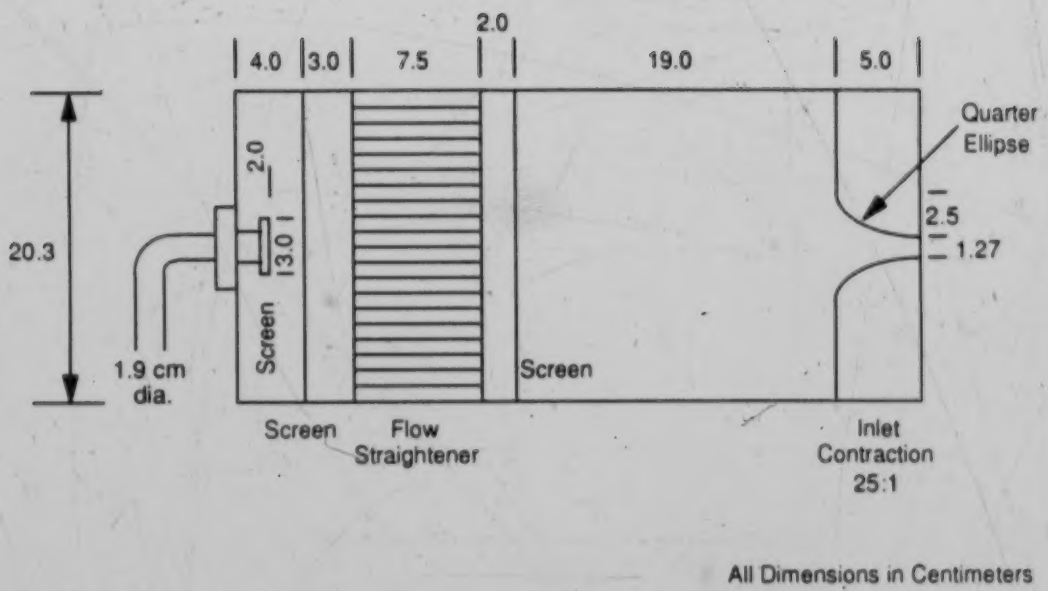

Figure 4.4: Detailed schematic of stilling chamber.

ratio, based on area, of 25 to 1. The quarter ellipse, based on the experimental system of Beavers *et al.* (1970), was chosen to provide a uniform entry profile to the straight section.

The elliptic shaped contraction was constructed by first machining the desired curve into one side of a plexiglass block. The block was cut at 45° into four identical V-shaped sections and the pieces were glued together to form the contraction. The resulting contraction had the elliptic shape in each duct wall.

In order to eliminate the development of swirl within the stilling chamber, flow straighteners were installed in the 90° elbow feeding the chamber and in the chamber itself. The downstream section of the 1.9 cm diameter 90° elbow was packed with 6.0 cm long and 0.3 cm o.d. stainless steel tubing. The flow straighter in the stilling chamber was constructed from plastic drinking straws, 0.8 cm in diameter and 7.5 cm in length, packed together to fill the cross section of the chamber.

A 3 cm diameter piece of mesh screen was used as a deflector to distribute the jet of fluid that entered the chamber from the 90° elbow. Fine mesh screens, with 0.110 mm wire diameter and 0.149 mm openings, were placed on each side of the stilling chamber flow straightener to help distribute the fluid throughout the chamber cross section and reduce the scale of any motions. The mean residence time of the fluid, to travel from the screen located downstream of the flow straightener to the contraction, was about 15 to 20 minutes depending on flow rate. This length of time should have been sufficient for any remaining small scales in the chamber to have been dissipated by viscosity.

4.1.3 Temperature Control

In order to eliminate the masking of centrifugally driven secondary flows by buoyancy driven secondary flows, temperature control was essential. Temperature control was also necessary to keep the viscosity of the working fluid constant. Therefore, a set point controller was used which held the temperature of the working fluid at $23.1°C \pm 0.1°C$.

The set point control mechanism consisted of a temperature sensor, a 500 W quartz glass heating rod, a 5 turn 25 cm diameter cooling coil (constructed from 0.95 cm diameter stainless steel tubing) connected to the tap water supply, and a motor driven stirrer. All of these components were placed in the reservoir of the curved duct apparatus. The temperature sensor and heating rod were connected to a relay that energized the heater in response to the set point temperature of the sensor. The purpose of the cooling coil was to offset the heating of the working fluid by the pump (≈ 35 W), and to provide sufficient heat loss to maintain proper controlling action of the heater. In order to compensate for the fluid lost from the system when an open system was used, a Haake model FS constant temperature bath connected to an external water source supplied the reservoir with fluid at the set point temperature.

The water temperature was monitored in the stilling chamber where the fluid first entered. A Fisherbrand 15-000A glass thermometer with $0.1°C$ resolution was used to measure the absolute temperature while a copper-constantan thermocouple connected to a chart recorder was used to monitor the temperature variation with time. The glass thermometer was calibrated in a calibration bath against a Fluke 2189A platinum resistor digital thermometer accurate to $0.01°C$. Accurate absolute temperature was required for the estimation of the working fluid viscosity.

According to Hille *et al.* (1985), for a Rayleigh number, $Ra = 10000$, buoyancy

effects can cause secondary velocities with a magnitude of 1% of the mainstream velocity when Reynolds number, $Re \geq 400$. Their estimate of the buoyancy effects were based on published results for straight and curved pipes, and straight rectangular ducts. The Rayleigh number, Ra, which is essentially a ratio of buoyancy forces to viscous forces is given as

$$Ra = \frac{g\beta {d_h}^3 \Delta T}{\nu \alpha} \tag{4.1}$$

where: g = gravitational acceleration
β = coefficient of thermal expansion
d_h = hydraulic diameter
ΔT = temperature difference
ν = kinematic viscosity
α = coefficient of thermal diffusivity

In order to maintain the Rayleigh number under 10000 in this experiment, it was required that temperature gradients in the working fluid be kept below $0.25°C$. Temperature control was more than adequate, so the only concern was to keep the working fluid at room temperature to avoid any convective currents caused by heat transfer from the surroundings.

On average the room temperature was typically $23.0°C$ with variations of $\pm 0.5°C$. The apparatus was not insulated because, for the flow rates used, a temperature difference of $0.5°C$ between the working fluid and room temperature resulted in a temperature difference between the reservoir and outlet overflow tank of less than $0.1°C$. This negligible temperature difference, indicating insignificant heat transfer from the surroundings to the working fluid, can be attributed to the low thermal conductivity of the plexiglass and high specific heat capacity of water.

On very hot summer days the room temperature could continually climb, becoming as high as $25.0°C$. During these days, the temperature difference between

the reservoir and outlet overflow tank would also continually climb becoming even greater than $0.25°C$. To avoid questionable results data was not collected on these days.

Another seasonal variation that affected the collection of data was the temperature of the tap water supply feeding the cooling coil in the reservoir. Given enough hot days in succession, the temperature of the tap water supply could become greater than the set point temperature ($23.1°C$) making temperature controlling impossible. The tap water source was typically around $8.0°C$ during the winter and $22.0°C$ during the summer. Cooling water flow rates ranged form 0.3 liters/min in the winter to around 1.0 liters/min in the summer.

4.2 Velocity Measurements

The flow velocity was measured with a single component Argon-ion laser-doppler velocimeter (LDV) operating in backscatter mode with a frequency tracker performing the signal processing. The system was composed of Dantec 55X modular optics with a 80 mm focal length front lens, a Bragg cell and a Dantec 55N10 Frequency Shifter. The frequency shifter was modified to produce shift frequencies that were one-half of the original specification values. This was done in order to allow frequency shifting in the lowest range of the Dantec 55N20 Doppler Frequency Tracker. A Coherent Innova 90-3 Argon-ion laser capable of 3 W output on all lines was used as the lasing source. All velocity measurements were made using the blue (488.0 nm) line with typical laser powers of 200 mW.

The probe volume, formed by the crossing point of the laser beams, is an ellipsoid with the axis in the direction of the beams much elongated. For the optical arrangement used in this study the probe volume had a diameter of 0.017 mm and a

length of 0.12 mm. With a duct dimension of 1.27 cm this gave about 100 resolvable points across the duct.

The technique of laser anemometry requires that there are suitable particles suspended in the flow to generate adequate doppler signals. The velocities that are measured are the velocities of the particles in the flow, therefore, accurate measurement of the flow depends on how closely the particles follow the flow. Given that the particles have inertia their motion will lag behind that of the fluid. Also, the particles have a settling velocity causing an additional velocity component in the direction of the gravity vector.

In order to estimate the dynamic response of a seeding particle and its settling velocity, Stoke's law can be used. Drain (1980) *pp.* 182–184, using Stoke's law, has derived a relationship for the time constant of a particle velocity given a step change in fluid velocity. The relationship is given as

$$\tau_p = \frac{2\rho_p {d_p}^2}{9\mu} \tag{4.2}$$

where: τ_p = time constant
ρ_p = density of particle
d_p = diameter of particle
μ = absolute viscosity

In this study the flow was seeded with irregularly shaped silicon carbide particles that had a mean diameter of 1.5×10^{-6} m. With a particle density, $\rho_p = 3.2 \times 10^3$ kg/m^3 and fluid viscosity, $\mu = 9.3 \times 10^{-4}$ kg/m s, the dynamic response of the particles were calculated to be, $\tau_p = 1.7 \times 10^{-6}$ s. Using Stoke's law and assuming that the particles can be treated as spheres, as was done in the previous calculation, the settling velocity was calculated to be 3×10^{-6} m/s. The time constant and settling velocities were so small that the measured particle velocities were taken to be the fluid velocities.

4.3 Flow Visualization

Flow visualization was accomplished by illuminating a cross plane of the square duct with a thin sheet of blue laser light and injecting a laser fluorescent dye into the flow. As the dye passed through the plane illuminated by the laser light its fluorescence was bright enough to allow photographs to be taken. Rhodamine 6G (also known as Rhodamine 590) at a concentration of 1×10^{-3} M was used as the dye source. Rhodamine B and Fluorescein at similar molar concentrations were also tried but did not give as bright of an illumination as the Rhodamine 6G.

4.3.1 Laser Light Sheet

Figure 4.5 shows the method used to create a sheet of laser light in a fixed $x' - z'$ plane. A beam splitter was placed in the beam path between the laser and LDV optics to provide a laser beam at 90° to the original beam path. A precision mirror was placed in the path of the 90° beam to direct the beam along a radial line of the curved section. A 10 mm focal length cylindrical lens was then used to fan the beam out into a 1.5 mm thick sheet of light. This method, which resulted in a light sheet 20° upstream from the LDV measurement location, was used for all of the flow visualization photographs.

The maximum beam power that could be achieved in the light sheet was only about 200 mW, even though the maximum laser output on the blue line was around 550 mW. The beam splitter, which was placed at 45°, provided a 65/35 split of the incoming laser beam. The power split was not 50/50 as one would expect because the beam being emitted from the laser was circularly polarized rather than linearly polarized. Circularly polarized light was required for the LDV optics so that proper polarization of the crossing beams could be maintained while rotating the optics.

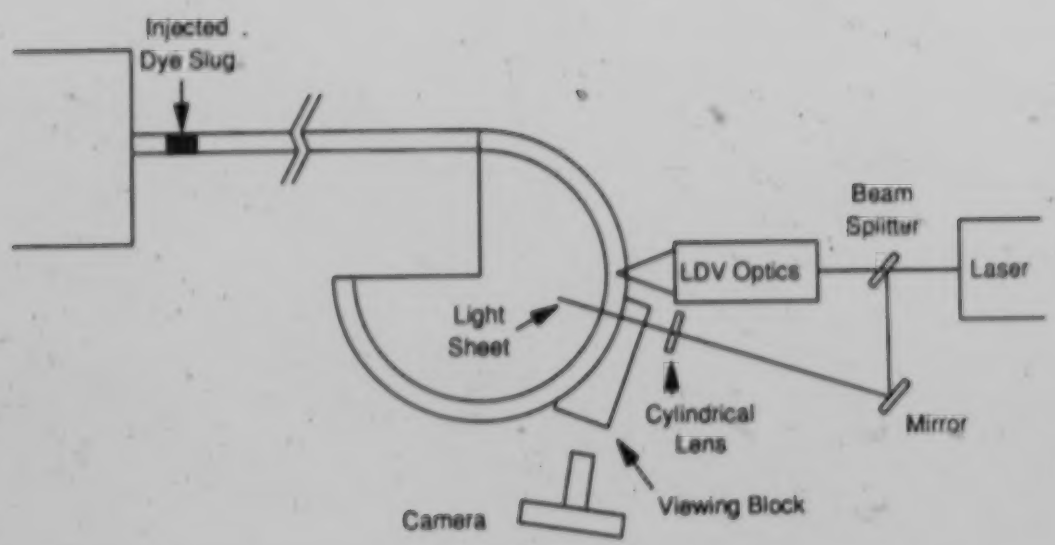

Figure 4.5: Schematic of fixed laser light sheet.

A portable light sheet, utilizing fiber optic cable, was also developed so that the flow structure could be observed in the axial direction without having to rotate the experimental apparatus. Figure 4.6 shows a schematic of the fiber optic light sheet which was directly modeled after the technique presented by Koga *et al.* (1987). The basic principal of a fiber optic light sheet is to transport the laser beam by fiber optic cable, and then re-collimate the beam at the output end and send it through a cylindrical lens.

The input coupler of the portable light sheet was used to launch the incoming laser beam into the core of the 250 μm multi-mode fiber optic cable. The 40× microscope objective on the input coupler was used to focus the incoming laser beam to a point. In order to launch the beam into the fiber optic cable, adjustment screws on the assembly holding the optical cable were used to position the cable end at the focal point of the microscope objective. At the output coupler, the reverse procedure was followed by placing the 40× microscope objective at the focal point of the optical cable to produce a wide diverging beam. Two spherical lenses, with focal lengths of 19.0 mm and 62.9 mm, were placed in the beam path to create a converging beam that was then passed through the 10 mm focal length cylindrical lens. At the beam waist of the converging light source, a 1 mm wide and 2.5 cm long sheet of light was produced.

4.3.2 Photographing Secondary Flows

As seen in figure 4.5, the curved section was fitted with a movable viewing block that allowed photographs to be taken through a flat surface. A thin film of water placed between the curved section and viewing block allowed a clear view of the illuminated section. The viewing block was held in place by two elastic bands stretched between the viewing block and support pins at the center of the curved

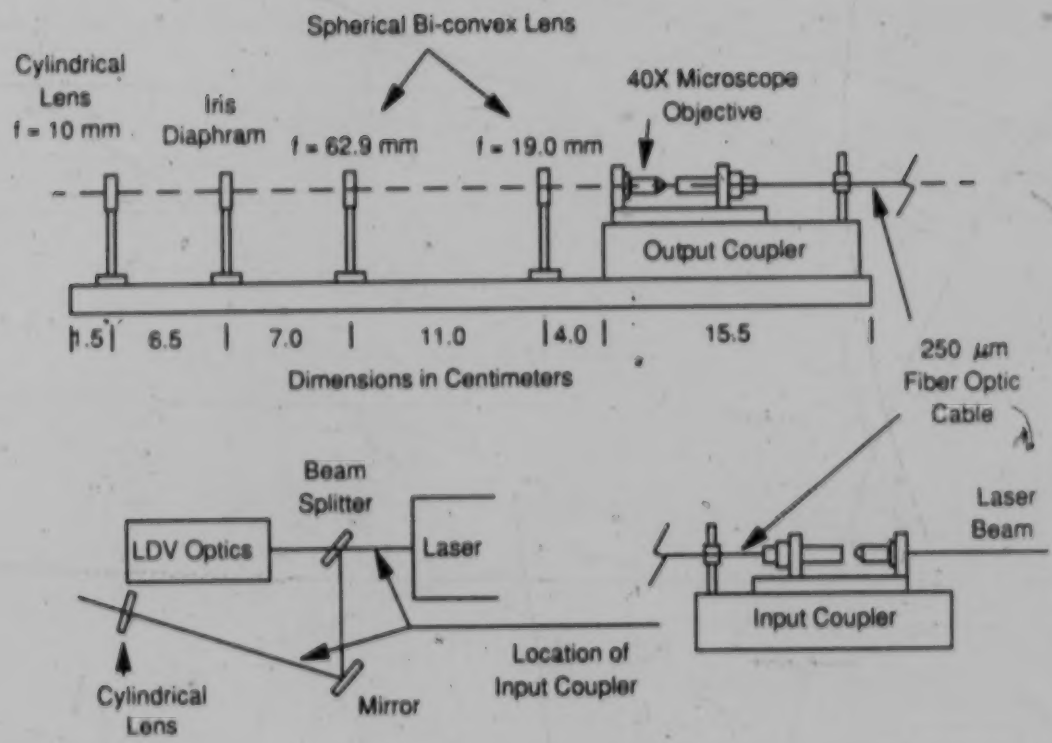

Figure 4.6: Schematic of fiber optic light sheet.

section.

A typical photograph involved injecting a slug of dye into the upstream end of the straight section and waiting for it to pass through the illuminated plane. Approximately 1–2 cc of dye was injected by quickly turning on and off a syringe pump fitted with a syringe containing the fluorescent dye. A momentary increase in flow rate would occur due to the injection of the dye, but the fluctuation would quickly die out having no effect on the photographed flow patterns. A photograph was usually taken as the trailing end of the dye slug moved through the illuminated plane, resulting in a clear view of the illuminated plane.

Flow patterns were photographed with a 35 mm Nikon SLR camera fitted with a 105 mm Nikon lens and a Nikon TC-200 2× teleconverter. A No. 12 Kodak Wratten Gelatin filter was attached to the lens assembly to attenuate the blue light of the illuminating sheet but still allow the light from the fluorescing dye to pass through. Good separation of the two colors was achieved since the peak fluorescence of the dye was around 580.0-600.0 nm (Yarborough, 1974), while the illuminating sheet was at 488.0 nm. Typical exposure times were from 1/30 to 1/100 second with a lens aperture of $f4$ and ISO (ASA) setting of 800. P800/1600 Kodak Ektachrome professional slide film was used because of its fast speed and fine grain size. When taking photographs, stray reflections were minimized by covering the curved section with black felt.

4.3.3 Digital Enhancement of Photographs

Digital enhancement of the photographed flow patterns was required to trim off unwanted reflections and linearly stretch the photographs in the radial direction. The different refractive indexes between water and air, and the refraction of light at the curved surface interface between the viewing block and duct, caused the viewed

image to be compressed in the radial direction. Reflections of the illuminated flow patterns appeared around the duct boundary, but had no adverse effect on viewing the desired image.

Photographs were digitized with the assistance and equipment of Campbell (1991). The technique consisted of illuminating the image of the flow patterns contained on a slide, and then capturing the image digitally with a Hitachi VKC360 video camera connected to a Data Translation 2871 digital frame grabbing board. The resulting digital images of the flow patterns had a resolution of 512 pixels in the vertical direction and 480 pixels in the radial direction. When the digital images were displayed on a VGA monitor, only 16 grey levels were available even though the original images were digitized in black and white with an intensity level of 0 to 255 for each pixel location.

Editing and layout of the digital images was done using the graphics capabilities of WordPerfect 5.1. The digital image was first displayed on a VGA graphics screen, then stored in a WordPerfect file using their screen capture program (GRAB.COM). The screen capture program allowed selection of any part of the screen, so preliminary cropping of the images was possible. Once an image was in the WordPerfect environment it could be stretched independently in either direction. This allowed production of a square image that was accurately cropped at the duct boundaries.

Chapter 5

Experimental Errors

An experimental measurement of a quantity will always deviate from the true value of the quantity because of errors introduced by the equipment or measurement technique. The difference between the true value and the measured value is the error in the measurement. In the strictest sense, the true value of a quantity is never known, so it is not possible to assign a specific numeric value to the error. This being the case, it is necessary to come up with a best estimate of the magnitude of the unknown error. The term "uncertainty" is usually used to indicate the best estimate of a particular error. In this study, errors that lent themselves to an uncertainty analysis were treated using the method presented in Appendix A.

5.1 Uncertainty in Dean Number

An experimentally determined Dean number, Dn, will be subject to uncertainty because of the individual uncertainties in the parameters comprising the Dean

number. The Dean number, as used in this study, is given as:

$$Dn = \frac{Re}{\sqrt{R_c}} = \frac{\overline{v'_\theta} d_h}{\nu \sqrt{R_c}} = \frac{\dot{m}}{\rho \nu \sqrt{R}} \frac{2\sqrt{a}}{(a+b)} \tag{5.1}$$

where: Re = Reynolds number
R_c = curvature ratio, R/d_h
$\overline{v'_\theta}$ = mean axial velocity
d_h = hydraulic diameter, $2ab/(a+b)$
$\dot{m}$ = mass flow rate
ρ, ν = density and kinematic viscosity
a, b = duct dimensions

The rightmost formulation of the Dean number in equation 5.1 is in the form that contains all of the measured and inferred quantities that were used to calculate it.

The uncertainty in an experimentally determined Dean number was estimated by using the method outlined in Appendix A. An expression for the fractional uncertainty in Dean number was derived by the applying equation A.3. The expression is given as:

$$\frac{\Delta Dn}{Dn} = \sqrt{\left(\frac{\Delta \dot{m}}{\dot{m}}\right)^2 + \left(\frac{\Delta \rho}{\rho}\right)^2 + \left(\frac{\Delta \nu}{\nu}\right)^2 + \left(\frac{1}{2}\frac{\Delta R}{R}\right)^2 + \left(\frac{1}{2}\frac{\Delta b}{b}\right)^2} \tag{5.2}$$

Before simplification, equation 5.2 had terms with $(a+b)$ in them, however for a square duct, where $a = b$, the $(a+b)$ terms can be replaced with either $2a$ or $2b$. This simplification was only made at the end of the analysis, because it was desired to treat each duct dimension as independent during the analysis.

The mass flow rate was determined from the mass of water collected in a 60–100 s interval. Given that timing was done with a hand held stopwatch, the uncertainty in reaction time was the major cause of uncertainty in the mass flow rate. For a typical reaction time of about 0.1 s, the uncertainty in one measurement of mass flow

rate was about 0.1%. An uncertainty of 0.1% was also calculated from a statistical analysis of repeated measurements of the same flow rate.

The density and kinematic viscosity of the working fluid varied directly with any temperature variations. Therefore, with temperature control to 0.1°C the uncertainty in density was 0.002%, while the uncertainty in the kinematic viscosity was 0.25%. Both duct walls were machined to 1.27 cm with a tolerance of ±0.0025 cm which resulted in an uncertainty of 0.2% in their dimensions. The radius of the duct was 19.196 cm with a machining tolerance of ±0.0025 cm resulting in an uncertainty of 0.013% in that dimension. Substitution of these individual uncertainties into equation 5.2 results in an uncertainty of ±0.3% in an experimentally determined Dean number.

5.2 Uncertainties in LDV Calibration

A LDV measures the velocity of particles as they pass through the crossing point of the laser beams. The particles scatter the laser light producing a signal that has been doppler shifted by an amount that is directly proportional to the velocity of the particle. Measuring the doppler frequency, the particle velocity is calculated from the relation

$$v_p' = \frac{\lambda}{2\sin(\phi/2)} f_d \qquad (5.3)$$

where: v_p' = velocity of particle
λ = wavelength of laser light
ϕ = crossing angle between beams
f_d = measured doppler frequency

The calibration factor, $c_f = \lambda/(2\sin(\phi/2))$, is a constant depending on the laser light wavelength and the beam crossing angle. Since the laser wavelength is known,

one way to determine the calibration factor is to measure the beam crossing angle. Another method of determining the calibration factor is to calculate it from the measurement of a known velocity standard.

In determining the calibration factor, a systematic or bias error will always be introduced by the calibration technique. Unlike random errors, which introduce scatter into the measured values, a bias error in the calibration factor will introduce a systematic shift in all velocity measurements. Therefore, it is important to be able to estimate the uncertainty that will be introduced into the calibration factor by the calibration technique.

5.2.1 Measurement of Beam Crossing Angle

One method of determining the calibration factor is to measure the beam crossing angle. In order to measure the beam crossing angle, the tangent of the crossing angle can be determined by projecting the beams on a surface at a known distance from the crossing point and measuring the spacing of the beams. Due to space restrictions, the furthest distance that a suitable measuring surface could be located was 1 m from the crossing point. At this distance, a 1 mm uncertainty in determining the beam spacing would result in a 0.75% uncertainty in the calibration factor. It seemed possible to make at least an error of 1 mm in the measurement of the beam spacing, so it was decided to use a known velocity to determine the calibration factor.

5.2.2 Spinning Wheel as Velocity Standard

When using a known velocity to determine the calibration factor (i.e. $c_f = v'_{cal}/f_d$), error can be introduced by both the uncertainty in the known velocity as well as the uncertainty in the measured doppler frequency. A reasonable estimate

of the error, using the method given in Appendix A, is

$$\frac{\Delta c_f}{c_f} = \sqrt{\left(\frac{\Delta v'_{cal}}{v'_{cal}}\right)^2 + \left(\frac{\Delta f_d}{f_d}\right)^2} \tag{5.4}$$

where: $\Delta c_f/c_f$ = uncertainty in calibration factor
$\Delta v'_{cal}/v'_{cal}$ = uncertainty in known velocity
$\Delta f_d/f_d$ = uncertainty in measured doppler frequency

The fully developed flow profile in the straight section could be used as the known velocity standard if it had developed properly. Since this was not known *a priori*, a velocity standard independent of the flow was required. The velocity standard that was used was a wheel of known diameter rotating at a constant angular velocity.

The surface velocity of a 2.915 cm ±0.001 cm (i.e. 0.03% uncertainty) diameter chuck rotating at constant angular velocity was used as the initial velocity standard. The chuck was attached to a mixing motor which revolved at ≈ 47 rpm. The rotational speed of the motor was determined by timing the interval required for 60 revolutions of the chuck with a hand held stop watch. With a reaction time of about 0.1 s, the uncertainty in the rotational speed of the chuck was approximately 0.15%. Since $v'_{cal} = r_c\omega_c$, where r_c is the radius of the chuck and ω_c is the angular velocity of the chuck, the uncertainty in v'_{cal} was $\sqrt{(\Delta r_c/r_c)^2 + (\Delta\omega_c/\omega_c)^2} \approx 0.15\%$.

The measured doppler frequency had an uncertainty of at least ± 0.1 kH which was caused by the resolution of the tracker processor. Noise in the doppler signal added to the uncertainty in the detected doppler frequency, therefore the actual uncertainty was probably higher than ± 0.1 kH. For the doppler frequency measured from the spinning wheel, a reasonable estimate of the uncertainty in the measurement would be about 0.25%.

Only one measurement of the doppler frequency was used to determine the calibration factor from the spinning wheel. For an uncertainty of 0.15% in the

velocity standard and 0.25% in the measured doppler frequency, equation 5.4 estimates the bias uncertainty in the calibration factor to be ±0.30%. This is the standard deviation of the uncertainty in the calibration factor, so the maximum uncertainty could be as high as three standard deviations or ±0.90%. It can be seen that the uncertainty in the calibration factor, as a result of using the spinning wheel, is mainly due to the uncertainty in the measured doppler frequency. However in hindsight, the uncertainty could have been reduced by taking more than one independent velocity measurement of the spinning wheel.

5.2.3 Inlet Profile as Velocity Standard

Calibrating the LDV independent of the flow apparatus allowed the straight section inlet profile to be examined. Figure 5.1 shows the measured inlet profiles at two different Reynolds numbers compared to the analytically predicted profile. Agreement is very good, confirming that the inlet profile has reached the fully developed state in this range of Reynolds numbers. Given that the inlet profile was well behaved, it was decided to use the inlet profile as the standard in subsequent calibrations. In order to determine the calibration factor from a measurement of the inlet profile, the measured data was fitted to the analytically predicted profile.

When using the inlet profile as the velocity standard, the uncertainty in the calibration factor will depend on the bias errors in the flow velocities and measured doppler frequencies. Since the inlet profile is defined by an analytical function, only the average velocity needs to be specified in order to define the entire profile. Therefore, a systematic or bias error can be introduced into the calibration factor by a bias error in the calculated mean velocity. The mean velocity can be determined

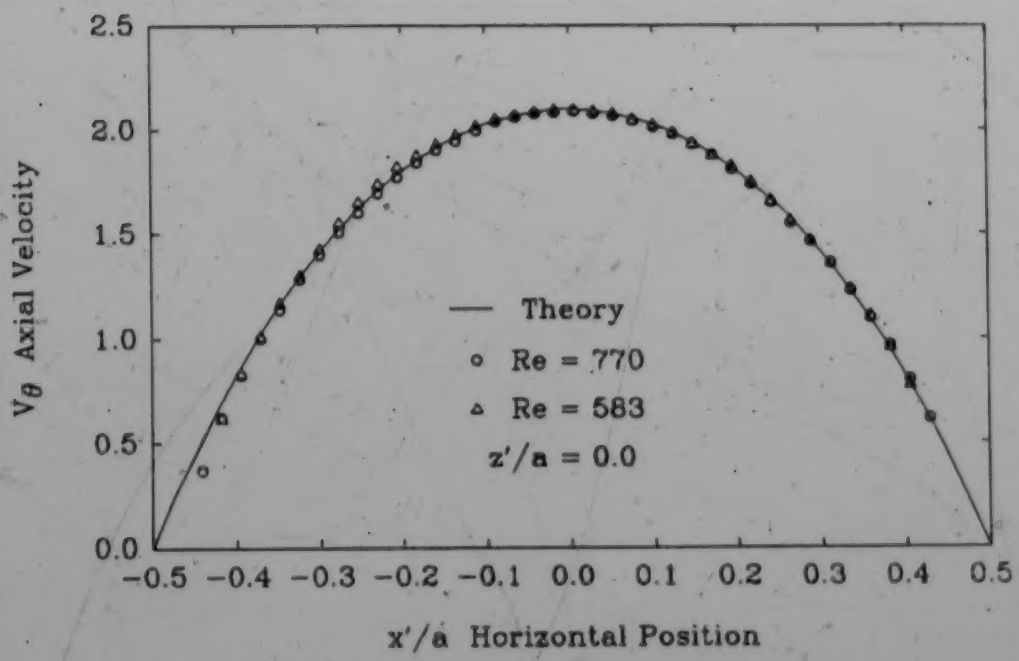

Figure 5.1: Comparison of measured inlet profiles to analytical prediction.

from the following relationship:

$$\overline{v'_\theta} = \frac{\dot{m}}{\rho a b} \tag{5.5}$$

where: $\overline{v'_\theta}$ = average velocity
$\dot{m}$ = mass flow rate
ρ = density
a = duct width
b = duct height

Using equation 5.5 and equation 5.4, it is possible to derive an expression for the uncertainty in the calibration factor when using the inlet profile as the velocity standard. The expression is given as:

$$\frac{\Delta c_f}{c_f} = \sqrt{\left(\frac{\Delta \dot{m}}{\dot{m}}\right)^2 + \left(\frac{\Delta \rho}{\rho}\right)^2 + \left(\frac{\Delta a}{a}\right)^2 + \left(\frac{\Delta b}{b}\right)^2 + \left(\frac{\Delta f_d}{f_d}\right)^2} \tag{5.6}$$

As mentioned before, the typical uncertainties in $\dot{m}$, ρ, a and b were 0.1%, 0.002%, 0.2% and 0.2% respectively. Since many velocity measurements were used to fit the analytical profile, the uncertainty introduced by the measured doppler frequencies was less than the uncertainty for an individually measured doppler frequency.

An estimate of the bias uncertainty caused by all of the measured doppler frequencies was calculated by dividing the uncertainty of an individually measured doppler frequency by the square root of the total number of velocity measurements used to fit the analytical profile. The theoretical basis for this estimation is given in Ang and Tang (1975) *pp.* 231–232. In order to apply this estimate to the measured doppler frequencies, it was assumed that individual errors that occurred in the measured doppler frequencies were random. This is a good assumption since the individual error in a measured doppler frequency is caused by the tracker resolution and noise contained within the doppler signal. The only place the assumption breaks down is in the measurements near the wall, where reflections introduce a biased shift

into the measured doppler frequency. The number of points where this occurred was small, so the effect was ignored.

In order to determine the calibration factor, both a horizontal and vertical profile were measured at the corresponding duct centerlines. In total, about 70 independent velocity measurements were made while measuring the velocity profiles. Since both profiles were used in fitting the measurements to the analytical prediction, the uncertainty caused by all of the measured doppler frequencies was $1/\sqrt{70}$ of the uncertainty in an individually measured doppler frequency. As seen in the previous section, the uncertainty in an individual doppler frequency was 0.25%, so the uncertainty caused by using 70 measured doppler frequencies is less than 0.03%. Substitution of the appropriate uncertainties into equation 5.6 resulted in an estimated uncertainty of $\pm 0.3\%$ in the calibration factor. As mentioned before this an estimate for the standard deviation, so the maximum error could be three standard deviations or $\pm 0.9\%$. It must be remembered that the probability is around 0.7 that the error will be within one standard deviation, and 0.95 that it will be within two standard deviations. It can be seen from equation 5.6 that the majority of the uncertainty in the calibration factor, when using the inlet profile as the standard, is caused by the uncertainty in the duct dimensions. Not much can be done to improve the uncertainty, since tighter machining tolerances, when working with plexiglass, are not easily obtainable. Therefore, when the inlet profile is used as the velocity standard, the uncertainty introduced by the duct dimensions has to be accepted.

From the preceding analyses, it can be seen that the most accurate determination of the calibration factor is from an accurate measurement of the beam crossing angle, or from many measurements of a reliable standard. Measuring the crossing angle is an attractive method because it limits the error to one source and is a quick task to

perform. In this study, the method of measuring the angle would have to have been more reliable to give satisfactory results. Given the equipment used in this study, the most accurate calculation of the calibration factor could have been obtained by making many measurements of the spinning wheel. A large number of repeats could have reduced the uncertainties associated with the measured doppler frequencies and measured rotation rates to a negligible amount. Despite this, the majority of the velocity data in this study was acquired with a calibration factor determined with the inlet profile as the velocity standard.

5.3 Uncertainties in Velocity Measurements

Once the LDV had been calibrated, a typical velocity measurement was subject to uncertainty because of the uncertainty in the calibration factor and the uncertainty in the measured doppler frequency. Other sources of uncertainty in velocity measurements were the systematic errors associated with the bias in the output of the tracker processor, changes in the calibration factor due to traversing the laser beams through a curved surface, positioning errors due to traversing the apparatus while holding the LDV stationary, and positioning errors caused by incorrectly locating the duct walls. Each possible source of error was investigated to determine its effect on the accuracy of a velocity measurement.

5.3.1 Uncertainty in a Typical Velocity Measurement

The uncertainty in a velocity measurement will at least include the calibration uncertainty and the uncertainty in the measured doppler frequency. Most of the velocity measurements in this study are presented normalized by the mean velocity, so the uncertainty in a non-dimensional velocity will also include the uncertainty

in the mean velocity. The normalized axial velocity, v_θ, given in terms of all the measured or inferred quantities used to calculate it is:

$$v_\theta = \frac{v'_\theta}{\overline{v'_\theta}} = \frac{c_f f_d \rho a b}{\dot{m}} \tag{5.7}$$

where: v_θ = non-dimensional axial velocity
v'_θ = dimensional axial velocity
$\overline{v'_\theta}$ = average axial velocity
c_f = calibration factor
f_d = measured doppler frequency
ρ = density
a, b = duct dimensions
$\dot{m}$ = mass flow rate

Applying the method of Appendix A, the uncertainty in a calculated value of v_θ is:

$$\frac{\Delta v_\theta}{v_\theta} = \sqrt{\left(\frac{\Delta c_f}{c_f}\right)^2 + \left(\frac{\Delta f_d}{f_d}\right)^2 + \left(\frac{\Delta \rho}{\rho}\right)^2 + \left(\frac{\Delta a}{a}\right)^2 + \left(\frac{\Delta b}{b}\right)^2 + \left(\frac{\Delta \dot{m}}{\dot{m}}\right)^2} \tag{5.8}$$

As given previously, the uncertainties in c_f, ρ, a, b and $\dot{m}$ were 0.3%, 0.002%, 0.2%, 0.2% and 0.1% respectively. All of these uncertainties directly contributed towards a biased shift in the measured profile. The uncertainty in f_d was 0.25% for any individual reading, but the bias introduced for the whole profile depended on the number of measurements that were taken. That is, the individual uncertainties in f_d would cause scatter about a smaller biased shift in the measured profile caused by the uncertainties in all of the measured doppler frequencies. The appropriate uncertainty estimate required that the uncertainty for an individual doppler frequency measurement be divided by the square root of the number of readings taken. A typical velocity profile involved the measurement of about 35 points, so the uncertainty in f_d to be used in equation 5.8 would be 0.04%. Substitution of the above uncertainty values into equation 5.8 results in an uncertainty in v_θ of $\pm 0.45\%$.

The estimate of the uncertainty in v_θ is very realistic as can be seen from the measured velocity profiles presented in figure 6.2. At the center of the duct, where the profiles are relatively flat and positioning of the LDV probe volume is not critical, the measured values at $Re = 583$ and 770 are typically within 0.5%-0.75% of the analytical curves.

5.3.2 Output Bias of Tracker Processor

The tracker processor gave an incorrect doppler frequency if wall reflections were high or if the range and gain were set incorrectly. When measuring near a wall, strong reflections caused the shift frequency to appear in the doppler signal, which in turn caused the tracker to give erroneous results. The magnitude of this effect can be seen in figure 5.2, where the velocities calculated from the doppler frequencies measured by the tracker processor are compared to the velocities calculated from the doppler frequencies measured by an unbiased FFT Spectrum Analyzer. The solid line is the numerically predicted velocity profile. Near the wall, where the reflections were the highest, the tendency was for the tracker processor to measure low. The tendency to measure low is most likely a result of the tracker locking on to a frequency somewhere between the doppler frequency and the lower shift frequency.

Significant error could be introduced into a measured doppler frequency if the tracker had not been set to the proper range. Figure 5.3 shows the same velocity profile measured using two different ranges of the tracker. The difference between the measured profiles is about 5% in the central region of the profiles. The reason the higher tracker range setting resulted in incorrect velocity values was because the frequency of the doppler signal ($\approx$ 20 kH in this case) was in the bottom end of the range. Therefore, to guard against this type of error, care was exercised to ensure that the proper tracker range was being used.

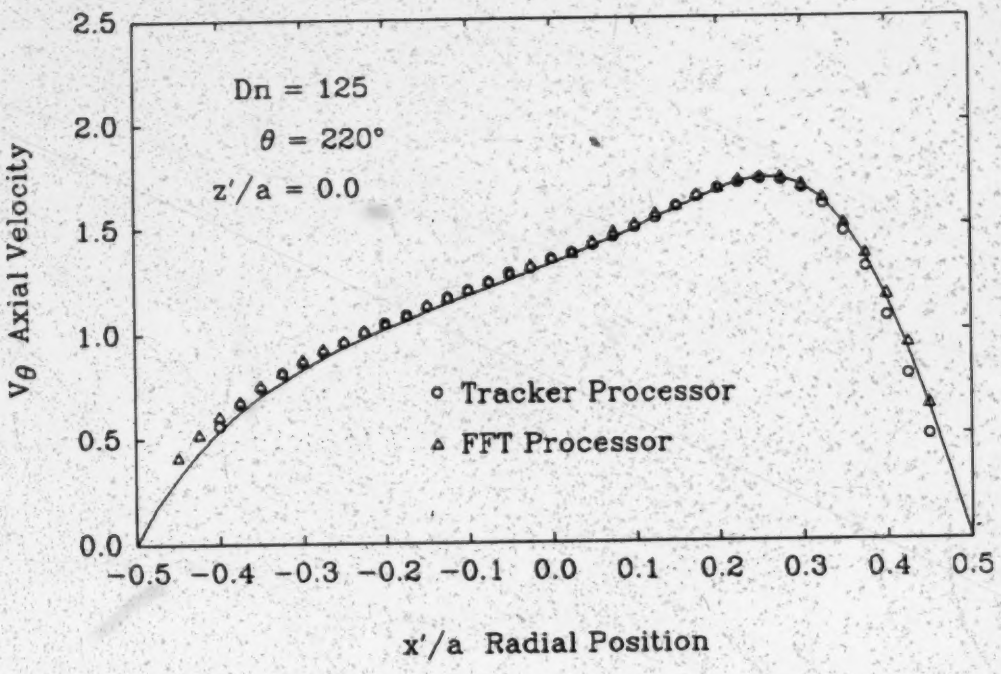

Figure 5.2: Comparison of velocities determined with tracker processor to velocities determined with FFT Spectrum Analyzer.

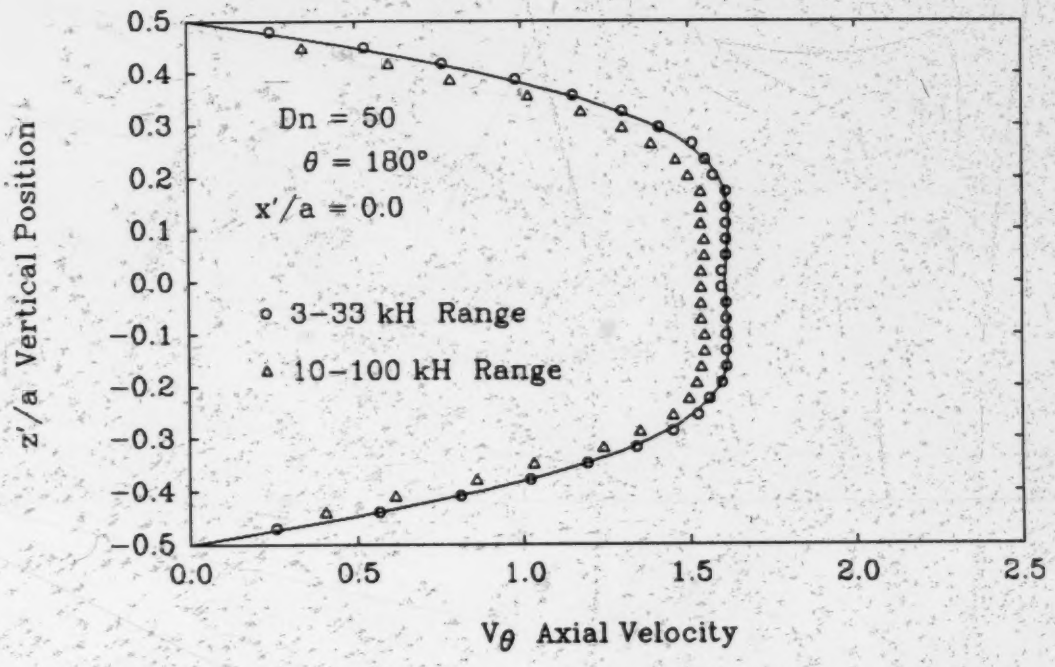

Figure 5.3: Comparison of velocities calculated from doppler frequencies determined with 3-33 kH and 10-100 kH ranges of the tracker processor.

A measured doppler frequency was sensitive to the gain setting of the tracker processor when the doppler signal contained a lot of noise. Noisy doppler signals were encountered near the walls and also when the concentration of seeding particles became too low. However, with proper seeding, most of the measurements taken away from the walls did not exhibit high sensitivity to the gain setting.

5.3.3 Effect of Curved Wall

Velocity measurements were performed by passing the laser beams of the LDV through the curved outer wall of the duct. Refraction of the laser beams at the curved interfaces between the air, plexiglass and water affected the calibration factor of the LDV. The distance of the crossing point from the wall determined the crossing angle of the beams, so the calibration factor continuously changed as the crossing point was traversed across the duct. Also, as the distance of the crossing point from the outer wall changed, the ratio of the distance traversed in water to that traversed in air was affected. Appendix B contains a detailed treatment of the changes in calibration factor and traversing ratio when traversing across the duct.

Figures 5.4 and 5.5 show how the calibration factor and traversing were affected by the refraction effects at the curved surfaces when traversing along a radial line. Figure 5.4 shows the correction factor that had to be applied to the measured results in order to compensate for the changing calibration factor. The fringe spacings, d_f and d_a, are the calibration factors in the fluid and air respectively. The refraction effect at the curved surfaces caused errors in the calibration factor of about 0.25% at the outer wall and 2% at the inner wall. The correction curve assumes that the beams traverse across the duct on a radial line. All measured velocities were adjusted using the correction factors presented in figure 5.4.

Figure 5.5 shows a plot of the distance traversed in air compared to the distance

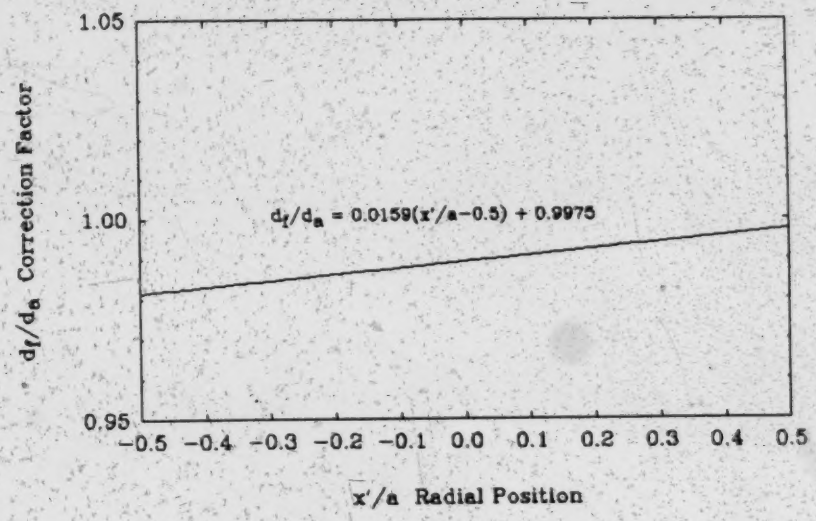

Figure 5.4: Correction factor as a function of radial position in duct.

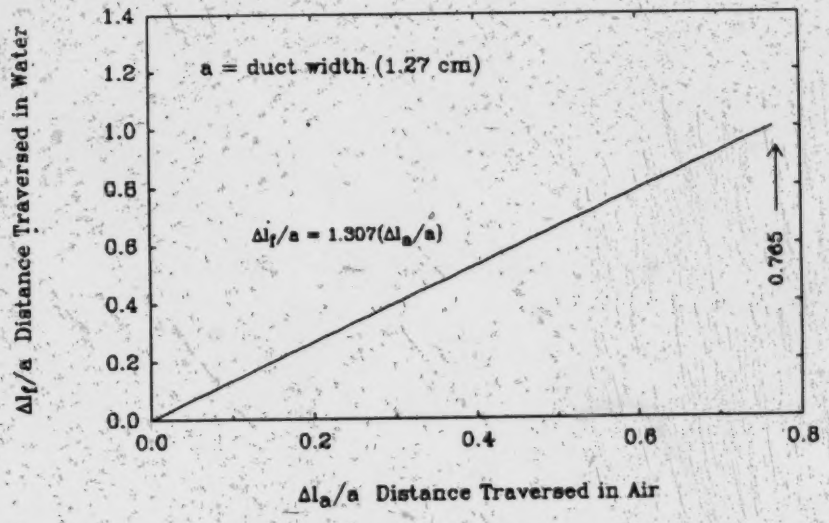

Figure 5.5: Traversing distance in water compared to traversing distance in air.

traversed in water. When the apparatus was traversed one unit, the actual distance the crossing point traversed in the water was more than one unit. However, as long as the ratio of the distance traversed in water to the distance traversed in air is constant, the traversing distances in air can be used to calculate the non-dimensional duct positions. A non-dimensional duct position was calculated by dividing the distanced traversed in air from the outer wall by the total distance traversed in air to go across the duct. Based on the linear relationship shown in figure 5.5, it was assumed that the traversing ratio was a constant. As a result of this assumption, calculated duct positions were shifted from the actual duct positions. The maximum error in calculated duct positions occurred near the center of the duct, where calculated duct positions were shifted by about 0.4% from the actual duct positions.

5.3.4 Traversing Errors

One effect of holding the LDV stationary while traversing the apparatus was that the path of the crossing point did not follow a radial line. Due to the physical size and design of the apparatus, the curved section end of the apparatus could slide 3–4 mm to the side as it was traversed forward to move the crossing point across the duct. As a result, the position of the crossing point would move in the axial direction. The position was about 1° out in the axial direction when the crossing point had reached the inside wall. For a fully developed flow this is not a problem, but in a developing region where strong axial gradients exist, significant error could result. In this study the observed axial gradients were not large enough for this effect to be significant.

The non-dimensional position in the duct was always calculated from the traversing distances in air. It these calculations it was assumed that traversing

was on a radial line. However, the actual path of the crossing point was not on a radial line, so the error associated with this assumption had to be determined. In order to determine the actual position of the crossing point in the duct, a general ray tracing program for the laser beams was developed. The method, along with the necessary equations, is presented in Appendix B. Given a position of the apparatus relative to the LDV, the program would calculate the position of the crossing point in the duct and the corresponding correction to the calibration factor.

In order to model the sliding of the apparatus, the crossing point was positioned on the outer wall and then traversed on a straight line that was at an angle to the radial path line. The traversing was stopped when the crossing point contacted the inner wall. The non-dimensional radial duct positions were calculated using the traversing distances in air assuming that the angled path line was a radial line. As a result, the calculated duct positions were shifted from the actual positions in the duct. The effect that the shift had on an axial velocity profile can be seen in figure 5.6. The solid line is a numerically-calculated fully developed profile at $Dn = 125$. The triangles are the calculated velocity values from each grid point of the numerical prediction plotted at the shifted duct positions.

The calculated duct positions were based on the apparatus sliding 4.5 mm to the side as it was traversed forward. A maximum error in position of about 0.6% occurs in the central region of the duct. As seen from the triangles in figure 5.6, the effect of the positioning error is to shift the velocity values downward. It is interesting to note that the positioning error was about 0.4% when traversing was on a radial line. This suggests that the majority of the positioning error in the radial direction is due to the fact that the traversing ratio is not a constant. In addition, the corrections to the calibration factor for the sliding apparatus analysis, were almost identical to the ones calculated from the radial path analysis.

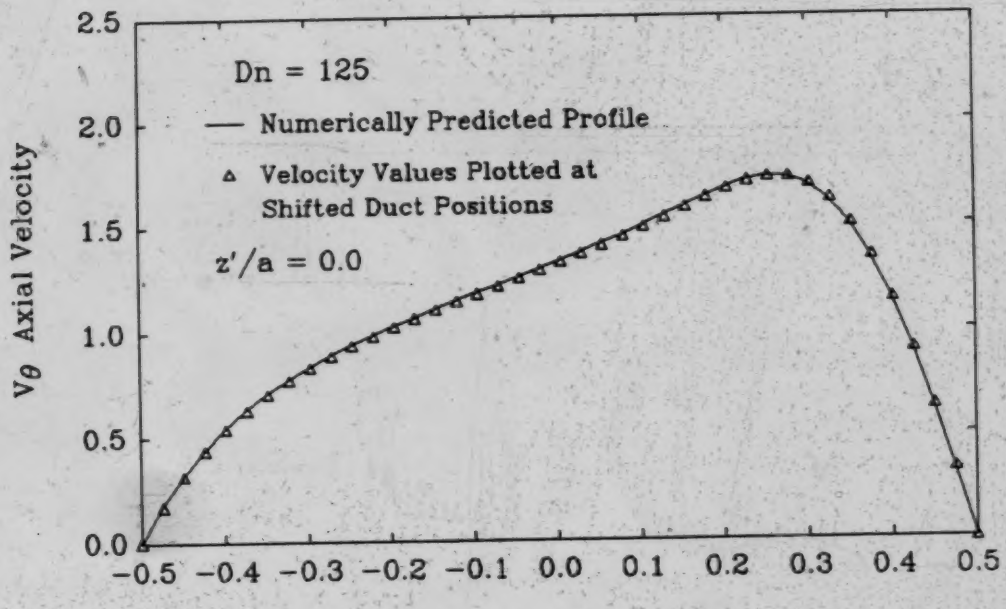

Figure 5.6: Numerically predicted velocity profile compared to calculated velocity values from each grid point of the numerical prediction plotted at the shifted duct positions.

5.3.5 Errors in Measuring Vertical Profiles

When measuring a vertical profile, a shift in radial position was observed when the direction of traversing was reversed. Figure 5.7 shows the shift in the vertical profile that resulted from a change in the traversing direction once the top duct wall was reached. The cause of this shift was probably due to movement in the traversing mechanism as the weight of the apparatus was redistributed on the screw threads when traversing direction changed. The shift was between 0.5–1.0 mm which corresponds to a 5% error in duct position.

For a typical vertical profile, the apparatus was traversed vertically to position the crossing point at the vertical duct center. The apparatus was then traversed in the radial direction to set the desired radial position. Once the radial position was set, the apparatus was again traversed in the vertical direction to position the crossing point on the bottom or top duct wall. Using this as the starting position, the apparatus was once again traversed vertically to measure a vertical profile. The amount of shift in the radial direction was minimized by ensuring that the screw threads had supported the weight of the apparatus in the same manner when the radial position was set as when the measurements were made.

Given the radial movement of the apparatus when measuring vertical profiles, it was impossible to completely eliminate a radial shift. Correction for a radial shift was made by scaling the measured vertical profile to match the common point in the measured horizontal profile at the same axial location. The correction was only applied to the vertical profiles that were measured at $x'/a = 0.0$. It was assumed that the shape of the vertical profile would remain constant for small changes in radial position. The validity of this assumption is seen in figure 5.8 where the vertical profile at $Dn = 50$ and $x'/a = 0.0$ is compared to the profiles corresponding to a $\pm 5\%$ shift in duct position. For higher Dean numbers, the shape of the vertical

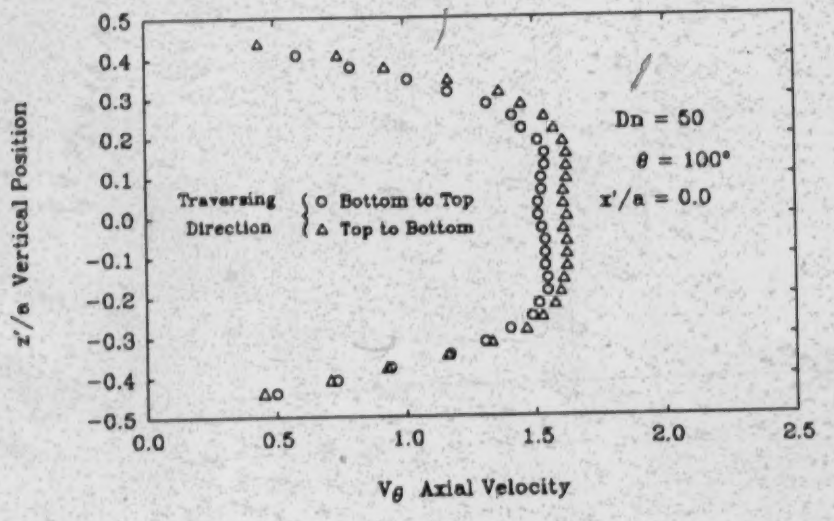

Figure 5.7: Effect of traversing direction on measured vertical profile.

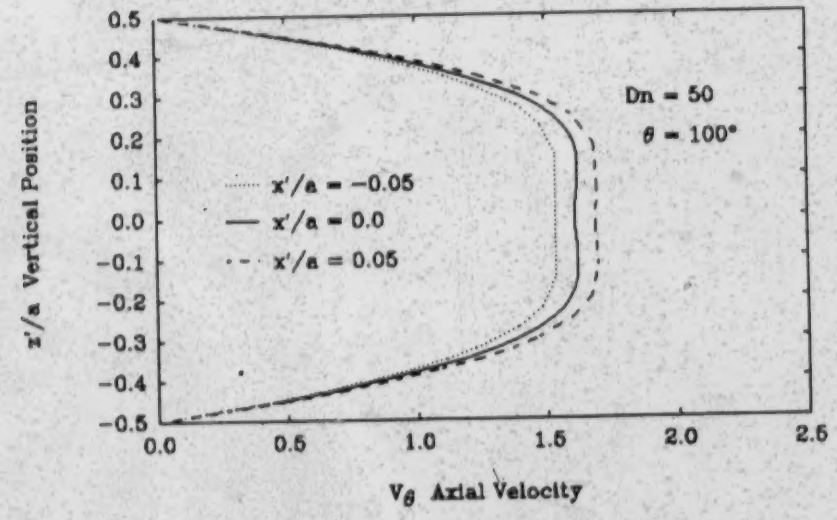

Figure 5.8: Shape of vertical profile at $x'/a = 0.0$ compared to the shape of the profiles corresponding to a $\pm 5\%$ change in duct position.

profiles around $x'/a = 0.0$ also remained constant.

5.3.6 Wall Location Error

A systematic error in radial position could be introduced by incorrectly locating the inner side wall of the duct. In order to determine if the beam crossing point was on a wall, the output of the LDV was monitored on an oscilloscope. When positioning the crossing point on the outer wall, a well defined maximum occurred in the output indicating the crossing point was on the wall. However, when positioning of the crossing point on the inner wall, the signal seemed to remain fairly strong with no well defined maximum as the crossing point was traversed through the wall. The signal quality also varied with axial position, so no truly objective method for finding the inner wall was discovered.

The top graph in figure 5.9 is an example of the error that resulted from incorrectly locating the inner wall in the fully developed flow region. In the developing flow region it would not be apparent whether a difference was due to this effect, or to the fact that the numerical profiles might be in error due to the assumptions associated with the formulation of the 3-D code. In figure 5.9 the wall location error was a result of interpreting the LDV output to indicate the beam crossing point was on the wall, when in fact the crossing point was still in the fluid.

Interpreting the width of the duct to be narrower than it actually was, caused the radial positions of the measured velocities to be linearly stretched toward the inner wall. A point on the outer wall experienced no shift, while the point believed to be on the inner wall experienced the maximum shift. By correcting the measured profile to fit the numerical prediction, as was done in the bottom graph of figure 5.9, it is seen that the error in locating the inner wall was 0.2 mm. It was very

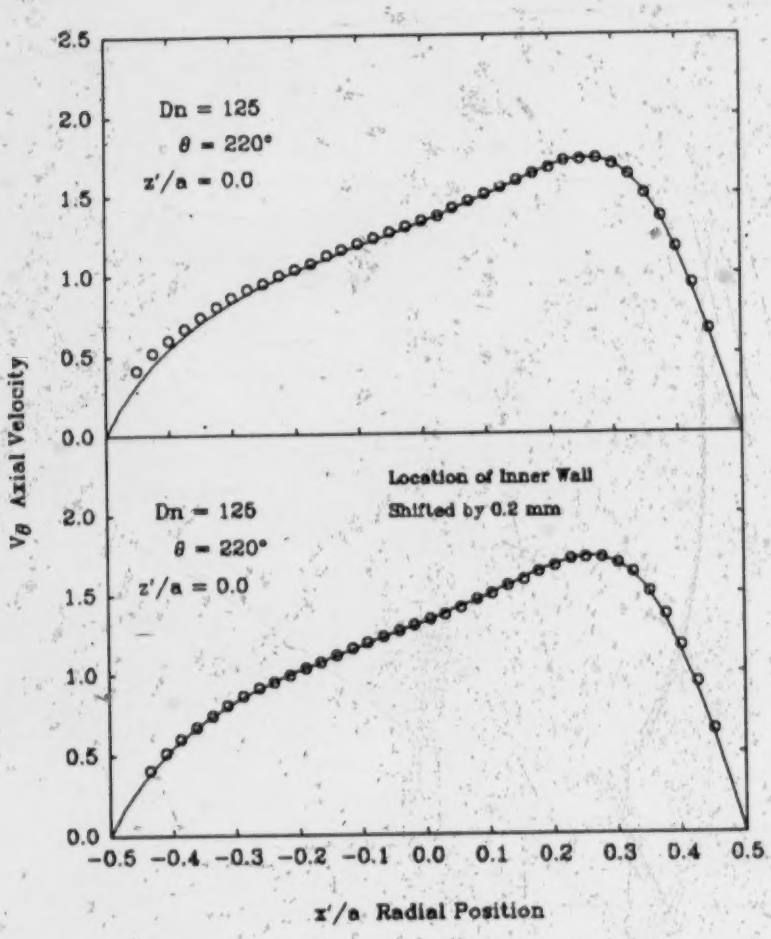

Figure 5.9: Correction to radial positions of measured axial velocities by relocation of inner side wall of duct.

conceivable that an error of 0.2 mm in locating the inner could have been made, considering that the probe volume itself was 0.12 mm long in the radial direction.

The natural tendency when locating the inner wall was to interpret the LDV output such that the calculated width of the duct would be too narrow. Reflected light from the laser beams, as the probe volume approached the wall, caused a strong output signal from the LDV. This signal could easily have been misinterpreted as indicating the location of the wall when in fact the probe volume was still in the fluid. The type of error shown in figure 5.9 would support this. Given this tendency, it was necessary to use judgement to locate the inner wall as best as possible. Therefore, the maximum error in locating the inner wall that could be expected using this approach would probably be about 2%-3%.

5.4 Summary

The uncertainty in an experimentally determined Dean number was estimated to be ±0.3%. Using the straight section inlet velocity profile as the velocity standard, the uncertainty in the calibration factor was estimated to be ±0.3%. It was estimated that the uncertainty in a typical experimentally determined non-dimensional axial velocity, v_θ, was about ±0.45%. As was seen in the measured velocity profiles presented in figure 6.2, the estimated uncertainty was in good agreement with the actual difference between the measurements and analytical predictions in the central region of the duct. Therefore, if the measured velocities are not subject to any further bias introduced by the signal processor, errors larger that 0.5% in measured velocities are a result of position errors in the duct. The refraction of the laser beams at the curved interfaces between the air, plexiglass and water, caused the calibration factor to change as the crossing point was traversed

across the duct. However, the effect was compensated for by using the analysis presented in Appendix B. Non-dimensional duct positions were calculated using the traversing distances in air, assuming that traversing had taken place on a radial line, and that the traversing ratio was a constant. The actual traversing ratio was not quite constant, so a small shift was introduced into the duct positions. The maximum amount of the shift was about 0.4% at the center of the duct. Sliding of the apparatus while the crossing point was traversed across the duct, resulted in the actual traversing path not being on a radial line. The effect on calculated duct positions in the radial direction was minimal, but a shift of 1° occurred in the axial position.

Due to the traversing mechanism, an uncertainty of ±5% in the radial position was encountered when measuring a vertical velocity profile. Since the shape of the vertical profiles near the center of the duct was constant, it was possible to scale the measured values to correspond to the desired radial position. Errors in locating the inner wall with the LDV caused shifts in the calculated radial duct positions of 2%-3%. When measuring a radial velocity profile, this shift caused the velocity measurements to be in error. Since the velocity profiles had strong gradients in the radial direction, errors of up to 5% could occur in the central region of the duct.

Chapter 6

Investigation of Developing Flows

In order to investigate the flow development, flow visualization and axial velocity measurements were performed at three Dean numbers, Dn = 125, 137 and 150. Starting at an axial position of 20°, axial velocity profiles were measured every 20° up to an axial position of 240°. Photographs were taken at each location to visualize the development of the secondary flows. Using the parabolized formulation of the three-dimensional Navier-Stokes equations, numerical simulations of the flow development corresponding to the measurements were performed.

6.1 Inlet Flow

The inlet condition to the curved section that was used in this study was a fully developed laminar straight duct flow. The analytical solution for the fully developed axial velocity distribution of a laminar flow through a rectangular duct, as given in Shah and London (1978), is:

$$v'_\theta(x',z') = -\frac{4a^2c_2}{\mu\pi^3}\sum_{n=1,3,5,\ldots}^{\infty}\frac{1}{n^3}(-1)^{(n-1)/2}\left[1-\frac{\cosh(n\pi z'/a)}{\cosh(n\pi b/2a)}\right]\cos\left(\frac{n\pi x'}{a}\right) \quad (6.1)$$

$$\overline{v'_\theta} = -\frac{a^2 c_2}{12\mu}\left[1 - \frac{192}{\pi^5}\left(\frac{a}{b}\right)\sum_{n=1,3,5,\ldots}^{\infty}\frac{1}{n^5}\tanh\left(\frac{n\pi b}{2a}\right)\right] \qquad (6.2)$$

$$-a/2 \leq x' \leq a/2 \qquad -b/2 \leq z' \leq b/2$$

where: $v'_\theta(x', z')$ = axial velocity
$\overline{v'_\theta}$ = mean axial velocity
a, b = duct width and height respectively
μ = absolute viscosity
c_2 = pressure gradient in axial direction

The coordinate system for the duct cross section is the same as that illustrated in figure 3.1. Some of the coefficients in the above equations are different that those presented in Shah and London (1978), because the duct width and height were taken as a and b rather than $2a$ and $2b$.

In the numerical simulations of developing flow the inlet velocity profile was required as an initial condition. Instead of calculating the inlet velocity profile using equations 6.1 and 6.2, the three-dimensional code used in this study (i.e. computer code developed by Sankar *et al.* (1988)) calculated the inlet profile using a simple approximation. The simple approximation, as given in Shah and London (1978), for the non-dimensional axial velocity is:

$$v_\theta = \left(\frac{m+1}{m}\right)\left(\frac{n+1}{n}\right)\left[1 - \left(\frac{2z'}{b}\right)^n\right]\left[1 - \left(\frac{2x'}{a}\right)^m\right] \qquad (6.3)$$

For a square cross section, where $a = b$, the value of the exponents are $m = n = 2.2$. The form of equation 6.3 is also slightly different from the form presented in Shah and London because of the different definitions used for the duct dimensions.

The velocity profile determined from the analytical solution (i.e. equations 6.1 and 6.2) is compared to the simple approximation of equation 6.3 in figure

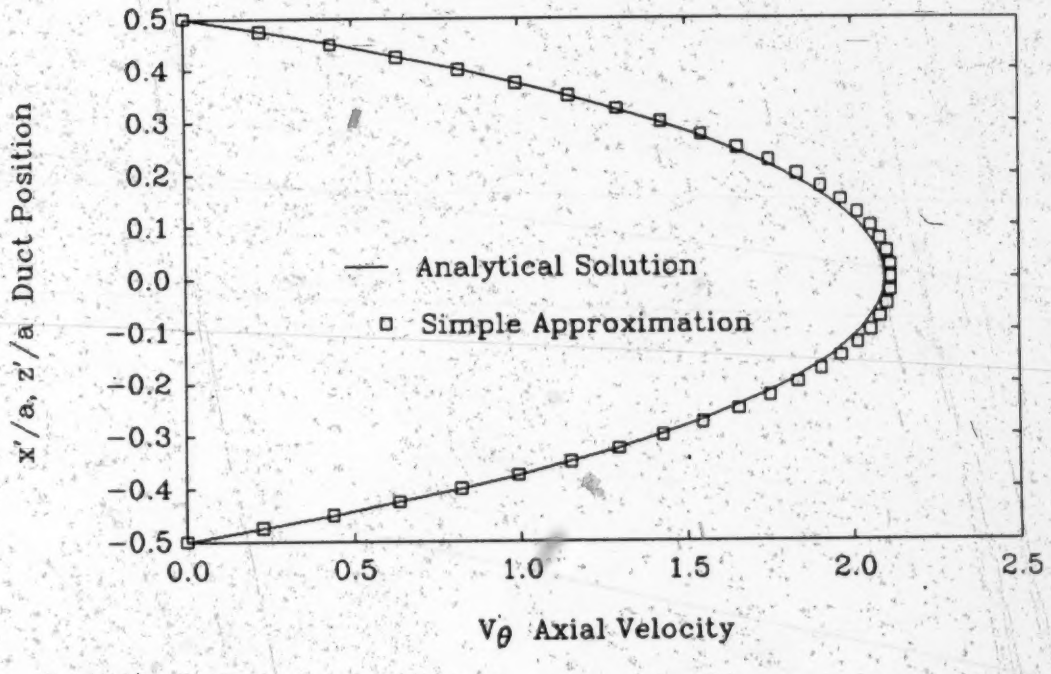

Figure 6.1: Comparison of inlet velocity profiles calculated from analytical and approximate formulations.

6.1. The velocity profiles shown are for the horizontal or vertical duct centerline. The simple approximation predicts values that are higher than the analytical solution in the central region of the duct. The maximum non-dimensional velocity predicted by the analytical solution at $x'/a = z'/a = 0.0$ is 2.096, while the simple approximation predicts a value of 2.116 at the same location. The difference is only 1%, so the simple approximation is a good estimate of the analytical solution. Considering that mass is conserved in the simple approximation, some profiles off of the centerlines must have regions where the analytical solution is higher than the simple approximation.

Figure 6.2 shows the analytically predicted profiles compared to the velocity profiles that were measured at 5 hydraulic diameters upstream of the curved section inlet. Horizontal and vertical axial velocity profiles were measured at the horizontal and vertical duct centerlines respectively. The measured data is in excellent agreement with the analytical prediction, confirming that for each of the Reynolds numbers investigated, the measured velocity profile had reached the fully developed state.

It was mentioned previously that the actual velocity profile that occurs at the start of a curved section will deviate from a fully developed straight duct profile. The reason for this is that, due to the elliptic nature of the flow, the curved section will have an effect on the flow upstream of its inlet. The magnitude of the effect will depend on the radius of curvature of the curved duct and the Reynolds number of the approach flow. The sharper the radius of curvature and the smaller the approach flow Reynolds number the greater the effect will be.

In axial velocity measurements for a square duct with $R_c = 2.3$ and approach flow $Re = 790$, Humphrey *et al.* (1977) observed that there was a noticeable deviation ($\approx 5\%$ in the axial velocity at the duct centerline and start of inlet section) from a

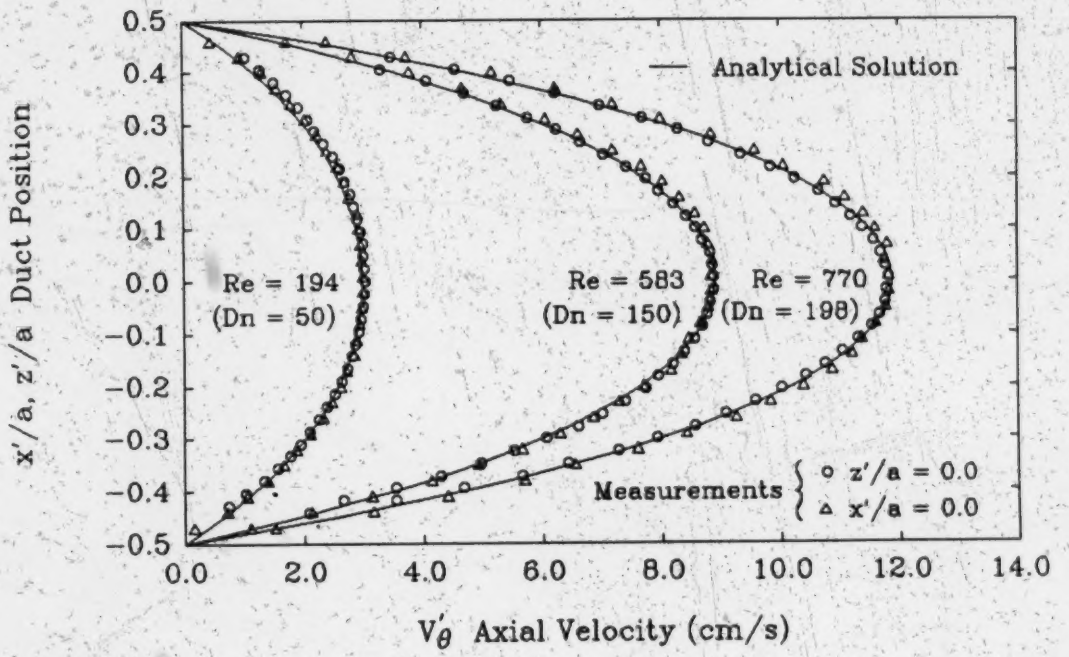

Figure 6.2: Comparison of measured inlet velocity profiles to analytical predictions (measurement location: 5 hydraulic diameters upstream of inlet).

fully developed profile in the region 0 to 5 hydraulic diameters upstream of the start of the curved section. At the start of the curved section inlet, the secondary flow structure had already been formed with secondary velocities as high as 15% of the mean axial velocity. Secondary velocities, 7% of the mean velocity, were present at 0.3 hydraulic diameters upstream of the inlet, but no vortex structure was evident.

In the apparatus used in this study, the straight section inlet profiles were measured at 5 hydraulic diameters upstream of the start of the curved section. Due to the large curvature ratio, $R_c = 15.1$ and approach flow Reynolds number, $Re = 500$–700, no deviations of the measurements from the analytically predicted profiles were observed. It seems reasonable that, based on the results of Humphrey *et al.*, the deviation of the inlet profile at the start of the curved section would be small for the curvature ratio and flow rates used in this study.

6.2 Flow Development at Dn=125

Development of the axial velocity profiles with downstream position at $Dn = 125$ is shown in figures 6.3 through 6.14. The outer wall of the duct is at $x'/a = 0.5$. For each downstream position, the measured horizontal axial velocity profile at the horizontal duct centerline (i.e. $z'/a = 0.0$) is compared to the numerically predicted profile. Vertical axial velocity profiles, measured at the vertical centerline of the duct (i.e $x'/a = 0.0$) at two downstream positions, are shown in figures 6.15 and 6.16. The numerical prediction of secondary flow development is presented in figure 6.17 in the form of arrow plots showing the secondary velocity vectors. All secondary velocities have been normalized with the mean axial velocity to show the relative strength of the secondary flow with downstream position. The outer wall is on the right hand side of each arrow plot, and the length of the mean axial velocity vector

is equal to the length of the duct walls. Flow visualization of the development of the secondary flow patterns is shown in figure 6.18. Again the outer wall is on the right hand side.

The development of the axial velocity profiles shown in figures 6.3 through 6.14 is similar to the observations of Austin and Seader (1974) for flow in a curved pipe, and Hille *et al.* (1985) for flow in a curved duct of square cross section. The profiles exhibit the characteristic initial transfer of momentum to the outer wall, with a back-transfer of momentum as the secondary flow becomes developed. The overall agreement with the numerical predictions is good, indicating that the parabolic assumption is valid at this Dean number. A slight increase in the axial velocity near the central region of the duct at 240° suggests that some exit effect might have been present.

In the fully developed region, which occurred after an axial position of about 100°, it can be seen that the measured velocities are slightly in error. The error appears to be systematic in nature, causing the measured values to be generally higher than the predictions. The radii of the circular symbols showing the measured velocities represent a 2% error at $v_\theta = 1.5$, and a 3% error at $v_\theta = 1.0$. Using this as a guide, the majority of the velocity errors in the central region of the duct are between 2% and 3%. Given that the uncertainty in v_θ was $\pm 0.45\%$, the errors were obviously caused by positioning errors in the duct. The consistently lower values of the measurements near the outer wall are likely due to the tendency of the tracker processor to measure low in this region (refer to chapter five; Output Bias of Tracker Processor).

As the flow initially developed, the fully developed straight duct inlet profile, with its velocity maximum at the duct center, was quickly skewed toward the outer wall. This large transfer of axial momentum is seen at 20° in figure 6.3, where the

axial velocity maximum has been shifted toward the outer wall. This initial transfer of momentum is a result of the fluid in the straight duct flowing toward the outer wall of the curved section which is in line with the straight duct axis. Examining the secondary velocity arrow plot at 20° in figure 6.17, it can be seen that a strong secondary flow toward the outer wall is present, and a return flow at the top and bottom walls of the duct has been established. The return flow has been set up in response to the favorable pressure gradient caused by the high pressure region at the outer wall. The maximum flow velocity toward the outer wall is 16% of the mean, while the maximum velocity in the region returning fluid toward the inner wall is 22.5% of the mean.

At 40° from the inlet, the peak in the axial velocity profile has decreased and started to move back toward the duct center. In addition, the axial velocity near the inner wall has increased. This redistribution of axial momentum is a result of the secondary flow transporting the high momentum fluid at the outer wall to the inner wall. From the arrow plot at 40°, it can be seen that the strength of the secondary flow toward the outer wall has decreased, as the initial linear momentum of the straight duct flow has been dissipated. The maximum secondary velocity directed toward the outer wall on the duct centerline is 5.3% of the mean, while the inward flow at the top and bottom walls has a maximum secondary velocity of 12.5% of the mean.

At 60° from the inlet, some further transfer of axial momentum from the outer wall toward the duct center has occurred, filling in the central region of the profile. The maximum secondary velocities have not significantly changed from the values at 40°, as is evident in the arrow plot at 60°. At 80° there is a slight decrease in the axial momentum in the central region of the duct, but no more appreciable changes occur after 100°. After 80° the secondary velocities settle down to maximum

values of 6.2% and 12.9% of the mean in the outward and inward flows respectively. Judging from the axial velocity measurements and the arrow plots of the secondary flow, it can be concluded that after 100° the flow has become fully developed.

Flow visualization in figure 6.18 shows that symmetry about the horizontal duct centerline was retained throughout the entire development process. This symmetry was also confirmed by the measured vertical axial velocity profiles shown in figures 6.15 and 6.16. Flow visualization is useful in showing the boundaries of the cells, but no velocity information can be obtained. The cell boundaries are traced out by the dye as the secondary flow carries the fluid around the cross section. Given the ratio of the mean axial velocity to the secondary velocities, a fluid particle will on average rotate once around the top or bottom half of the duct approximately every 70° to 80° of axial length. This effect is evident in the flow visualization at 20° and 40°, since the dye has not yet completed one revolution in the cross section.

In the studies of Austin and Seader (1974) and Humphery *et al.* (1977), double peaks in the axial velocity profiles were observed in the development of axial velocity. This was not observed in this study because the curvature of the duct was not strong enough. In strongly curved ducts as compared to gently curved ducts, more axial momentum is initially transferred toward the outer wall, so the secondary flow will bring fluid with higher momentum to the inner wall. This causes the slow moving fluid at the inner wall to be displaced toward the duct center leaving high momentum fluid at the inner wall, thus creating the double peak. Maximum secondary velocities of 23% of the mean in our study as compared to 65% of the mean in the study of Humphery *et al.* (1977) shows the effect that stronger curvature has in increasing the strength of the secondary flow.

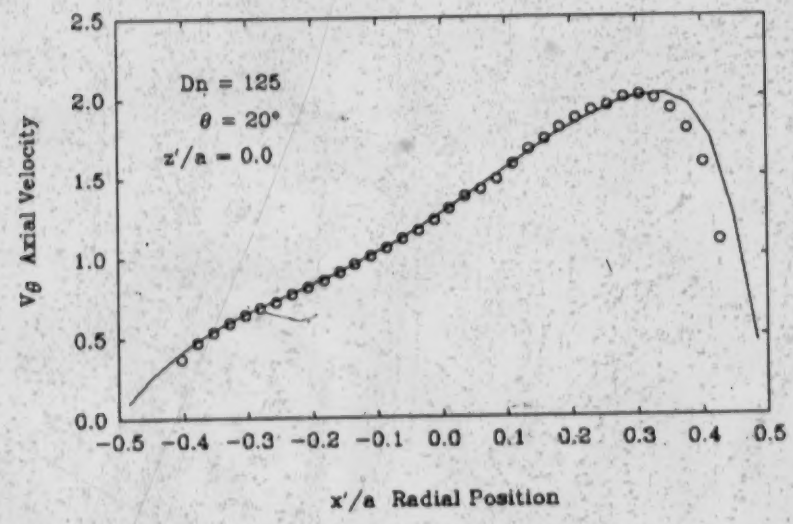

Figure 6.3: Measured velocity profile compared to numerical simulation at $Dn = 125$, $\theta = 20°$ and $z'/a = 0.0$.

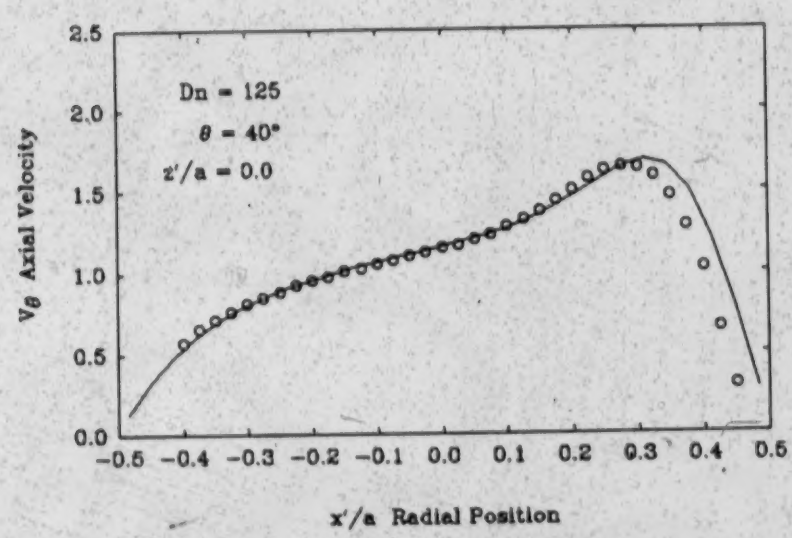

Figure 6.4: Measured velocity profile compared to numerical simulation at $Dn = 125$, $\theta = 40°$ and $z'/a = 0.0$.

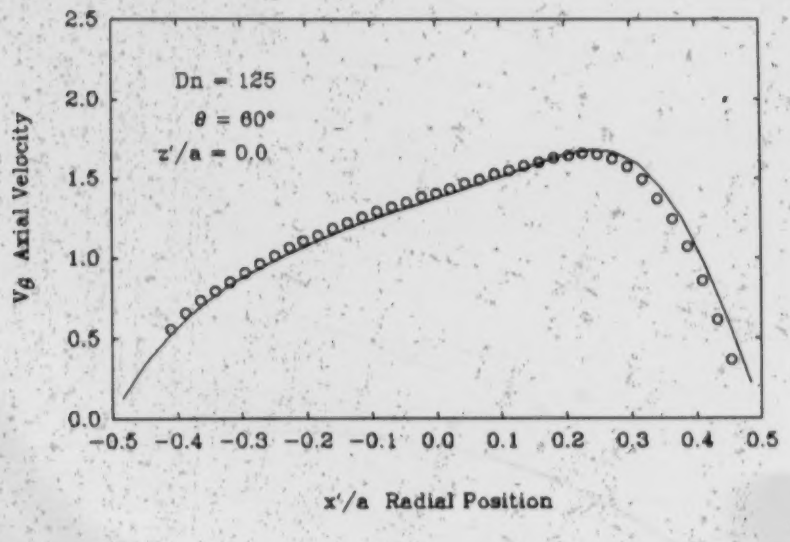

Figure 6.5: Measured velocity profile compared to numerical simulation at $Dn = 125$, $\theta = 60°$ and $z'/a = 0.0$.

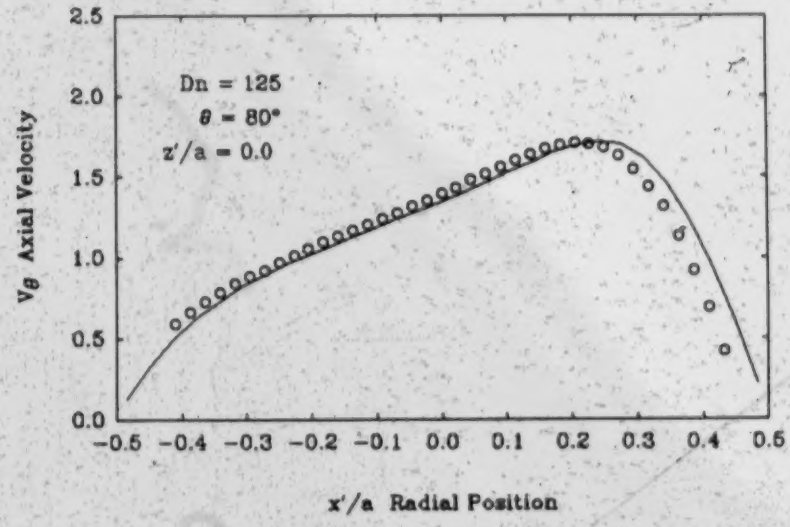

Figure 6.6: Measured velocity profile compared to numerical simulation at $Dn = 125$, $\theta = 80°$ and $z'/a = 0.0$.

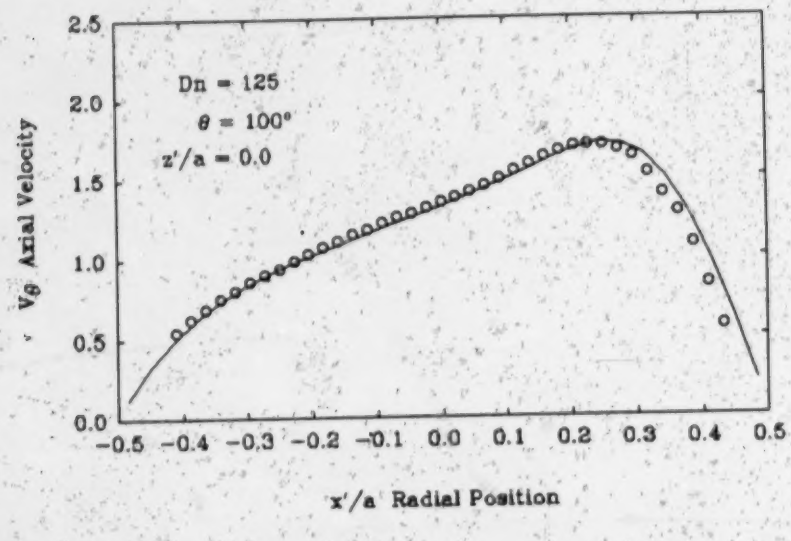

Figure 6.7: Measured velocity profile compared to numerical simulation at $Dn = 125$, $\theta = 100°$ and $z'/a = 0.0$.

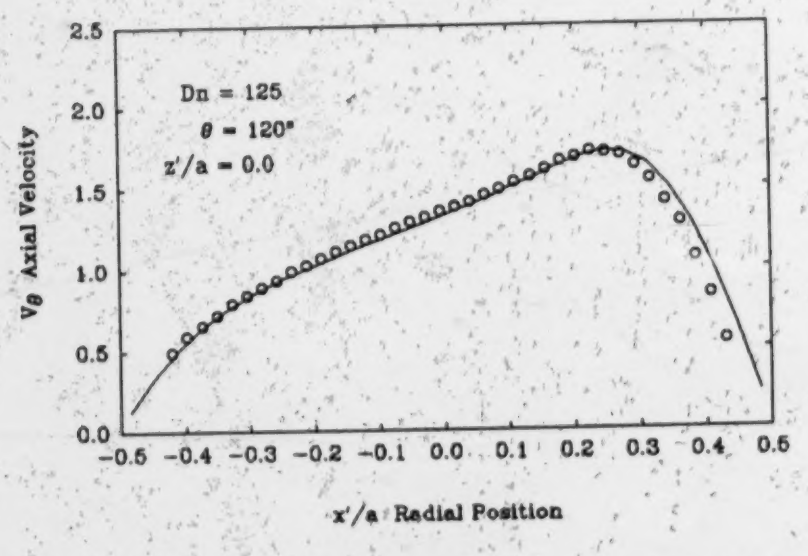

Figure 6.8: Measured velocity profile compared to numerical simulation at $Dn = 125$, $\theta = 120°$ and $z'/a = 0.0$.

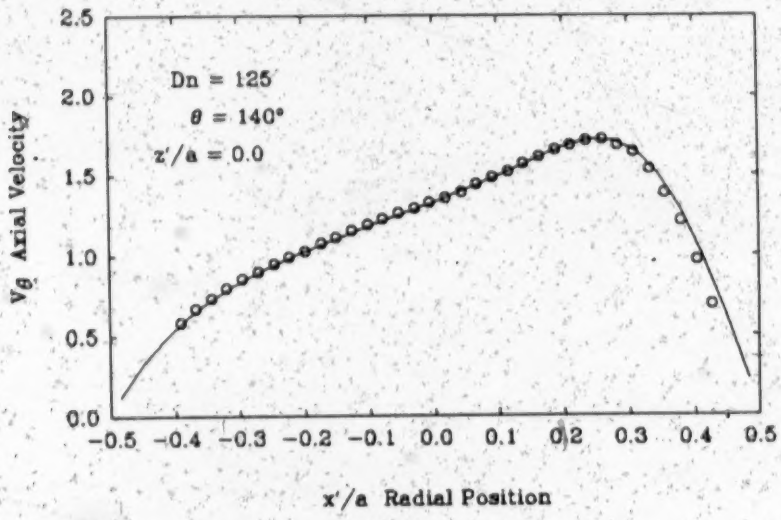

Figure 6.9: Measured velocity profile compared to numerical simulation at $Dn = 125$, $\theta = 140°$ and $z'/a = 0.0$.

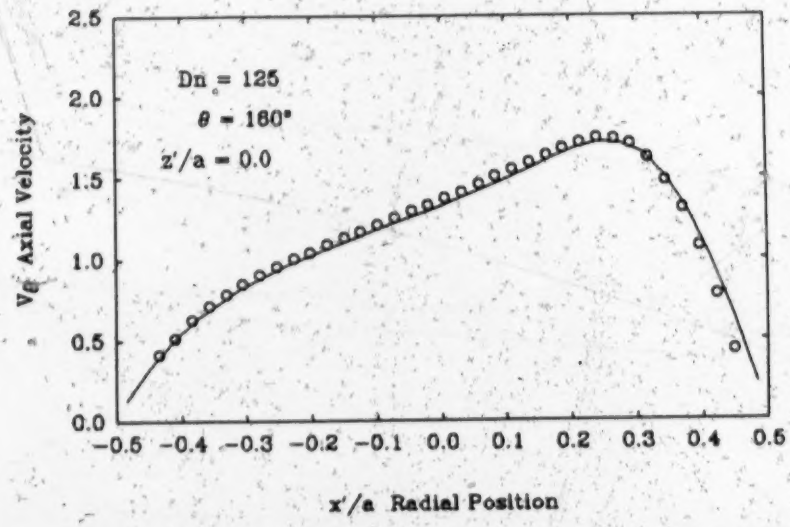

Figure 6.10: Measured velocity profile compared to numerical simulation at $Dn = 125$, $\theta = 160°$ and $z'/a = 0.0$.

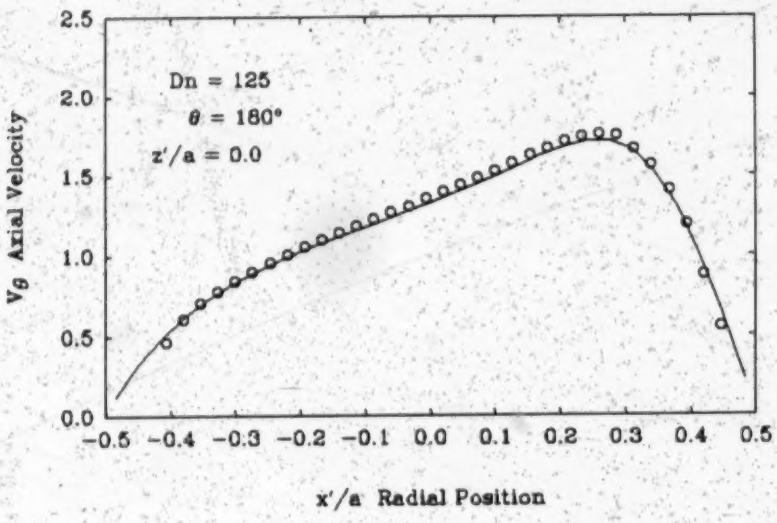

Figure 6.11: Measured velocity profile compared to numerical simulation at $Dn = 125$, $\theta = 180°$ and $z'/a = 0.0$.

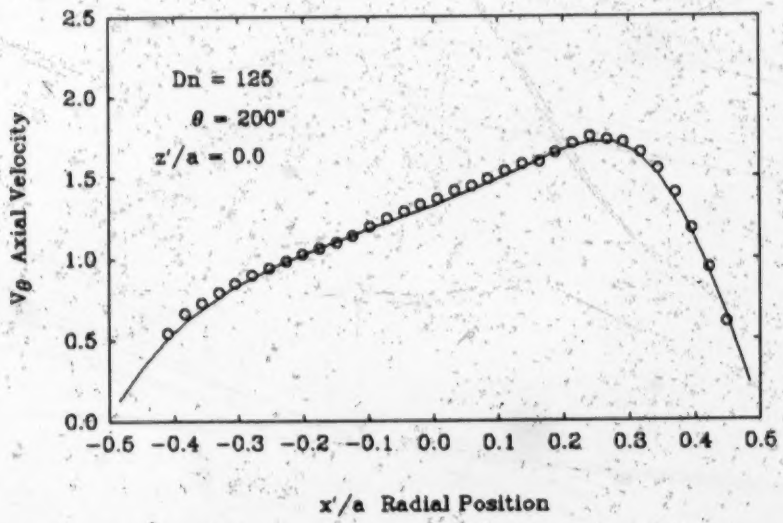

Figure 6.12: Measured velocity profile compared to numerical simulation at $Dn = 125$, $\theta = 200°$ and $z'/a = 0.0$.

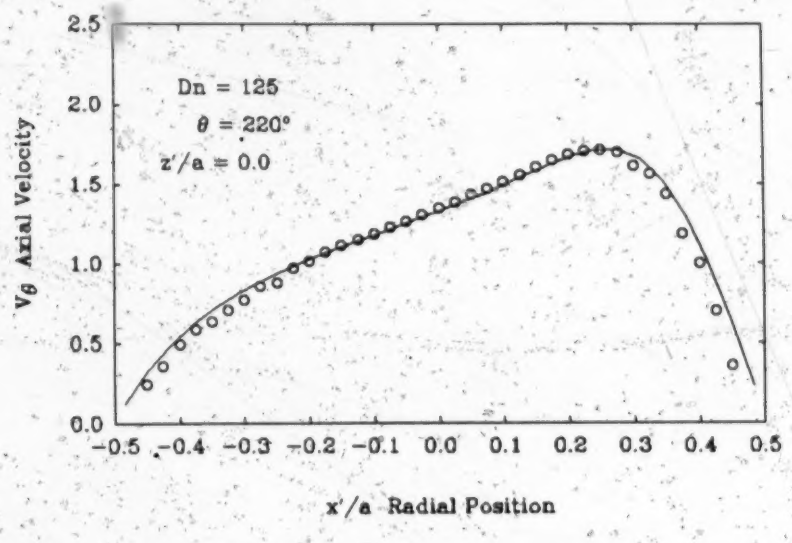

Figure 6.13: Measured velocity profile compared to numerical simulation at $Dn = 125$, $\theta = 220°$ and $z'/a = 0.0$.

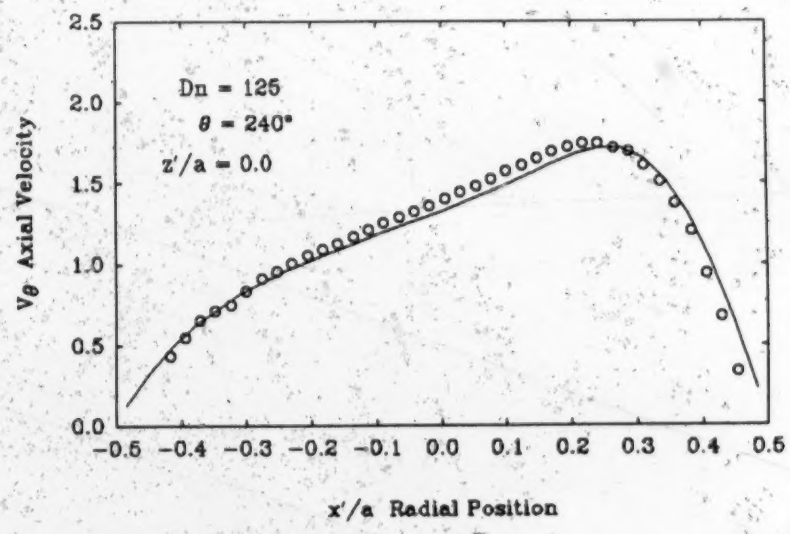

Figure 6.14: Measured velocity profile compared to numerical simulation at $Dn = 125$, $\theta = 240°$ and $z'/a = 0.0$.

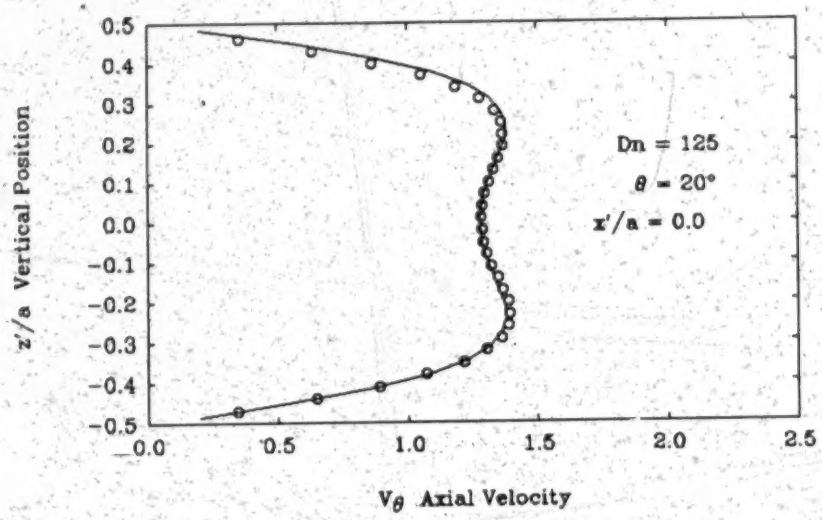

Figure 6.15: Measured velocity profile compared to numerical simulation at $Dn = 125$, $\theta = 20°$ and $x'/a = 0.0$.

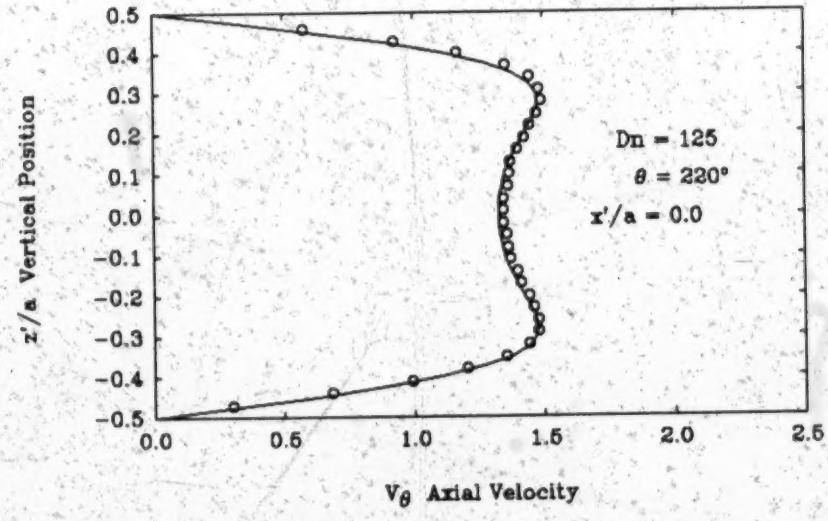

Figure 6.16: Measured velocity profile compared to numerical simulation at $Dn = 125$, $\theta = 220°$ and $x'/a = 0.0$.

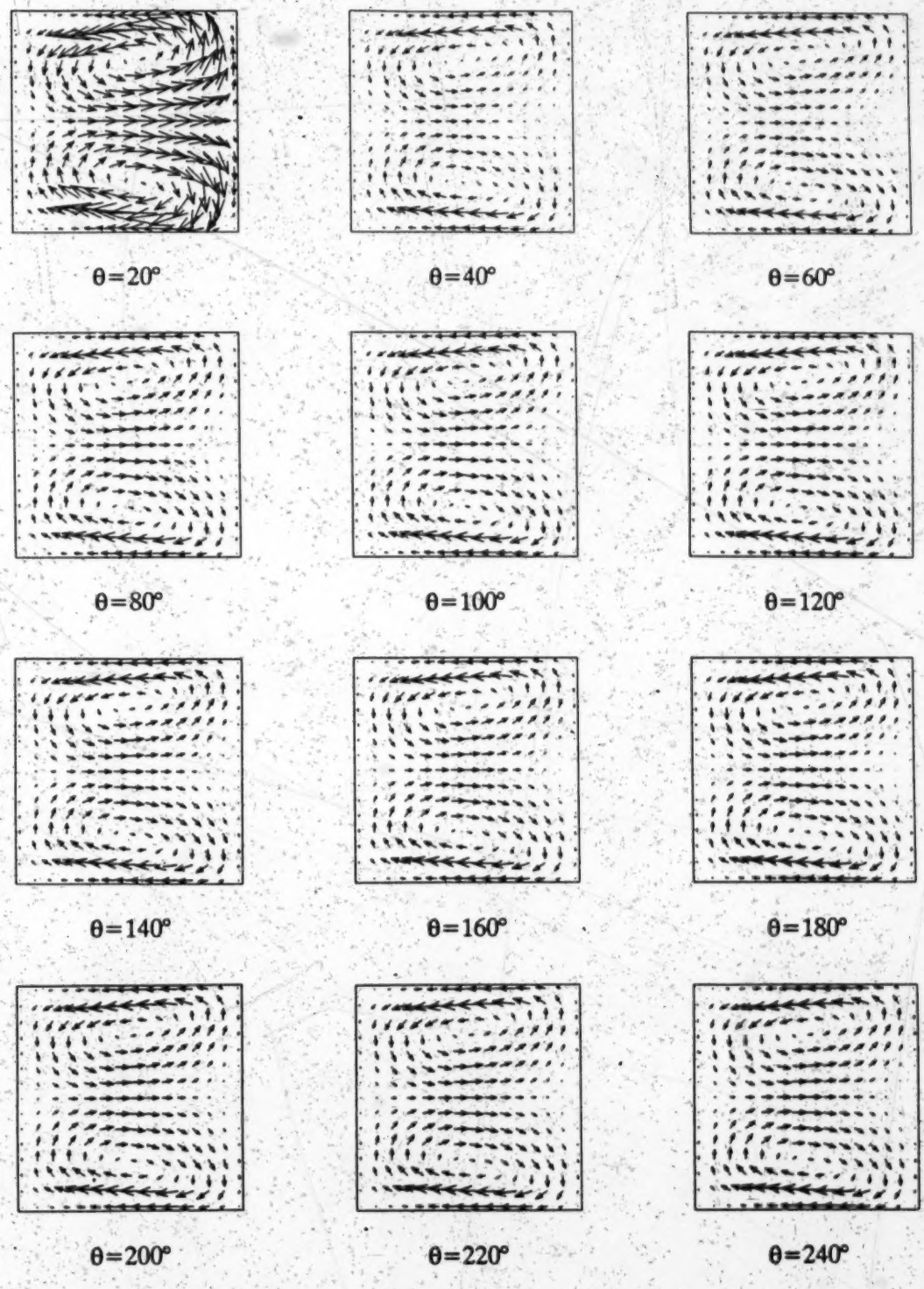

Figure 6.17: Arrow plots showing secondary flow development every 20° at $Dn = 125$.

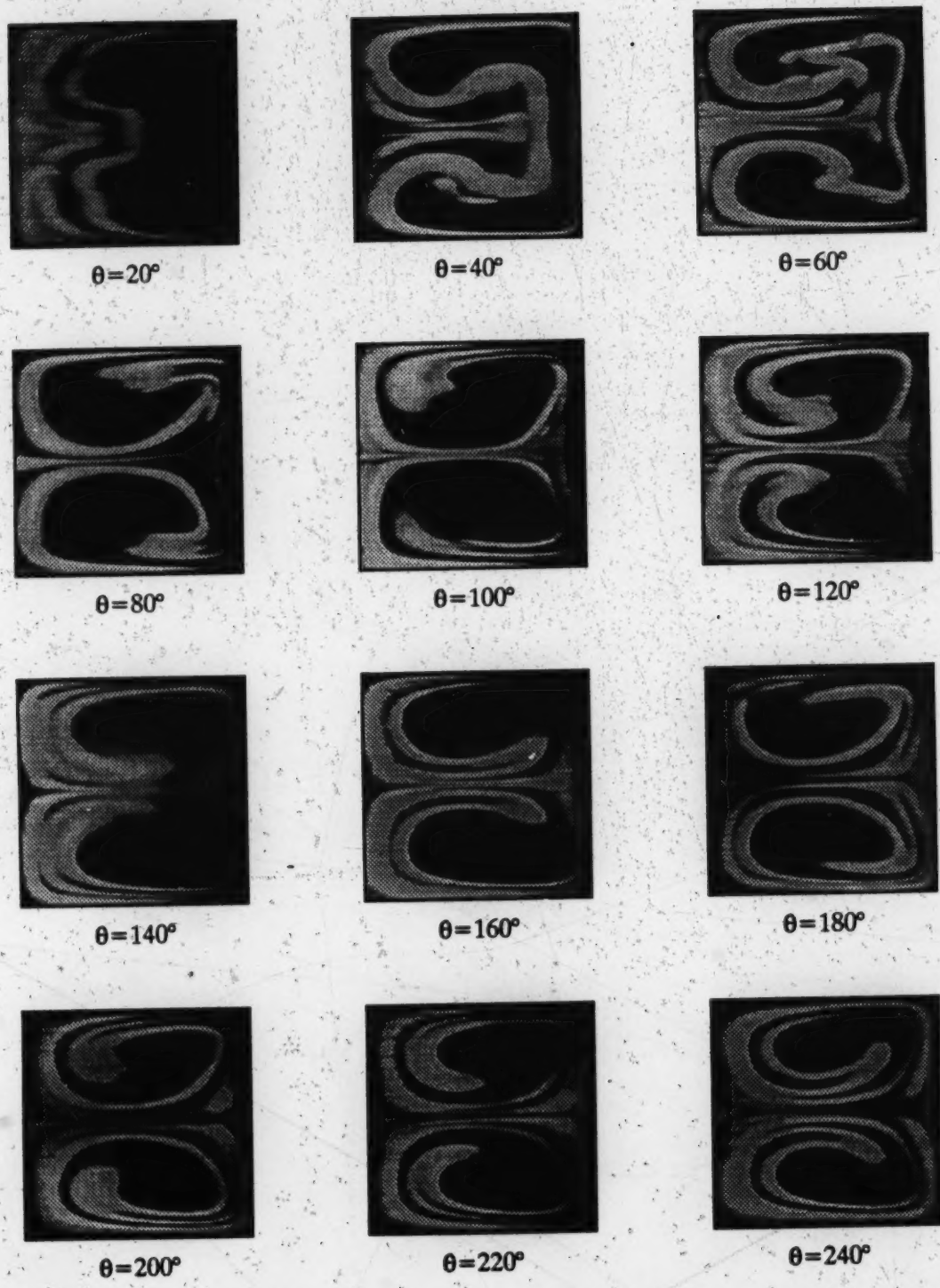

Figure 6.18: Flow visualization showing secondary flow development every 20° at $Dn = 125.5$.

6.3 Flow Development at Dn=137

Development of the axial velocity profiles with downstream position at $Dn = 137$ is shown in figures 6.19 through 6.30. The outer wall of the duct is at $x'/a = 0.5$. For each downstream position, the measured horizontal axial velocity profile at the horizontal duct centerline (i.e. $z'/a = 0.0$) is compared to the numerically predicted profile. The numerical prediction of secondary flow development is presented in figure 6.31 in the form of arrow plots showing the secondary velocity vectors. As in the case of $Dn = 125$, all secondary velocities have been normalized with the mean axial velocity to show the relative strength of the secondary flow with downstream position. As before, the outer wall is on the right hand side of each plot and the length of the mean axial velocity vector is equal to the length of the duct walls. Flow visualization of the development of the secondary flow patterns is shown in figure 6.32. Again the outer wall is on the right hand side.

The initial development of the axial velocity profiles at $Dn = 137$ is very similar to the development at $Dn = 125$. Up to $\theta = 80°$ the axial velocity profiles for the two Dean numbers are almost identical. Flow visualization and arrow plots up to $\theta = 80°$ are also very similar for the two cases. The numerical predictions of the secondary flows revealed that the maximum secondary velocities, on average, differed by about 0.5% in this initial development region. These observations show that the initial flow development at $Dn = 137$ is to a two-vortex structure.

After $\theta = 80°$ the flow development at $Dn = 137$ starts to differ from the development observed at $Dn = 125$. At $Dn = 125$ the axial velocity profile was fairly well established by $\theta = 80°$, with no further changes observed with axial position. However, the axial velocity profile at $Dn = 137$ and $\theta = 100°$ is starting to show a slight shift of the maximum axial velocity back toward the duct center.

Examining the flow visualization at $\theta = 100°$ in figure 6.32, it is seen that an additional pair of vortices are starting to form at the outer wall. In response to the additional vortices, the peak in the axial velocity profile is starting to shift back toward the duct center. The magnitude of the secondary flows at the outer wall are very small, as is evident from the arrow plot.

From the flow visualization in figure 6.32, it is seen that the additional vortices continue to grow with downstream distance. The vortices are still growing at 240°, indicating that the flow has not reached a fully developed state. The numerical prediction of secondary velocities indicate that slightly over 300° of development length are required until the maximum radial velocities settle down to constant values. Once the secondary velocities have reached a constant value, the maximum radial velocity that occurs on the horizontal duct centerline in the additional vortex pair is about 10% of the mean axial velocity. The maximum secondary velocity in the larger vortex pair is about 11.5% of the mean. As in the case of Dn=125, this occurs near the top and bottom walls in the flow returning fluid to the inner wall.

The response of the axial velocity profiles to the increasing size and strength of the additional vortex pair is an increasing shift of the maximum velocity back toward the duct center. With the opposite sense of rotation as compared to the large vortices, the second vortex pair is able to transfer high momentum fluid toward the duct center and cause the velocity maximum to shift.

Comparing the measured velocity profiles to the numerical simulations at $\theta = 180°$, 200° and 220°, it can be seen that the numerical simulation predicts a faster growth rate of the additional vortices than observed. The larger vortex strength predicted by the simulation causes a larger shift in the maximum of the axial velocity. This is evident from the difference between the measurements and the numerical predictions near the outer wall. The difference at each location (i.e. $\theta = 180°$,

200° and 220°) is larger than the 2–3% positioning error, so it is clearly due to the different growth rates of the additional vortex pair. The faster growth rate of the additional vortices is also evident by comparing the arrow plots with the flow visualization. The reason the simulation differs from the experiments is because the numerical formulation neglects elliptic effects in the axial direction and ignores gradients of the radial velocity in the axial direction.

From the flow visualization in figure 6.32, it is seen that the additional vortices retained their symmetry about the horizontal centerline throughout the investigated development length. This is contrary to the asymmetric development that was observed by Hille *et al.* (1985). This difference might be do to the stronger curvature of their duct or possible physical asymmetries in their apparatus, given that the four-vortex solutions are unstable to asymmetric perturbations. However, the existence of their additional pair was first observed after $\theta = 108°$, in qualitative agreement with the present study.

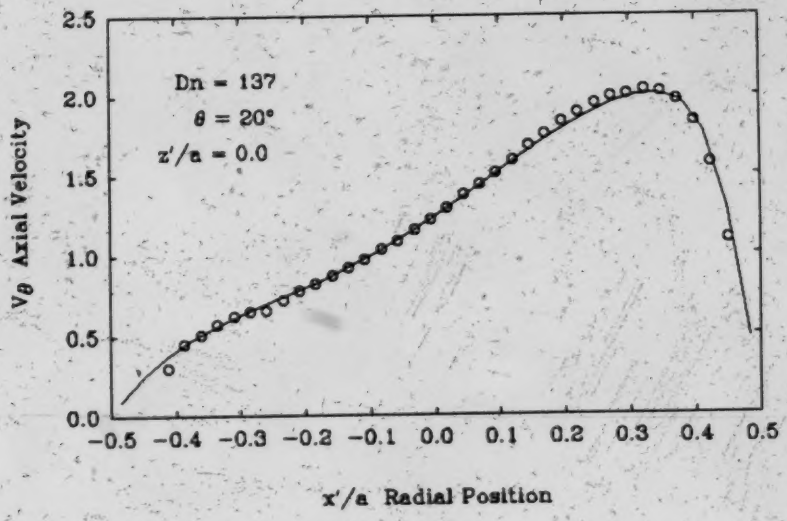

Figure 6.19: Measured velocity profile compared to numerical simulation at $Dn = 137$, $\theta = 20°$ and $z'/a = 0.0$.

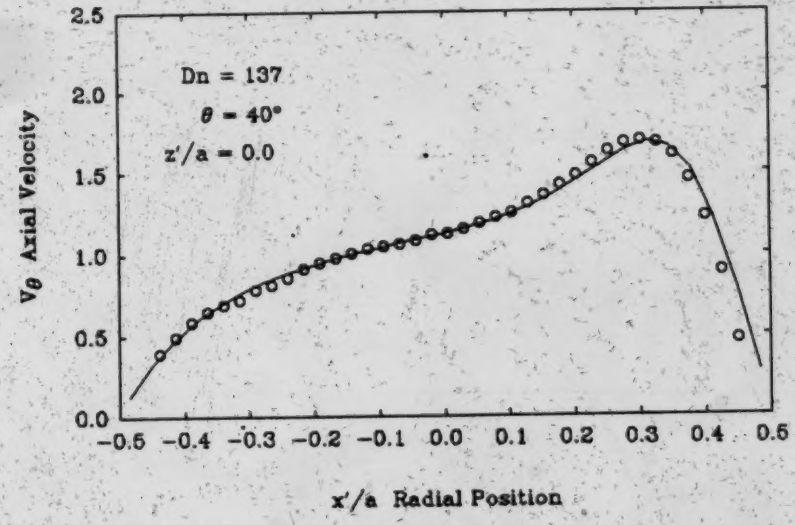

Figure 6.20: Measured velocity profile compared to numerical simulation at $Dn = 137$, $\theta = 40°$ and $z'/a = 0.0$.

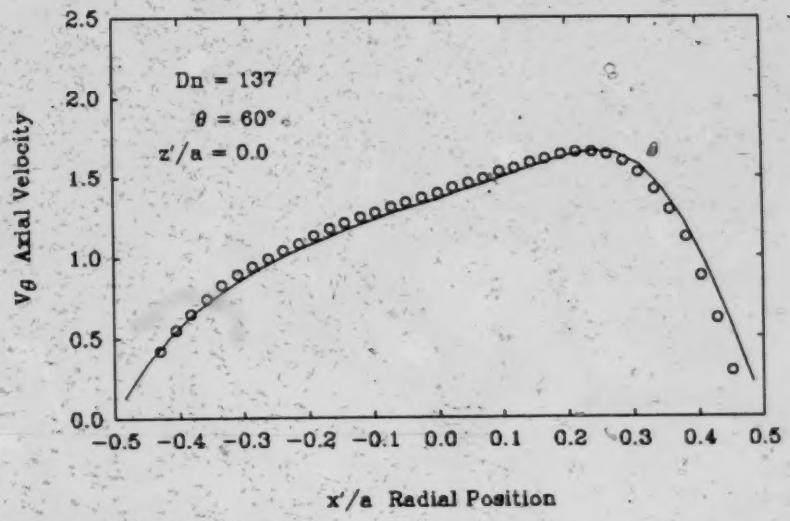

Figure 6.21: Measured velocity profile compared to numerical simulation at $Dn = 137$, $\theta = 60°$ and $z'/a = 0.0$.

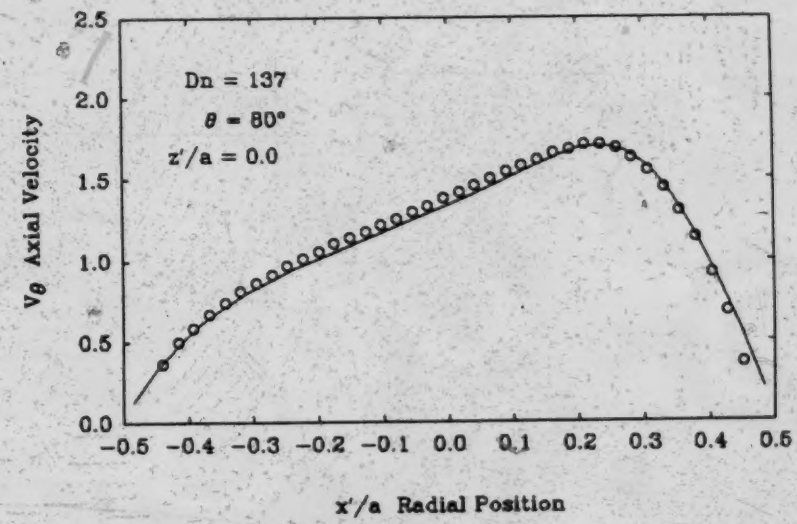

Figure 6.22: Measured velocity profile compared to numerical simulation at $Dn = 137$, $\theta = 80°$ and $z'/a = 0.0$.

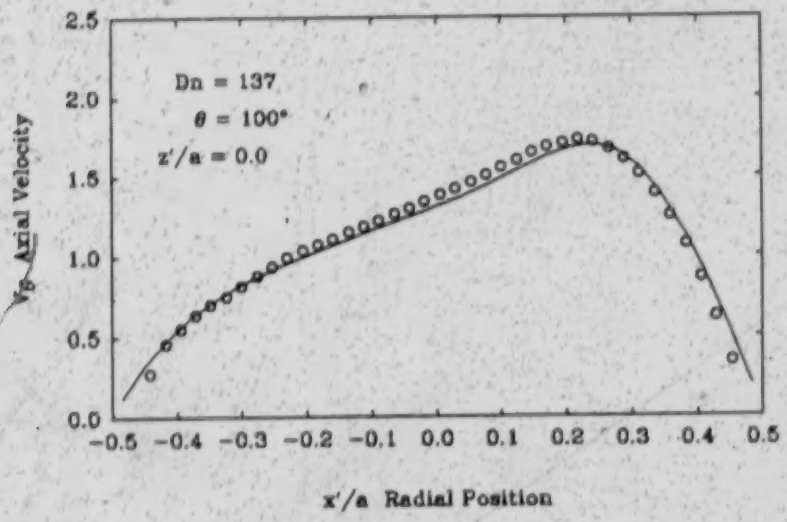

Figure 6.23: Measured velocity profile compared to numerical simulation at $Dn = 137$, $\theta = 100°$ and $z'/a = 0.0$.

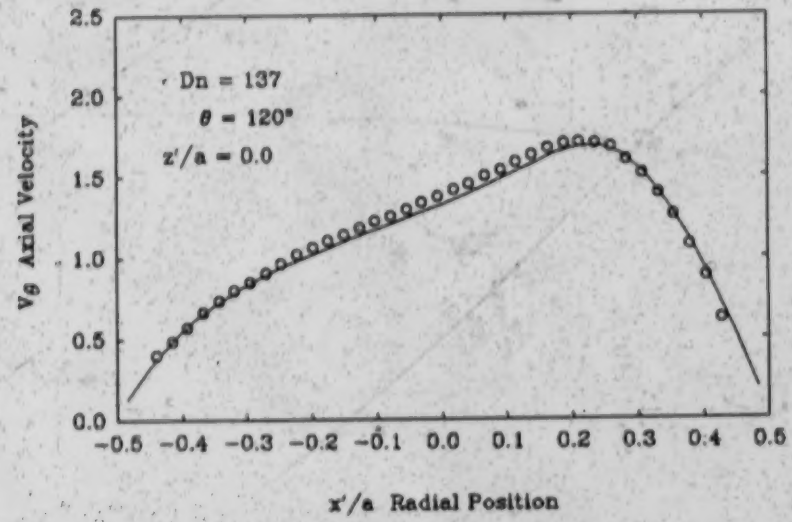

Figure 6.24: Measured velocity profile compared to numerical simulation at $Dn = 137$, $\theta = 120°$ and $z'/a = 0.0$.

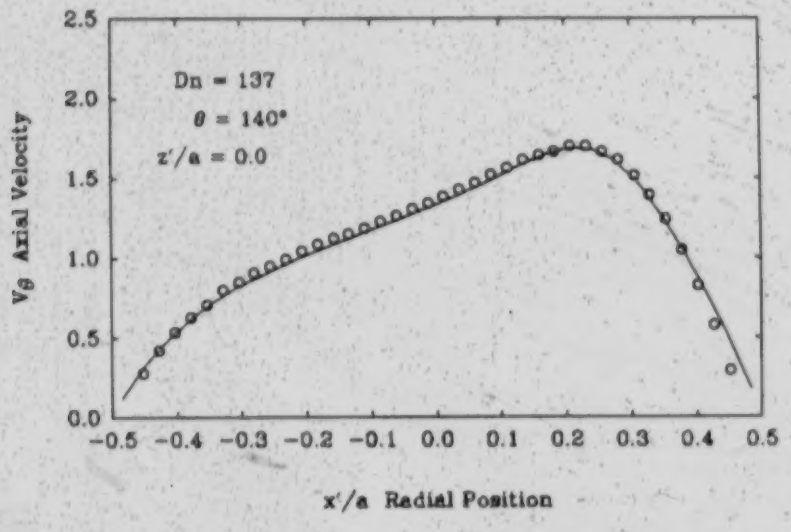

Figure 6.25: Measured velocity profile compared to numerical simulation at $Dn = 137$, $\theta = 140°$ and $z'/a = 0.0$.

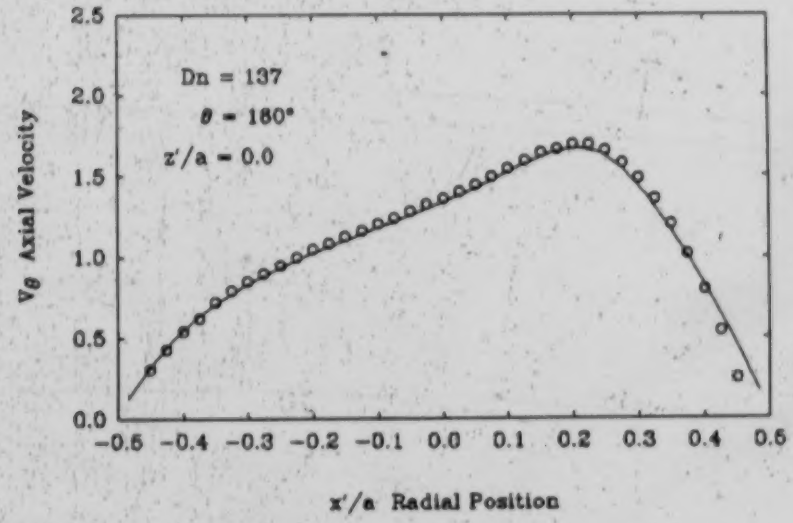

Figure 6.26: Measured velocity profile compared to numerical simulation at $Dn = 137$, $\theta = 160°$ and $z'/a = 0.0$.

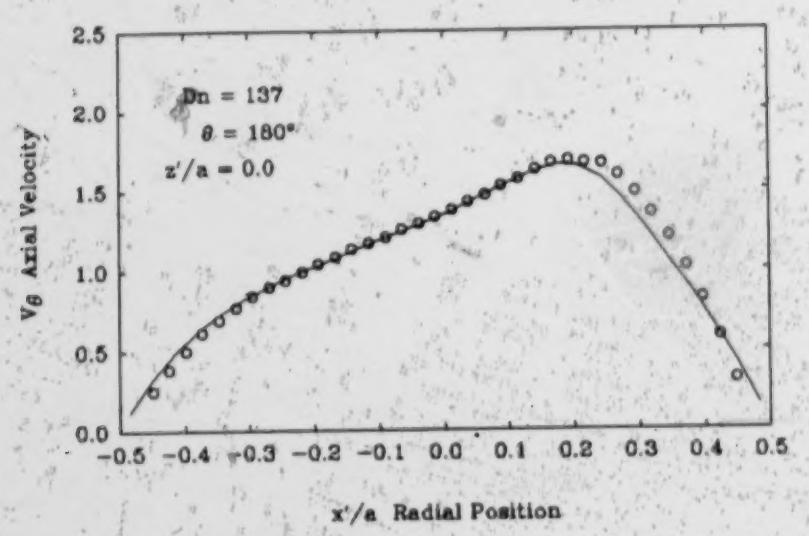

Figure 6.27: Measured velocity profile compared to numerical simulation at $Dn = 137$, $\theta = 180°$ and $z'/a = 0.0$.

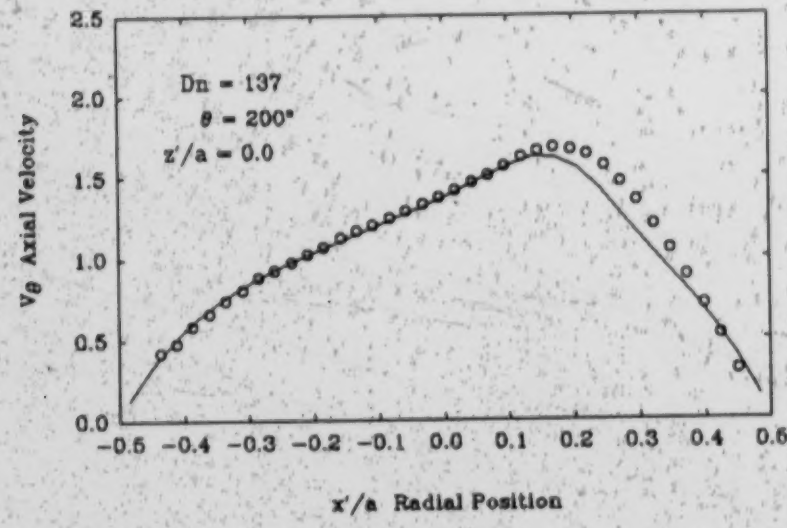

Figure 6.28: Measured velocity profile compared to numerical simulation at $Dn = 137$, $\theta = 200°$ and $z'/a = 0.0$.

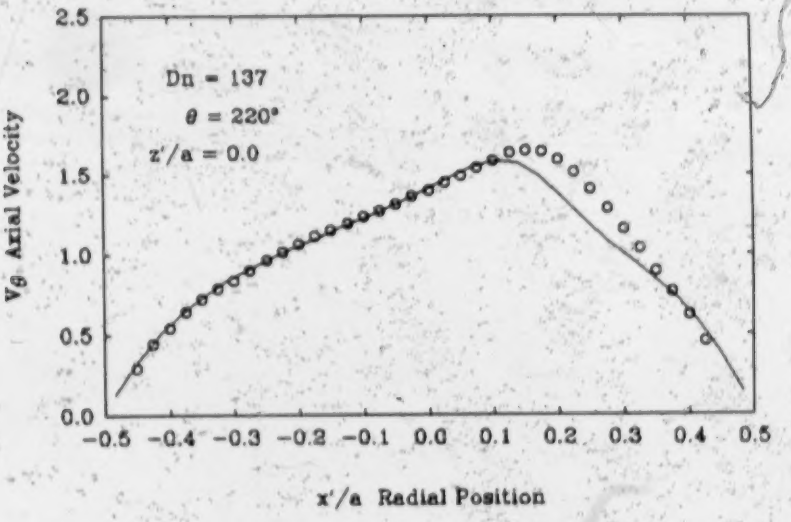

Figure 6.29: Measured velocity profile compared to numerical simulation at $Dn = 137$, $\theta = 220°$ and $z'/a = 0.0$.

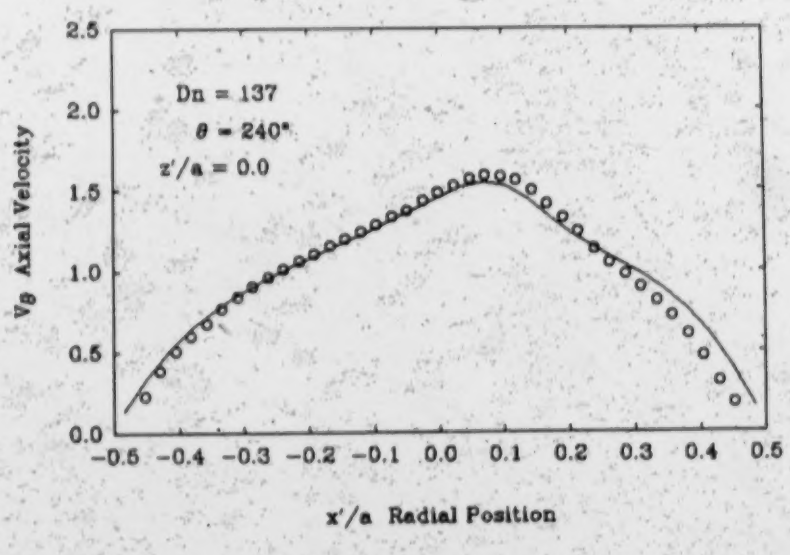

Figure 6.30: Measured velocity profile compared to numerical simulation at $Dn = 137$, $\theta = 240°$ and $z'/a = 0.0$.

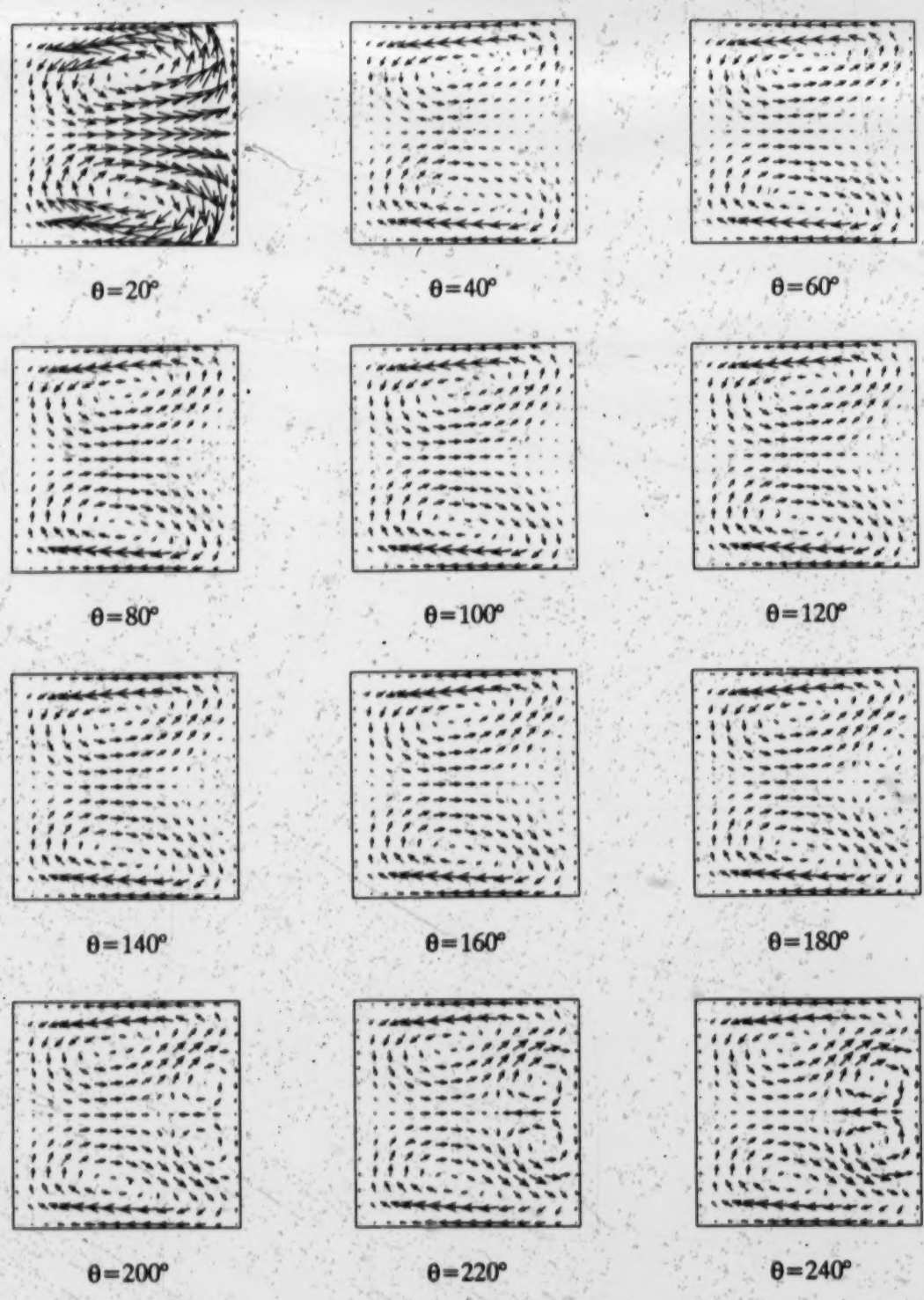

Figure 6.31: Arrow plots showing secondary flow development every 20° at $Dn = 137$.

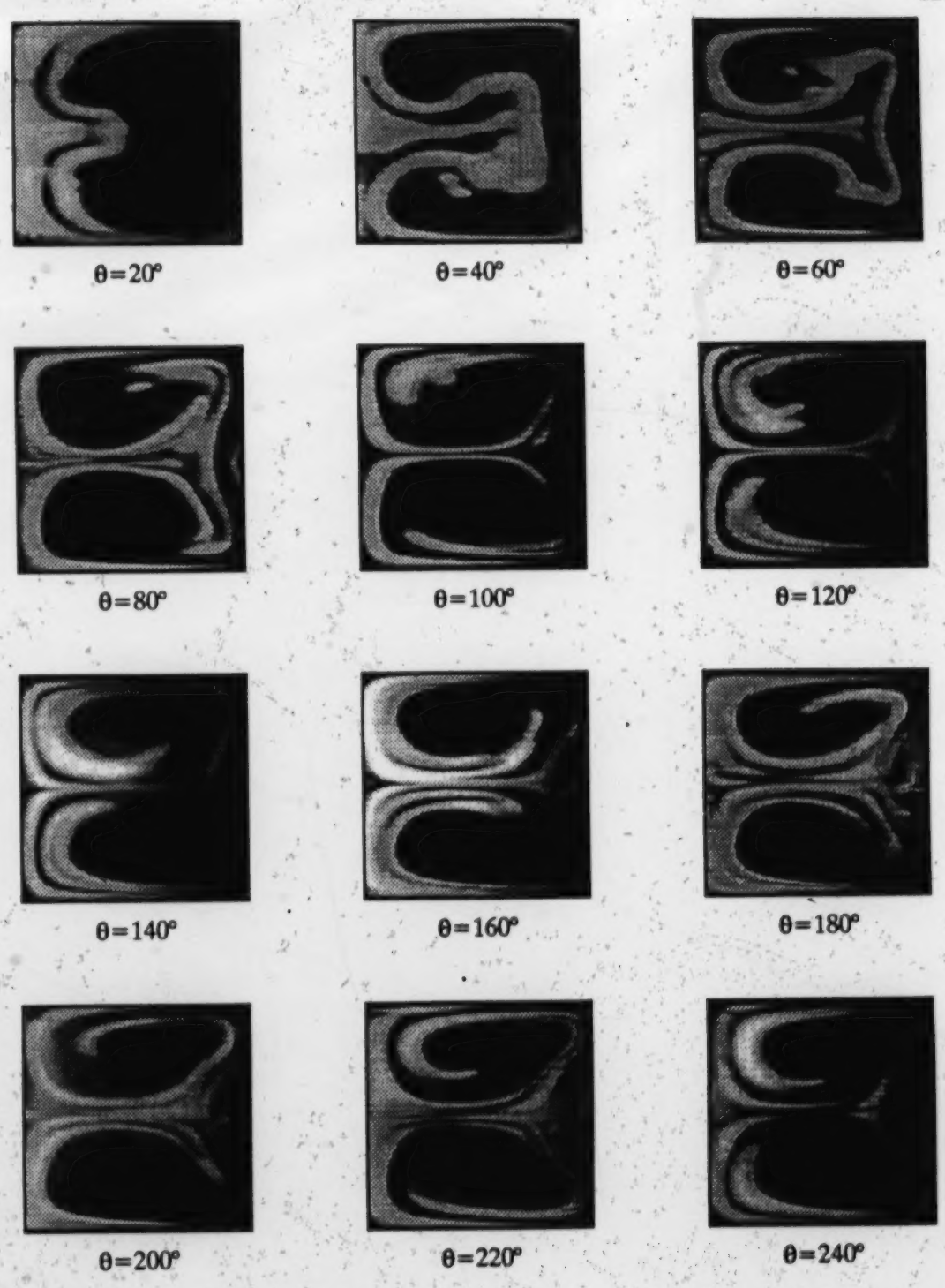

Figure 6.32: Flow visualization showing secondary flow development every 20° at $Dn = 137.1$.

6.4 Flow Development at Dn=150

Development of the horizontal axial velocity profiles with downstream position at $Dn = 150$ is shown in figures 6.33 through 6.44, and the development of the vertical axial velocity profiles are shown in figures 6.45 through 6.56. For each downstream position, the measured axial velocity profile at the duct centerline is compared to the numerically predicted profile. The numerical prediction of secondary flow development is presented in figure 6.57 in the form of arrow plots showing the secondary velocity vectors. All secondary velocities have been normalized with the mean axial velocity to show the relative strength of the secondary flow with downstream position. The outer wall is on the right hand side of each plot and the length of the mean axial velocity vector is equal to the length of the duct walls. Flow visualization of the development of the secondary flow patterns is shown in figure 6.58. Again the outer wall is on the right hand side.

The flow development up to $\theta = 60°$ is essentially the same at $Dn = 150$ as it was for $Dn = 137$ and $Dn = 125$, as indicated by the axial velocity profiles, arrow plots and flow visualization. At $\theta = 20°$, the predicted maximum secondary velocity at the top and bottom walls was 24.8% of the mean, as compared to 23.7% and 22.5% for $Dn = 137$ and $Dn = 125$ respectively. The slight increase in the secondary flow velocity is a direct result of the increased centrifugal force at the higher Dean numbers. It is not surprising that the initial flow development is similar, given that for each case the secondary flow is induced in response to the pressure gradient set up by the fluid moving toward the outer wall.

At $\theta = 80°$ the flow visualization in figure 6.58 suggests that an additional pair of vortices is starting to form at the outer wall. Similar to the flow development at $Dn = 137$, the axial velocity profile at $Dn = 150$ and $\theta = 80°$ is starting to show the

back-transfer of momentum toward the duct center in response to the appearance of the additional vortices. The appearance of the additional vortices occur at an earlier downstream position for $Dn = 150$ than for $Dn = 137$. From the flow visualization sequence, it is seen that the additional vortices continue to grow in the downstream direction, however at a faster rate than at $Dn = 137$.

Comparing the horizontal axial velocity profiles at $\theta = 140°$ and $\theta = 160°$ to the numerical simulation, it can be seen that the numerical simulation predicts a slightly faster growth rate of the additional vortices. This is evident by the larger shift in the axial velocity profiles toward the duct center for the numerical simulations. As in the case of $Dn = 137$, the observed difference is not due to experimental uncertainty in the measured velocities.

Comparison of the arrow plots and flow visualization at $\theta = 140$ and $\theta = 180°$ show the larger vortices predicted by the numerical simulation. From $\theta = 180°$ to $\theta = 240°$, the measured axial velocity profiles and flow visualization are in good agreement with the numerical simulation. Both measurements and numerical predictions indicate that by $\theta = 240°$ the flow has reached a fully developed state. Once the secondary velocities have reached a constant value, the maximum radial velocity that occurs on the horizontal duct centerline in the additional vortex pair is about 11% of the mean axial velocity. This is slightly larger than the maximum value of 10% at $Dn = 137$. For both $Dn = 150$ and $Dn = 137$, the maximum secondary velocity in the larger vortex pair is about 11.6% of the mean axial velocity.

The measured vertical profiles of axial velocity in figures 6.45 through 6.56, and the flow visualization in figure 6.58 reveal that the flow development was symmetric about the horizontal duct centerline. The measured vertical profiles are in good agreement with the numerical predictions except for the tendency of the measurements to be slightly higher than the numerically predicted values. This

is consistent with the horizontal profiles and as mentioned before is a result of positioning errors in the duct. The common measured point on the horizontal and vertical profile (i.e. $x'/a = z'/a = 0.0$) has the same value, so the appearance of a larger difference from the prediction in the vertical profile is only a result of the stretched velocity axis. The large dip in the vertical axial velocity profile at $\theta = 40°$ is a result of the secondary flow redistributing the axial momentum in the initial development region. This dip in the vertical profile was also observed by Austin and Seader (1974) for developing flow in a curved pipe.

The onset of the additional pair of vortices at $Dn = 150$ and $Dn = 137$ is consistent with the instability explanation given by Cheng *et al.* (1976). Recalling from the literature review, Cheng *et al.* believed that a centrifugal instability like the one that occurred in Dean's (1928b) instability problem was responsible for the appearance of the additional vortices. Near the outer wall, where the axial velocity is decreasing with increasing distance from the center of curvature of the duct, there is a centrifugally unstable region. If the axial velocity becomes large enough, viscous effects can no longer hold the two-vortex structure in place, thus the additional vortices appear.

The flow development at $Dn = 150$, 137 and 125 showed that the initial flow development was to a two-vortex structure. At $Dn = 125$, the centrifugal forces are not large enough to cause the formation of the additional vortices, so the two-vortex flow structure remains intact. However, at $Dn = 137$ viscous effects can no longer retain the two-vortex structure, so the additional pair of vortices starts to form. At $Dn = 150$ the centrifugal forces are even stronger, so the formation of the additional vortices starts earlier and their growth rate is faster.

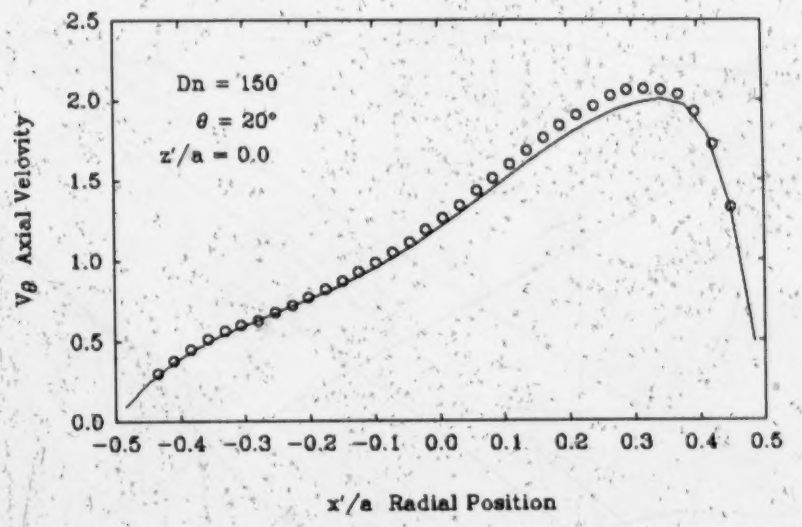

Figure 6.33: Measured velocity profile compared to numerical simulation at $Dn = 150$, $\theta = 20°$ and $z'/a = 0.0$.

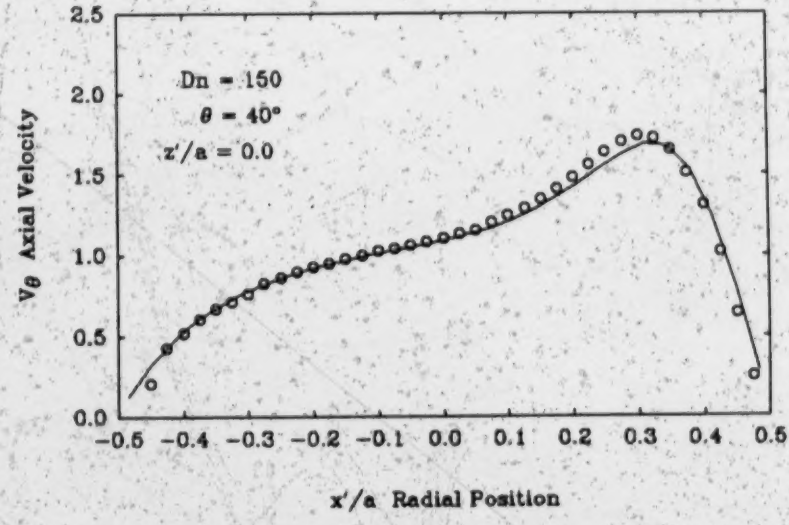

Figure 6.34: Measured velocity profile compared to numerical simulation at $Dn = 150$, $\theta = 40°$ and $z'/a = 0.0$.

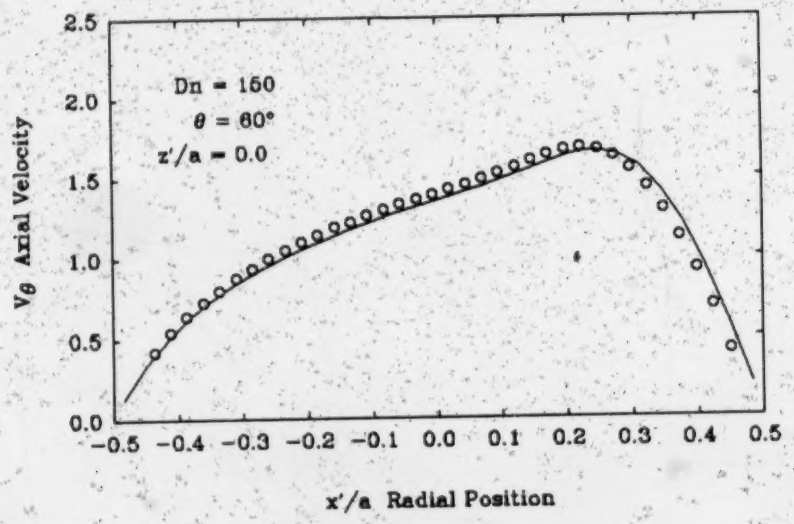

Figure 6.35: Measured velocity profile compared to numerical simulation at $Dn = 150$, $\theta = 60°$ and $z'/a = 0.0$.

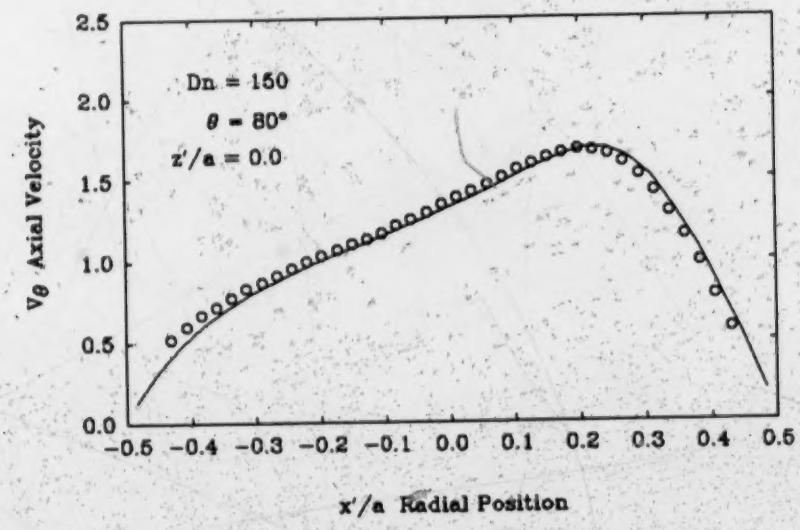

Figure 6.36: Measured velocity profile compared to numerical simulation at $Dn = 150$, $\theta = 80°$ and $z'/a = 0.0$.

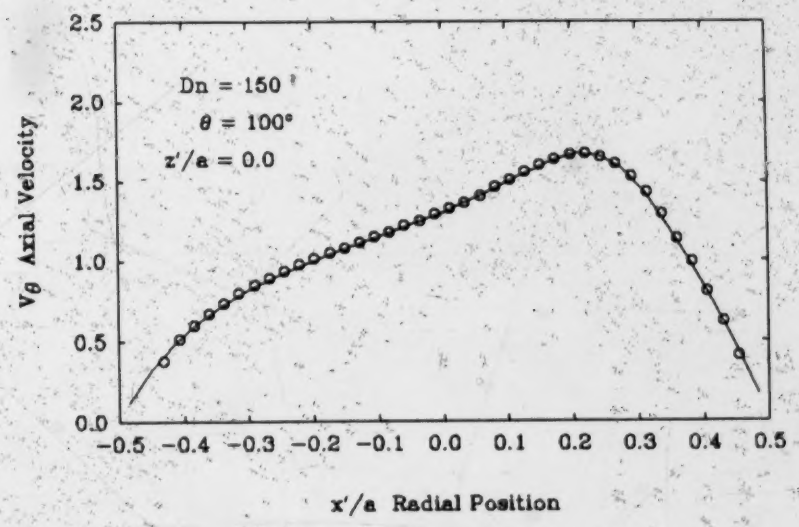

Figure 6.37: Measured velocity profile compared to numerical simulation at $Dn = 150$, $\theta = 100°$ and $z'/a = 0.0$.

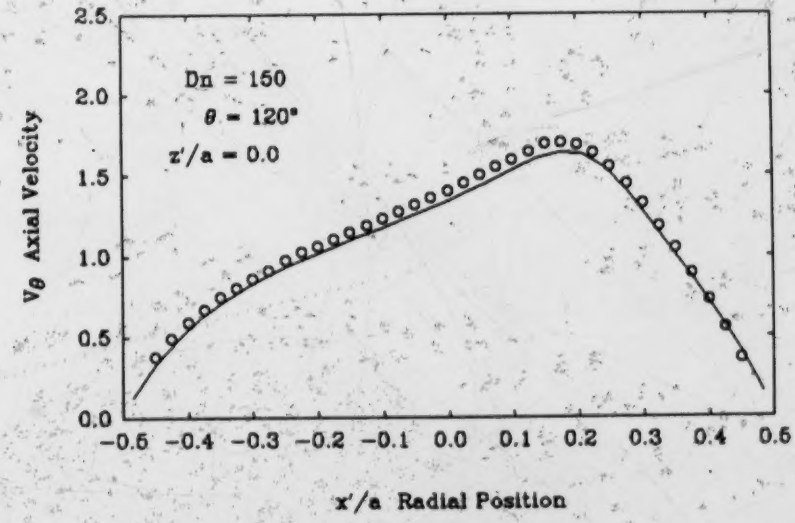

Figure 6.38: Measured velocity profile compared to numerical simulation at $Dn = 150$, $\theta = 120°$ and $z'/a = 0.0$.

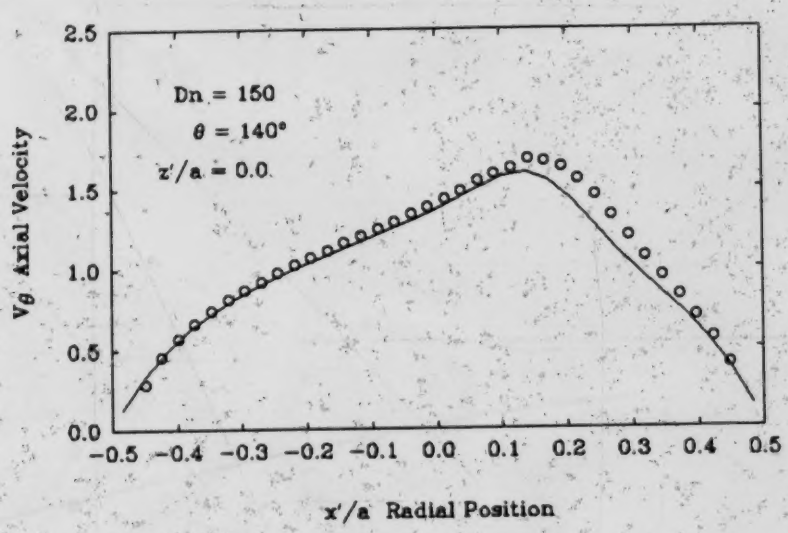

Figure 6.39: Measured velocity profile compared to numerical simulation at $Dn = 150$, $\theta = 140°$ and $z'/a = 0.0$.

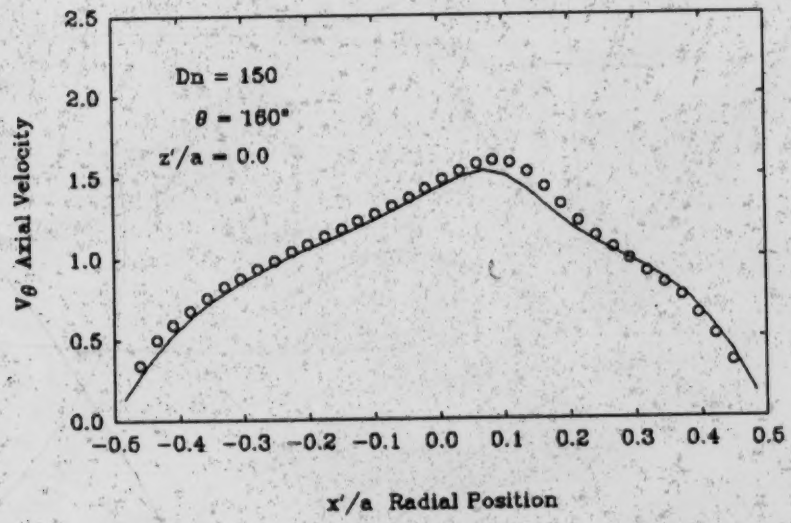

Figure 6.40: Measured velocity profile compared to numerical simulation at $Dn = 150$, $\theta = 160°$ and $z'/a = 0.0$.

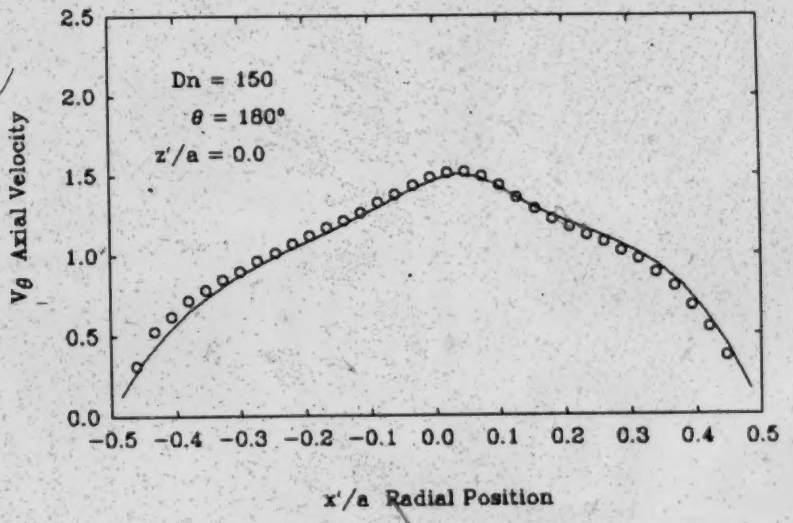

Figure 6.41: Measured velocity profile compared to numerical simulation at $Dn = 150$, $\theta = 180°$ and $z'/a = 0.0$.

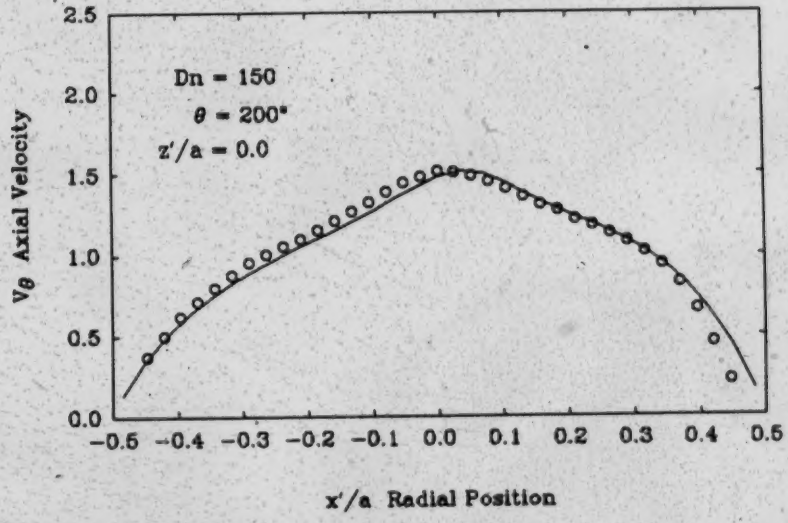

Figure 6.42: Measured velocity profile compared to numerical simulation at $Dn = 150$, $\theta = 200°$ and $z'/a = 0.0$.

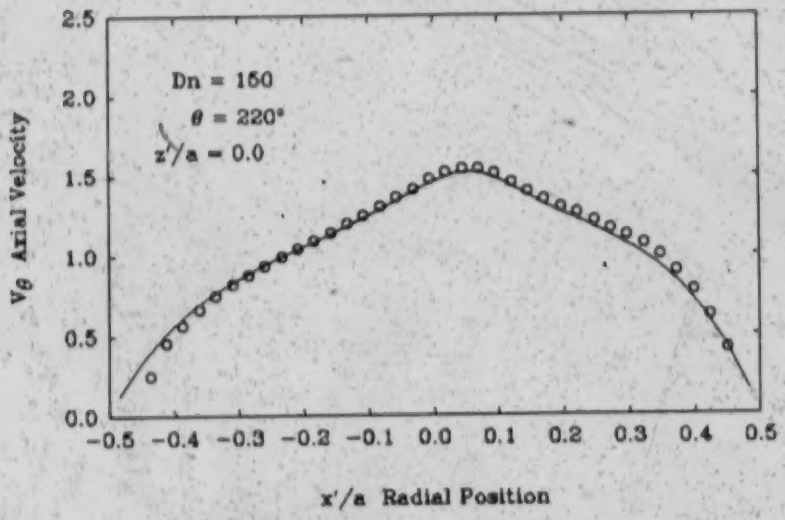

Figure 6.43: Measured velocity profile compared to numerical simulation at $Dn = 150$, $\theta = 220°$ and $z'/a = 0.0$.

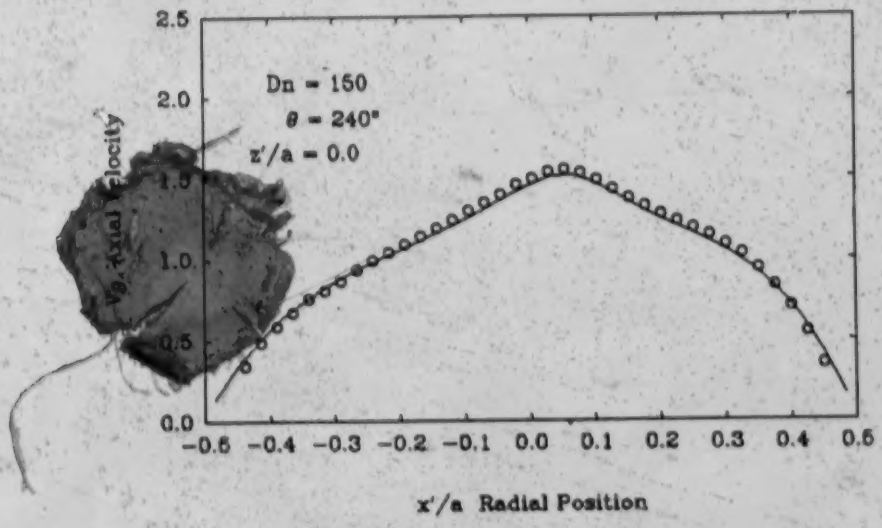

Figure 6.44: Measured velocity profile compared to numerical simulation at $Dn = 150$, $\theta = 240°$ and $z'/a = 0.0$.

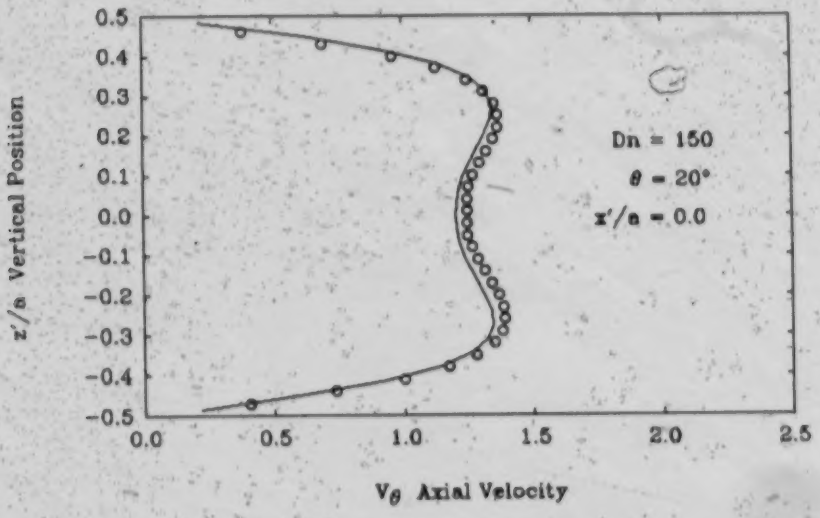

Figure 6.45: Measured velocity profile compared to numerical simulation at $Dn = 150$, $\theta = 20°$ and $x'/a = 0.0$.

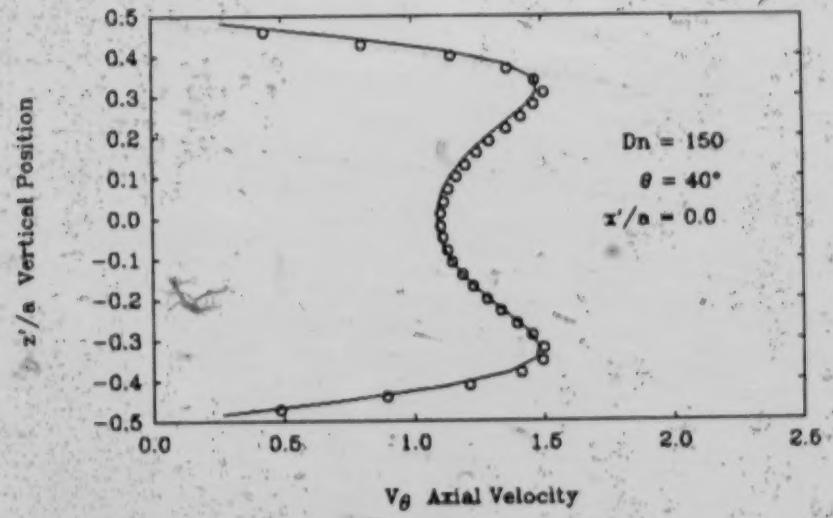

Figure 6.46: Measured velocity profile compared to numerical simulation at $Dn = 150$, $\theta = 40°$ and $x'/a = 0.0$.

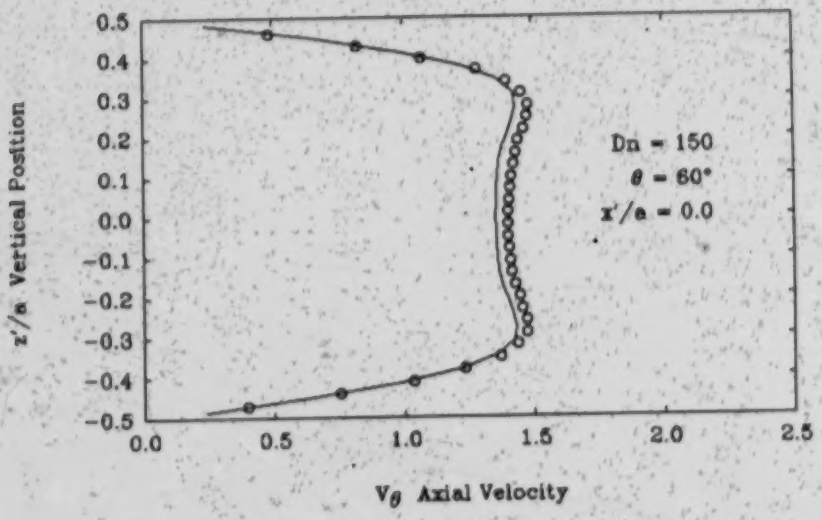

Figure 6.47: Measured velocity profile compared to numerical simulation at $Dn = 150$, $\theta = 60°$ and $r'/a = 0.0$.

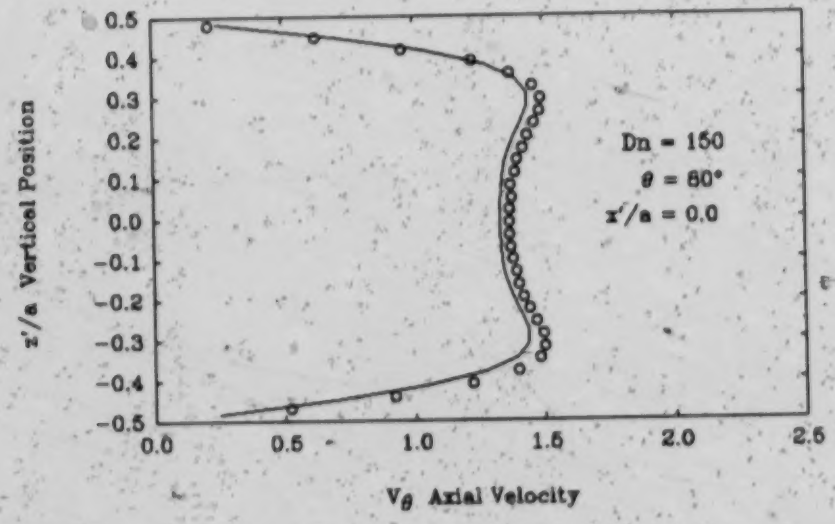

Figure 6.48: Measured velocity profile compared to numerical simulation at $Dn = 150$, $\theta = 80°$ and $r'/a = 0.0$.

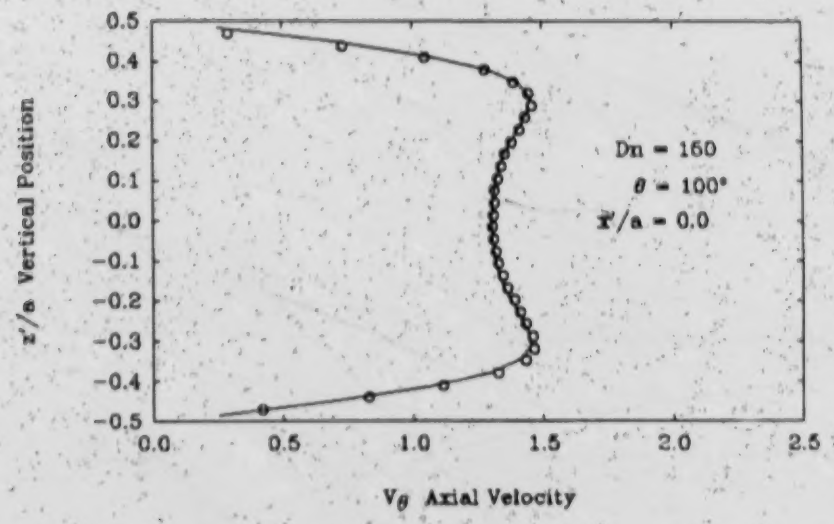

Figure 6.49: Measured velocity profile compared to numerical simulation at $Dn = 150$, $\theta = 100°$ and $x'/a = 0.0$.

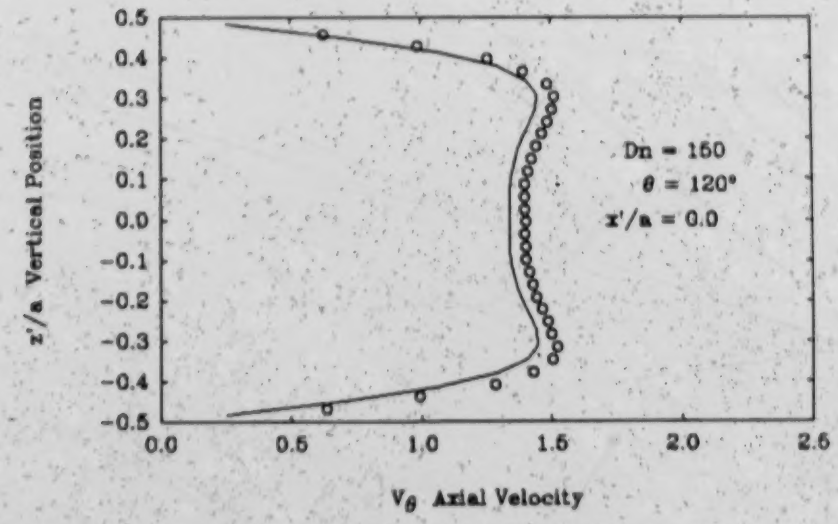

Figure 6.50: Measured velocity profile compared to numerical simulation at $Dn = 150$, $\theta = 120°$ and $x'/a = 0.0$.

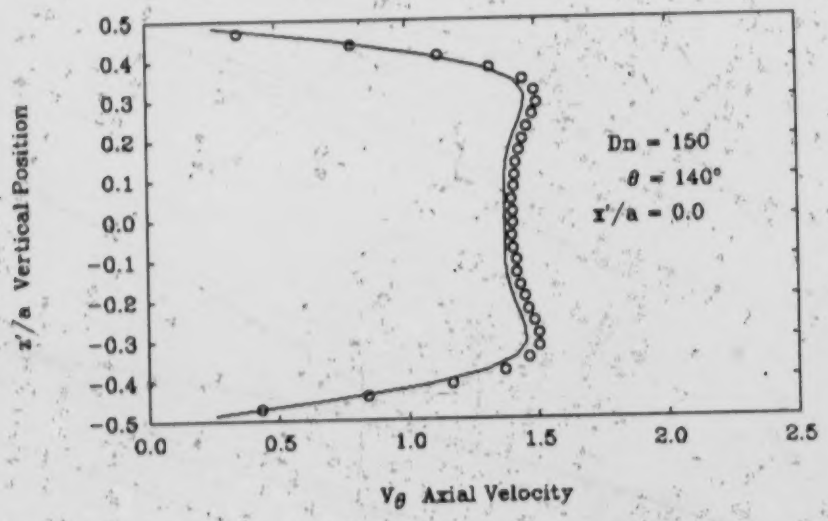

Figure 6.51: Measured velocity profile compared to numerical simulation at $Dn = 150$, $\theta = 140°$ and $x'/a = 0.0$.

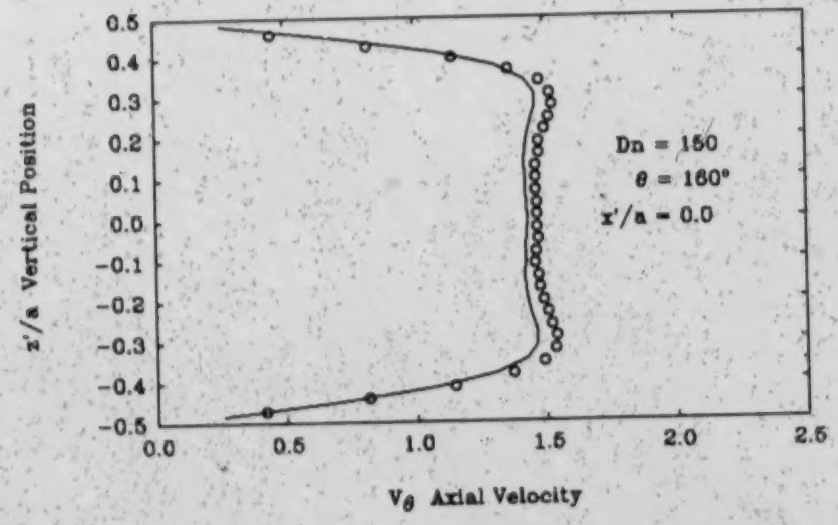

Figure 6.52: Measured velocity profile compared to numerical simulation at $Dn = 150$, $\theta = 160°$ and $x'/a = 0.0$.

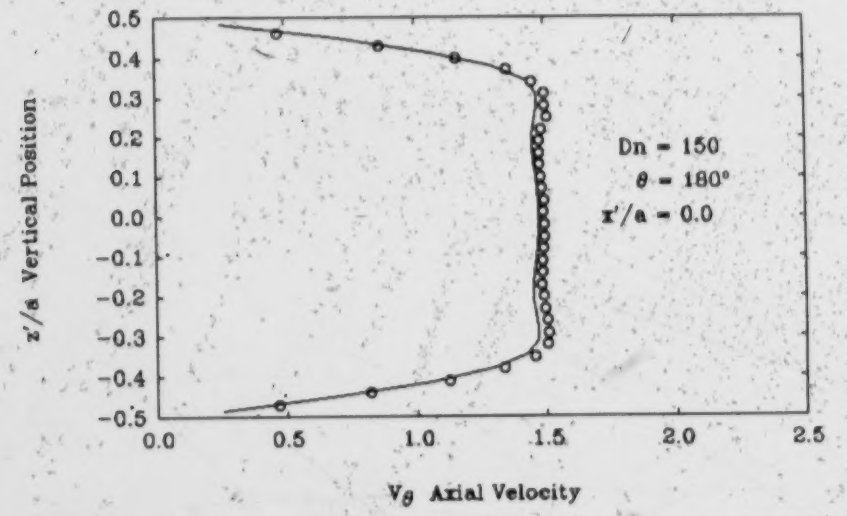

Figure 6.53: Measured velocity profile compared to numerical simulation at $Dn = 150$, $\theta = 180°$ and $x'/a = 0.0$.

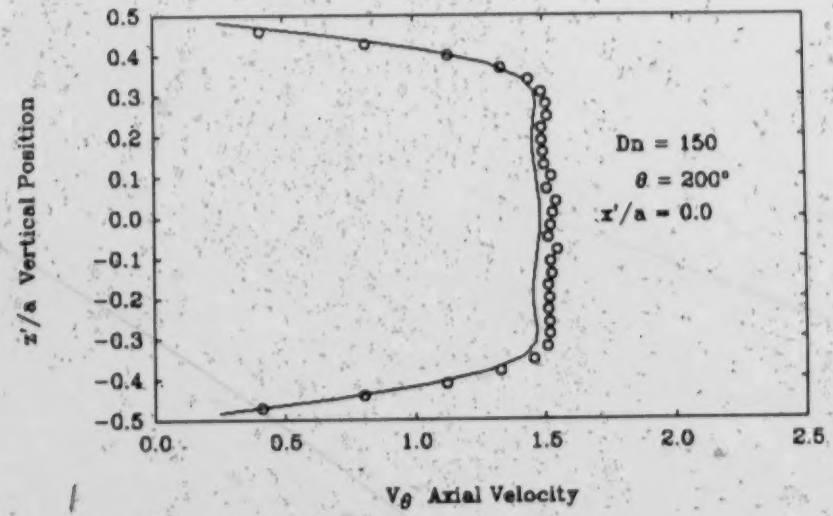

Figure 6.54: Measured velocity profile compared to numerical simulation at $Dn = 150$, $\theta = 200°$ and $x'/a = 0.0$.

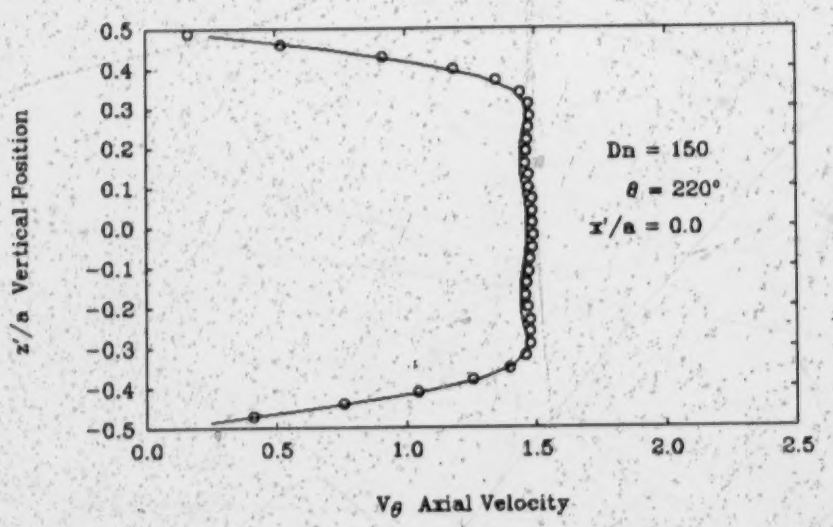

Figure 6.55: Measured velocity profile compared to numerical simulation at $Dn = 150$, $\theta = 220°$ and $x'/a = 0.0$.

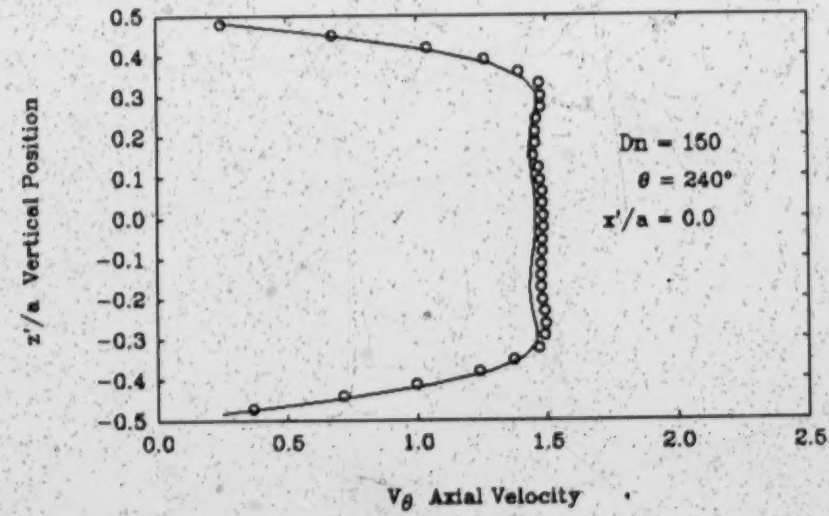

Figure 6.56: Measured velocity profile compared to numerical simulation at $Dn = 150$, $\theta = 240°$ and $x'/a = 0.0$.

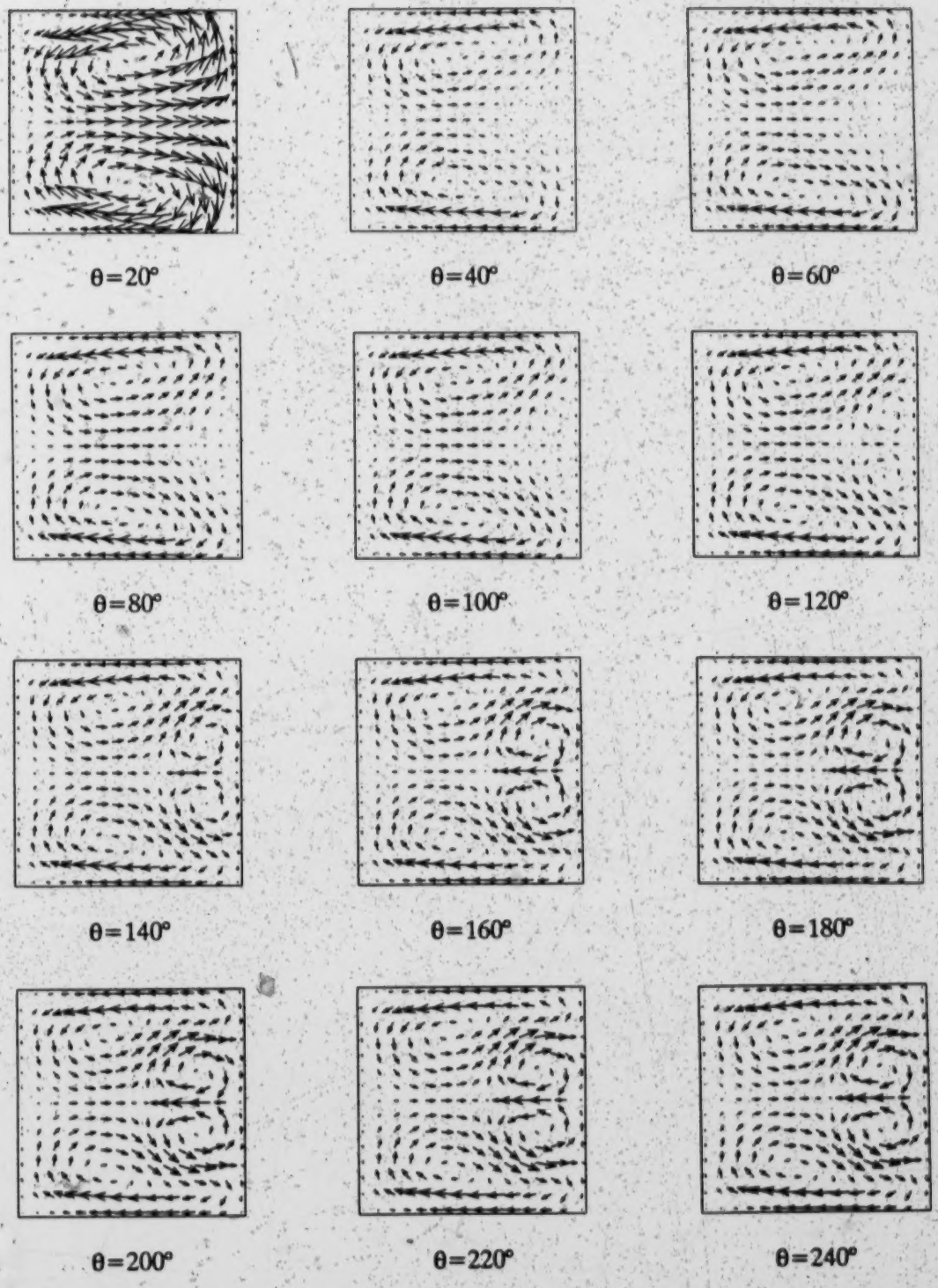

Figure 6.57: Arrow plots showing secondary flow development every 20° at $Dn = 150$.

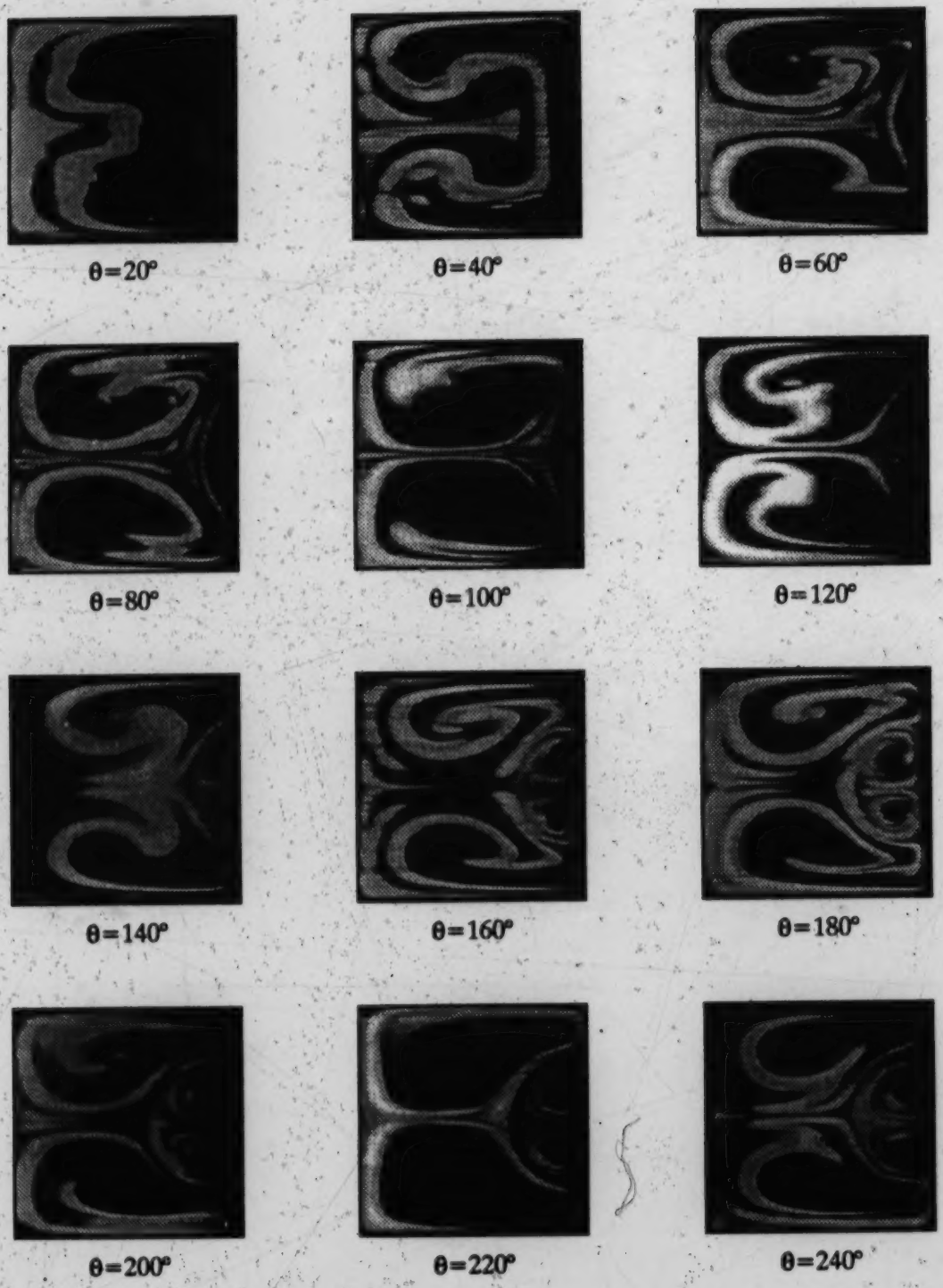

Figure 6.58: Flow visualization showing secondary flow development every 20° at $Dn = 149.9$.

6.5 Development Length

The widely accepted definition of development length is the axial length required for the flow to reach an axially invariant state (i.e. fully developed state). In this study, development length is defined as the length required to reach the flow state that is predicted by the two-dimensional numerical simulations. Since four-vortex flows are predicted to be unstable to asymmetric perturbations, they may appear for some axial length, but farther downstream give way to time and/or spatial oscillations. The numerical simulations in chapter eight suggest that a truly axially invariant four-vortex flow does not exist. However, within the axial length of the experimental apparatus used in this study, axially invariant four-vortex flows were observed.

In order to determine if a flow has reached an axially invariant state, the state of some parameter can be monitored with downstream position. In this study, the axial velocity at $x'/a = 0.24$ and $z'/a = 0.0$ was monitored with axial position to determine if the flow had reached the state predicted by the two-dimensional numerical solution. Compared to the axial velocities at other duct positions, the axial velocity at $x'/a = 0.24$ and $z'/a = 0.0$ experienced the largest change when going from a two-vortex to a four-vortex flow, so it was concluded that this location would be the most sensitive to changes in the flow in the axial direction. A numerical simulation of the flow development at $Dn = 137$ is presented in figure 6.59. The simulation is presented in the form of a state diagram, with the axial and radial velocities at $x'/a = 0.24$ and $z'/a = 0.0$ as the state variables. The development length to reach the same solution as predicted by the two-dimensional simulation, is shown to be approximately 315°. At this location, the radial and axial velocity are no longer changing, indicating that axial velocity development is complete, and that the secondary flow structure has been established. The radial velocity

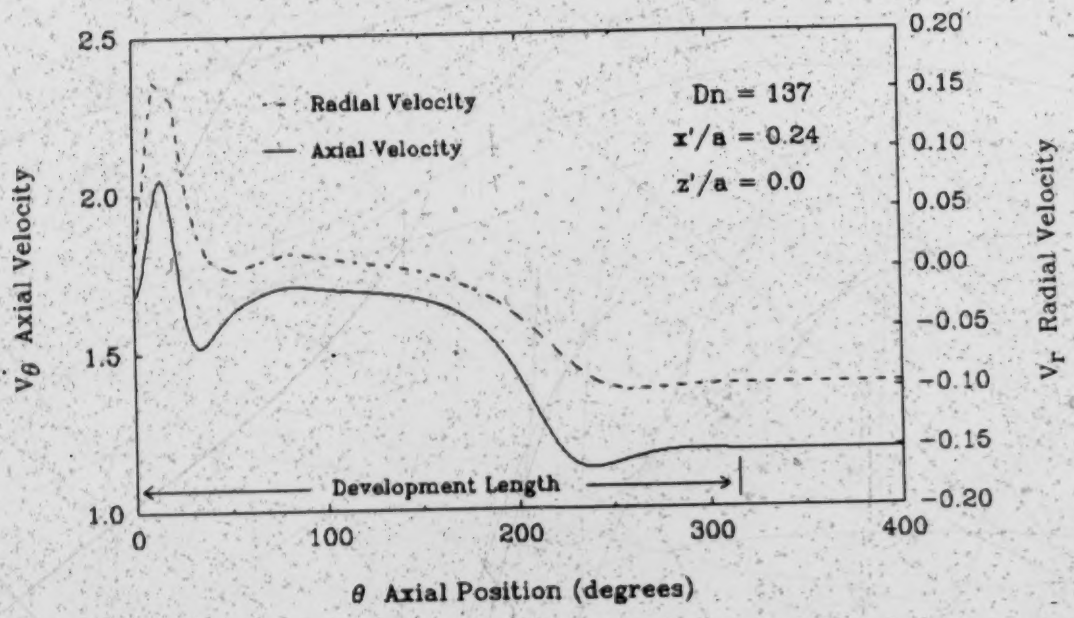

Figure 6.59: Numerically calculated state diagram showing the development with axial position of the axial and radial velocities at $Dn = 137$, $x'/a = 0.24$ and $z'/a = 0.0$.

at $x'/a = 0.24$ and $z'/a = 0.0$ is very near the location of the maximum velocity in the additional vortex pair, so it is a good indicator of the development of the secondary flow structure. Comparing the axial velocity development to the radial velocity development at $x'/a = 0.24$ and $z'/a = 0.0$, suggests that the axial velocity at this location is a good indicator of the overall flow development.

Experimentally determined state diagrams for the flow development at Dn = 125, 137 and 150 are compared to numerical predictions in figures 6.60, 6.61 and 6.62 respectively. For $Dn = 125$, the measured flow development is in very good agreement with the numerical simulation. The measured values are slightly lower in the fully developed region (i.e. $\theta \geq 100°$), suggesting a systematic positioning error. At $Dn = 137$, it is obvious that the flow has not yet reached the predicted two-dimensional solution. After 180°, the state diagram clearly shows that the numerical simulation predicts a faster growth rate of the additional vortex pair. At $Dn = 150$, it is seen that by $\theta = 220°$ the flow has reached the solution predicted by the two-dimensional simulation, clearly illustrating the shorter development length at $Dn = 150$ as compared to $Dn = 137$.

For $Dn = 137$, it was mentioned that the measured data in figure 6.61 showed a slower growth rate of the additional vortex pair than predicted by the numerical simulation. Similarly, the state diagram for $Dn = 150$ in figure 6.62 reveals the same effect at $120° \leq \theta \leq 160°$, however the difference between the measured and predicted values is not as large as it was for $Dn = 137$. The better agreement at a larger flow rate suggests that elliptic effects are becoming less important. This is not surprising since the viscous terms that were dropped in the three-dimensional parabolized formulation were multiplied by $1/Re$.

Figure 6.63 is a numerically generated state diagram showing the flow development at Dn = 125, 131, 133, 137 and 150. At $Dn = 125$, the flow develops

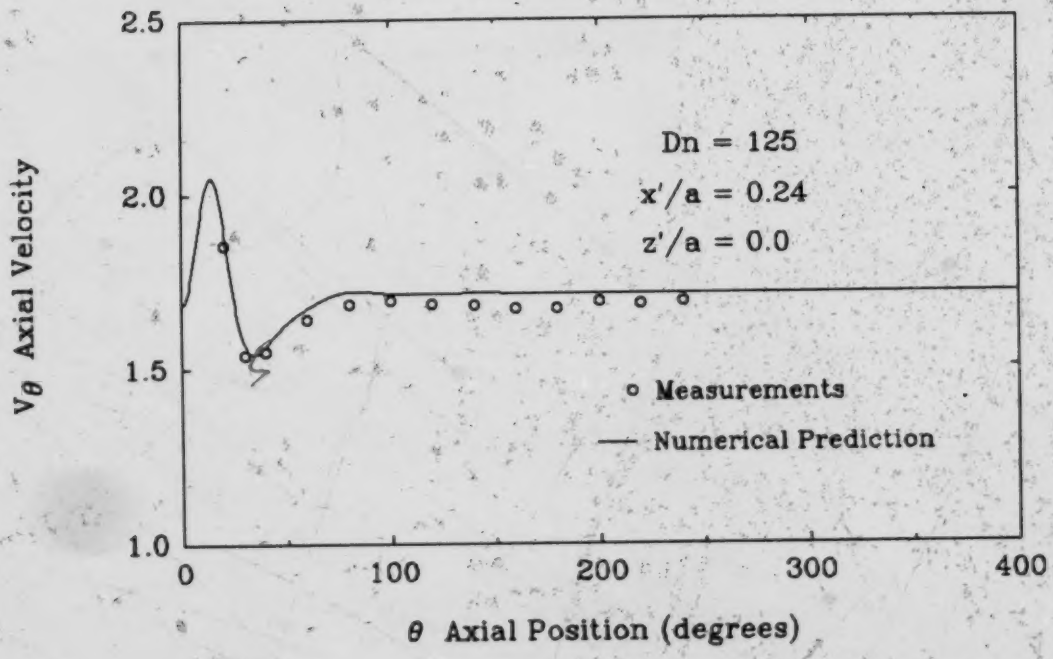

Figure 6.60: Experimentally determined state diagram compared to the numerically predicted state diagram of flow development at $Dn = 125$, $x'/a = 0.24$ and $z'/a = 0.0$.

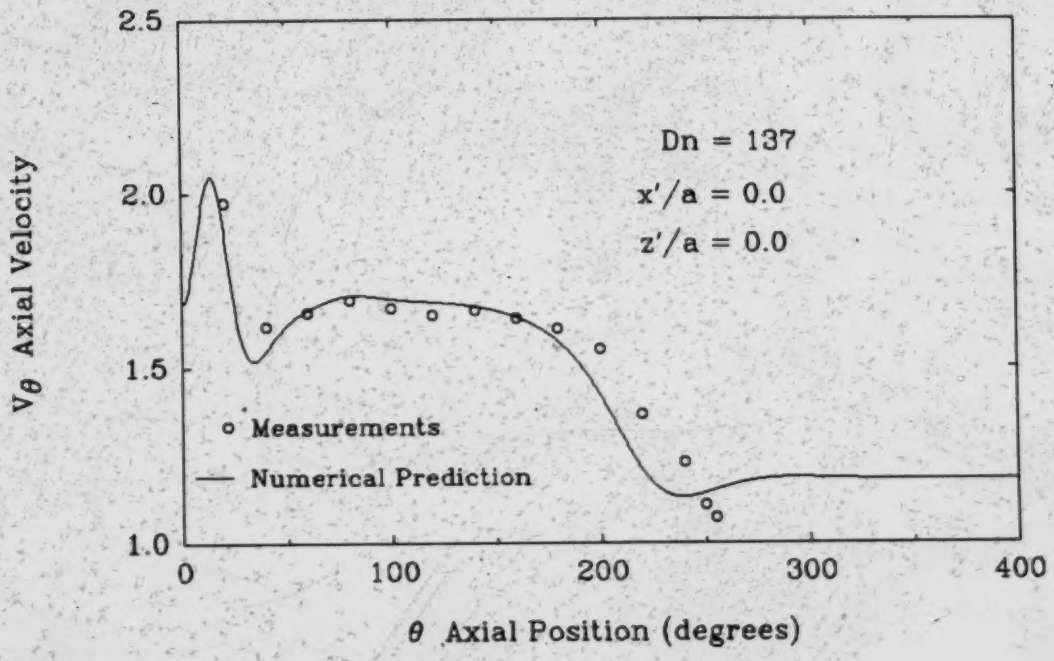

Figure 6.61: Experimentally determined state diagram compared to the numerically predicted state diagram of flow development at $Dn = 137$, $x'/a = 0.24$ and $z'/a = 0.0$.

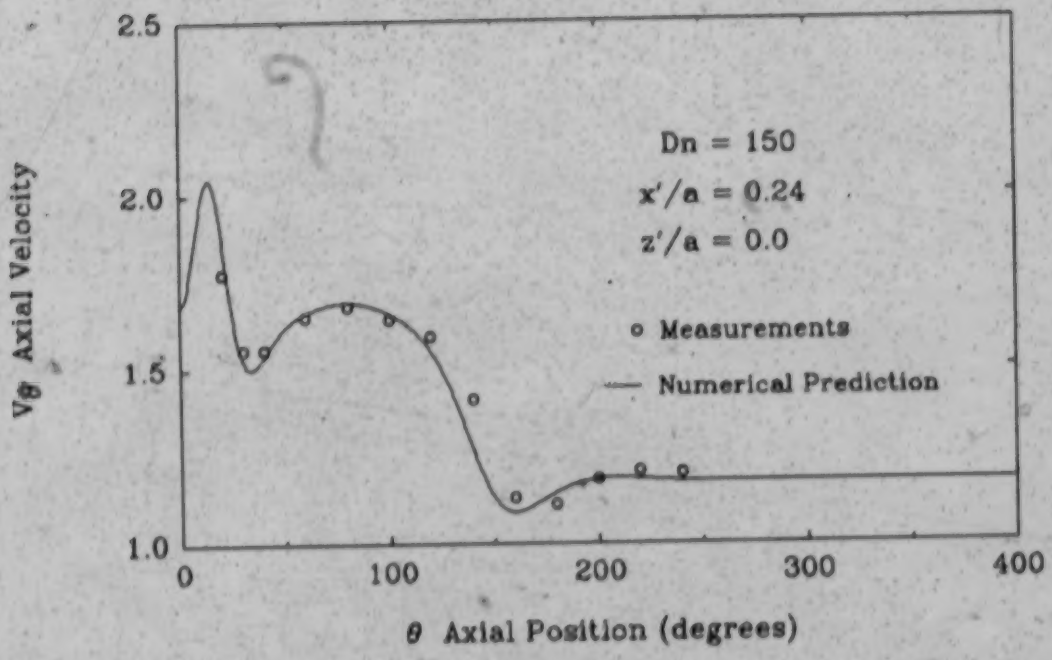

Figure 6.62: Experimentally determined state diagram compared to the numerically predicted state diagram of flow development at $Dn = 150$, $x'/a = 0.24$ and $z'/a = 0.0$.

into a two-vortex flow, while the flow at the other Dean numbers develops into a four-vortex flow. The decrease of development length with increasing Dean number for the four-vortex pattern is clearly indicated. For $\theta \leq 60°$, the flow development is essentially the same for all the Dean numbers. At around $\theta = 35°$, the difference in the minimum values is only an effect of the software plotting package. In figure 6.65, the same graph plotted at a slightly different size does not show this effect.

A numerically generated plot of development length versus Dean number is presented in figure 6.64. For the two-vortex or two-cell flows the increase of development length with Dean number is linear, while for the four-vortex flows a decrease in development with increasing Dean number is observed. A sharp increase in development length is seen for the four-vortex or four-cell flows as the Dean number approaches the critical value (i.e. limit point) for the transition from a two-vortex to a four-vortex flow. The development length appears to approach the critical value asymptotically, indicating an infinite development length at the critical value. This is consistent with smaller centrifugal forces requiring a longer axial length for the additional vortices to grow. The critical value predicted by the three-dimensional parabolic simulation has to be slightly less than $Dn = 130$, which was the smallest Dean number at which a four-cell flow was simulated. The critical value for the two-cell to four-cell transition, predicted by the two-dimensional simulation, was around $Dn = 130.9$.

In the numerical study of Ghia and Sokhey (1977) for a curved duct of square cross section, a numerical experiment showed that the development length for a four-vortex flow increased with increasing Dean number. In order to vary the Dean number, they held the Reynolds number constant and changed the curvature ratio. Using this approach, they missed the phenomena of decreasing development length with increasing Dean number when the curvature ratio is maintained constant.

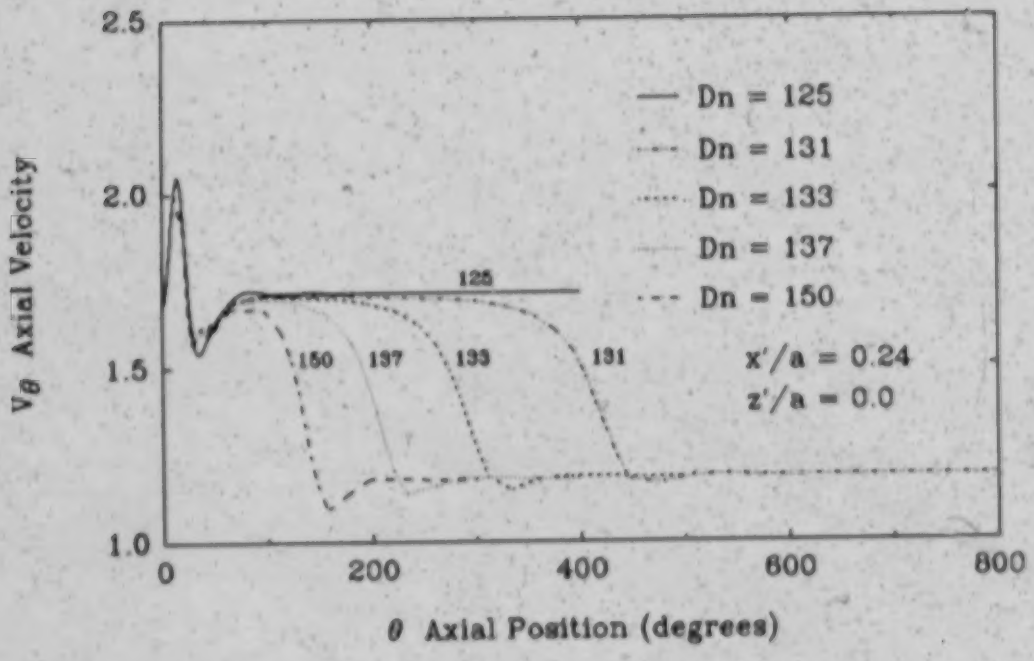

Figure 6.63: Numerically generated state diagram showing flow development at Dn = 125, 131, 133, 137 and 150.

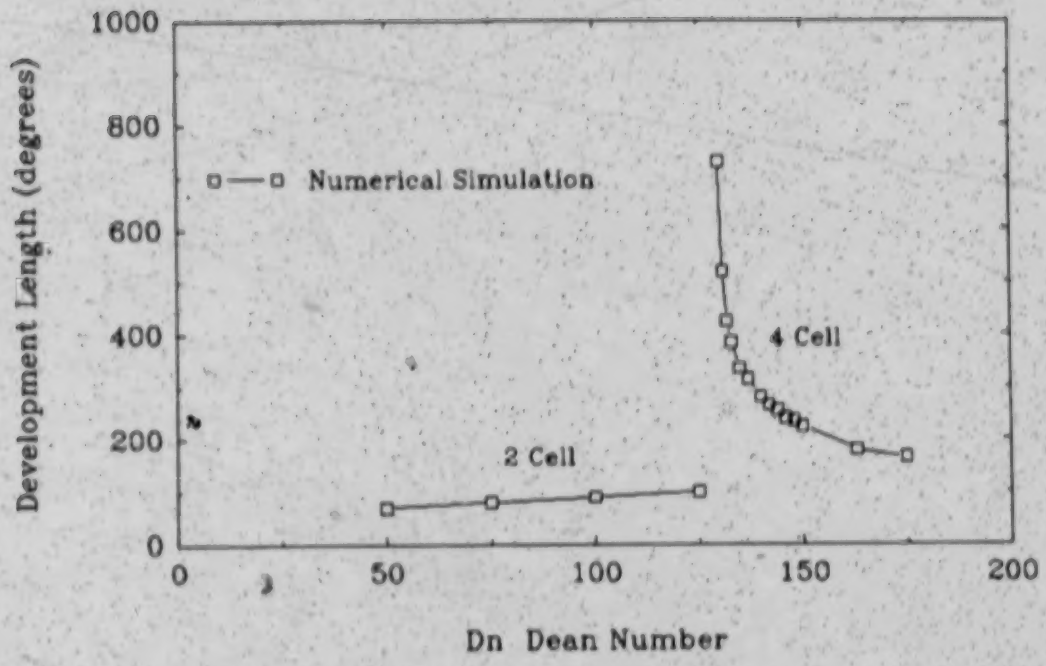

Figure 6.64: Numerical simulation of development length vs. Dean number.

In the flow visualization studies of Cheng *et al.* (1979) and Sugiyama *et al.* (1983), their flow visualization of the four-vortex flows in a square duct reveal different sizes of the additional vortex pair depending on Dean number. At the lower Dean numbers the size of the additional vortex pair was smaller. For a particular aspect ratio, the additional vortex pair should be about the same size at all Dean numbers when the flows are fully developed. The behavior observed in Cheng *et al.* and Sugiyama *et al.*, suggests that some of their flows were not fully developed as they had assumed.

In a numerical study by Soh (1988), for the flow development in a curved duct of square cross section, he suggested that the flow developed into different states depending on the inlet profile to the curved section. For a fully developed straight duct inlet profile, the flow appeared to develop to a two-vortex like state, while a free-vortex inlet profile developed into a four-vortex flow. In order to observe the effect that the inlet profile had on the flow development for the curvature ratio used in this study, a numerical experiment was carried out using a fully developed straight duct inlet profile and uniform inlet profile. Since Agrawal *et al.* (1978) found that a uniform inlet profile quickly develops into a free vortex, the flow development for a uniform inlet should be very similar to the flow development for a free-vortex inlet.

Figure 6.65 shows the flow development for a straight duct inlet profile compared to the flow development for a flat inlet profile. For each Dean number simulated, the flow develops to the same final state independent of the initial inlet profile. The four-vortex flows take longer to develop with a uniform inlet profile than with the fully developed straight duct inlet profile. The development to the same state is contrary to what Soh (1988) predicts, however the results of Soh are not definitive because of the short axial development length he used in his analysis. It is possible that for a larger development length the same final states might have been observed.

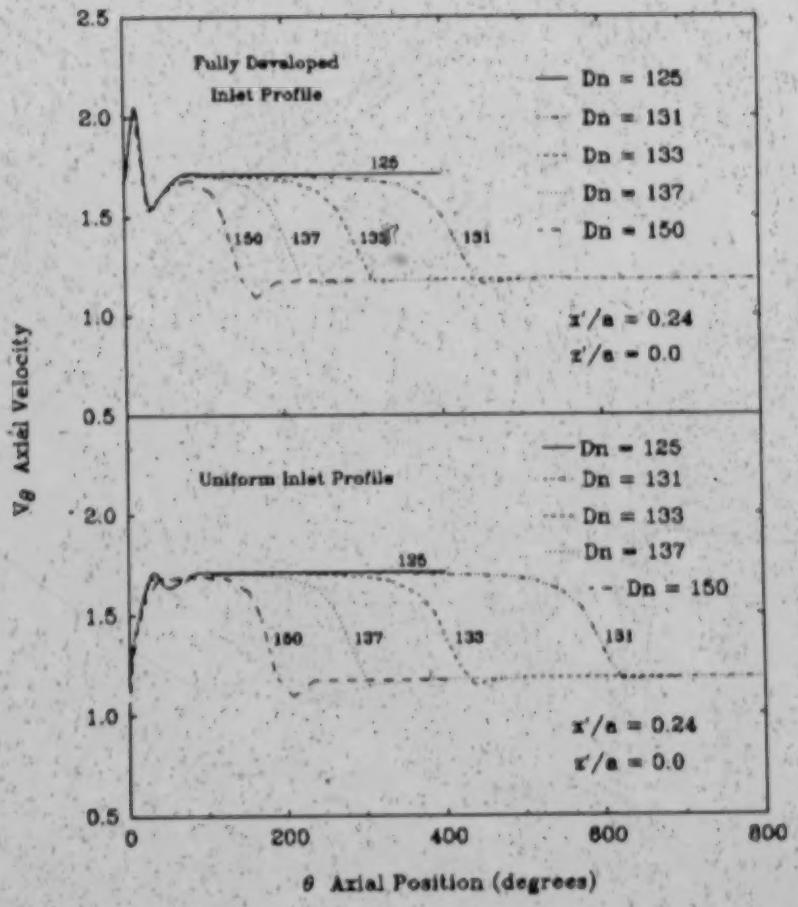

Figure 6.65: Comparison of numerically determined development lengths for a fully developed straight duct inlet profile and a uniform inlet profile.

On the other hand, it just might be that the different curvature ratio used in his analysis is responsible for a different behavior.

Chapter 7

Two-Dimensional Solution Structure

For fluid flow in a curved duct of square cross section, Winters (1987) numerically showed that the two-dimensional (2-D) solution structure was a complex bifurcation diagram with areas of multiple symmetric and asymmetric solutions. A linear stability analysis by Winters also showed that all solutions, except the symmetric two-cell branches were unstable to perturbations that broke the horizontal symmetry. Even though some of the solutions were also predicted to be unstable to symmetric perturbations, the symmetric four-cell flows were predicted to be stable for a perturbation that did not break the horizontal symmetry.

Given that symmetric four-cell flows were predicted to be unstable to asymmetric perturbations, Winters questioned whether they could be experimentally observed. The results presented in the previous chapter, showed that it is possible to experimentally observe the predicted two-dimensional flow at $Dn = 150$. Even though the four-vortex flow is unstable to asymmetric perturbations, the growth rate of such perturbations must be small if it is possible to observe the flow pattern

within the axial length of our apparatus. The ability to observe the symmetric flows within the axial length of the experimental apparatus can be attributed to the perturbation free inlet profile. However, it is still in question as to what would happen if enough axial length of the curved section was present for perturbations to grow so their effect could be fully realized.

Using the two-dimensional Navier-Stokes equations given in chapter three, the numerically predicted two-dimensional solution structure as a function of Dean number is shown in figure 7.1. The solution structure is in the form of a state diagram with the axial velocity at $x'/a = 0.25$ and $z'/a = 0.0$ as the state variable. The symmetry boundary condition imposed about the horizontal centerline only allowed symmetric solutions to be calculated. Between $Dn = 100$ and $Dn = 150$ it is seen that the solution structure contains a dual solution region with limit points at $Dn \simeq 114$ and $Dn \simeq 131$. Winters (1987) showed that the connection between the two-cell and four-cell branches is continuous, however the numerical formulation used in this study was not able to follow the solution around the limit points.

It must be remembered that figure 7.1 has been calculated for a curved duct of square cross section with a curvature ratio, $R_c = 15.1$. For other curvature ratios the solution structure will have the same appearance, but the location of the limit points will be different. Both Shanthini and Nandakumar (1986) and Winters (1987) have numerically shown that the Dn values of the two limit points increase as the duct becomes more tightly coiled (i.e. as R_c decreases). The two investigations have also revealed that when the aspect ratio reaches a value of around 1.4 the two-cell and four-cell branches become disconnected.

In order to generate the state diagram in figure 7.1, a solution was first obtained on the two-cell branch by specifying an appropriate value for the non-dimensional pressure gradient ($\Delta p = \partial p/\partial \theta = -235000$). Once a converged solution had been

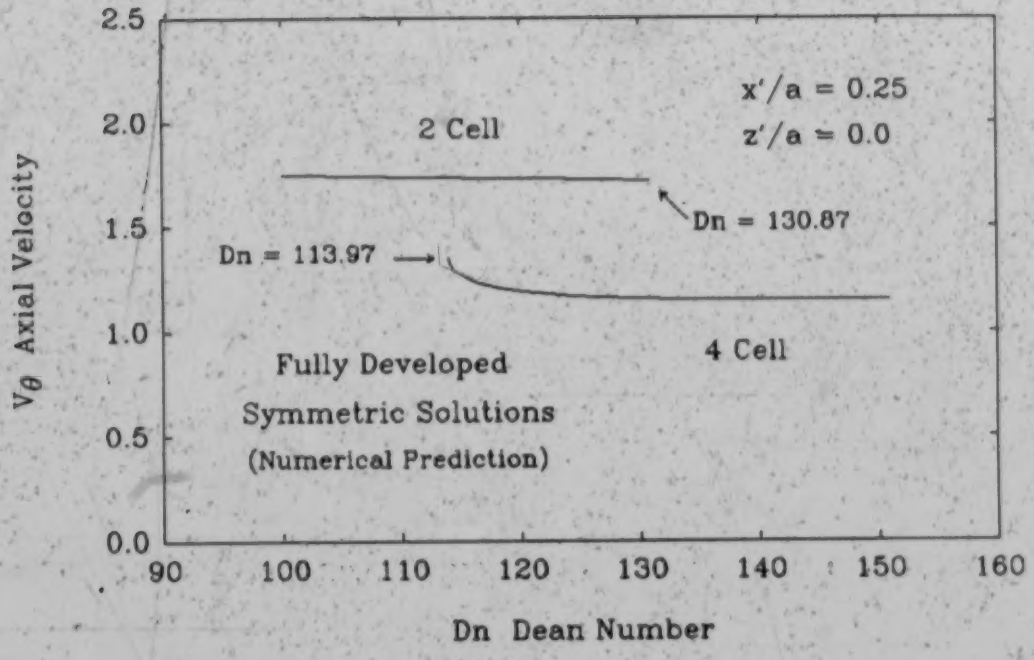

Figure 7.1: State diagram, with axial velocity at $x'/a = 0.25$ and $z'/a = 0.0$ as the state variable, showing the symmetric two-dimensional solution structure for a curved duct with $R_c = 15.1$.

obtained, the corresponding Dean number ($Dn \simeq 101$) was determined. Using this solution as an initial guess, the pressure gradient was gradually increased to trace the two-cell branch. When the pressure gradient was increased beyond $\Delta p = -324000$, the value corresponding to $Dn = 130.87$, the solution jumped to the four-cell branch. Starting with a converged four-cell solution, the four-cell branch was then followed for both increasing and decreasing Dean number. For a pressure gradient smaller than $\Delta p = -277500$, which corresponds to $Dn = 113.97$, the solution jumped back to the two-cell branch. The values of the limit points were calculated by using smaller increments in Δp as the limit points were approached. Using this method, the limit points were determined to within 0.25% of the exact values.

7.1 Experimental Difficulties in Observing Two-Dimensional Solution Structure

One of the goals of this study was to experimentally verify the two-dimensional solution structure that was numerically predicted in the previous section. An obvious problem in accomplishing this can be seen from figure 6.64. The lack of sufficient axial development length in the experimental apparatus prevents observation of the naturally developing four-cell flows below $Dn \simeq 150$. Given that measurements in the experimental apparatus were only possible to about 240°, an experimental "trick" (i.e. inlet perturbation) was required to reduce the development length of the four-cell flows that were below $Dn = 150$.

Figure 7.2 shows the natural occurring solution structure at $\theta = 220°$ if no inlet perturbation is used to induce the two-dimensional four-cell solutions below $Dn = 150$. Figures 7.3 and 7.4 show corresponding arrow plots and flow visualization of the secondary flow structure at $\theta = 220°$. The experimental data in figure

7.2 was acquired by measuring the axial velocity at $\theta = 220°$, $x'/a = 0.24$ and $z'/a = 0.0$ while the Dean number was varied. Unlike the numerically generated two-dimensional solution structure, no hysteresis effect was observed when the flow rate was reduced after having obtained a four-cell flow.

From figure 7.2 it can be seen that around $Dn = 130$ the value of v_θ is starting to change in response to the onset of the additional vortex pair. Given that the development length of the four-cell flow is infinite at the critical value, it is difficult to experimentally determine the two-cell to four-cell limit point. Flow visualization in figure 7.4 also indicates that the limit point is around $Dn = 130$, but it is impossible to determine a value with a high degree of accuracy. For instance, the flow visualization at $Dn = 129.9$ might represent a four-vortex flow where the additional vortices have not yet started to grow. Based on the axial velocity measurements and flow visualization, a best estimate of the experimentally determined two-cell to four-cell limit point is $Dn = 130 \pm 1\text{-}2\%$.

The numerical curve in figure 7.2 was generated by performing a developing flow simulation for each of a series of Dean numbers between $Dn = 100$ and $Dn = 150$. Once a developing flow simulation had been completed, the axial velocity at $\theta = 220°$, $x'/a = 0.24$ and $z'/a = 0.0$ was extracted and used in the construction of the state diagram. The difference between the numerical prediction and measurements in the region between $Dn = 133$ and $Dn = 145$ is a result of the numerical simulation predicting a faster growth rate of the additional vortices. This effect can also be seen by comparing the arrow plots and flow visualization in figures 7.3 and 7.4 respectively. A feature that is common to the numerical simulation and the experimental measurements is the difficulty in determining the value of the two-cell to four-cell limit point.

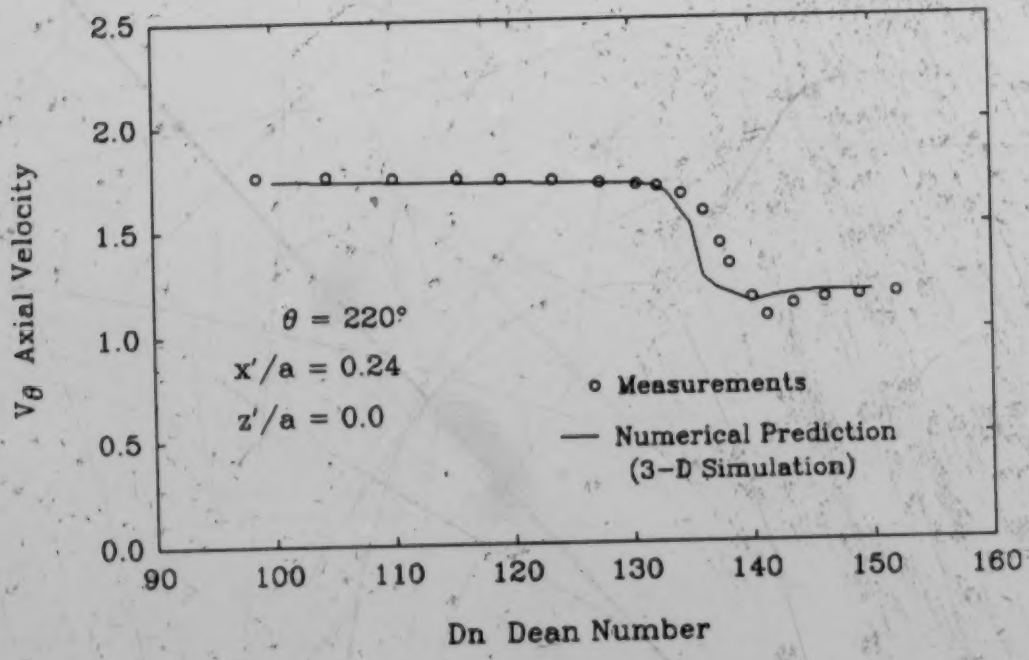

Figure 7.2: State diagram, with axial velocity at $x'/a = 0.24$ and $z'/a = 0.0$ as the state variable, showing the experimentally and numerically determined natural occurring solution structure at $\theta = 220°$.

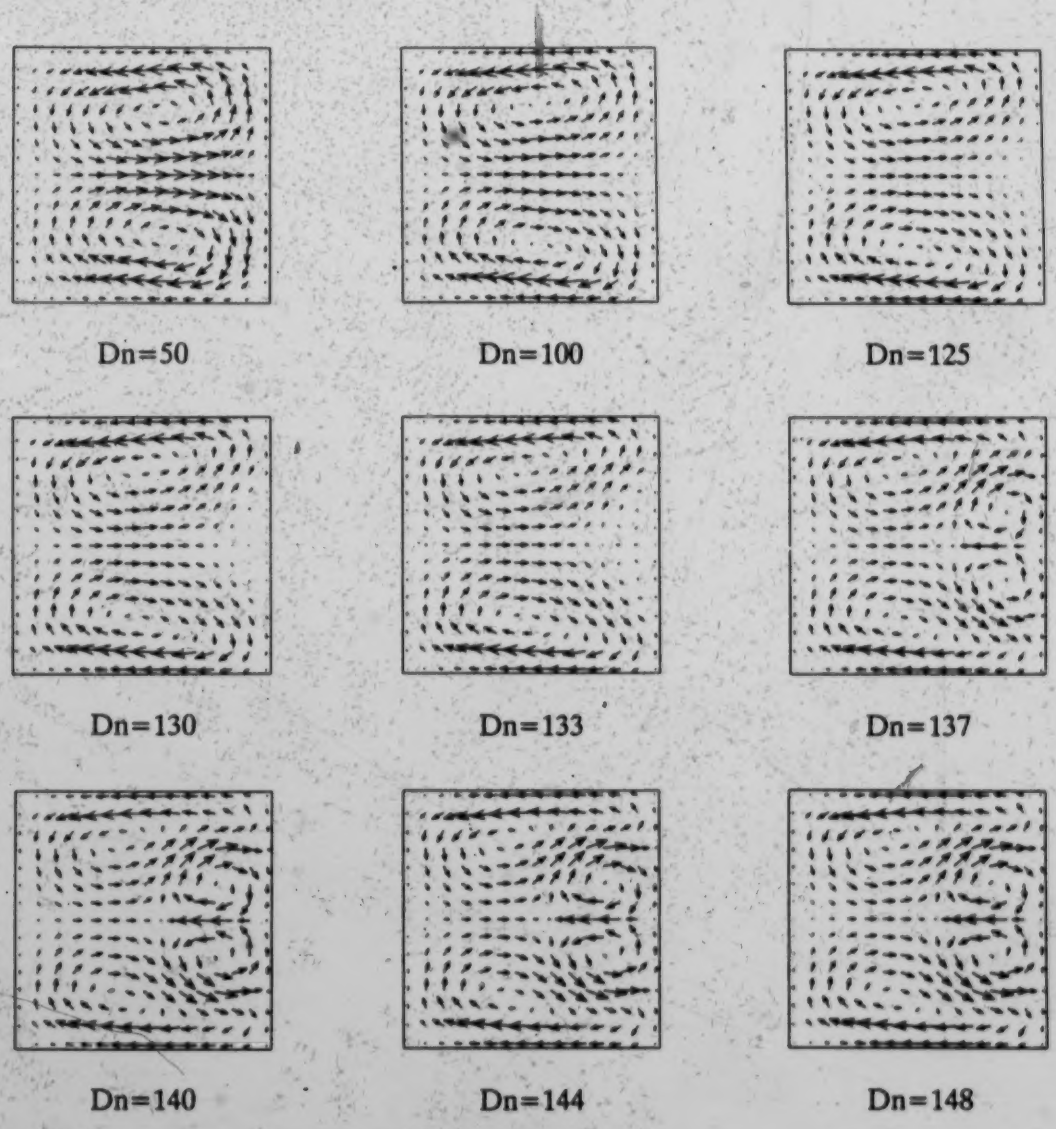

Figure 7.3: Arrow plots of secondary flow patterns at $\theta = 220°$ for the natural occurring solution structure.

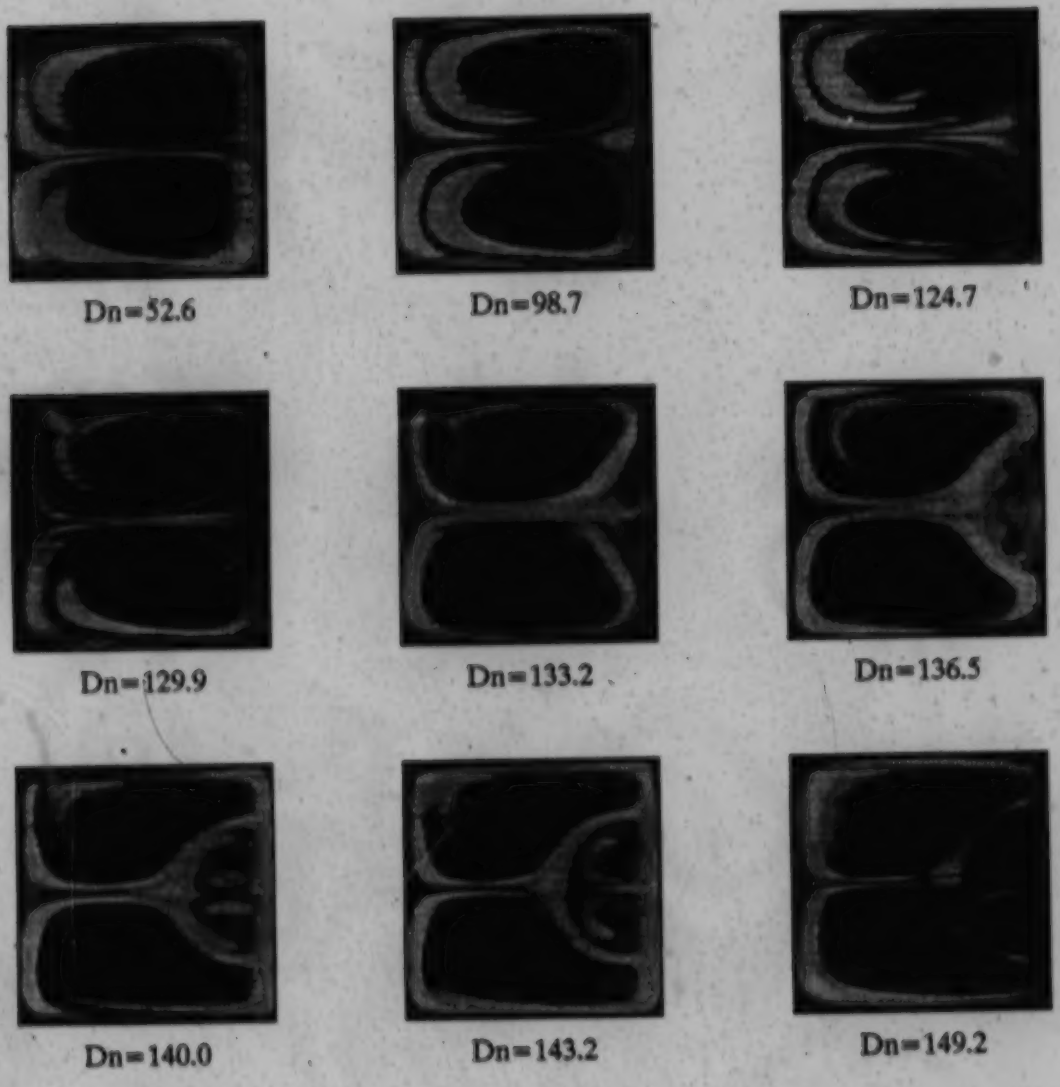

Figure 7.4: Flow visualization of secondary flow patterns at $\theta = 220°$ for the natural occurring solution structure.

7.2 Reduction of Development Length

In order to observe the four-cell flows at Dean numbers below $Dn \approx 150$, a perturbation was introduced at 5° downstream from the curved section inlet. A 0.4 mm diameter pin was inserted across the duct on a radial line at the duct's horizontal axis of symmetry ($z'/a = 0.0$). The appearance of the four-cell flows was very sensitive to the positioning of the pin. If the pin did not cause a symmetric perturbation, then the symmetric four-cell flows could not be observed. Instead, an asymmetric four-cell was observed when the inlet perturbation was asymmetric.

The size of the pin was kept small enough so that no undesirable effects were introduced from its wake. Assuming that the pin would see a maximum velocity equal to the value at the duct center of the straight section inlet, the pin Reynolds number, Re_{pin} (based on the pin's diameter), was 39 at $Dn = 150$. For Re_{pin} less than about 60, Schlichting (1979) *p.* 31 states that the wake behind a circular cylinder will be laminar with no appearance of a Kármán vortex street. Since the pin was not subjected to a Dean number higher than $Dn = 150$, the wake behind the pin would always have been free of a vortex street.

The effect of a pin placed symmetrically across the duct at $Dn = 137$ can be seen in figure 7.5. The circles are the measured flow development with no pin and the triangles show the flow development for the symmetrically placed pin. With the pin, the flow appears to have already become axially invariant by about $\theta = 40°$. Measured velocity profiles at $Dn = 137$, $\theta = 60°$, $\theta = 140°$ and $\theta = 220°$ compared to the numerically calculated 2-D profile in figure 7.6, verify that the flow throughout most of the duct's axial length is axially invariant. In figure 7.7, flow visualization of the flow development at $Dn = 133.9$ with a symmetrically positioned pin at $\theta = 5°$ shows that the secondary flow structure has been formed by $\theta = 60°$ and that it

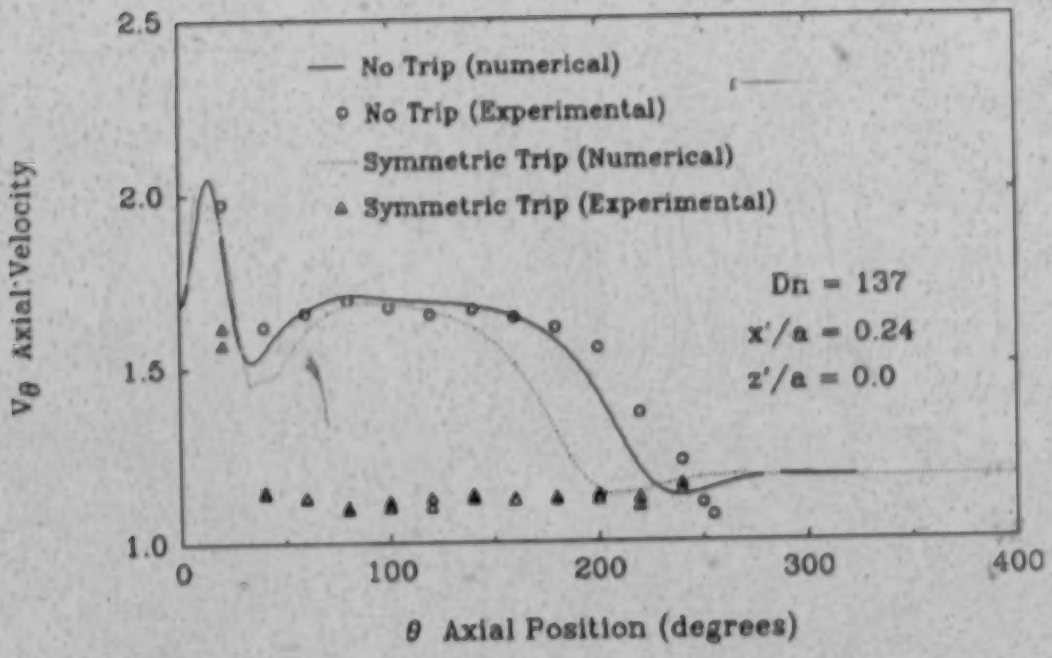

Figure 7.5: State diagram, with axial velocity at $x'/a = 0.24$ and $z'/a = 0.0$ as the state variable, showing the reduction in development length at $Dn = 137$ for an experimental and numerical symmetric trip.

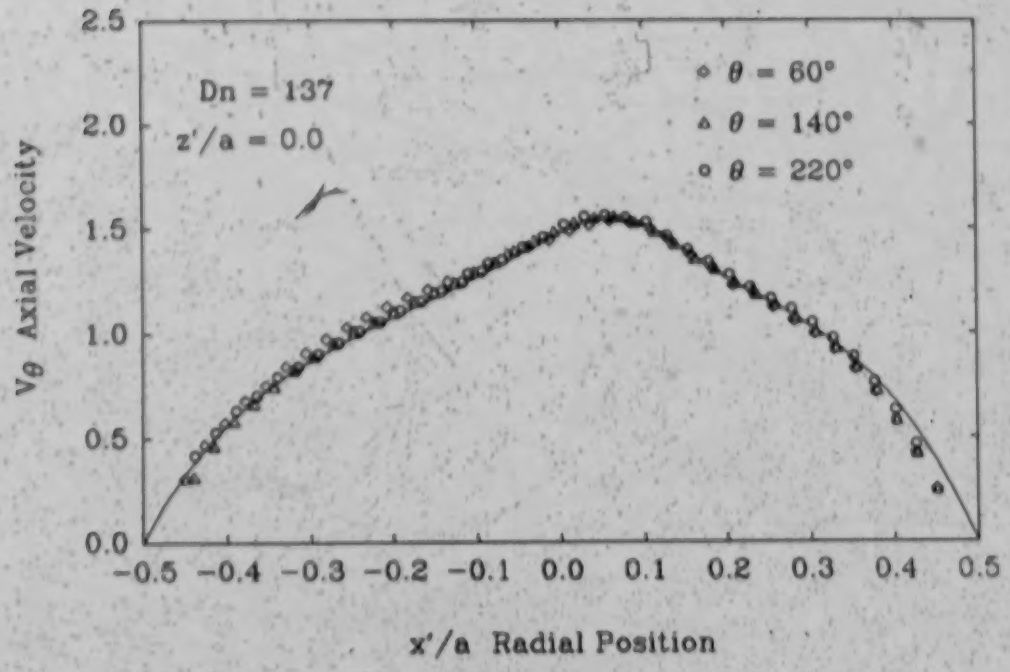

Figure 7.6: Measured axial velocity profiles, at $Dn = 137$, $\theta = 60°$, $140°$, $220°$ and $z'/a = 0.0$, with a symmetric trip at $\theta = 5°$ compared to numerically calculated fully developed profile.

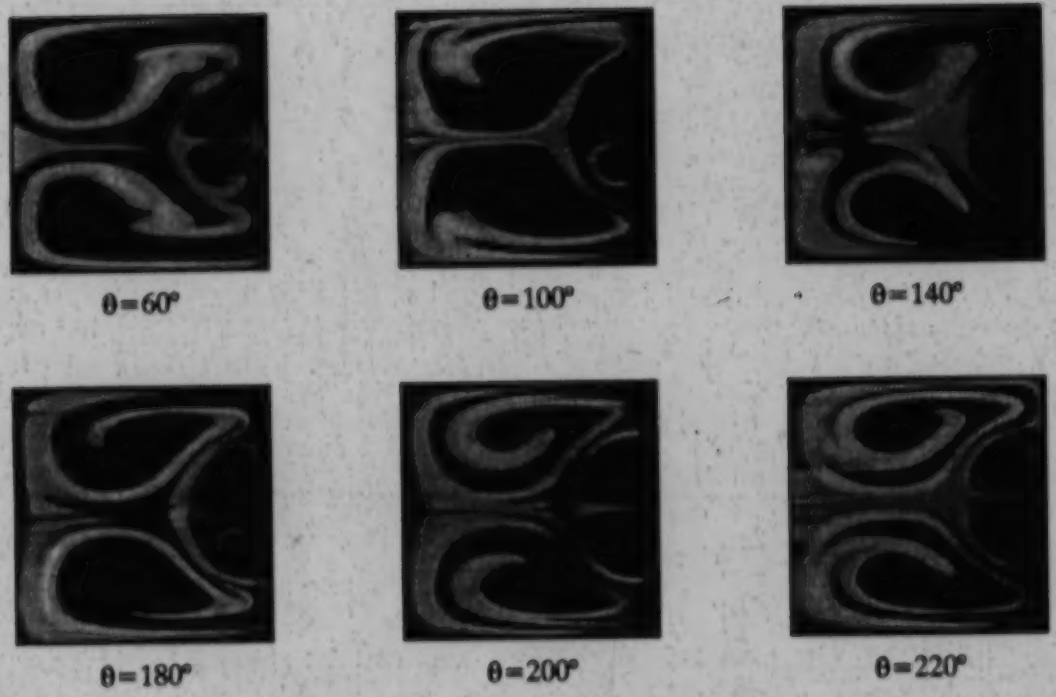

Figure 7.7: Flow visualization of flow development at $Dn = 133.9$ with a symmetric trip at $\theta = 5°$.

remains constant thereafter.

The symmetric trip was numerically modeled by setting the axial and radial velocity components to zero at the grid points on the duct's horizontal axis of symmetry. This was done at $\theta = 5°$ once a converged profile had already been obtained. The dotted line in figure 7.5 shows the numerically predicted flow development with a symmetric trip compared to the experimentally measured development with the symmetrically positioned pin (i.e. symmetric trip). The numerical simulation shows a reduced development length, but it is nowhere near to what was measured. The difference has to be due to the fact that the numerical trip (i.e. setting the velocities at $-0.5 \leq x'/a \leq 0.5$ and $z'/a = 0.0$ to zero) is not an accurate model of the pin's effect.

7.3 Experimental Observation of Dual Solutions

The experimentally observed two-dimensional solution structure at $\theta = 220°$ is shown in figure 7.8. The two-cell branch was determined up to $Dn = 130.5$ by measuring the state variable with no pin inserted at $\theta = 5°$. Since the two-cell to four-cell transition was expected to be around $Dn = 130$, the measured value at $Dn = 130.5$ may or may not actually be a two-cell flow. The entire four-cell branch was observed upon the symmetric insertion of the pin. Starting with a two-cell flow at $Dn \approx 125$, the pin was inserted and adjusted until a symmetric four-cell flow was observed. Once a four-cell flow had been obtained, the flow rate was increased or decreased to trace the solution branch. Using the pin as an experimental "trick" to observe the four-cell solution branch is consistent with the work of Benjamin (1978b) described in chapter two.

Figure 7.9 summarizes the role that the pin played in experimentally observing

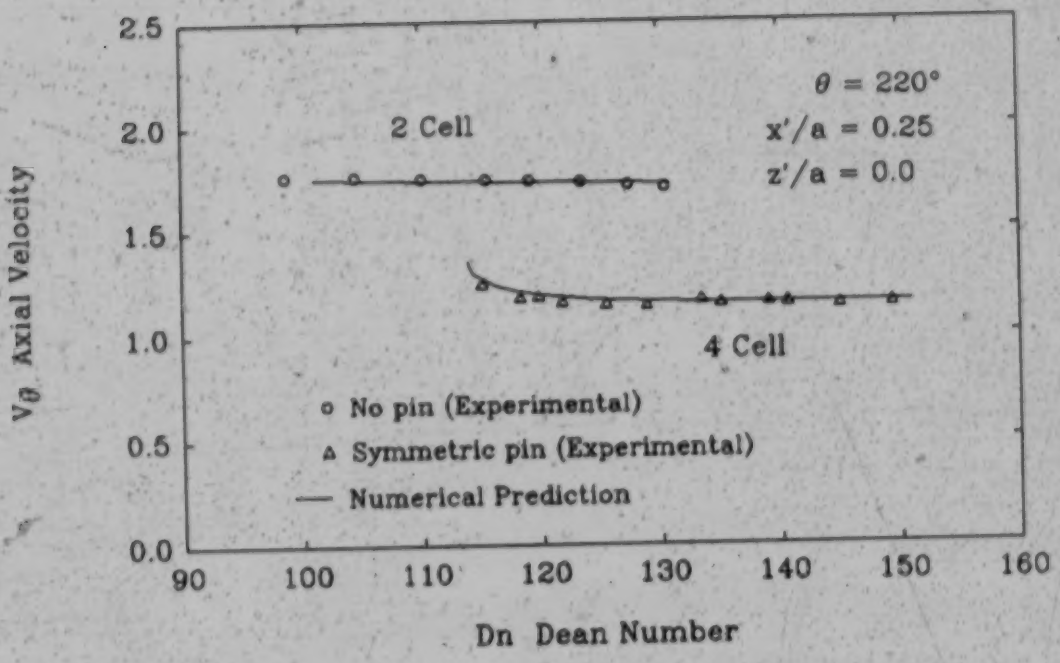

Figure 7.8: State diagram, with axial velocity at $x'/a = 0.25$ and $z'/a = 0.0$ as the state variable, showing the experimentally determined two-dimensional solution structure for a curved duct with $R_c = 15.1$.

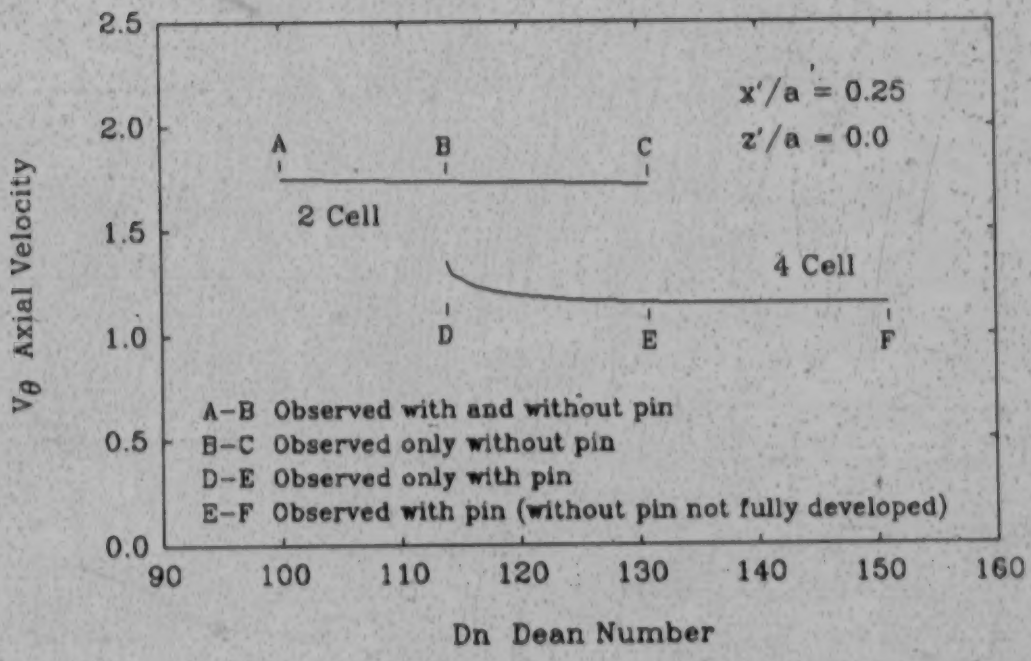

Figure 7.9: State diagram, with axial velocity at $x'/a = 0.25$ and $z'/a = 0.0$ as the state variable, used to illustrate role of pin in observing different regions of the 2-D solution structure.

different regions of the two-dimensional solution structure. The two-cell flows in region A–B and the four-cell flows in region E–F could be observed with and without the pin inserted at the inlet. However, in region E–F the four-cell flows below $Dn \approx 150$ were not fully developed if no pin was used. The four-cell flows in region D–$\tilde{E}$ could only be observed if the pin was used to induce the four-cell flows. Conversely, the two-cells flows in region B–C could only be observed without the pin inserted at the inlet.

In figure 7.8, the Dean number for the jump from the four-cell branch back to the two-cell branch appears to be close to the numerically predicted value of $Dn \simeq 114$. For Dean numbers above $Dn \simeq 118$, the four-cell flows would remain, but at $Dn = 115.1$ (the lowest experimentally observed value) the four-cell flow was only observed briefly. As the flow rate was decreased below $Dn \simeq 118$, the pin (located at $\theta = 5°$) was no longer effective in inducing the four-cell flow, so a two-cell flow developed. However, before the developing two-cell flow reached the downstream measurement position, it appeared that the four-cell structure being convected out of the duct had adjusted to the lower Dean number. Therefore, in order to observe the experimental point at $Dn = 115.1$, the flow rate was reduced and the lowest velocity value was recorded. Since the time scale for the flow to adjust to the lower flow rate was comparable to the convection time scale, the velocity value corresponding to the four-cell flow at $Dn = 115.1$ was only observed for a few seconds.

Figures 7.10 and 7.11 show the axial velocity profiles of a two-cell and four-cell flow respectively, measured at $Dn = 125$, $\theta = 220°$ and $z'/a = 0.0$. Flow visualization of the secondary flow patterns at $Dn = 123.4$ are compared to the numerically predicted secondary flow streamlines for a two-cell and four-cell flow in figures 7.12 and 7.13 respectively. From figures 7.10 through 7.13 it can be

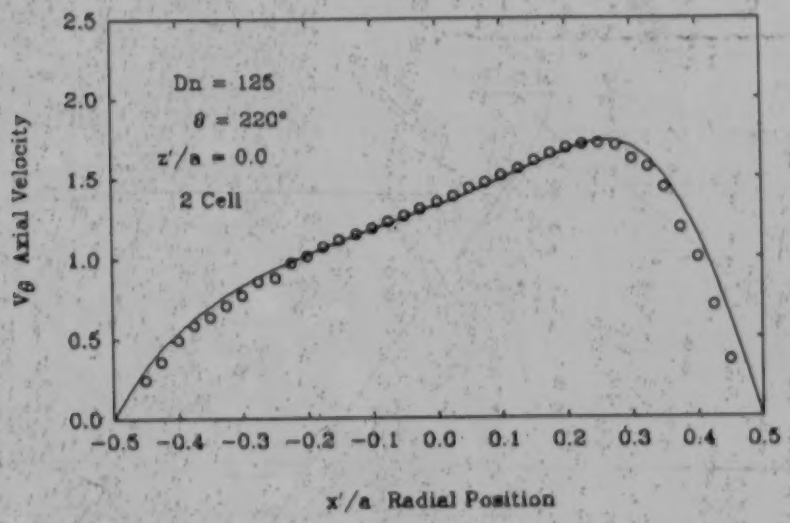

Figure 7.10: Measured axial velocity profile of a two-cell flow at $Dn = 125$, $\theta = 220°$ and $z'/a = 0.0$.

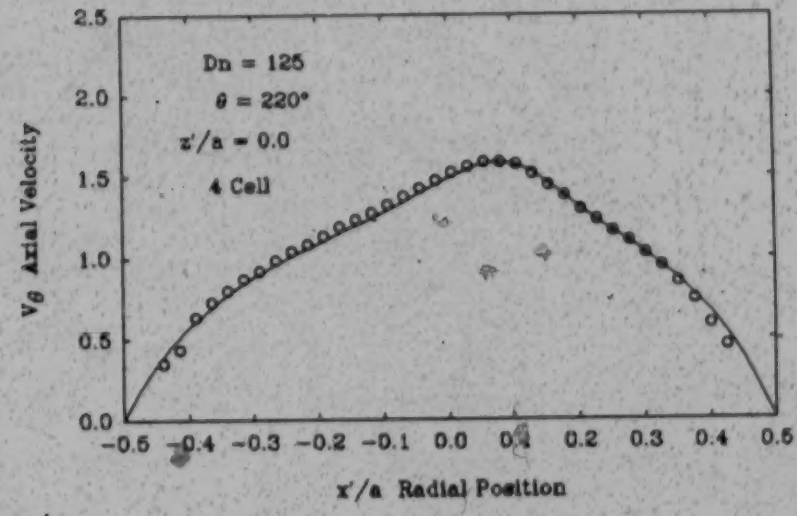

Figure 7.11: Measured axial velocity profile of a four-cell flow at $Dn = 125$, $\theta = 220°$ and $z'/a = 0.0$.

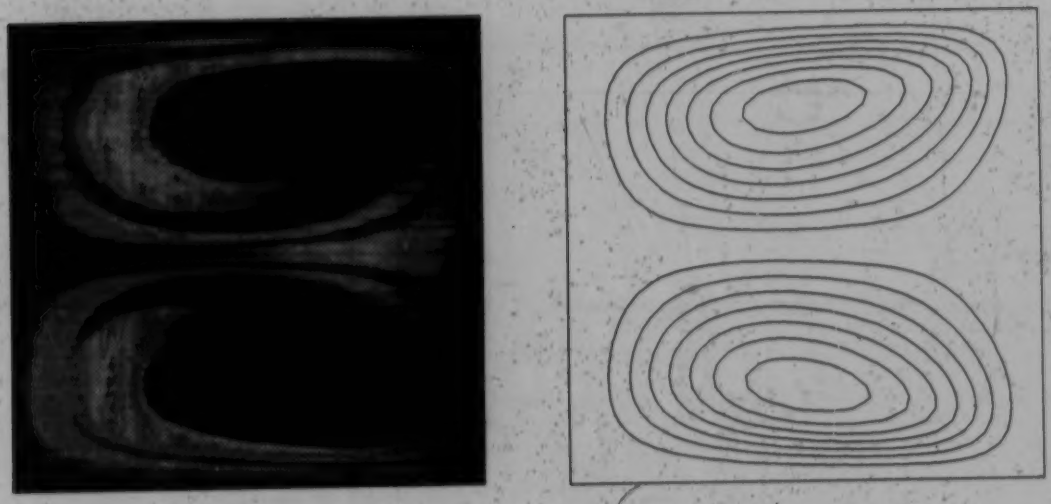

Figure 7.12: Flow visualization of two-cell flow compared to numerically predicted secondary flow streamlines at $Dn = 123.4$.

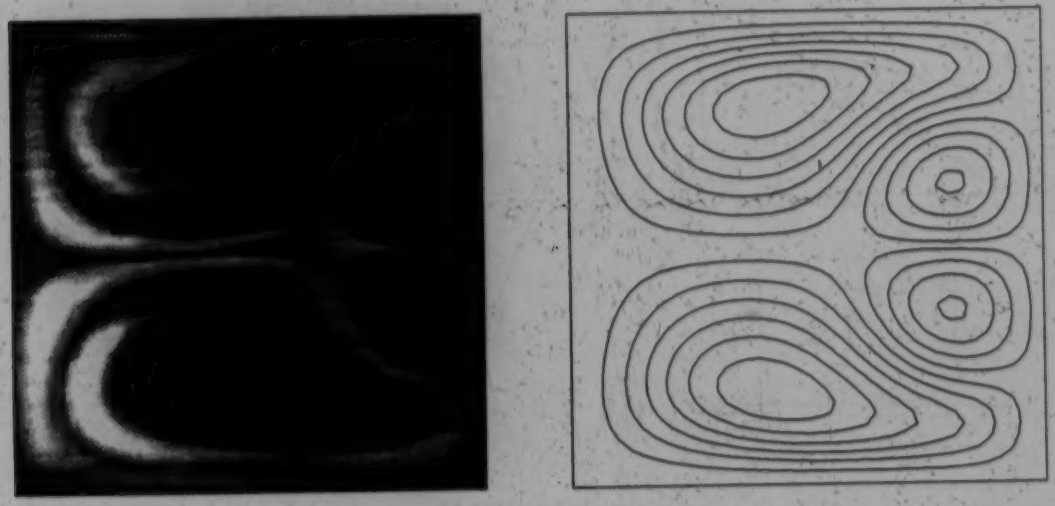

Figure 7.13: Flow visualization of four-cell flow compared to numerically predicted secondary flow streamlines at $Dn = 123.4$.

seen that the experimentally observed dual solutions at $Dn \simeq 125$ are in very good agreement with the numerical predictions.

7.4 Role of Pin in Inducing Four-Vortex Flows

The role of the pin in inducing the four-cell flows can be explained with the aid of the three-dimensional (3-D) plots of axial velocity in figures 7.14 and 7.15. The two-cell and four-cell axial velocity surfaces were numerically calculated using the two-dimensional vorticity stream-function formulation. The major difference between the two-cell and four-cell velocity surfaces is the depression at the horizontal line of symmetry in the four-cell velocity surface. The velocity gradients near the outer wall in the four-cell profile are necessary if the additional pair of vortices are to exist. In fact, the vorticity transport equation given in equation 3.13 reveals that it is the gradients of the axial velocity in the vertical direction that drive the secondary flow.

Figure 7.16 shows the measured axial velocity profiles in the vertical direction at $Dn = 125$, $\theta = 20^{\circ}$ and $x'/a = 0.32$ with and without the pin. Without the pin the profile is fairly uniform in the central region. However, upon the insertion of the symmetrically placed pin, the profile develops a depression. The vertical axial velocity gradients induced by the pin's presence cause the additional vortices to form at the outer wall. Given that the pin's role is to create the proper velocity gradients, the axial position of the pin should not be critical.

Figures 7.17 and 7.18 show the axial velocity profiles at the duct's horizontal and vertical axis of symmetry with and without the pin at $\theta = 5^{\circ}$. It is seen from figure 7.17 that the axial velocity in the region near the wall is reduced as a result of the presence of the pin. The axial velocity at the duct center, in figure 7.18, adjusts in order to satisfy continuity.

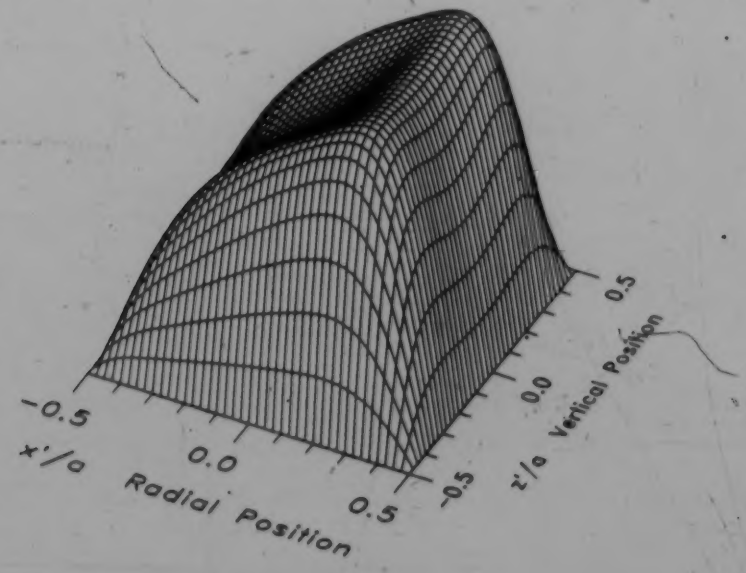

Figure 7.14: 3-D axial velocity plot of fully developed two-cell flow at $Dn = 123.4$.

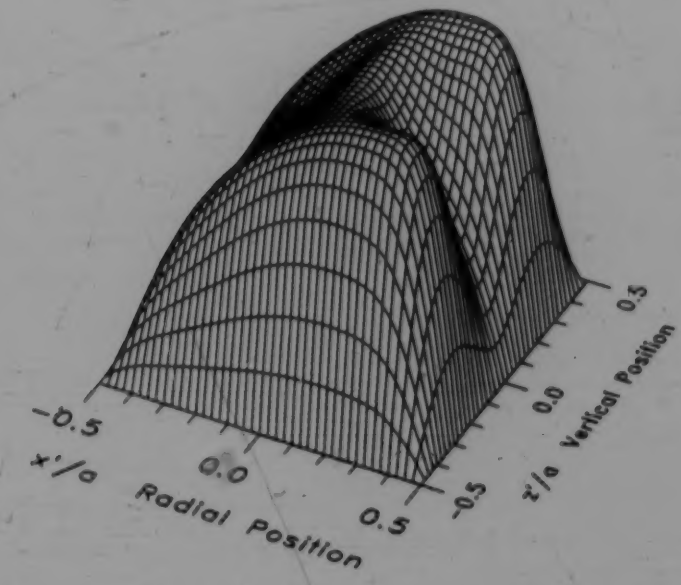

Figure 7.15: 3-D axial velocity plot of fully developed four-cell flow at $Dn = 123.4$.

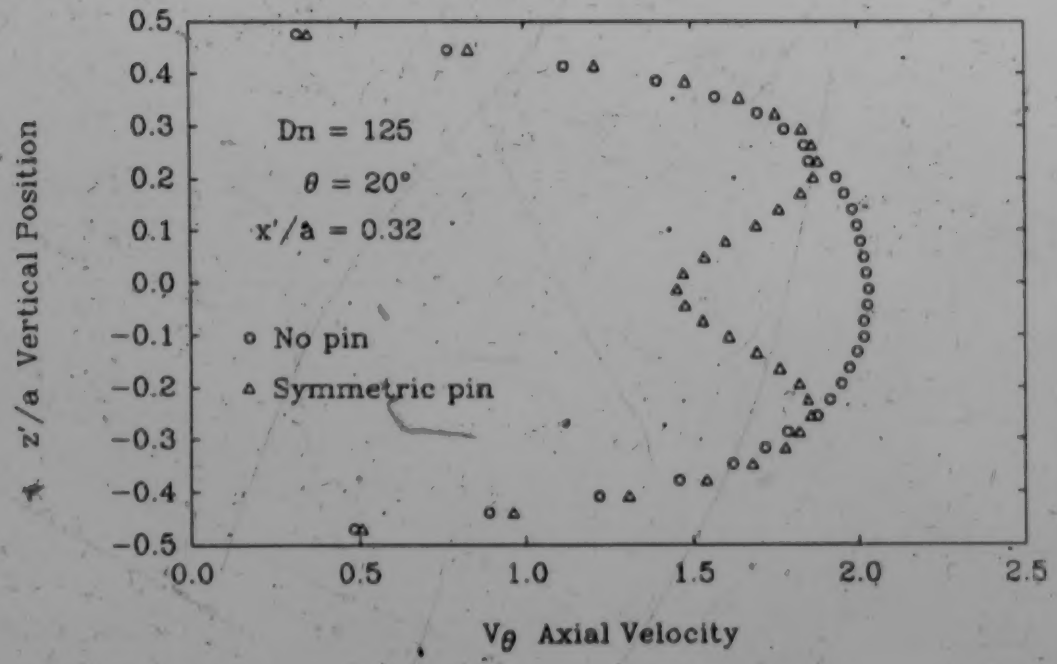

Figure 7.16: Measured axial velocity profile at $Dn = 125$, $\theta = 20°$ and $x'/a = 0.32$ with and without symmetric pin at $\theta = 5°$.

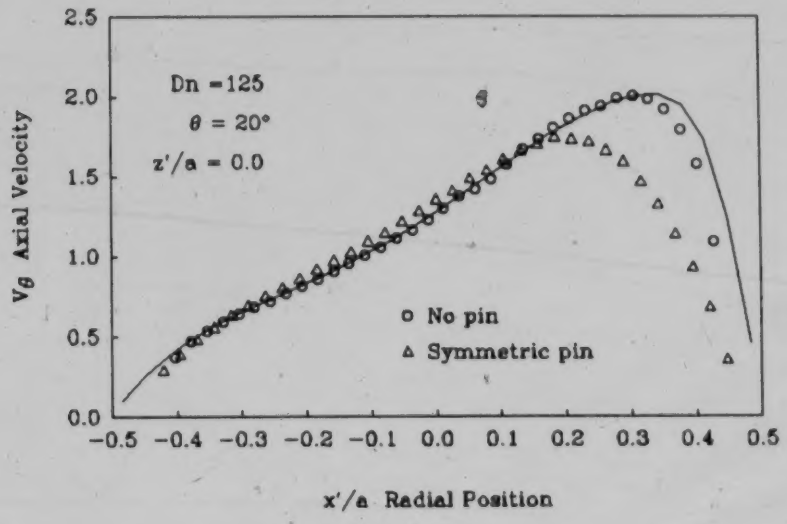

Figure 7.17: Measured axial velocity profile at $Dn = 125$, $\theta = 20°$ and $z'/a = 0.0$ with and without symmetric pin at $\theta = 5°$.

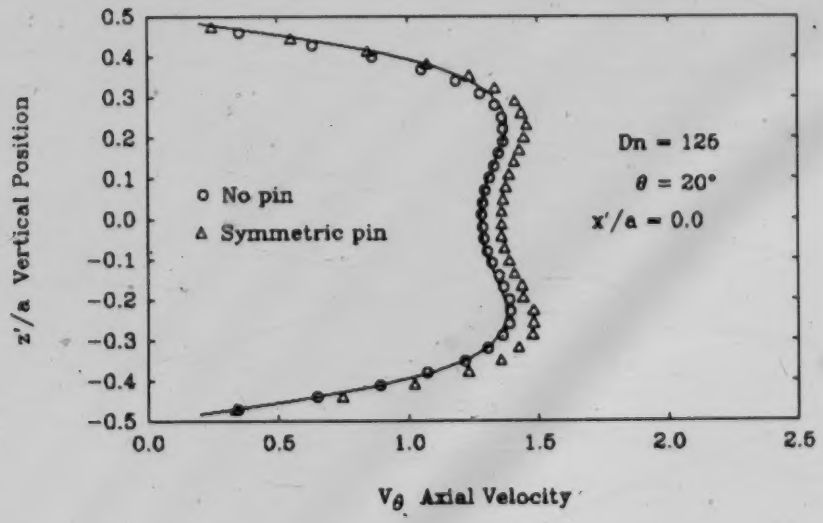

Figure 7.18: Measured axial velocity profile at $Dn = 125$, $\theta = 20°$ and $x'/a = 0.0$ with and without symmetric pin at $\theta = 5°$.

Chapter 8

Stability of Flows

The numerical studies of Winters (1987) and Yanase *et al.* (1988) demonstrated that the four-cell flows in curved ducts of both rectangular and circular cross section are unstable to asymmetric perturbations. In each case the four-cell flows were found to be stable for a symmetric disturbance, while the two-cell flows were found to be stable for any arbitrary disturbance. The use of a symmetric pin to experimentally induce the four-cell flows, as was shown in chapter seven, confirms that the flows are stable to symmetric disturbances. The fact that asymmetric four-cell flows were observed when the pin was not symmetrically positioned, also confirms that the symmetric four-cell flows are unstable to an asymmetric perturbation.

In the previous two chapters it was shown that for $Dn \leq 150$, the symmetric four-cell flows predicted by the two-dimensional Navier-Stokes equations could be experimentally observed within 240° of axial length. Given that four-cell flows are unstable to asymmetric perturbations, and that any experimental apparatus will have inherent asymmetries, suggests that the growth rate of such disturbances must be small in order to experimentally observe the flows. If an asymmetric disturbance is not introduced at the inlet, naturally occurring asymmetries might require large

axial lengths before their effects are observed. However, whether an asymmetric disturbance is deliberately introduced at the inlet or allowed to grow naturally, the question still remains as to what happens to the flow far downstream.

8.1 Steadiness of Flows

One possible way that the four-cell flows could respond to growing asymmetric perturbations is to develop time dependent fluctuations. In order to check the steadiness of the flows that were investigated, a point at $\theta = 240°$ was chosen, and the axial velocity was monitored for at least 80 minutes. The point at which the velocity was monitored at was on the horizontal line of symmetry (i.e. $z'/a = 0.0$) and at one quarter of the duct width from the outer wall (i.e. $x'/a = 0.25$). For the four-cell flows, this position was between the additional vortex pair at the outer wall, so any motion in the vortices could easily be detected.

It was necessary to know that the inlet conditions did not provide the source of any fluctuations, so the steadiness of the inlet flow had to be investigated. Figure 8.1 shows time records of the axial velocity at the center of the straight duct inlet section for $Re = 388.0$, 585.9 and 778.3. The three flow rates show that, for the range of Dean numbers investigated in the curved duct, the inlet flows are steady. The small fluctuations (i.e. noise) that are seen in the signals are a result of the inherent phase fluctuations associated with the doppler signals of the LDV.

Figure 8.2 shows the time records for a two-cell and four-cell flow at $Dn \simeq 125$. The two-cell flow time record at $Dn = 124.9$ has a slight rise in the first 600 seconds. This effect is likely due to the flow rate settling down to steady state. Since the two-cell flows are stable to any arbitrary perturbation, no time dependence is to be expected. The four-cell flow time record at $Dn = 125.4$ is fairly constant, but a slight

increase in the signal is noticeable between 4500 and 5000 seconds. This increase is likely due to a small asymmetric disturbance introduced by the accumulation of air bubbles on the pin, or a slight movement of the pin in the rubber mount. The axial velocity at the monitoring point was observed to be a minimum when the additional vortices were symmetric, so an increase of velocity indicated that the cells had become asymmetric.

Both four-cell flows at $Dn = 137.6$ and $Dn = 149.8$, shown in figures 8.3 and 8.4 respectively, were extremely steady for the 6000 second sample time, confirming that the flows were time independent. The non-dimensional velocity, v_θ, is slightly larger at $Dn = 137.6$ than at $Dn = 149.8$, since the flow at $Dn = 137.6$ has not developed by $\theta = 240°$. The steadiness of these four-cell flows also suggests that any asymmetries appearing in the induced four-cell flows below $Dn \leq 150$ are a result of asymmetries associated with the pin.

At $Dn \simeq 200$, the time records presented in figures 8.5 and 8.6 show the effect of heat transfer between the ambient air and working fluid. In figure 8.5, the signal starts at a value of $v_\theta \simeq 1.3$ and after about 2500 seconds (i.e about forty minutes) v_θ has increased to around 1.5. The increase of the axial velocity indicates an increasing asymmetry in the additional vortex pair near the outer wall. However, once the velocity reached the higher value, it remained there for the remainder of the sample time. In fact, figure 8.6 shows that, for an additional 6000 seconds after the end of the first time series, the velocity still remains constant.

The transient behavior observed in the first forty minutes of the time record shown in figure 8.5 is a result of the working fluid in the apparatus changing temperature. When the apparatus was first started up it had been sitting for some time, so the working fluid in the stilling chamber would have been at the ambient temperature. During the course of the measurement, the room temperature was

about 0.5° to 1° higher than the set point temperature of the working fluid, and as the fluid in the stilling chamber was replaced by the working fluid at the lower set point temperature, the initial transient was observed. Even though the system eventually reached a steady state condition, the temperature difference between the working fluid and ambient air caused an asymmetric four-cell flow to be observed at $\theta = 240°$. The fact that the asymmetry grew with time also confirmed that the effect was not an asymmetry in the apparatus that was just starting to appear at $Dn \simeq 200$.

The temperature effect was not observed at $Dn \leq 150$, even though the same temperature difference existed between the working fluid and the ambient air. This seems to suggest that the asymmetric four-cell at $Dn \simeq 200$ resulted from an asymmetric disturbance caused by buoyancy effects rather than a combined centrifugal and buoyancy effect. If the asymmetry in the vortices was a mixed convection effect, as in the studies of Yao and Berger (1978) and Sankar *et al.* (1986), the effect would have been more pronounced at the lower Dean numbers. Figure 8.7 shows an asymmetric four-cell flow at $Dn = 150$ and $\theta = 220°$ caused as a result of an asymmetric perturbation created by warming the first 20° of the curved section by the observers hand.

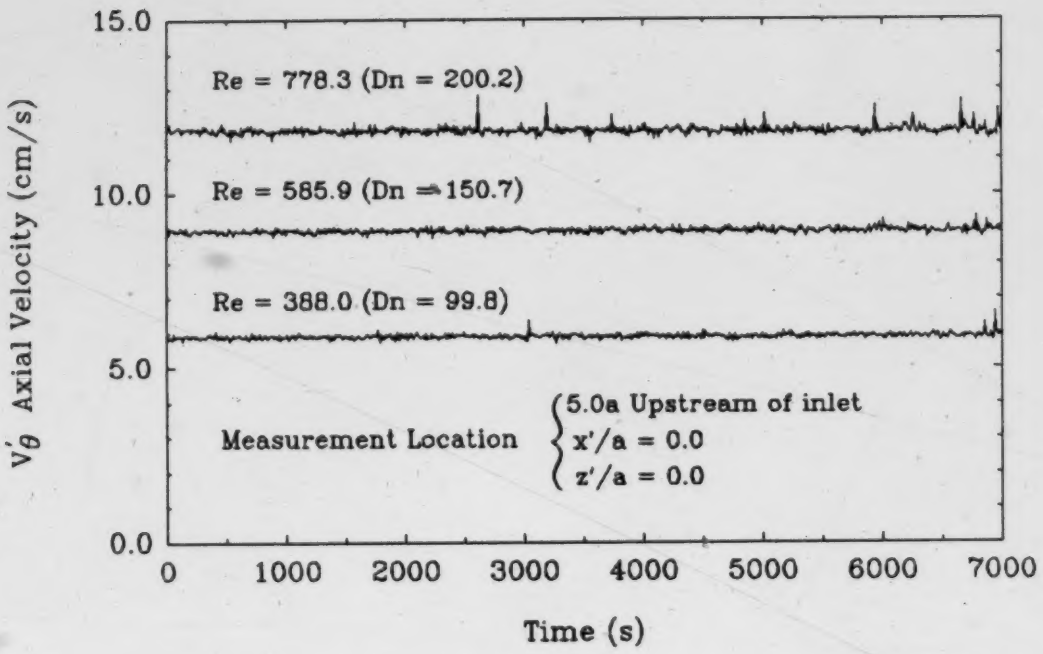

Figure 8.1: Time records of measured axial velocity in straight duct section at $x'/a = 0.25$ and $z'/a = 0.0$ showing steadiness of inlet flow for $Re = 388.0$, 585.9 and 778.3 (measurement location; $5a$ upstream of curved section inlet).

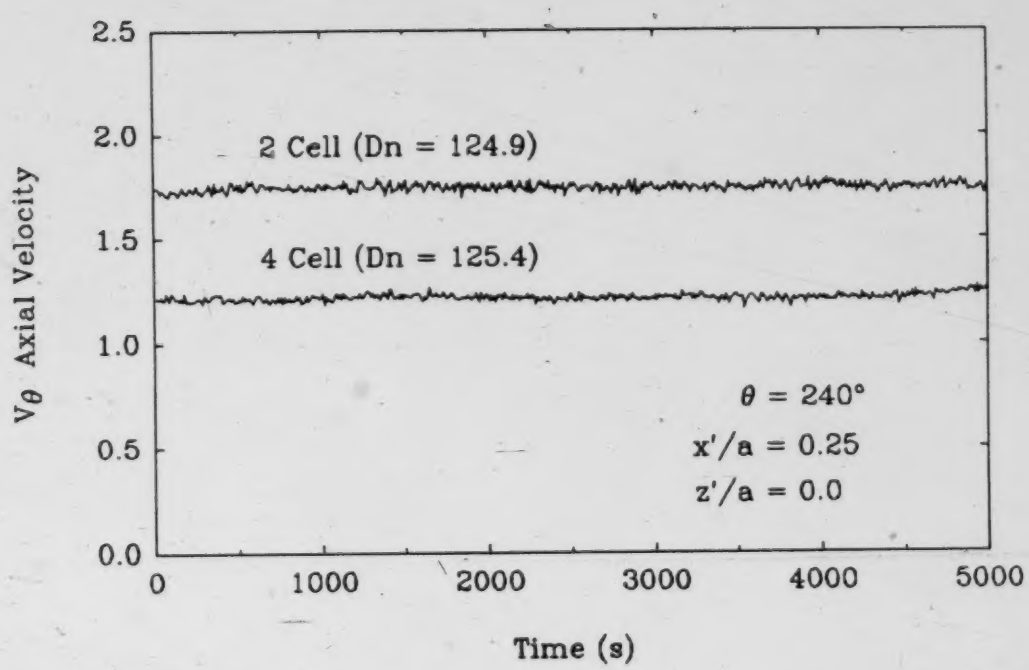

Figure 8.2: Time records of measured axial velocity at $Dn \simeq 125$, $\theta = 240°$, $x'/a = 0.25$ and $z'/a = 0.0$ showing steadiness of a two-cell and four-cell flow.

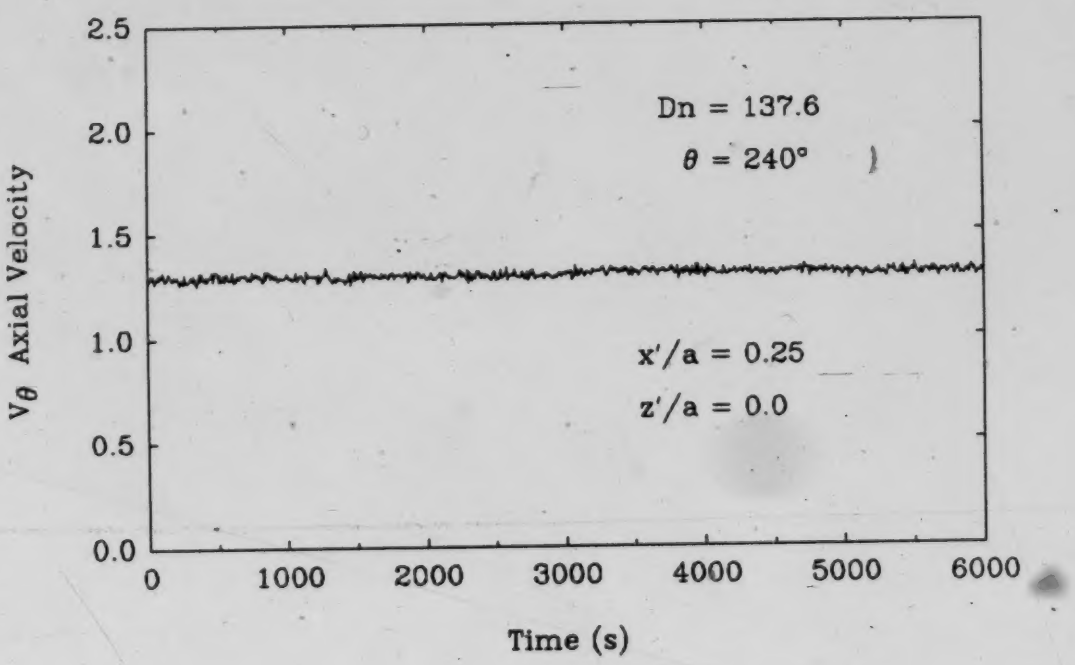

Figure 8.3: Time record of measured axial velocity at $Dn = 137.6$, $\theta = 240°$, $x'/a = 0.25$ and $z'/a = 0.0$ showing steadiness of the four-cell flow.

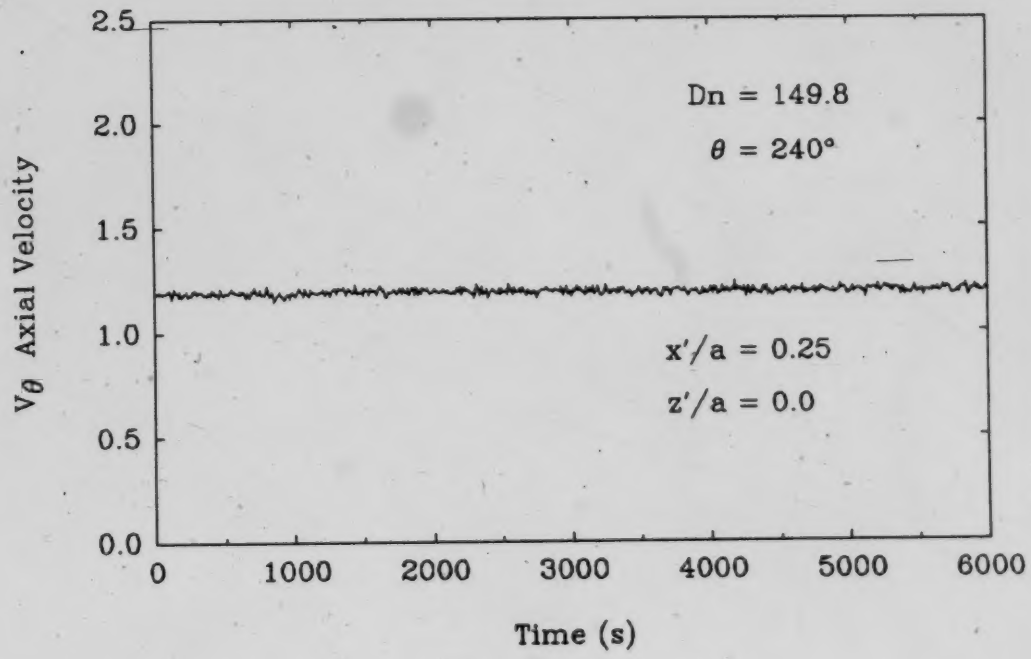

Figure 8.4: Time record of measured axial velocity at $Dn = 149.8$, $\theta = 240°$, $x'/a = 0.25$ and $z'/a = 0.0$ showing steadiness of the four-cell flow.

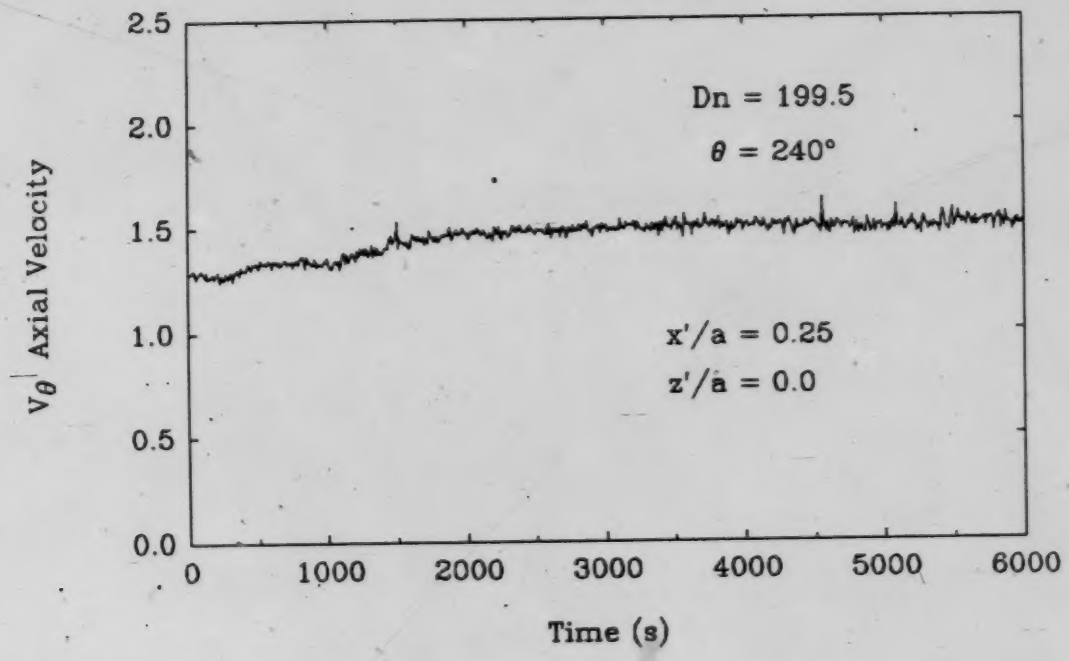

Figure 8.5: Time record of measured axial velocity at $Dn = 199.5$, $\theta = 240°$, $x'/a = 0.25$ and $z'/a = 0.0$ showing heat transfer related time dependence.

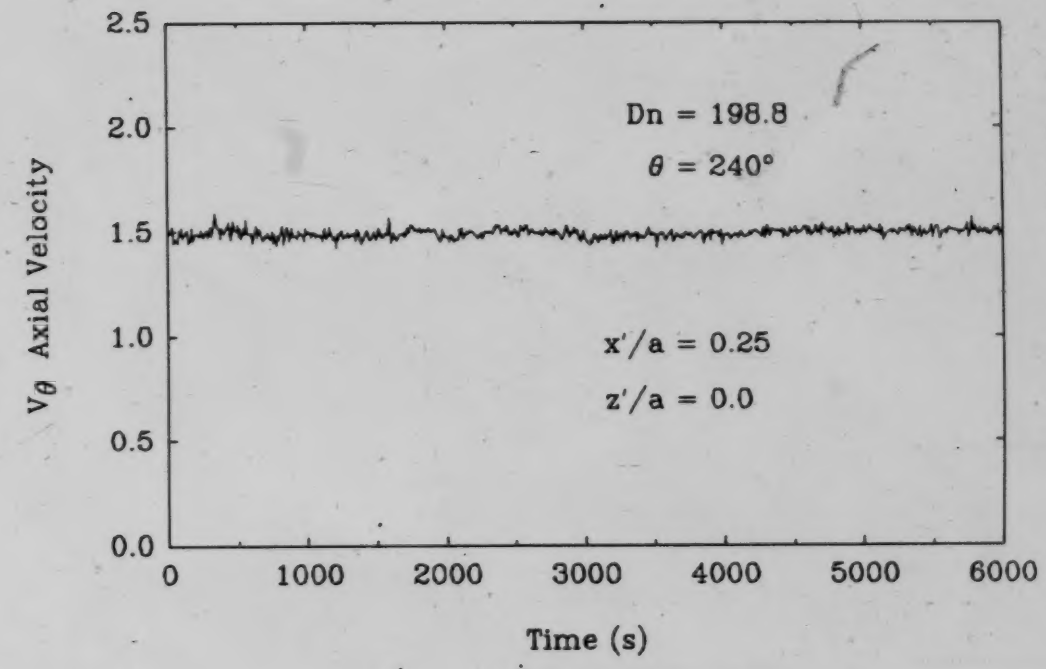

Figure 8.6: Time record of measured axial velocity at $Dn = 198.8$, $\theta = 240°$, $x'/a = 0.25$ and $z'/a = 0.0$ showing steadiness of an asymmetric four-cell flow.

Figure 8.7: Flow visualization of secondary flow patterns at $Dn = 150$ and $\theta = 220°$ showing asymmetry introduced into flow structure by warming inlet section with observer's hand.

8.2 Numerical Investigation of Flow Behavior at Large Axial Distances

In the experimental apparatus used in this study, measurement of the flow development was limited to an axial length of around 240°. This amount of development length was not sufficient to determine the ultimate state of the four-cell flows. Therefore, in order to conjecture what might happen, a numerical investigation of the flow development to large axial lengths was performed. Figures 8.8 through 8.12 show state diagrams of the numerically simulated flow development at $Dn = 125, 130, 137, 150$ and 200 respectively.

In figure 8.8, it is seen that at $Dn = 125$ the flow remains axially invariant after $\theta \approx 100°$. It is not surprising that the two-cell flow remains axially invariant, since it is supposedly stable to any arbitrary perturbation. In contrast, the four-cell flows at $Dn = 130, 137, 150$ and 200, shown in figures 8.9 through 8.12 respectively, eventually develop a spatial oscillation in the axial direction. The frequency of these oscillations increased as the Dean number was increased. As shown by Sankar *et al.* (1988), these oscillations are not a numerical artifact. They repeated some calculations with different axial step sizes and cross plane grid resolution and found that the nature of the oscillations and periods were sustained.

The oscillations in the axial velocity are a result of oscillations in the additional pair of vortices at the outer wall. Figures 8.14 through 8.16 show arrow plots of the secondary flow corresponding to the one cycle of the axial velocity shown in figure 8.13. From the arrow plots it is seen that the additional vortex pair starts to show a slight asymmetry beyond $\theta = 600°$. This is evident at $\theta = 620°$ to $\theta = 660°$ from the direction of the secondary velocity vectors near the outer wall on the horizontal line of symmetry. For a symmetric flow the velocity vectors would be purely radial,

but in this case a small vertical component in the downward direction is starting to appear. The arrow plots from $\theta = 680°$ to $\theta = 780°$ reveal the growing asymmetry in the additional vortex pair as they move downward in the cross section. The top cell appears to increase in size slightly while the bottom cell is compressed into the corner. The increase in axial velocity between $\theta = 600°$ and $\theta = 780°$, in the state diagram of figure 8.13, reflects the growing asymmetry of the additional vortex pair.

In the region from $\theta = 800°$ to $\theta = 860°$, the additional vortex pair disappears into the bottom vortex of the larger pair. By $\theta = 920°$ the larger vortex pair has readjusted to what appears to be a symmetric two-cell flow. The axial velocity at $\theta = 920°$, as seen in the state diagram of figure 8.13, has a value that is typical of a two-cell flow. After $\theta = 920°$, the additional vortex pair reappears and continues to grow in size until $\theta = 1040°$. As in the previous case, a slight asymmetry in the additional vortex pair at $\theta = 1040°$ is evident in the secondary velocity vectors near the outer wall on the horizontal line of symmetry. In contrast to the arrow plot at $\theta = 620°$, the secondary velocity vectors at $\theta = 1040°$ now reveal a small vertical component in the upward direction. Following the flow development to $\theta = 1200°$, it is seen that the asymmetry in the additional vortex pair grows as before. However, the movement of the cells is now toward the top of the duct.

Monitoring the axial velocity on the horizontal line of symmetry does not reveal that the additional vortex pair alternately moves up and down in the cross section. Figure 8.17 shows that, by monitoring the vertical velocity on the horizontal line of symmetry, a period of twice the length is found. Monitoring the radial velocity on the horizontal line of symmetry will also produce the same period as the axial velocity and obscure the fact that the vortices move up and down. Sankar *et al.* (1988) monitored both the axial and radial velocity on the horizontal line of symmetry, and as a result missed the fact that the additional vortices alternately move up and

down.

The oscillation of the flow between a two-cell and four-cell state is consistent with the fact that there is no stable two-dimensional flow predicted in the region immediately beyond the limit point of the two-cell to four-cell transition. Once the limit point is exceeded and a four-cell flow develops, numerical round-off introduces asymmetries which cause the additional vortex pair at the outer wall to experience a spatial oscillation. This behavior agrees with Winters (1987) prediction that four-cell flows are unstable to asymmetric perturbations. In the work of Sankar *et al.* (1988), they found that their four-cell flows at $Dn = 200$, for curvature ratios $R_c = 4$ and $R_c = 10$, remained axially invariant up to $\theta = 2500°$. However, after rerunning their simulations for larger axial lengths, it was found that sustained oscillations appeared.

In the state diagram of figure 8.18, the numerical simulation shows that at $Dn = 250$ the flow appears to eventually develop into an axially invariant two-cell state. The numerical study of Winters (1987) revealed that an isolated two-cell branch exists at this higher Dean number, so it is possible that the flow has been attracted to this state. Winters also predicted that the isolated two-cell branch was stable to any arbitrary perturbation. The breakdown of the four-cell flow to what appears to be an axially invariant two-cell state in figure 8.18, is consistent with the solution structure and stability characteristics predicted by Winters.

The above phenomena of a four-cell flow giving way to a stable two-cell flow also happens in the dual solution region between $Dn \simeq 114$ and $Dn \simeq 130$. Figure 8.19 shows the numerical prediction of flow development at $Dn = 110$, 125 and 137 with a four-cell flow inlet profile. The inlet profile used was the axially invariant four-cell profile calculated in the flow development simulation at $Dn = 150$. At $Dn = 110$, the two-cell flow is the unique solution to the two-dimensional equations, so the flow

quickly evolves to the two-cell state. After an initial adjustment region, the four-cell flow at $Dn = 125$ is axially invariant for about 500° before giving way to a two-cell flow. The use of a four-cell flow as the inlet profile was the only way that the dual solutions could be observed with the three-dimensional numerical formulation. The familiar spatial oscillation is again seen at $Dn = 137$, once the limit point of the two-cell to four-cell transition is exceeded.

The numerical investigation of flow development confirms the prediction that four-cell flows are unstable to asymmetric perturbations. In the regions of dual solutions, it was seen that the four-cell flow would give way to an axially invariant two-cell flow. If the axial length was sufficient in the experimental apparatus used in this study, it is plausible that the four-cell flows in the dual solution region (i.e. $Dn \simeq 114$ to $Dn \simeq 130$) would be observed to give way to two-cell flows. For Dean numbers higher than $Dn \simeq 130$, the flows might develop spatial oscillations or time dependence, or even some combination of the two. In the numerical study of Finlay *et al.* (1988) for flow in a curved channel, they found that travelling waves developed in the streamwise direction at higher Reynolds numbers. Their observation suggests that the same type of phenomena might be possible in a curved duct of finite aspect ratio. It must be kept in mind that the three-dimensional numerical formulation used in this study could not model time dependence, so the instabilities in the four-cell flows were forced to show up as spatial oscillations.

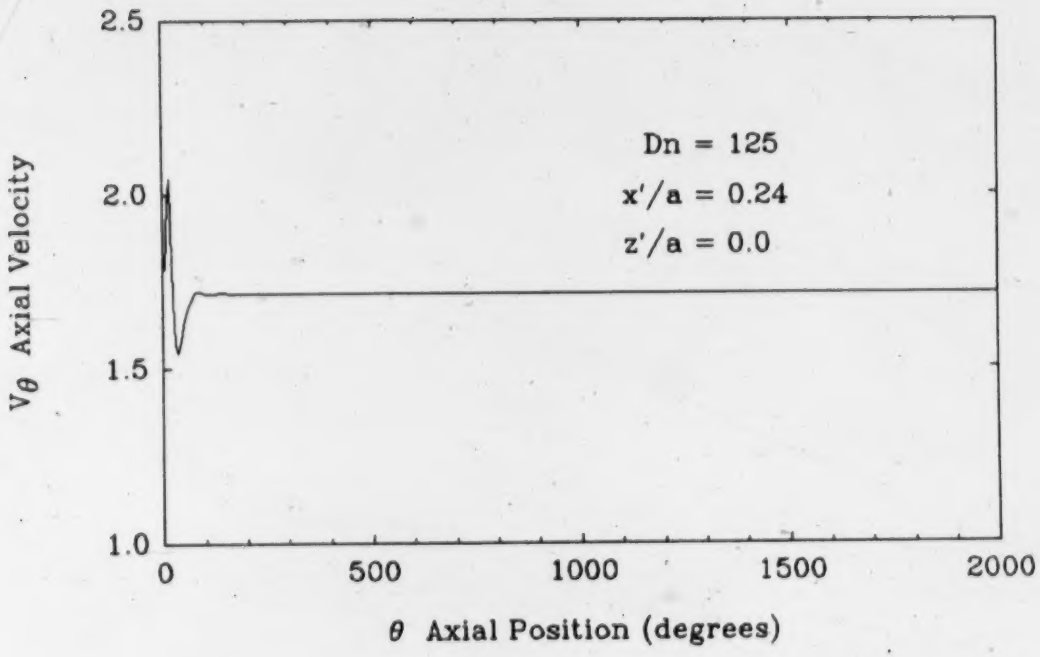

Figure 8.8: Numerically calculated state diagram, with axial velocity at $x'/a = 0.24$ and $z'/a = 0.0$ as the state variable, showing flow development to $\theta = 2000°$ at $Dn = 125$.

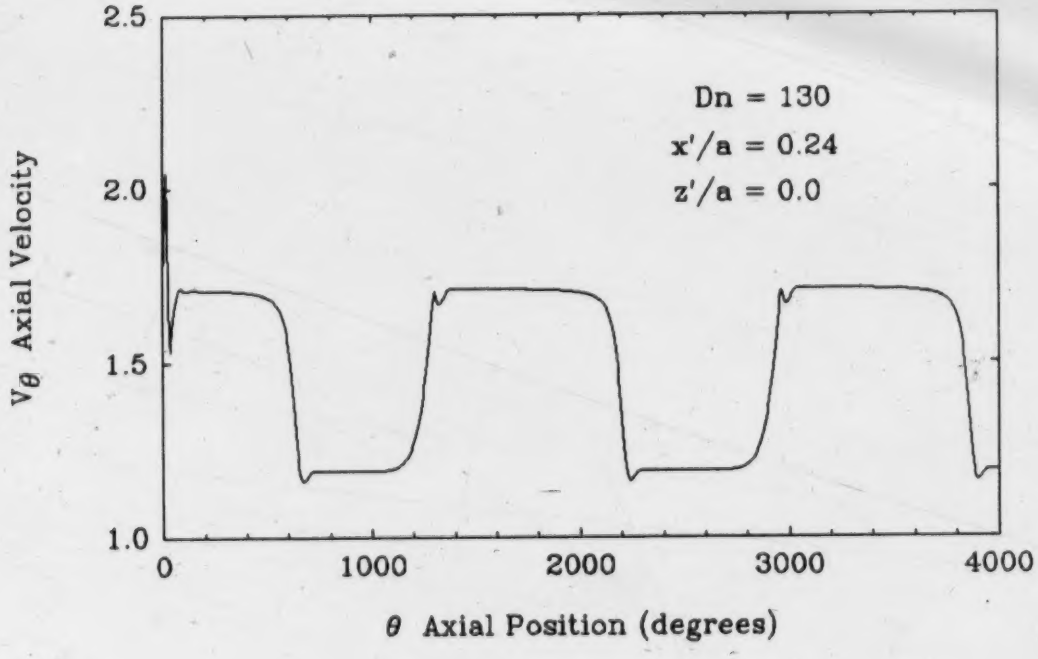

Figure 8.9: Numerically calculated state diagram, with axial velocity at $x'/a = 0.24$ and $z'/a = 0.0$ as the state variable, showing flow development to $\theta = 4000°$ at $Dn = 130$.

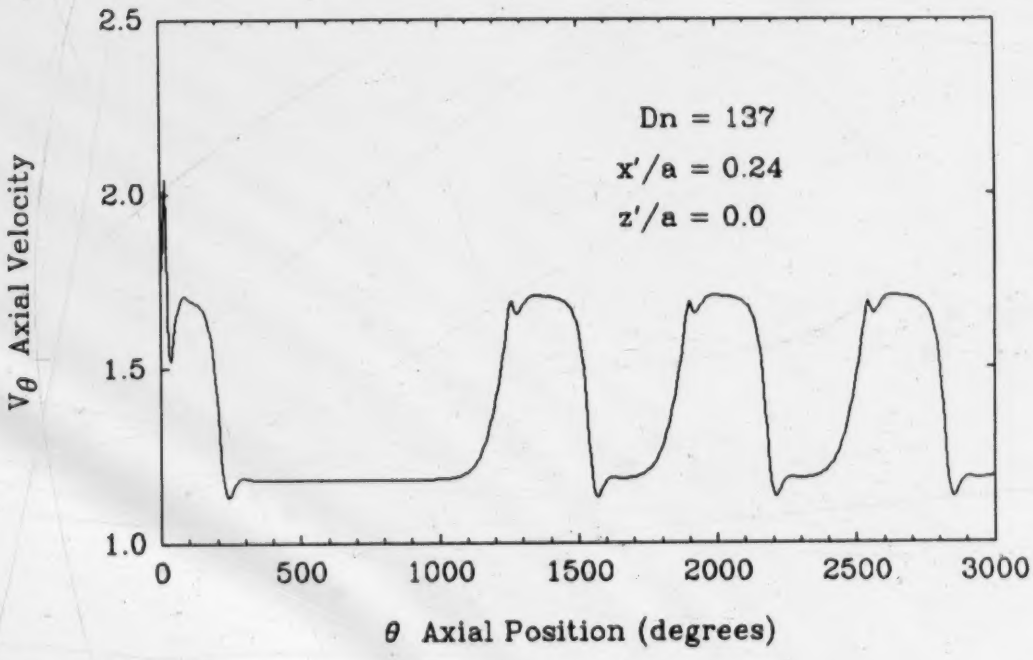

Figure 8.10: Numerically calculated state diagram, with axial velocity at $x'/a = 0.24$ and $z'/a = 0.0$ as the state variable, showing flow development to $\theta = 3000°$ at $Dn = 137$.

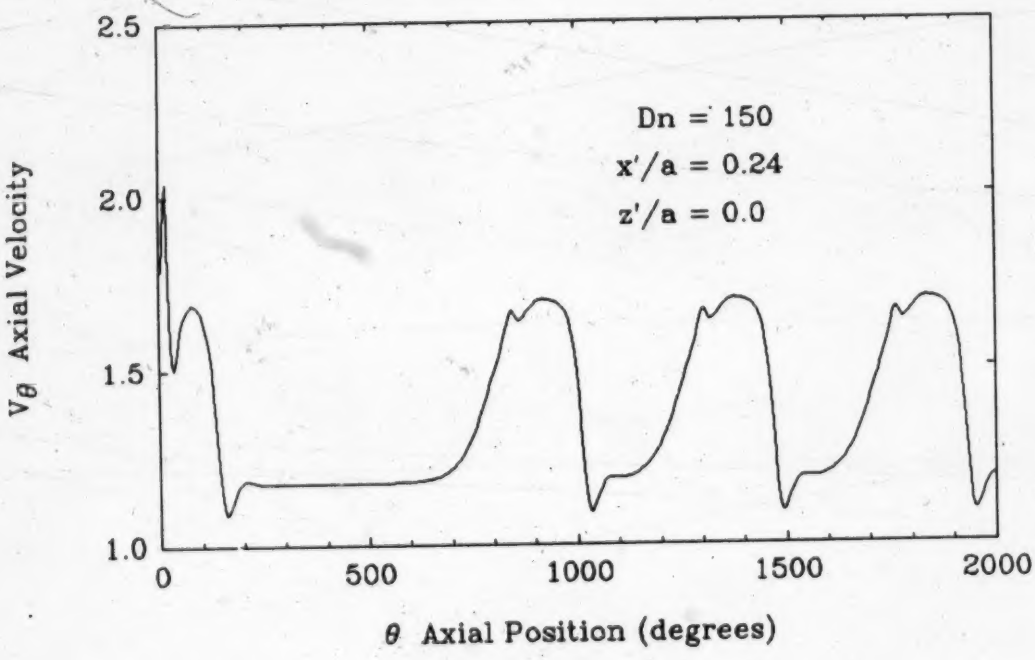

Figure 8.11: Numerically calculated state diagram, with axial velocity at $x'/a = 0.24$ and $z'/a = 0.0$ as the state variable, showing flow development to $\theta = 2000°$ at $Dn = 150$.

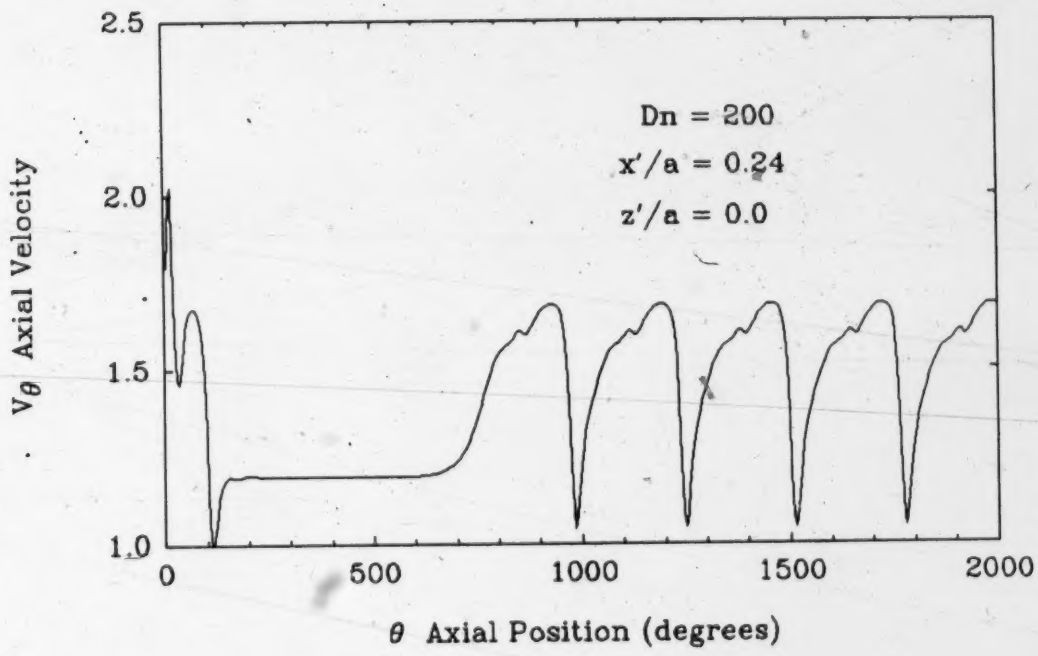

Figure 8.12: Numerically calculated state diagram, with axial velocity at $x'/a = 0.24$ and $z'/a = 0.0$ as the state variable, showing flow development to $\theta = 2000°$ at $Dn = 200$.

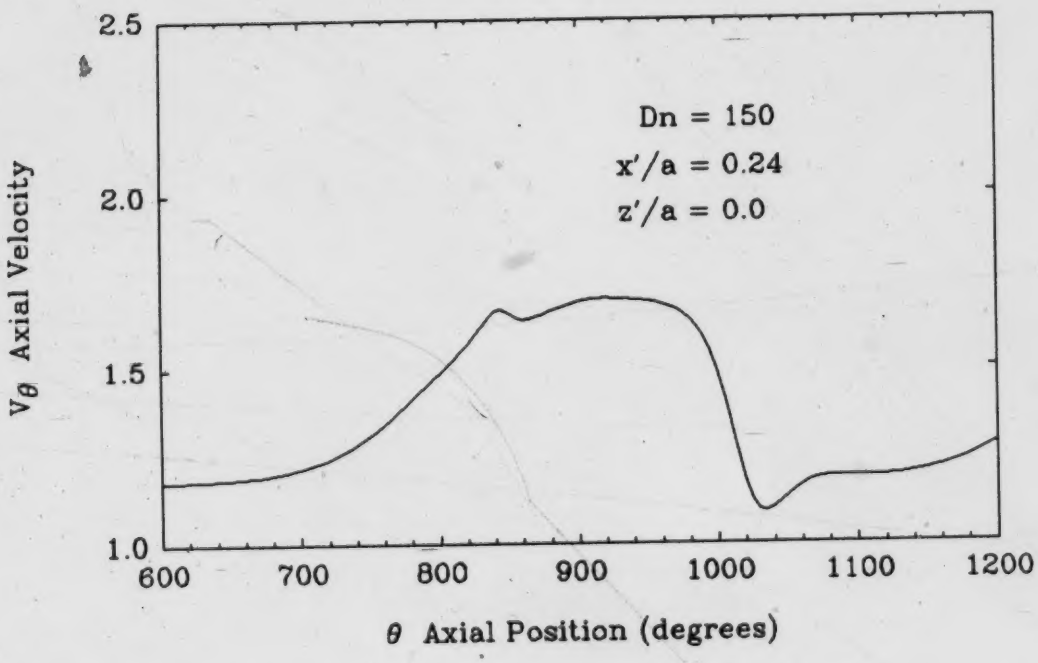

Figure 8.13: Numerically calculated state diagram, with axial velocity at $x'/a = 0.24$ and $z'/a = 0.0$ as the state variable, showing spatial oscillation between $\theta = 600°$ and $\theta = 1200°$ at $Dn = 150$.

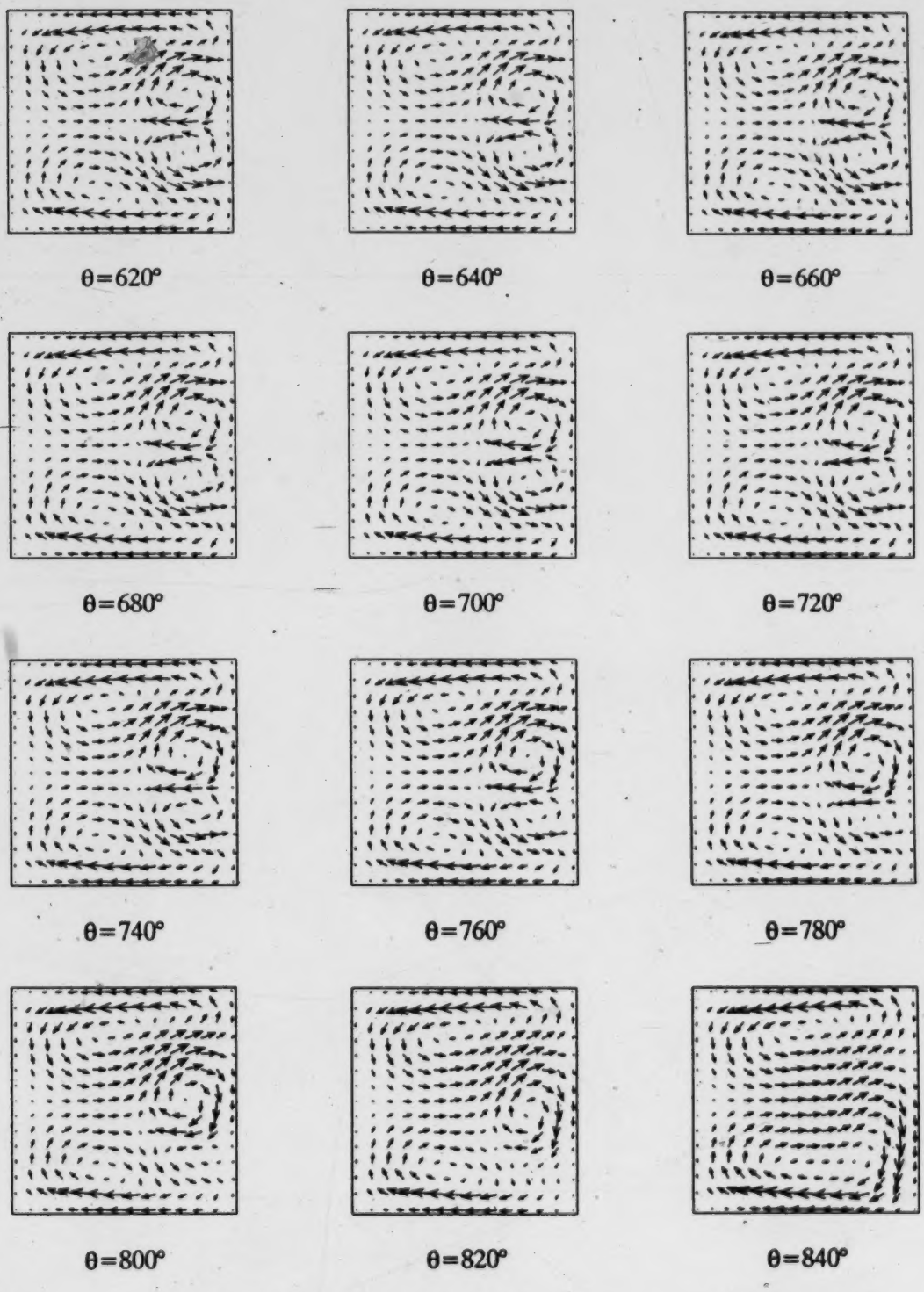

Figure 8.14: Arrow plots of the spatial oscillation at $Dn = 150$ showing the development of the secondary flow between $\theta = 620°$ and $\theta = 840°$.

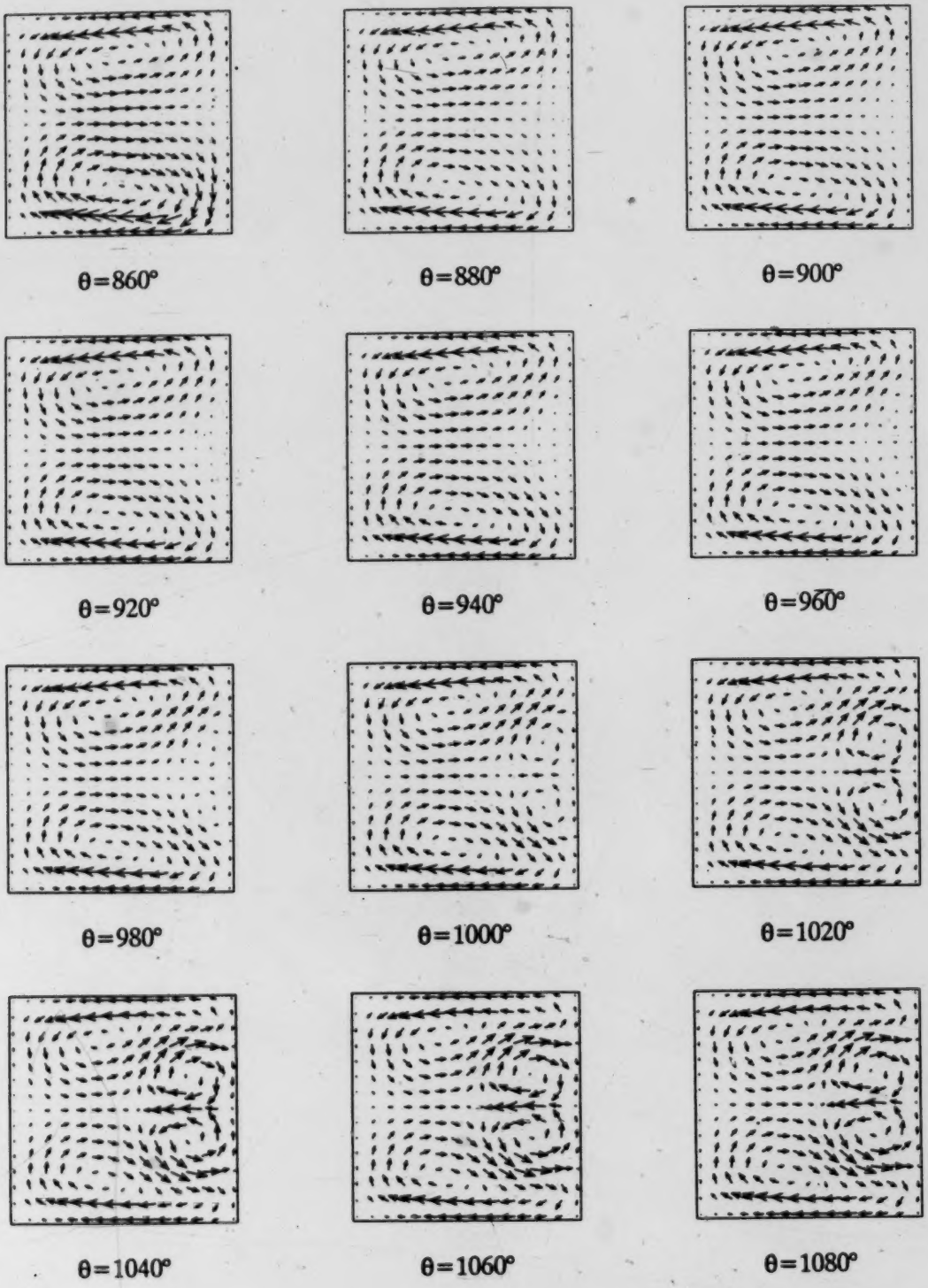

Figure 8.15: Arrow plots of the spatial oscillation at $Dn = 150$ showing the development of the secondary flow between $\theta = 860°$ and $\theta = 1080°$.

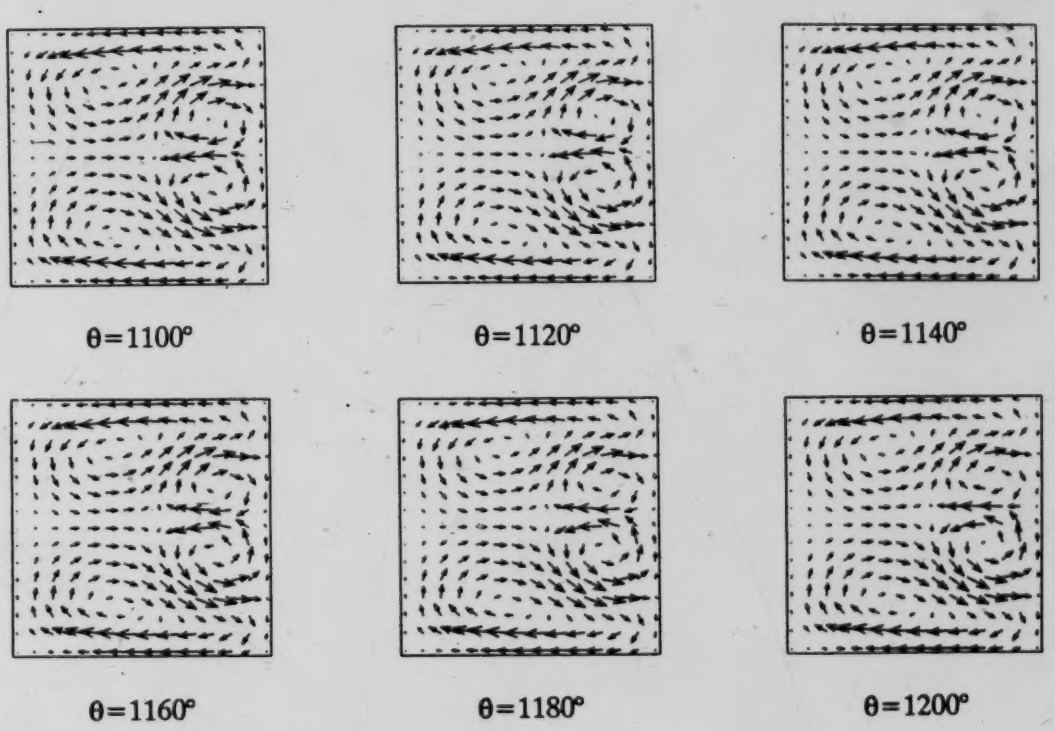

Figure 8.16: Arrow plots of the spatial oscillation at $Dn = 150$ showing the development of the secondary flow between $\theta = 1100°$ and $\theta = 1200°$.

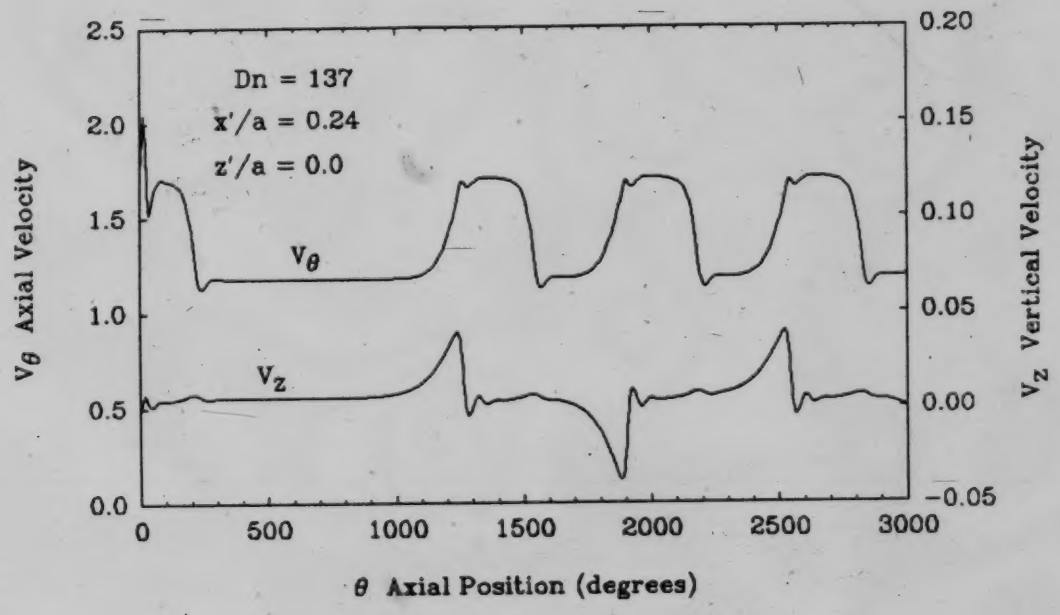

Figure 8.17: Numerically calculated state diagrams, with axial and vertical velocity at $Dn = 137$, $x'/a = 0.24$ and $z'/a = 0.0$ as the state variables, showing a comparison of the periods of oscillation in the axial and vertical directions.

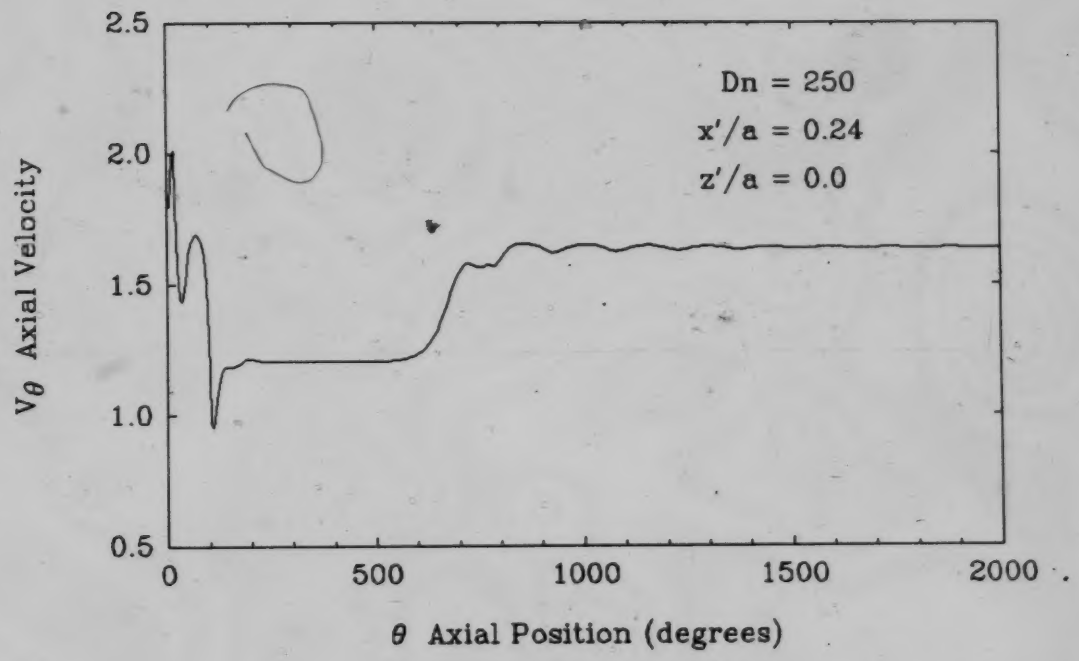

Figure 8.18: Numerically calculated state diagram, with axial velocity at $x'/a = 0.24$ and $z'/a = 0.0$ as the state variable, showing flow development to $\theta = 2000°$ at $Dn = 250$.

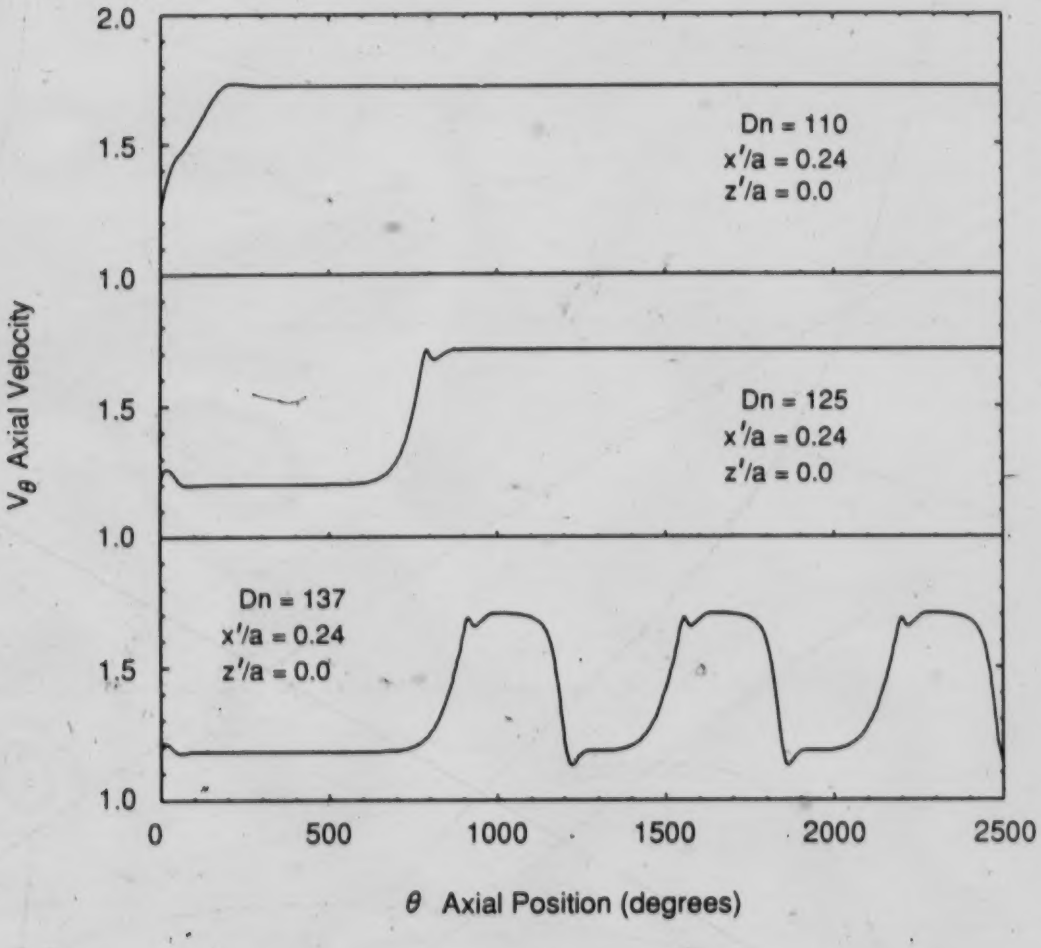

Figure 8.19: Numerically calculated state diagram, with axial velocity at $x'/a = 0.24$ and $z'/a = 0.0$ as the state variable, showing flow development to $\theta = 2500°$ at $Dn = 110$, 125 and 137 with a developed four-cell flow as the inlet condition.

8.3 Response of Flow to Asymmetric Inlet Perturbations

In chapter seven, it was shown that a symmetric perturbation decreased the development length of a four-cell flow without destroying the symmetry of the additional vortex pair. This confirmed that the four-cell flows were stable to symmetric perturbations. The numerical investigation of the previous section showed that, given enough axial length, asymmetries will develop and cause spatial oscillations. However, there is still some doubt as to how the flow will behave in the real situation. In order to study this, asymmetric perturbations were deliberately introduced at the inlet of the experimental apparatus in the hope of observing some far downstream behavior within the axial length of the apparatus.

In order to gain some insight into the effect of an asymmetric perturbation at the inlet, a numerical simulation was performed. Figure 8.20 shows a state diagram of the flow development at $Dn = 150$ for an asymmetric perturbation at $\theta = 5°$. The asymmetric perturbation was accomplished by setting the axial and radial velocities at $z'/a = 0.034$ to zero. This was done at all grid points across the width of the duct (i.e $-0.5 \leq x'/a \leq 0.5$). The simulation reveals that an asymmetric perturbation at the inlet results in the earlier appearance of the sustained spatial oscillations. It is easy to imagine that for different degrees of asymmetry in the inlet perturbation, the axial position of the spatial oscillations would correspondingly shift. Therefore, the spatial oscillation could be observed at one axial location by shifting the axial position of the oscillation with different asymmetric perturbations. The slight difference in the detail of an oscillation, between the dashed line and solid line, is an effect that has been solely introduced by the plotting package.

Varying degrees of asymmetry were introduced in the experimental apparatus by

rotating the pin. Small rotations of the pin, resulting in small vertical movements of the pin, broke the symmetry of the flow about the horizontal centerline (i.e $z'/a = 0.0$). In figure 8.21, flow visualization of the secondary flow patterns at $Dn = 133.9$ and $\theta = 220°$ show the patterns for various perturbations at $\theta = 5°$. As expected, with no perturbation at $\theta = 5°$, a developing four-cell flow is observed at $\theta = 220°$. Also, a symmetric perturbation at $\theta = 5°$ resulted in a developed four-cell flow at $\theta = 220°$. The three asymmetric perturbations, identified as 1, 2 and 3, have an increasing degree of asymmetry associated with them. This can be seen from the vertical profiles of axial velocity at $\theta = 20°$ presented in figure 8.22. The small difference between the axial velocity profiles of the symmetric perturbation and asymmetric perturbation #1, reveals the sensitivity of the secondary flow pattern observed at $\theta = 220°$ to the position of the pin.

From figure 8.21 it is seen that the three asymmetric perturbations cause an increasing asymmetry of the additional vortex pair at $\theta = 220°$ until they finally disappear into the top vortex. The progression actually happens in space. However, by manipulation of the pin at $\theta = 5°$ the progression can be observed at one axial location. Using the portable laser light sheet, the increasing asymmetry in the additional vortex pair and its subsequent disappearance into the larger vortex, as shown in figure 8.21, was observed within an axial length of about 40°. This is in very good agreement with the behavior shown by the three arrow plots at $\theta = 800°$ to $\theta = 840°$ in figure 8.14. The secondary flow structures at $\theta = 220°$, caused by the asymmetric perturbations, did not display any time dependence. This confirms that within the axial length of the experimental apparatus, there exists a spatial variation that resembles the numerically predicted spatial oscillation.

For the condition of an asymmetric trip at $\theta = 5°$, figure 8.23 shows a comparison between the experimentally measured state diagram of flow development

at $Dn = 137$ and the corresponding numerical prediction. The top graph shows that the asymmetric perturbation in the numerical simulation does not model the asymmetric perturbation caused by the pin in the experiment. The same inability to model the pin was observed for the case of the symmetric pin in figure 7.5. However, by shifting the numerically predicted curve 225° to the left, as shown in the bottom graph of figure 8.23, the numerical prediction agrees quite well with the measured data. The fact that part of a spatial oscillation is observable in the experimental apparatus suggests that they might exist for large axial lengths. However, without sufficient axial length to verify this, the state of the four-cell flow at large axial distances still remains an unknown.

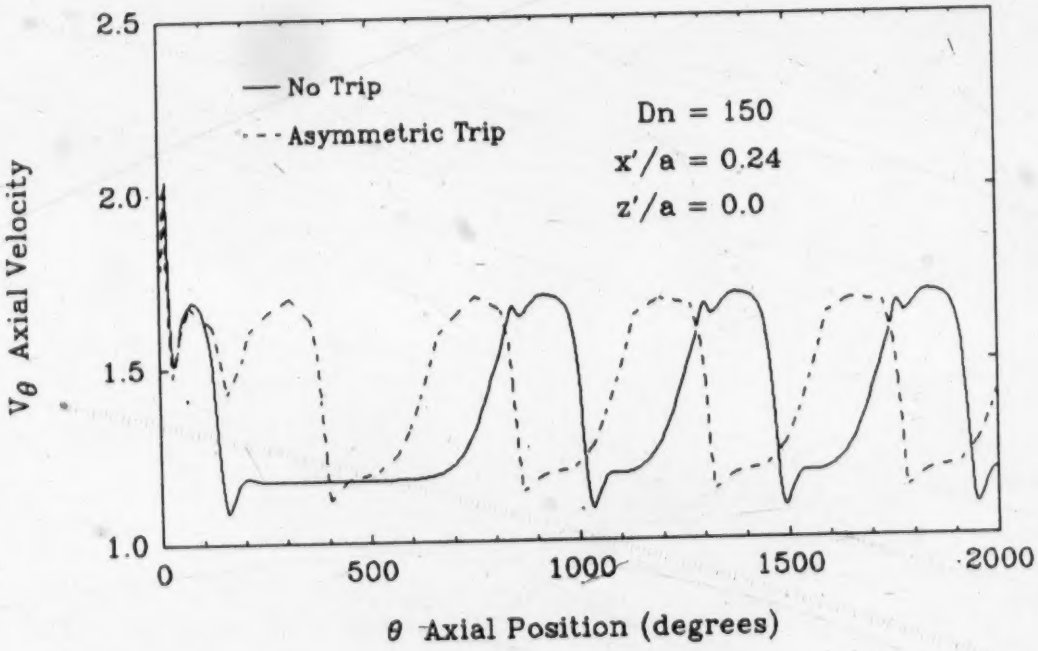

Figure 8.20: Numerically calculated state diagram, with axial velocity at $Dn = 150$, $x'/a = 0.24$ and $z'/a = 0.0$ as the state variable, showing flow development with and without an asymmetric perturbation at $\theta = 5°$.

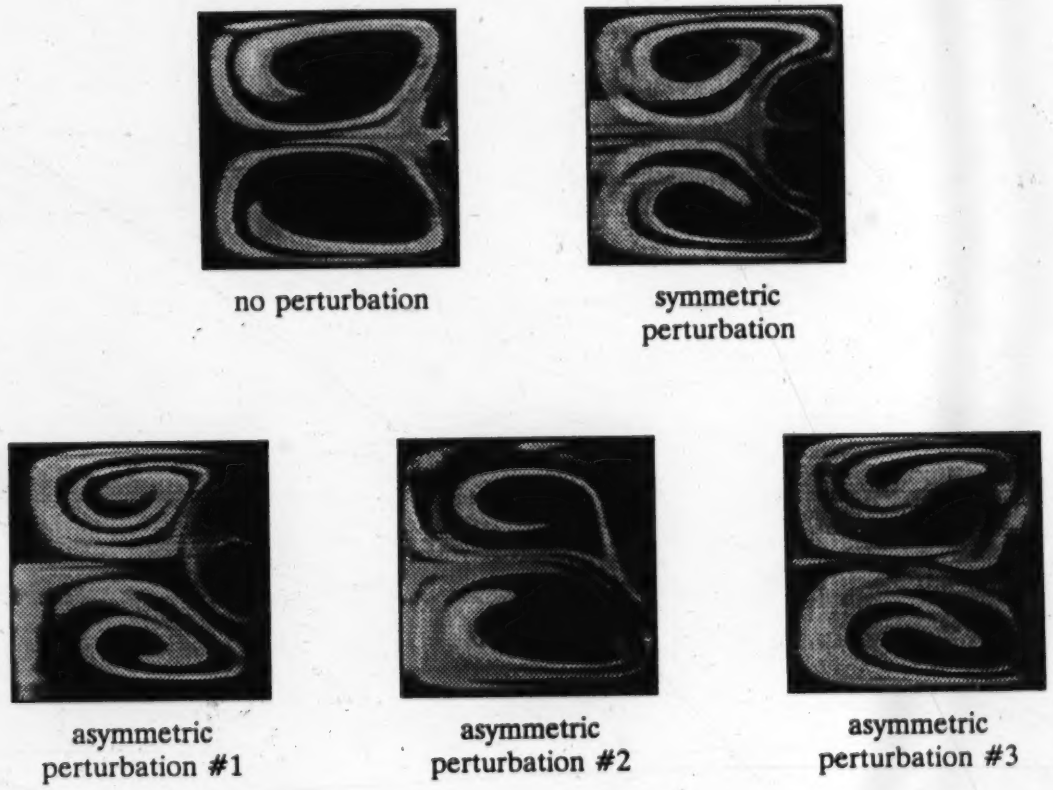

Figure 8.21: Flow visualization of secondary flow patterns at $Dn = 133.9$ and $\theta = 220°$ showing effect of different perturbations at $\theta = 5°$.

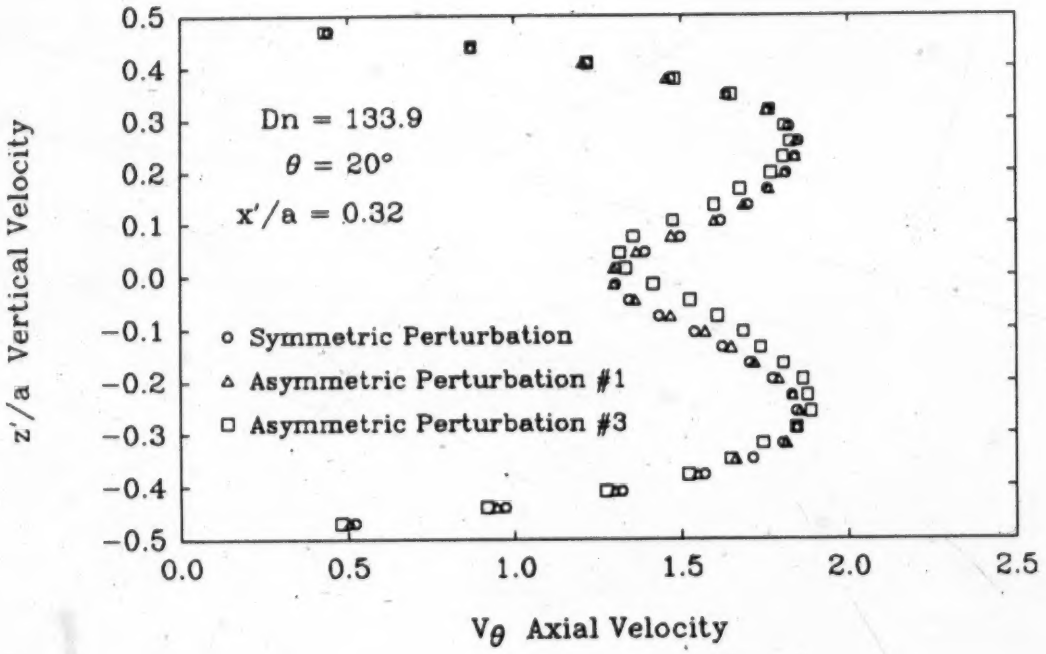

Figure 8.22: Vertical profiles of axial velocity measured at $Dn = 133.9$, $\theta = 20°$ and $x'/a = 0.32$ showing degree of asymmetry in axial velocity profile for different perturbations.

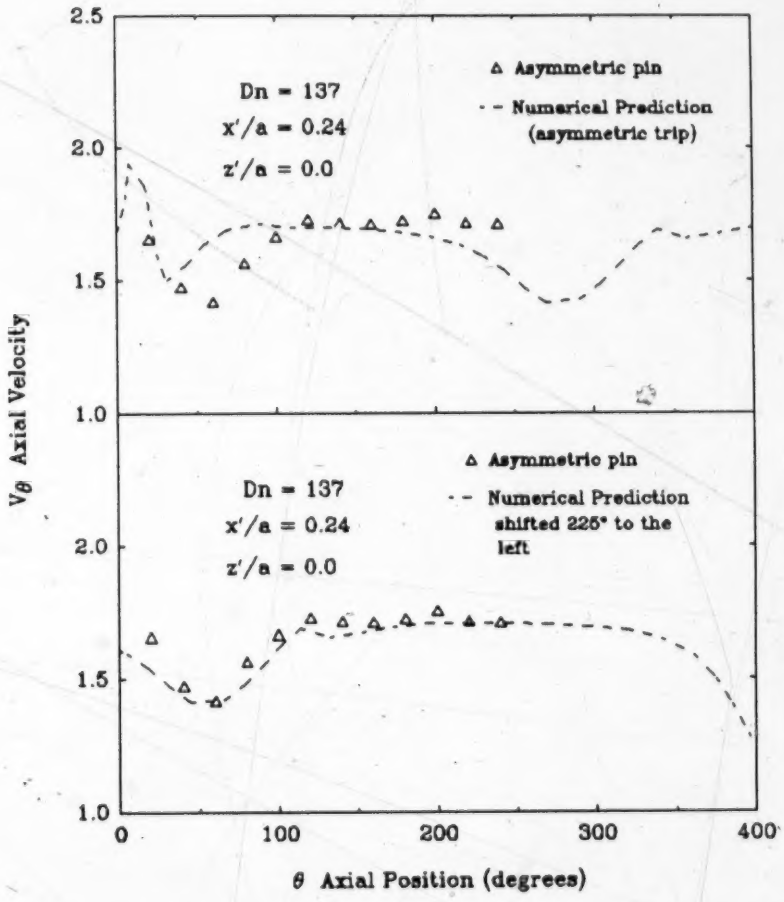

Figure 8.23: Measured state diagram, with axial velocity at $Dn = 137$, $x'/a = 0.24$ and $z'/a = 0.0$ as the state variable, compared to the numerically calculated state diagram with an asymmetric perturbation at $\theta = 5°$ (in bottom graph the numerical curve has been shifted 225° to the left in order to line up with the measured data).

Chapter 9

Conclusions and Recommendations

Axial velocity profiles of flow development were measured every 20° up to an axial length of $\theta = 240°$ at $Dn = 125$, 137 and 150 for a square duct of curvature ratio, $R_c = 15.1$. As expected, the flow at $Dn = 125$ developed into a symmetric two-vortex flow. Measurement of vertical velocity profiles and flow visualization confirmed the symmetry of the flow. At $Dn = 150$, the flow developed into the symmetric four-vortex state that was predicted by the steady two-dimensional Navier-Stokes equations. Flow visualization and measured vertical velocity profiles verified that the flow was symmetric. The axial velocity measurements and flow visualization at $Dn = 137$ revealed that by $\theta = 240°$ the flow had not yet developed to the state predicted by the two-dimensional equations. Numerical simulations of the flow development at $Dn = 125$, 137 and 150, using a steady three-dimensional parabolized formulation of the Navier-Stokes equations, were in good agreement with the measured axial velocities. Measurement of a developing four-vortex flow to its fully developed state (i.e. at $Dn = 150$) was accomplished for the first time in

this study. Also, the discovery of the decrease of development length with increasing Dean number for the four-vortex flows has not been previously reported.

Given that the development length of the four-cell flows decreased with increasing Dean number, a numerical investigation for Dean numbers below $Dn = 175$ was performed to reveal more detail. At the limit point of the two-cell to four-cell transition the development length appeared to be infinite, while at $Dn = 175$ the development length was calculated to be about 165°. The faster development of the additional vortices for a larger centrifugal force (i.e. larger Dn), is consistent with the suggestion of Cheng *et al.* (1976) that the formation of the additional vortex pair is due to a centrifugal instability.

Using a symmetrically positioned pin at $\theta = 5°$ to induce the four-cell flows, it was shown for the first time that the predicted symmetric two-dimensional solution structure for $Dn \leq 150$ could be experimentally observed. The pin reduced the development length of the four-cell flows, allowing the two-dimensional solutions to be observed within the 240° axial length of the experimental apparatus. The experimentally determined limit points of the two-cell to four-cell transition and the four-cell to two-cell transition were in good agreement with the numerically predicted values of $Dn \simeq 131$ and $Dn \simeq 114$ respectively. Axial velocity profiles and flow visualization were taken of a dual solution at $Dn = 123.4$.

Winters (1987) numerical prediction that four-cell flows are stable to symmetric perturbations, but unstable to asymmetric perturbations, was experimentally confirmed for the first time. The fact that a symmetrically positioned pin was able to induce a symmetric four-cell flow showed that a four-cell flow was stable to a symmetric perturbation. If the pin was not positioned symmetrically (i.e. asymmetric perturbation), a symmetric four-cell flow could not be observed. Given that four-cell flows were unstable to asymmetric perturbations, a numerical study

was performed to determine what might happen to the flow at large axial lengths. The numerical simulation suggested that, in the regions where there were no stable two-dimensional solutions, the four-cell flows would develop to a state involving sustained spatial oscillations. In a dual solution region, the numerical simulations showed that the four-cell flow would give way to a stable two-cell flow. An experimental investigation showed the existence of a time-independent spatial variation resembling the initial part of a spatial oscillation. The spatial variation was observed within the axial length of the apparatus by deliberately inserting asymmetric perturbations at $\theta = 5°$. This suggests that a sustained spatial oscillation might be observed farther downstream.

9.1 Future Studies

Given that the four-cell flows are unstable to asymmetric perturbations, the question as to what happens to the flows farther downstream still exists. The parabolized steady three-dimensional equations used for the numerical simulations were restricted to show instabilities in space, so they could not predict any time dependent motions. Even though no time dependence was observed in the flows measured within the axial length of the experimental apparatus, it is possible that the unstable four-cell flows might develop time dependence farther downstream. It would be expected that the growth rate of the asymmetric disturbances would increase with increasing Dean number. Therefore, experiments at higher Dean numbers might show time dependence within the axial length of the present apparatus. In order to numerically determine time-dependent behavior, a numerical formulation would be required that retained the time dependant terms.

In order to confirm the existence of spatial oscillations, an experimental

apparatus with a longer axial length is required. For the axial lengths required to observe a complete spatial oscillation, a helically coiled duct would have to be used. If the pitch of the helix was kept low, the asymmetry introduced by the pitch should not drastically affect the qualitative behavior of the flow.

9.2 Equipment Improvements

The factor that caused the largest source of error in the velocity measurements was the inaccuracy in positioning the crossing point in the duct cross section. Traversing the experiment while holding the crossing point stationary and not being able to accurately locate the duct walls resulted in the positioning problem. Given the velocity gradients that existed in the radial direction, it is easy to see how a small error in position can cause a large error in the measured velocity. In order to improve the positioning accuracy it is essential that the experiment be held stationary and the crossing point traversed. Since determining the location of the walls is critical to the accurate placement of the beam within the cross section, a pin-hole section for the LDV optics would be extremely useful. A pin-hole section would filter unwanted reflections when the crossing point was near the wall, allowing more accurate determination of when the crossing point was actually on the wall.

References

Agrawal Y., Talbot L. and Gong K. (1978) Laser anemometer study of flow development in curved circular pipes. *J. Fluid Mech.* **85** *pp.* 497–518

Akiyama M. (1969) Laminar forced convection heat transfer in curved rectangular channels. M.Sc. Thesis, Mechanical Engineering Department, University of Alberta, Edmonton, Alberta, Canada

Akiyama M. and Cheng K. C.(1971) Boundary vorticity method for laminar forced convection heat transfer in curved pipes. *Int. J. Heat Mass Transfer.* **14** *pp.* 1659–1675

Alder M. (1934) Strömung in gekrümmten Rohren *Z. Angew. Math. Mech.* **14** *pp.* 257–275

Ang A. H-S. and Tang W. H. (1975) *Probability Concepts in Engineering Planning and Design* Volume 1- Basic Principals, John Wiley & Sons.

Austin L. R. and Seader J. D. (1973) Fully developed viscous flows in coiled circular pipes. *AIChE J.* **19** *pp.* 85–94

Austin L. R. and Seader J. D. (1974) Entry region for steady viscous flow in coiled circular pipes. *AIChE J.* **20** *pp.* 820–822

Barua S. N. (1963) On secondary flow in stationary curved pipes. *Q. Jour. Mech. Appl. Math.* **16** *pp.* 61–77

Baylis J. A. (1971) Experiments on laminar flow in curved channels of square cross section. *J. Fluid Mech.* **48** *pp.* 417–422

Beavers G. S., Sparrow E. M. and Magnuson R. A. (1970) Experiments on hydrodynamically developing flow in rectangular ducts of arbitrary aspect ratio. *Int. J. Heat Mass Transfer.* **13** *pp.* 689–702

Benjamin T. B. (1978a) Bifurcation phenomena in steady flows of a viscous fluid, I. Theory. *Proc. R. Soc. Lond. A.* **359** *pp.* 1–26

Benjamin T. B. (1978b) Bifurcation phenomena in steady flows of a viscous fluid, II. Experiments. *Proc. R. Soc. Lond. A.* **359** *pp.* 27–43

Berger S. A., Talbot L. and Yao L-S. (1983) Flow in curved pipes. *Ann. Rev. Fluid Mech.* **15** *pp.* 461–512

Campbell R. (1991) Image processing techniques for analysis of full color turbulent jet images. M.Sc. Thesis, Mechanical Engineering Department, University of Alberta, Edmonton, Alberta, Canada

Cheng K. C. and Akiyama M. (1970) Laminar forced convection heat transfer in curved rectangular channels. *Int. J. Heat Mass Transfer.* **13** *pp.* 471–490

Cheng K. C., Lin R-C. and Ou J-W. (1975) Graetz problem in curved square channels. *Journal of Heat Transfer, Trans. ASME* **97** *pp.* 244–248

Cheng K. C., Lin R-C. and Ou J-W. (1976) Fully developed laminar flow in curved rectangular channels. *Journal of Fluids Engineering, Trans. ASME* **98** *pp.* 41–48

Cheng K. C., Nakayama J. and Akiyama M. (1979) Effect of finite and infinite aspect ratios on flow patterns in curved rectangular channels. *Flow Visualization (Tokyo, Japan, 1977)*, Hemisphere, Washington *pp.* 181–186

Cheng K. C. and Yeun F. P. (1987) Flow visualization studies on secondary flow patterns in straight tubes downstream of a 180 deg bend and in isothermally heated horizontal tubes. *Journal of Heat Transfer, Trans. ASME* **109** *pp.* 49–54

Choi U. S., Talbot L. and Cornet I. (1979) Experimental study of wall shear rates in the entry region of a curved tube. *J. Fluid Mech.* **93** *pp.* 465–489

Collins W. M. and Dennis S. C. R. (1975) The steady motion of a viscous fluid in a curved tube. *Q. J. Mech. Appl. Math.* **28** *pp.* 133–156

Cuming H. G. (1952) The secondary flow in curved pipes. *Aeronaut. Res. Counc. Rep. Mem.*, No. 2880

Daskopoulos P. and Lenhoff A. M. (1989) Flow in curved ducts: bifurcation structure for stationary ducts. *J. Fluid Mech.* **203** *pp.* 125–148

Dean W. R. (1927) Note on the motion of fluid in a curved pipe. *Phil. Mag. Ser.* **7**, *Vol.* **4**, *No.* **20** *pp.* 208–223

Dean W. R. (1928a) The stream-line motion of fluid in a curved pipe. *Phil. Mag. Ser.* **7**, *Vol.* **5**, *No.* **30** *pp.* 673–695

Dean W. R. (1928b) Fluid motion in a curved channel. *Proc. Roy. Soc. London A* **121** *pp.* 402–420

Dean W. R. and Hurst, J. M. (1959) Note on the motion of fluid in a curved pipe. *Mathematika* **6** *pp.* 77–85

Dennis S. R. C. (1980) Calculation of the steady flow through a curved tube using a new finite difference method. *J. Fluid Mech.* **99** *pp.* 449–467

Dennis S. R. C. and Ng M. (1982) Dual solutions for steady laminar flow through a curved tube. *Q. J. Mech. Appl. Math.* **35** *pp.* 305–324

Drain L. E. (1980) *The Laser-Doppler Technique* Wiley, New York.

Durst F., Melling A. and Whitelaw J. H. (1976) *Principals and Practice of Laser-Doppler Anemometry* Academic Press

Eustice J. (1910) Flow of water in curved pipes. *Proc. Roy. Soc. London A* **84** *pp.* 107–118

Eustice J. (1911) Experiments on stream-line motion in curved pipes. *Proc. Roy. Soc. London A* **85** *pp.* 119–131

Eustice J. (1925) Flow of fluids in curved passages. *Engineering* Nov. 13, 1925 *pp.* 604–605

Fearn R. M., Mullin T. and Cliffe K. A. (1990) Nonlinear flow phenomena in a symmetric sudden expansion. *J. Fluid Mech.* **211** *pp.* 595–608

Finlay W. H., Keller J. B. and Ferziger J. H. (1988) Instability and transition in curved channel flow. *J. Fluid Mech.* **194** *pp.* 417–456

Ghia K. N. and Sokhey J. S. (1977) Laminar incompressible viscous flow in curved ducts of regular cross-section. *Journal of Fluids Engineering, Trans. ASME* **99** *pp.* 640–648

Goldstein R. J. and Kreid D. K. (1967) Measurement of laminar flow development in a square duct using a laser-doppler flowmeter. *Journal of Applied Mechanics, Trans. ASME* **34** *pp.* 813–818

Greenspan A. D. (1973) Secondary flow in a curved tube. *J. Fluid Mech.* **57** *pp.* 167–176

Hawthorne W. R. (1951) Secondary circulation in fluid flow. *Proc. Roy. Soc. London A* **206** *pp.* 374–387

Hille P., Vehrenkamp R. and Schulz-Dubois E. O. (1985) The development and structure of primary and secondary flow in a curved square duct. *J. Fluid Mech.* **151** *pp.* 219–241

Humphrey J. A. C., Taylor A. M. K. and Whitelaw J. H. (1977) Laminar flow in a square duct of strong curvature. *J. Fluid Mech.* **83** *pp.* 509–527

Humphrey J. A. C. (1978) Numerical calculation of developing laminar flow in pipes of arbitrary curvature radius. *Can. J. Chem. Engng* **56** *pp.* 151–164

Humphrey J. A. C., Iacovides H. and Launder B. E. (1985) Some numerical experiments on developing laminar flow in circular- sectioned bends. *J. Fluid Mech.* **154** *pp.* 357–375

Itō H. (1951) Theory on laminar flows through curved pipes of elliptic and rectangular cross-sections. *Rep. Inst. High Speed Mech., Tohoku Univ., Sendai Jpn.* **1** *pp.* 1–16

Itō H. (1969) Laminar flow in curved pipes. *Z. Angew. Math. Mech.* **11** *pp.* 653–663

Itō H. (1987) Flow in curved pipes. *JSME International Journal* **30** *No.* 262 *pp.* 543–552

Joseph B., Smith E. P. and Alder R. J. (1975) Numerical treatment of laminar flow in helically coiled tubes of square cross section. Part 1. Stationary helically coiled tubes. *AIChE Journal* **21**, *No.* 5 *pp.* 965–974

Kluwick A. and Wohlfahrt H. (1984) Entry flow in weakly curved ducts. *Ingenieur-Archiv* **54** *pp.* 107–120

Kluwick A. and Wohlfahrt H. (1986) Hot-wire-anemometer study of the entry flow in a curved duct. *J. Fluid Mech.* **165** *pp.* 335–353

Koga D. J., Abrahamsom S. D. and Eaton J. K. (1987) Development of a portable laser sheet. *Experiments in Fluids* **5** *pp.* 215–216

Larrain J. and Bonilla C. F. (1970) Theoretical pressure drop in laminar flow of a fluid in a coiled pipe. *Trans. Soc. Reol.* **14** *pp.* 135–147

Ludwieg H. (1951) Die ausgebildete Kanalströmung in einem rotierenden System. *Ingenieur-Archiv* **19** *pp.* 296–308

Manlapaz R. L. and Churchill S. W. (1980) Fully developed laminar flow in a helically coiled tube of finite pitch. *Chem. Eng. Commun.* **7** *pp.* 57–78

Masliyah J. H. (1980) On laminar flow in curved semicircular ducts. *J. Fluid Mech.* **99** *pp.* 469–479

Mori Y. and Nakayama W. (1965) Study on forced convection heat transfer in curved pipes (1st report, laminar region). *Int. J. Heat Mass Transfer.* **8** *pp.* 67–82

Mori Y., Uchida Y. and Ukon T. (1971) Forced convection heat transfer in a curved channel with a square cross section. *Int. J. Heat Mass Transfer.* **14** *pp.* 1787–1805

Nandakumar K. and Masliyah J. H. (1982) Bifurcation in steady laminar flow through curved tubes. *J. Fluid Mech.* **119** *pp.* 475–490

Nandakumar K., Masliyah J. H. and Law H.-S. (1985) Bifurcation in steady laminar mixed convection flow in horizontal ducts. *J. Fluid Mech.* **152** *pp.* 145–161

Nandakumar K. and Masliyah J. H. (1986) Swirling flow and heat transfer in coiled and twisted pipes. *Advances in Transport Processes* Wiley Eastern, New Delhi **4** *pp.* 49–112

Nandakumar K., Raszillier H. and Durst F. (1991) Flow through rotating rectangular ducts. in press *Phys. Fluids A* **3** *pp.* 770–781

Nandakumar K. and Weinitschke H. J. (1991) A bifurcation study of mixed convection heat transfer in horizontal ducts. accepted in *J. Fluid Mech.*

Olson D. E. and Snyder B. (1985) The upstream scale of flow development in curved circular pipes. *J. Fluid Mech.* **150** *pp.* 139–158

Patankar S. V., Pratap V. S. and Spalding D. B. (1974) Prediction of laminar flow and heat transfer in helically coiled pipes. *J. Fluid Mech.* **62** *pp.* 539–551

Pfister G., Schmidt H., Cliffe K. A. and Mullin T. (1988) Bifurcation phenomena in Taylor-Couette flow in a very short annulus. *J. Fluid Mech.* **191** *pp.* 1–18

Sankar S. R., Nandakumar K. and Masliyah J. H. (1986) Mixed convection in heated curved square ducts. *Proceedings of the 4th International Conference on Heat Transfer*, San Francisco (Hemisphere, New York, 1986), Vol. 4, *pp.* 1407–1412

Sankar S. R., Nandakumar K. and Masliyah J. H. (1988) Oscillatory flows in coiled square ducts. *Phys. Fluids* 31 *No.* 6 *pp.* 1348–1358

Sankaraiah M., and Rao Y. V. N. (1973) Analysis of steady laminar flow of an incompressible newtonian fluid through curved pipes of small curvature. *Journal of Fluids Engineering, Trans. ASME* **95** *pp.* 75–80

Schneck H. (1979) *Theories of Engineering Experimentation*, 3rd. edition, McGraw Hill, New York

Schlichting H. (1979) *Boundary-Layer Theory* 7th. edition, McGraw-Hill

Shah R. K. and London A. L. (1978) Laminar flow forced convection in ducts. *Advances in Heat Transfer*, Academic Press

Shanthini W. (1985) Bifurcation phenomena of generalized newtonian fluids in curved rectangular ducts. M.Sc. thesis, Chemical Engineering Department, University of Alberta, Edmonton, Alberta, Canada

Shanthini W. and Nandakumar K. (1986) Bifurcation phenomena of generalized newtonian fluids in curved rectangular ducts. *Journal of Non-Newtonian Fluid Mechanics* **22** *pp.* 35–60

Singh M. P. (1974) Entry flow in a curved pipe. *J. Fluid Mech.* **65** *pp.* 517–539

Smith F. T. (1976) Fluid flow into a curved pipe. *Proc. Roy. Soc. London A* **351** *pp.* 71–87

Soh W. Y. and Berger S. A. (1984) Laminar entrance flow in a curved pipe. *J. Fluid Mech.* **148** *pp.* 109–135

Soh W. Y. (1988) Developing fluid flow in a curved duct of square cross-section and its fully developed dual solutions. *J. Fluid Mech.* **188** *pp.* 337–361

Stewatrson K., Cebeci T. and Chang K. C. (1980) A boundary-layer collision in a curved duct. *Q. J. Mech. Appl. Math.* **33** *pp.* 59–75

Sugiyama S., Hayashi T. and Yamazaki K. (1983) Flow characteristics in the curved rectangular channels (visualization of secondary flow). *Bulletin of the JSME* **26** *pp.* 964–969

Tabarrok B. and Lin R. C. (1978) Laminar flow and heat transfer in curved ducts. *1st International Conference on Numerical Methods in Laminar and Turbulent Flow*

Talbot L. and Wong S. J. (1982) A note on boundary-layer collision in a curved pipe. *J. Fluid Mech.* **122** *pp.* 505–510

Taylor A. M. K. P., Whitelaw J. H. and Yianneskis M. (1982) Curved ducts with strong secondary motion: velocity measurements of developing laminar and turbulent flow. *Journal of Fluids Engineering, Trans. ASME* **104** *pp.* 350–359

Thomson J. (1876) On the origin of windings of rivers in alluvial plains, with remarks on the flow of water round bends in pipes. *Proc. Roy. Soc. London A* **25** *pp.* 5–8

Topakogula, H. C. (1967) Steady state laminar flows of an incompressible viscous fluid in curved pipes. *J. Math. & Mech.* **16** *pp.* 1321–1337

Truesdell L. C. and Adler R. J. (1970) Numerical treatment of fully developed laminar flow in helically coiled tubes. *AIChE J.* **16** *pp.* 1010–1015

Van Dyke M. (1978) Extended stokes series: laminar flow through a loosely coiled pipe. *J. Fluid Mech.* **86** *pp.* 129–145

Weinitschke H. J., Nandakumar K. and Sankar S. R. (1990) A bifurcation study of convective heat transfer in porous media. *Phys. Fluids A* **2** *No.* 6 *pp.* 912–921

Williams, G. S., Hubbell, C. W. and Finkell, G. H. (1902) Experiments at Detroit, Michigan on the effect of curvature on the flow of water in pipes. *Trans. ASCE* **47** *pp.* 1–196

Winters K. H. and Brindley R. C. G. (1984) Multiple solutions for laminar flow in helically-coiled tubes. *AERE Rep.* 11373, AERE Harwell, UK.

Winters K. H. (1987) A bifurcation study of laminar flow in a curved tube of rectangular cross-section. *J. Fluid Mech.* **180** *pp.* 343–369

Yanase S., Goto N. and Yamamoto K. (1988) Stability of dual solutions of the flow in a curved circular tube. *Journal of the Physical Society of Japan* **57** *No.* 8 *pp.* 2602–2604

Yang Z.-H. and Keller H. B. (1986) Multiple laminar flows through curved pipes. *Appl. Num. Maths.* **2** *pp.* 257–271

Yao L.-S. and Berger S. A. (1975) Entry flow in a curved pipe. *J. Fluid Mech.* **67** *pp.* 177–196

Yao L.-S. and Berger S. A. (1978) Flow in heated curved pipes. *J. Fluid Mech.* **88** *pp.* 339–354

Yao L.-S. and Berger S. A. (1988) The three-dimensional boundary layer in the entry region of curved pipes with finite curvature ratio. *Phys. Fluids* **31** *pp.* 486–494

Yarborough J. M. (1974) cw dye laser emission spanning the visible spectrum. *Applied Physics Letters* **24** *No.* 12 *pp.* 629–630

Yee G., Chilukuri R. and Humphery J. A. C. (1980) Developing flow and heat transfer in strongly curved ducts of rectangular cross section. *Journal of Heat Transfer, Trans. ASME* **102** *pp.* 285–291

Yeung W. S. (1980) Laminar boundary-layer flow near the entry of a curved circular pipe. *Journal of Applied Mechanics, Trans. ASME* **47** *pp.* 697–702

Appendix A

Uncertainty Analysis Method

The uncertainty in a variable, X, can be estimated if the equation that governs the variable is known. Given the governing equation, $X = f(A, B, C, D)$, the uncertainty in X can be estimated from the known uncertainties in A, B, C and D. Taking the total derivative of X results in:

$$dX = \frac{\partial f}{\partial A}dA + \frac{\partial f}{\partial B}dB + \frac{\partial f}{\partial C}dC + \frac{\partial f}{\partial D}dD \qquad \text{(A.1)}$$

For small errors dX can be replaced by ΔX to give:

$$\Delta X = \frac{\partial f}{\partial A}\Delta A + \frac{\partial f}{\partial B}\Delta B + \frac{\partial f}{\partial C}\Delta C + \frac{\partial f}{\partial D}\Delta D \qquad \text{(A.2)}$$

Equation A.2 can not be used directly to calculate ΔX, since the signs of the other uncertainties are not known. In order to get around this, both sides of equation A.2 can be squared, allowing the mean square uncertainty to be used. If the quantities A, B, C and D are statistically independent and symmetrically distributed random variables (Schenck, 1979 *p.* 76), the cross products will disappear leaving:

$$(\Delta X)^2 = \left(\frac{\partial f}{\partial A}\Delta A\right)^2 + \left(\frac{\partial f}{\partial B}\Delta B\right)^2 + \left(\frac{\partial f}{\partial C}\Delta C\right)^2 + \left(\frac{\partial f}{\partial D}\Delta D\right)^2 \qquad \text{(A.3)}$$

Consider the following function for X:

$$X = \frac{A^m B}{C D^n} \tag{A.4}$$

Taking the partial derivatives and substituting into equation A.3 gives:

$$(\Delta X)^2 = \left(\frac{mA^{m-1}B}{CD^n}\Delta A\right)^2 + \left(\frac{A^m}{CD^n}\Delta B\right)^2 + \left(\frac{A^m B}{C^2 D^n}\Delta C\right)^2 + \left(\frac{nA^m B}{CD^{n+1}}\Delta D\right)^2 \tag{A.5}$$

Dividing through by equation A.4 results in the following expression for the fractional uncertainty:

$$\left(\frac{\Delta X}{X}\right)^2 = \left(\frac{m\Delta A}{A}\right)^2 + \left(\frac{\Delta B}{B}\right)^2 + \left(\frac{\Delta C}{C}\right)^2 + \left(\frac{n\Delta D}{D}\right)^2 \tag{A.6}$$

Anytime the functional relationship of a variable is of the form of equation A.4, the fractional uncertainty in the variable will have the form of equation A.6. An interesting point to note, is that the exponent of a variable shows up as a weighting factor in the fractional uncertainty.

Appendix B

Correcting Velocity for Surface Curvature

The calibration factor of a LDV is determined by the wavelength of the laser light and the crossing angle between the beams (i.e. $c_f = \lambda/2\sin(\phi/2)$). When the laser beams pass through a flat surface into a fluid with a different refractive index than air, both the beam crossing angle and wavelength of the laser light in the fluid differ from their values in air. However, this is not a problem, because the changes in the crossing angle and wavelength cancel each other resulting in the same calibration factor in the fluid as was in air. This result is independent of the refractive index of the fluid as long as the beams pass through a flat surface.

Due to the difference in the refractive index between the fluid and air, the distance traversed in the fluid is different from the distance traversed in air. When the beams pass through a flat surface from air into the fluid this traversing ratio is a constant. A detailed treatment of this can be found in Durst *et al.* (1976) *p.* 18.

The above results are no longer valid when the laser beams pass from air through

a curved surface into a fluid. The curvature of the surface affects the calibration factor in the fluid and traversing ratio. The reason for this effect is illustrated in figure B.1. As a laser beam passes through the curved plexiglass wall, the beam is refracted twice, both as it enters the curved wall and when it exits the curved wall. The angle that the refracted beam makes with the normal, θ_{s1}, on the entering surface is different than the angle that the incident beam makes with the normal, θ_{s2}, on the exiting surface. The result of this is that the angle of the refracted beam entering the fluid, θ_f, and the resulting beam crossing angle, θ_c, depend on the angles that the beam makes with the normals as the beam passes through the curved wall. In addition, the traversing ratio is no longer a constant as the crossing point is traversed. If the traversing path of the laser beams is along a radial line, then the crossing point remains on the radial line with only its radial position being affected by the traversing ratio. However, when the beams are not traversed along a radial line, the position of the crossing point is affected in both the radial and tangential directions. In addition, the probe volume can become inclined to the radial direction.

B.1 Traversing Along a Radial Line

It is possible to determine the beam crossing angle and to track the position of the crossing point along a radial line. This can be accomplished by following the path of a beam as it passes through the curved wall into the fluid. A convenient way to track the position of the crossing point is to start with the crossing point on the inside surface of the curved plexiglass wall. Referring to figure B.1, when the crossing point is on the inside surface is the following relationships apply:

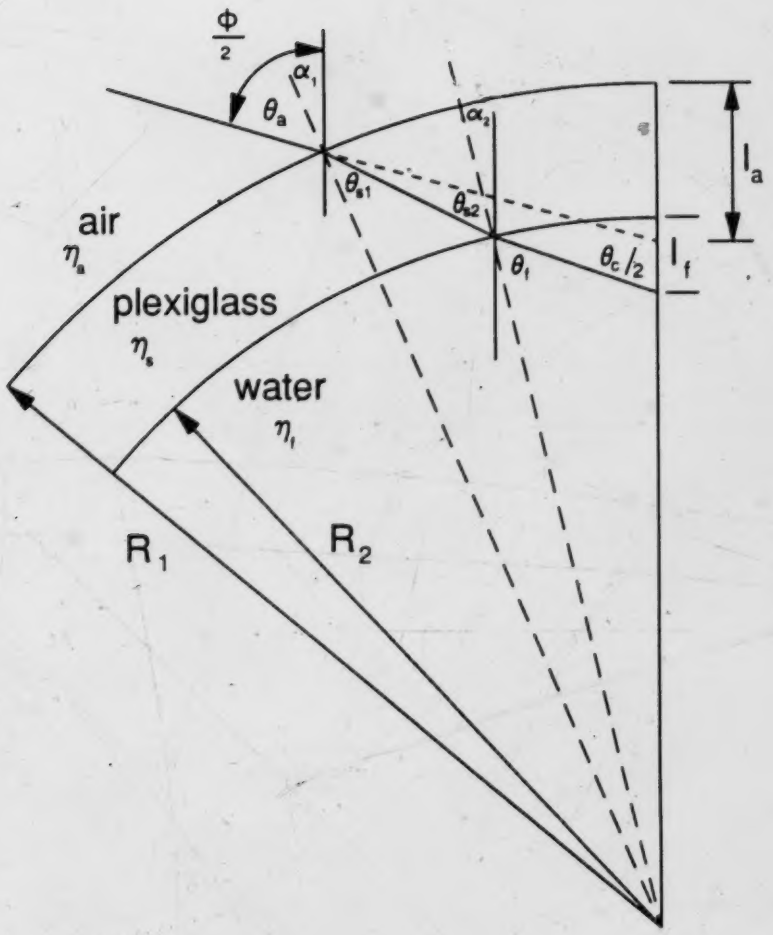

Figure B.1: Schematic of laser beam passing through a curved surface.

$$\tan(\alpha_{1i} + \theta_{s1}) = \frac{R_1 \sin \alpha_{1i}}{R_1 \cos \alpha_{1i} - R_2}$$

$$\theta_{s1} = \arcsin(\frac{\eta_a}{\eta_s} \sin \theta_a) \tag{B.1}$$

$$\theta_a = \frac{\phi}{2} - \alpha_{1i}$$

where:
- α_{1i} = angle that normal to outer surface makes with vertical (i.e. radial) when crossing point is on inner surface
- θ_{s1} = angle refracted beam makes with normal
- ϕ = crossing angle of beams in air
- θ_a = angle incident beam makes with outer surface normal
- R_1, R_2 = outer and inner radius of surface
- η_a, η_s = refractive index of air and surface

Now that the crossing point has been positioned on the inside surface, it is possible to traverse the beams and determine the corresponding angles, α_1 and α_2, that the outer and inner surface normals make with the vertical (i.e. radial). Once α_1 and α_2 have been determined, it is possible to trace the beam path and calculate the the crossing angle, θ_c.

The distance traversed in air to move the crossing point from the outer surface of the plexiglass to the inner surface is given by:

$$l_{ai} = \frac{R_1 \sin \alpha_{1i}}{\tan \frac{\phi}{2}} + R_1(1 - \cos \alpha_{1i}) \tag{B.2}$$

Traversing the crossing point a distance $l_a = \Delta l_a + l_{ai}$, where Δl_a is the distance traversed in air after contacting the inner surface, the angle α_1 is given by:

$$[l_a - R_1(1 - \cos \alpha_1)] \tan \frac{\phi}{2} = R_1 \sin \alpha_1 \tag{B.3}$$

Once equation B.3 has been solved to determine α_1, the angles θ_a and θ_{s1} can be determined from the following relationships:

$$\begin{aligned} \theta_a &= \frac{\phi}{2} - \alpha_1 \\ \theta_{s1} &= \arcsin\left(\frac{\eta_a}{\eta_s}\sin\theta_a\right) \end{aligned} \tag{B.4}$$

The relationship for θ_{s1} was determined by using Snell's law of refraction. Since the angles α_1 and θ_{s1} have been determined, the angle α_2 can be calculated using the following relationship:

$$[R_1\cos\alpha_1 - R_2\cos\alpha_2]\tan(\alpha_1 + \theta_{s1}) \doteq [R_1\sin\alpha_1 - R_2\sin\alpha_2] \tag{B.5}$$

Having solved equation B.5 for α_2, it is now possible to determine θ_{s2}, and the resulting angle of refraction, θ_f,

$$\begin{aligned} \theta_{s2} &= \alpha_1 + \theta_{s1} - \alpha_2 \\ \theta_f &= \arcsin\left(\frac{\eta_g}{\eta_f}\sin\theta_{s2}\right) \end{aligned} \tag{B.6}$$

As before, the relationship for θ_f has been determined by using Snell's law of refraction. The crossing angle of the laser beams θ_c in the fluid is then simply $2(\alpha_2 + \theta_f)$. The actual distance that the crossing point has traversed in the fluid from the inner surface is given by:

$$\Delta l_f = \frac{R_2\sin\alpha_2}{\tan\dfrac{\theta_c}{2}} + R_2(1 - \cos\alpha_2) \tag{B.7}$$

The calibration factor or fringe spacing of the LDV in the fluid can be compared to that of the calibration factor in air resulting in:

$$\frac{d_f}{d_a} = \frac{\eta_a}{\eta_f}\frac{\sin\frac{\phi}{2}}{\sin\frac{\theta_c}{2}} \tag{B.8}$$

Using the calibration factor in air as the standard, equation B.8 is the correction factor to be applied to measured velocity values. Figure B.2 shows the variation

of the correction factor as a function of the position of the crossing point in the duct. Figure B.3 compares the distance traversed in the fluid, Δl_f, to the distance traversed in air, Δl_a. The relationship in figure B.3 is for all practical purposes a straight line, therefore the traversing ratio can be taken to be constant. The curves in figures B.2 and B.3 were calculated using $R_1 = 19.98$ cm, $R_2 = 19.83$ cm, $\phi = 15.7°$, $\eta_a = 1.0$, $\eta_s = 1.49$ and $\eta_f = 1.33$.

B.2 Traversing Along an Arbitrary Path

Given an arbitrary traversing path of the experiment relative to the laser it is desirable to be able to calculate the path that the crossing point takes. In addition, the resulting beam crossing angle at each position must be determined. In order to achieve this, it is necessary to be able to determine the position of the crossing point for any given laser position relative to the apparatus.

Figure B.4 shows a typical laser beam passing through a cylindrical curved surface which has its origin at (0,0) in a cartesian coordinate system. As the beam passes through the curved wall it first contacts the outer surface of the wall and is refracted. The refracted beam then contacts the inner surface of the wall where it is again refracted as it enters the fluid. The beam, which can be treated as a ray of light, always travels in a straight line. However, its direction will change if it is refracted. The path of the beam is given by the equation of a line:

$$\begin{aligned} (y - y_o) &= m(x - x_o) \\ m &= \frac{1}{\tan\theta} \end{aligned} \tag{B.9}$$

where: x_o, y_o = coordinates of a point on beam path
θ = angle that beam makes with vertical (clockwise is the positive direction).

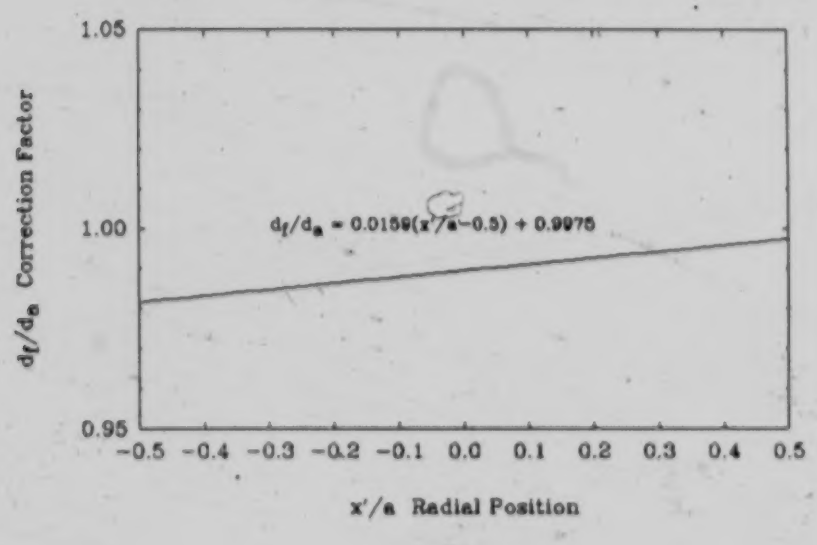

Figure B.2: Correction factor as a function of radial position in duct.

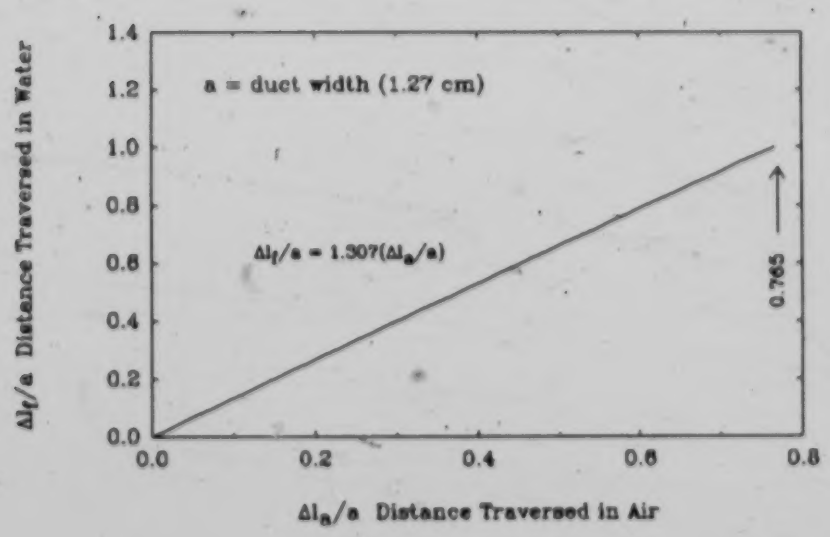

Figure B.3: Traversing distance in water compared to traversing distance in air.

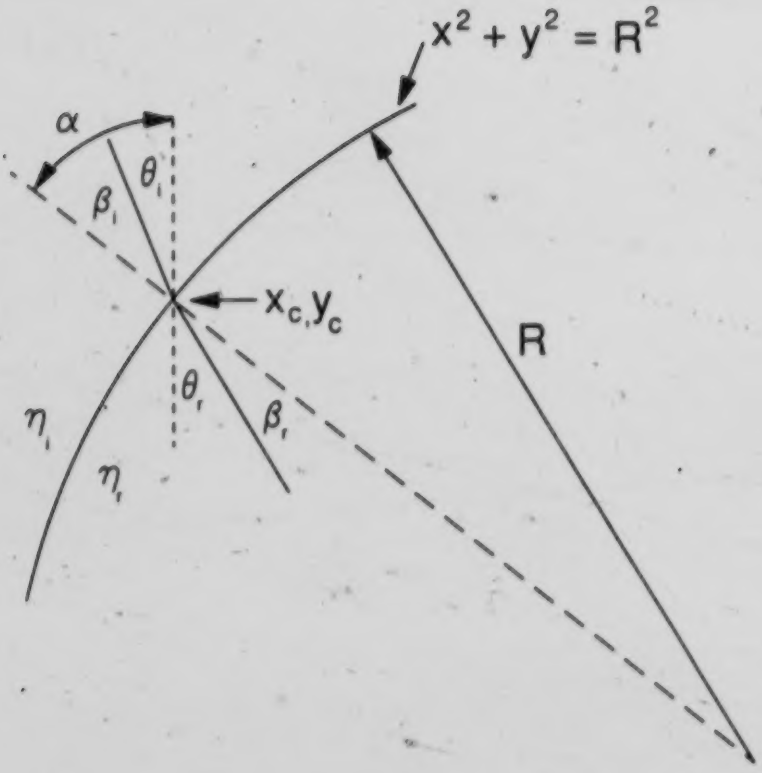

Figure B.4: Schematic of typical laser beam passing through a circular curved surface.

The starting values of x_o and y_o are the coordinates of the crossing point (i.e. focal point of lens) in air. The location where the beam strikes the outer surface of the wall is the intersection point of a line with a circle given by:

$$\begin{aligned}(1+m^2)x_c + 2mbx_c + (b^2+R^2) &= 0 \\ b &= -mx_o + y_o\end{aligned} \tag{B.10}$$

Equation B.10 can be solved using the quadratic equation then substituting the proper root into equation B.9 to get y_c. The angle the surface normal makes with the vertical at the point of intersection is given by:

$$\alpha = \arcsin(\frac{x_c}{R}) \tag{B.11}$$

The angle that the incident beam makes with the normal is:

$$\beta_i = \theta_i - \alpha \tag{B.12}$$

The angle that the refracted beam makes with the normal, as given by Snell's law of refraction, is:

$$\beta_r = \arcsin(\frac{\eta_i}{\eta_r}\sin\beta_i) \tag{B.13}$$

The angle that the refracted beam makes with the vertical is:

$$\theta_r = \beta_r + \alpha \tag{B.14}$$

Once x_c, y_c and θ_r have been determined, equations B.9 through B.14 can be used again to calculate the intersection point of the refracted beam with the inner surface of the wall, and to determine the angle, γ, that the beam entering the fluid makes with the vertical.

The path of the beam in the fluid is described by the equation of a straight line as given in B.9. Using the relationships in B.9 through B.14, the equations for both

laser beam paths in the fluid can be determined. The crossing point of the two beams in the fluid is the intersection between the two lines given by:

$$x_{cross} = \frac{(b_1 - b_2)}{(m_2 - m_1)} \tag{B.15}$$

y_{cross} can be determined by back substitution into one of the equations of the beam paths. If the angle that each beam makes with the vertical as it enters the fluid is γ_1 and γ_2, then the crossing angle is given by:

$$\theta_c = \gamma_2 - \gamma_1 \tag{B.16}$$

Since the traversing path might not be along a radial line, the beam crossing point may become inclined to the vertical axis by an amount:

$$\theta_{inc} = \frac{\gamma_2 + \gamma_1}{2} \tag{B.17}$$

The subscript 1 refers to the laser beam which initially is at a negative angle to the vertical before passing through the wall into the fluid, while the subscript 2 refers to the positive angle beam.

The above equations formed the core of a computer program that was used to calculate the crossing point coordinates, and the crossing and inclination angles, given a location of the front lens of the LDV relative to the apparatus. Using the program to traverse along a radial line gave identical results to the radial traversing analysis.

Appendix C

Physical Properties

C.1 Water

At 23.1°C, the properties of water used in this study were:

$$\mu = 9.304 \times 10^{-4} \text{ kg/m s}$$

$$\rho = 9.975 \times 10^{2} \text{ kg/m}^3$$

$$\nu = 0.9327 \times 10^{-6} \text{ m}^2\text{/s}$$

$$\eta = 1.33$$

where μ, ρ, ν and η are the absolute viscosity, density, kinematic viscosity and refractive index respectively.

The absolute viscosity was calculated from an equation given in the *CRC Handbook of Chemistry and Physics* 70th. edition (1989–1990) *p.* F–40. For a temperature between 20°C and 100°C, the viscosity, μ_T, is given by the following relationship:

$$\log_{10}\frac{\mu_T}{\mu_{20}} = \frac{1.3272(20-T) - 0.001053(T-20)^2}{T+105} \qquad \text{(C.1)}$$

where μ_{20}, the absolute viscosity at $20°C$, is taken as 1.002×10^{-3} kg/m s. For $T = 23.1°C$, the value of absolute viscosity is 9.304×10^{-4} kg/m s.

The value for the density of water was taken from a table in *Perry's Chemical Engineering Handbook* (1984) *p.* 3–75. The value for kinematic viscosity was calculated using the above values for the absolute viscosity and density. At $23.1°C$, the kinematic viscosity, ν, where $\nu = \mu/\rho$, was calculated to be 0.9327×10^{-6} m^2/s.

The refractive index of water was taken from Halliday and Resnick (1974) *Fundamentals of Physics p.* 670.

C.2 Plexiglass

The properties of the plexiglass used in this study were:

$$\rho = 1.18 \times 10^3 \text{ kg/m}^3$$

$$\eta = 1.49$$

where ρ and η are the density and refractive index respectively. The properties were taken from a catalog distributed by Johnston Industrial Plastics.

C.3 Rhodamine Dye

Rhodamine 6G, or also known as Rhodamine 590 ($C_{28}H_{30}N_2O_3 \cdot HCl$), with mol. wt. = 479.02 g/mol., was the dye used in the flow visualization experiments in this study.

C.4 Silicon Carbide Particles

The silicon carbide seeding particles were obtained from T.S.I. (Part# 10081). The physical properties of the particles were:

$$\rho = 3.2 \times 10^3 \text{ kg/m}^3$$

$$\eta = 2.65$$

$$\text{mean diameter} = 1.5 \times 10^{-6} \text{ m}$$

$$\text{geometric standard deviation} = 1.4$$

$$\text{particle shape} = \text{irregular}$$

ρ and η are the density and refractive index respectively. The properties were supplied on the product label.

Appendix D

Tabulated Data

θ Axial Position	Dean Number
20°	125.9
40°	125.2
60°	125.8
80°	124.9
100°	124.8
120°	125.0
140°	125.0
160°	124.7
180°	124.7
200°	124.8
220°	125.0
240°	125.4

Table D.1: Dean numbers of measured horizontal velocity profiles at $Dn = 125$.

θ Axial Position	Dean Number
20°	137.0
40°	137.0
60°	137.1
80°	137.3
100°	137.3
120°	137.4
140°	137.3
160°	136.9
180°	137.3
200°	137.2
220°	137.2
240°	137.5

Table D.2: Dean numbers of measured horizontal velocity profiles at $Dn = 137$.

θ Axial Position	Dean Number
20°	149.9
40°	149.5
60°	149.5
80°	150.5
100°	150.4
120°	149.4
140°	149.5
160°	149.8
180°	150.3
200°	150.1
220°	150.2
240°	150.3

Table D.3: Dean numbers of measured horizontal velocity profiles at $Dn = 150$.

θ Axial Position	Dean Number
20°	150.0
40°	149.6
60°	148.8
80°	149.7
100°	149.4
120°	149.5
140°	149.4
160°	149.9
180°	149.3
200°	150.7
220°	150.3
240°	150.4

Table D.4: Dean numbers of measured vertical velocity profiles at $Dn = 150$.

Dean Number	Development Length
50	70°
75	80°
100	90°
125	100°
130	730°
131	520°
132	425°
133	385°
135	335°
137	315°
140	280°
142	265°
144	255°
146	240°
148	235°
150	225°
163	180°
175	165°

Table D.5: Tabulated data for figure 6.64.